Imperial College of Science, Technology and Medicine
Department of Materials
Centre for Nuclear Engineering

Atomistic Scale Simulation of Materials for Future Nuclear Reactors

Simon C. Middleburgh

Submitted in part fulfilment of the requirements for the degree of
Doctor of Philosophy in Materials of Imperial College, January 2012

Abstract

Atomic scale simulations have been carried out on three systems that are being considered for use in future nuclear energy applications, both fission and fusion based.

Uranium dioxide and chromium doped fuel are considered in the early chapters in order to understand the processes important in high burnup nuclear fuel. The oxygen stoichiometry of the uranium dioxide lattice was found to have a large effect on both fission product solution and crystal swelling. Predictions were found to replicate experimental data well. Transport properties of cations via uranium vacancies in hyperstoichiometic UO_{2+x} have been studied for the first time on the atomic scale. Understanding the arrangement of U^{5+} cations around a migrating species has proved important for identifying low energy migration process.

Zirconium diboride and beryllium have also been studied. Zirconium diboride is of interest due to its use as a burnable poison for some advanced fuel types and also because of its ability to resist very high temperatures. The variation in stoichiometry of ZrB_2 was found to accommodate excess boron but very little excess zirconium. The accommodation of the boron-10 transmutation products, lithium and helium, are also studied with helium being released from the lattice via a low energy process.

Beryllium is of importance as a potential cladding for fission fuel and in fusion reactors. The intrinsic defect behaviour has been discussed for the first time in this thesis while extrinsic species present in beryllium alloys through alloying, manufacturing processes or environmental exposure have also been studied. Again, helium was found to be readily released from the lattice but only as an interstitial species and not as a substitutional defect.

The copyright of this thesis rests with the author and no quotations from it or information derived from it may be published without the prior written consent of the author.

© S.C. Middleburgh 2012



1,229 Days

Jo Dixon

Acknowledgements

This has undoubtedly been the most interesting, emotional and life-changing chapter of my life. When I started this project, I had no idea where it was going to take me and the kind of people I was going to meet. I want to thank everyone for making my choice to do a PhD the best decision of my life.

I would like to thank Westinghouse Electric Sweden AB for funding my PhD through the FPP3 project. Everyone in BTP made me feel welcome every time I stayed and I always look forward to my next visit. Jonathan Wright, Karin Backman and Radek Jošek made my time in Sweden particularly interesting and enjoyable, thank you. I would like to specifically thank Lars Hallstadius for his un-ending interest and support for my work throughout my PhD.

All of my thanks and appreciation go to my supervisor, Robin for his help, support and willing to take me on as a member of the ASG and get me through a PhD. The number of times that you magically managed to solve my problems, in my research and in 'real life' was pretty impressive. My thanks and the reasons for them could probably take up an entire chapter but I will stop here and just say it has been a pleasure and I am looking forward to seeing you 'down under' for a pint. Thank you.

Paul, you have been a true friend and I will keep all of the great memories that I have of our drinks in Västerås and London dearly. I am forever indebted to you for introducing me to the beauty of science and re-vitalising my drive to be a good scientist. And thank you for introducing me to the plethora of science fiction films out there. I can't wait for the next time we are watching a film on a 3 metre screen with a glass of single malt.

All my gratitude goes to all of the members of the ASG and other colleagues in the RSM that have helped me in my time here. Dave and Alex, my original post-docs who introduced me to the sustained drinking culture of the ASG and really looked after me for the first year or so, Michael for all of his support, conversations (I'm so glad you finally got your Jag), pints and coding skills, Sam for taking me on 'tea and a stand' trips and Clare for her amazing support, smile and enthusiasm for helping. Clare, I don't think I'll ever be a dancer (but thanks for trying). Thank you Christabel for being there every step of the

way, I can't wait to see you in Australia.

Emma, you have been there for me every step of the way. You are a remarkable woman and an amazing friend. Your everlasting loyalty, smile and energy have made my PhD a joy.

Mark, I hope you manage to finally visit Stonehenge and get your own photo of it. I am forever grateful for you arranging the trip down to HMS Drake, it has been a pleasure (sorry about the giraffes).

Elly, you have always been there for me and I am so thankful for so much to you. From day 1, seven years ago as undergraduates you have watched my back, made me laugh, protected me from squirrels, challenged me, drank with me (too much) and provided a golden lining to my life at Imperial. I am thankful that I can call you my friend. We have been through a lot together but there is much, much more to come. I can't wait to see you at some far flung corner of the world.

When I started this PhD I was organised enough not to have a place to live. Luckily, Nanna Toby took me under her wing and we spent a lovely Autumn together in Barking. Your tea, toast and conversation was my ignition switch every day. I will never forget our shopping trips and conversations. Poppa Sid was a great inspiration to me. You always will be.

Poppa Marc and Nanna Tel, thank you for finding my amazing flat and being there for me. The soup, comfy bed and friendly faces were so important to me. You were there whenever I needed you and for that I thank you so much.

Jo, you helped me face the world every day and I don't know how I would have finished this thesis without you. Thank you for supporting me, loving me and not letting me give up. I'm sure we will share uncountable bottles of bubbly together. There is no zoo too far for us to go to. Thank you my love.

Rob, thanks for being there as a friend and brother. You are going to be an amazing doctor. It is just a shame you support Chelsea.

Mum and Dad. You have been a constant source of food, tea and love. Without you, this

endeavour would not have been possible. Mum, thank you for always being there on the end of the phone and making home such a lovely place to go back to, I wonder if chocolate cake travels well? Dad, thank you so much for being there for me every step of the way and feeding and watering me - you can have your flat back now.

Dedication

For Cath,

Your love of life and the world have inspired me every day since we last met and will do so forever.



Contents

Abstract **i**

Acknowledgements **iii**

1 Introduction **1**

1.1 Nuclear Power 1

1.1.1 Introduction 1

1.1.2 Light Water Reactor Design 4

1.1.3 Other Current Reactor Designs 6

1.2 Nuclear Fuel 8

1.2.1 Introduction 8

1.2.2 UO_2 Fuel Fabrication 9

1.2.3 In-Reactor Fuel Behaviour 17

1.2.4 Effects of Stoichiometry 22

1.2.5 Dopants in UO_2 25

1.2.6 Controlling Fuel Burn-Up 29

1.3 Nuclear Applications of Beryllium 31

1.4 Atomic Theory 34

1.4.1 Point Defects in Crystalline Solids 34

1.4.2 Transport in Crystalline Solids 36

1.5 Aims of this Work 37

2 Calculation Methods **39**

2.1 Introduction to Atomic Scale Simulations 39

2.2 Empirical Potentials 40

2.2.1 Introduction 40

2.2.2 The Shell Model 44

2.2.3 Empirical Potentials Simulations 46

2.3 Quantum Mechanical Methods 46

2.3.1 Introduction 46

2.3.2 Born-Oppenheimer Approximation 47

2.3.3 Implementing the Born-Oppenheimer Approximation 48

2.4 Static Calculations 53

2.4.1 Supercell Methods 53

2.4.2 The Mott-Littleton Method 58

3 Solution of Dopants and Fission Products in Uranium Dioxide **64**

3.1 Introduction 64

3.2 Solution Energies of Trivalent Oxides into UO_2 65

3.2.1 Trivalent Cation Solution into Stoichiometric UO_2 65

3.2.2 Reaction into Hyper-stoichiometric UO_2 75

3.2.3 Validation of Chromium Charge State 78

3.3 Defect Relaxation Volumes in Uranium Dioxide 79

3.3.1 Tetravalent Cations 80

3.3.2 Trivalent Cations 82

3.3.3 Divalent Cation 86

3.3.4 Lattice Parameter Variation with Burnup 88

3.4 Summary 90

4 Effect of Trivalent Cations on the Transport Processes In Uranium Dioxide 93

4.1 Introduction 93

4.2 Migration Processes 94

4.3 Uranium Vacancy Cluster Morphology and Migration 95

4.3.1 $0 \times U^{5+}$ Cations 96

4.3.2 $1 \times U^{5+}$ Cation 97

4.3.3 $2 \times U^{5+}$ Cations 100

4.3.4 $3 \times U^{5+}$ Cations 108

4.3.5 $4 \times U^{5+}$ Cations 111

4.3.6 Summary of Uranium Vacancy Migration in Undoped UO_{2+x} and Future Work Required 113

4.4 Trivalent Cation and Vacancy Cluster Morphology 113

4.4.1 Binding of Trivalent Cations To Vacancies 114

4.4.2 Diffusion of Cr^{3+} in UO_{2+x} Fuel 118

4.4.3 Summary of Trivalent Cation Migration and Effect on Vacancy Migration 122

5 Point Defects and Transmutation Products in Zirconium Diboride 124

5.1 Introduction 124

5.2 Structure of ZrB_2 125

5.3 Computational Details 127

5.4 Intrinsic Defect Processes of ZrB_2 129

5.4.1 Point Defects in ZrB_2 130

5.4.2 Variation of Stoichiometry of ZrB_2 132

5.5 Helium and Lithium Defects in ZrB_2 134

5.5.1 Accommodation of He and Li 135

5.5.2 Transport of He and Li Through ZrB_2 137

5.6 Summary 140

6 Defects and Transport Processes in Beryllium 142

6.1 Introduction 142

6.2 Structure of Beryllium and the Intermetallics $FeBe_5$, $FeAlBe_4$, Be_2C and $MgBe_{13}$ 143

6.2.1 Beryllium 143

6.2.2 Fe-Al-Be Intermetallics 146

6.2.3 Be_2C 148

6.2.4 $Be_{13}Mg$ 148

6.3 Intrinsic Defect Processes of Beryllium 149

6.3.1 Defect Formation Energies 149

6.3.2 Migration Activation Energies of Intrinsic Defects 151

6.4 Extrinsic Defect Processes in Beryllium 153

6.4.1 Accommodation and solution of defect species in the Be lattice . . . 155

6.4.2 Gas Species Hydrogen, Oxygen and Helium 156

6.4.3 Carbon in Beryllium 161

6.4.4 Magnesium in Beryllium 162

6.4.5 Silicon in Beryllium 162

6.4.6 Aluminium in Beryllium 162

6.4.7 Iron in Beryllium 163

6.4.8 The $FeAlBe_4$ Intermetallic 164

6.5 Defects in the $FeBe_5$ and $FeAlBe_4$ Intermetallics 166

6.5.1 $FeBe_5$ 166

6.5.2 $FeAlBe_4$ 168

6.6 Summary 169

7 Ongoing and Future Work **173**

7.1 Atomic Scale Simulations of Nuclear Fuel 173

7.1.1 Transport in UO_2 173

7.1.2 Dopants and Fission Products at Grain Boundaries and Surfaces . . 174

7.1.3 Dopant and Fission Product Effect on the Formation of High Burnup Structure 177

7.1.4 DFT Approach to Diffusion of Dopants in Uranium Dioxide 177

7.1.5 Doping of ThO_2 and $(MA,U)O_2$ 179

7.2 Atomic Scale Simulations of Burnable Poisons 181

7.2.1 Irradiation of ZrB_2 181

7.2.2 Li and Impurity Effects on Diffusion 182

7.2.3 HfB_2-ZrB_2-SiC System 182

7.3 Atomic Scale Simulations of Beryllium 183

A Kröger-Vink Nomenclature **185**

Bibliography **186**

List of Tables

1.1 Comparison of Current Reactor Designs (Taken from [2, 18]). 7

2.1 Buckingham potential parameters used throughout this work. 43

3.1 Defect relaxation volumes of tetravalent cations accommodated in UO_2 . . . 82

3.2 Defect volumes for trivalent cations accommodated in UO_2 (via oxygen vacancy compensation, equation 3.18) and UO_{2+x} (via U^{5+} ion compensation, equation 3.19). Neutral defect cluster formation is assumed in each case. . . 83

3.3 Defect relaxation volumes of divalent cations accommodated in UO_2 andUO_{2+x}. 87

4.1 Summary of uranium cation migration energies (eV) into a V_U'''' balanced by U^{5+} cations. All migration processes processes are for U^{4+} ions migrating into a vacancy as opposed to U^{5+} as these were found to be universally lower.112

5.1 Symmetrically distinct sites within the P6mmm space group showing the position (multiplicity and Wyckoff letter), symmetry, coordinates and what occupies the site within ZrB_2. 125

5.2 Comparison of lattice vectors with exchange-correlation functionals in ZrB_2. 127

5.3 Intrinsic ZrB_2 defect energies calculated in a 4×4×3 supercell. 130

5.4 He and Li incorporation energies in ZrB_2. 136

5.5 He and Li diffusion Mechanism energies in ZrB_2 where X is either Li or He . 137

6.1 Comparison of calculated lattice constants with data from experimental studies. 147

6.2 Intrinsic Be defect formation energies calculated using a 5×5×4 supercell (values calculated using a 4×4×3 supercell are reported in brackets). 150

6.3 Accommodation energies of He, H, O, C, Fe, Al, Mg and Si in Be (eV). . . . 155

6.4 Solution energies of He, H from H_2, O from O_2, Fe from $FeBe_5$, Al from Al metal, C from Be_2C, Mg from $Be_{13}Mg$ and Si from Si solid into Be (eV). . . 156

6.5 Intrinsic defect energies within $FeBe_5$ (eV). 166

6.6 Elastic constants (c) and bulk modulus (K) for cubic $FeBe_4$. 167

6.7 Solution energies of H_2, He, O_2, Al, C from Be_2C, Mg and Si in $FeBe_5$ (eV). 167

6.8 Elastic constants (c) and bulk modulus (K) for cubic $AlFeBe_4$. 168

6.9 Solution energies of H_2, He and O_2 in $FeAlBe_4$ (eV). 168

List of Figures

1.1 Chicago Pile 1 - Drawing showing the graphite and blocks surrounding the uranium core. The cadmium control rods are shown to be inserted horizontally into the pile [4]. 2

1.2 Pressurised water reactor design - Reactor containment is shown housing the reactor itself, containing the fuel, and the steam generator. The components outside of the reactor containment are used to convert the steam generated in the containment to useful electricity (Taken from [13]). 4

1.3 Prototype fast breeder reactor flow diagram. The sodium circuits and steam circuits are labelled (Taken from [18]). 7

1.4 Economical uranium global resources (OECD/NEA Reasonably Assured Resources Category). Total resources are 2438100 tU. It should be noted that some countries not shown here have known uranium resources (e.g. Pakistan, India and Czech Republic). Adapted from [31]. 10

1.5 Extraction process detailing the various steps to producing U_3O_8 for further processing. Adapted from [31]. 10

1.6 Micrograph showing the polished cross section of a number of UO_2 powder particles produced by the AUC route at Westinghouse Electric Sweden (Taken by Hans Bergvist and Wubeshet Sahle at KTH, Sweden). 13

1.7 Light water reactor UO_2 fuel pellet. 14

1.8 Various material transport processes possible during sintering illustrated with two spherical particles after necking. The processes are: **1.** Viscous flow (η) **2.** Gas diffusion (D_g) , evaporation/condensation (Δp) **3.** Surface diffusion (D_s) **4.** Lattice diffusion between the grain boundary or grain surface to the neck (D_l) **5.**Grain boundary diffusion (D_g). Adapted from [43]. . 15

1.9 Fission reaction showing a U_{92}^{235} atom reacting with a neutron to produce three neutrons and two different fission products, Ba_{56}^{141} and Ke_{36}^{92}. 17

1.10 Typical fission yield after 2.9 % FIMA [51] 18

1.11 Metallic precipitates (light spots) on the grain boundaries of MOX fuel [64] 19

1.12 Painted schematic of fission gas release. The fission gas species (red) can be seen to be trapped at either an internal gas bubble (intragranular) shown in white or at a grain boundary bubble (intergranular) shown in black. 21

1.13 Micrograph showing the interlinked porosity that develops as fission gas is released from the grains to the grain boundary in polycrystalline UO_2 (taken from [71]). 22

1.14 Intragranular bubbles in UO_2 irradiated to 23 GWd/t. The intragranular bubbles are near spherical. Also shown are intergranular bubbles around the grain boundaries (taken from [72]). 23

1.15 The Oxygen-Uranium system phase diagram by Okamoto [80]. 23

1.16 The change in Arrhenious energy for the migration of cations with stoichiometry in UO_2 taken from [61]. 24

1.17 The triple alpha nucleosynthesis process showing the fusion of He_2^4 nuclei to first produce Be_4^8 and then the C_6^{12} nucleus. 32

1.18 Design for the ITER tokomak fusion reactor. The Be layer on the blanket layer is highlighted. Taken from [110]. 33

1.19 Illustration of an interstitial migration showing how the energy may change as the migrating species moves through the crystal showing the energy barrier to migration (E_m). 37

2.1 Varying interaction energy due to Coulombic interactions of like-charged ions (blue) and oppositely charged ions (red) as a function of the interionic separation distance, r_{ij}, described by the first expression in equation 2.1. . . 41

2.2 Interaction energy as a function of the interionic separation due to the Buckingham pairwise interactions between U^{4+} and O^{2-} ions (blue) and O^{2-} and O^{2-} ions (red) as described by the second and third parts of equation 2.1. The O^{2-}-O^{2-} interaction includes a 'C' term whilst for the U^{4+}-O^{2-} the 'C' term is zero. 42

2.3 The representation of an ion in the Dick and Overhauser shell model [140]. The shell is shown in blue, the core in red and both are attached to eachother with a spring. 45

2.4 Displacement of the shell of an ion due to a point charge. A negative charge will push away the negative shell and a positive charge will attract the negative shell. 45

2.5 Diagram illustrating the difference between the all-electron potential and wave-functions with the pseudopotential and wave-function. The cut-off radius for the pseudopotential is shown. Figure based on that given in [151]. 52

2.6 The formation of 2×2×2 supercells from primitive and unit fluorite cells. . . 54

2.7 Illustration of the two region approach used to carry out Mott-Littleton defect energy calculations. The defect in the centre (light green) is surrounded by three concentric spheres, region I (green), region IIa (red) and region IIb (blue). 58

2.8 Example of how a defect energy will vary with region I size. Here the region II radius is varied around an oxygen vacancy in UO_2. In these calculations the region IIa radius was kept constant at 34 Å. 59

3.1 Showing the variation in solution energy with oxygen vacancy and trivalent interstitial defect compensation mechanisms given in equations 3.1 and 3.2 when defects are treated as isolated. 67

3.2 Oxygen vacancy cluster that is predicted to form, accommodating two trivalent cations. The red cube represents the vacant oxygen ($V_O^{\bullet\bullet}$) and the green spheres represent the trivalent cations residing on a uranium site (T_U'). . . . 68

3.3 Uranium interstitial cluster that is predicted to form, accommodating four trivalent cations. The green spheres represent the trivalent cations, with the central trivalent cation being the ($\frac{1}{2}$,$\frac{1}{2}$,$\frac{1}{2}$) interstitial site. 69

3.4 Showing the variation in solution energy with oxygen vacancy and trivalent interstitial defect compensation mechanisms given in equations 3.1 and 3.2 when defects are treated as clustered. 70

3.5 Binding energy of the constituent defects that make up the $\{2T_U':V_O^{\bullet\bullet}\}^\times$ cluster for a range of trivalent cations. The smaller cations are more bound (i.e. with a greater negative energy). 71

3.6 Schematic of the formation of an oxygen Frenkel defect pair (both defects shown on the left in orange, the vacancy as a cube and interstitial as a sphere. 72

3.7 The drive for the defects produced during solution to cluster forming the $\{2T_U':V_O^{\bullet\bullet}\}^\times$ cluster. Cations that have values lower than 1.0 are predicted to form clusters while trivalent cations above are predicted to enter UO_2 by forming isolated defects. 74

3.8 Uranium 5+ cluster that may form, accommodating a trivalent cation. The navy blue sphere represents the oxidised uranium ($U_U^\bullet$), the green sphere represents a trivalent cation sitting on a uranium site (T_U'). 76

3.9 Showing the variation in solution energy of various trivalent metal oxides into UO_{2+x} as a function of cation radius. Both reactions involving hyperstoichiometry in the uranium dioxide lattice compensated by oxygen interstitials (equation 3.11) and uranium vacancies (equation 3.12) are considered. 77

3.10 Illustration of reaction 3.13. On the left, a Cr^{3+} cation is charge balanced by a U^{5+} cation to maintain an overall "4+" charge in the lattice. On the right, the Cr takes on a "4+" charge and no longer needs to be charge balanced by another defect. 79

3.11 Variation in defect relaxation volume for tetravalent cations in UO_2 as a function of their ionic radius. 81

3.12 Defect volumes for trivalent cations accommodated in UO_2 (via oxygen vacancy compensation, equation 3.18) and UO_{2+x} (via U^{5+} ion compensation, equation 3.19). Neutral defect cluster formation is assumed in each case. . . 85

3.13 Defect volumes for divalent cations accommodated in UO_2 (via oxygen vacancy compensation, equation 3.20) and UO_{2+x} (via U^{5+} ion compensation, equation 3.21). Neutral defect cluster formation is assumed in each case. . . 87

3.14 Variation of UO_2 unit cell volume with burnup due to fission products using concentrations from [58], compared to data from Une *et al.* [59] and Davies and Ewart [60]. 89

4.1 Diffusion of a species (red sphere) by a sequential movement of a vacancy (box) in a (100) FCC plane of UO_2. 94

4.2 Diffusion of a species (red sphere) by the capture then release of a vacancy (box) in a (100) FCC plane of UO_2. 95

4.3 The lowest energy cluster containing one uranium vacancy and one U^{5+} ion (note: this is not a charge neutral cluster). The uranium vacancy is represented by a blue cube and the U^{5+} ion as a green sphere. The migrating U^{4+} cation is represented by a solid blue sphere. 97

4.4 The energy barrier (eV) to migration for a U^{4+} cation migrating into a uranium vacancy in the <110> direction for all calculated cluster morphologies plotted against the cluster stability relative to the most stable arrangement of $\{V_U'''':U_U^{\bullet}\}'''$ cluster. 98

4.5 The cluster morphology that produces the smallest barrier to migration that contains two uranium vacancies, one migrating U^{4+} cation and 1 U^{5+} ion. The uranium vacancy is represented by a blue cube and the U^{5+} ion as a green sphere. The migrating U^{4+} cation is represented by a solid blue sphere half way between uranium lattice sites. 99

4.6 The lowest energy cluster containing one uranium vacancy and 2 U^{5+} ions (note: this is not a charge neutral cluster). The uranium vacancy is represented by a blue cube and the U^{5+} ions as green spheres. 101

4.7 This is the cluster that will facilitate the migration of a U^{4+} ion to migrate into a vacancy with the lowest total energy. The uranium vacancies are represented by a blue cube and the U^{5+} ions as green spheres. 102

4.8 The energy barrier to migration for a U^{4+} cation migrating into a uranium vacancy in the <110> direction for all calculated cluster morphologies plotted against the morphology stability relative to the most stable arrangement of $\{V_U'''':2U_U^{\bullet}\}''$ cluster. The line represents the migration energy for the lowest cluster morphology arrangement minus the relative cluster energy to calculate whether a migration is more or less favourable than that for the most stable cluster. 103

4.9 The cluster that will allow the migration of a U^{4+} ion to migrate into a vacancy with the lowest energy with two U^{5+} ions in the cluster. The uranium vacancies are represented by a blue cube and the U^{5+} ions as green spheres. The migrating U^{4+} ions is represented by a solid dark blue sphere. 104

4.10 The cluster that will facilitate the migration of a U^{5+} ion into a vacancy with the lowest energy. The uranium vacancies are represented by a blue cube and the U^{5+} ions as green spheres. 105

4.11 The energy barrier to migration for a U^{5+} cation migrating into a uranium vacancy in the <110> direction for all calculated cluster morphologies plotted against the morphology stability relative to the most stable arrangement of $\{V_U''''{:}2U_U^{\bullet}\}''$ cluster. The line represents the migration energy for the lowest cluster morphology arrangement minus the relative cluster energy to calculate whether a migration is more or less favourable than that for the most stable cluster. 106

4.12 The cluster that will allow the migration of a U^{5+} ion to migrate into a vacancy with a low energy and an morphology close to the ground state morphology. The uranium vacancies are represented by a blue cube and the U^{5+} ions as green spheres. 107

4.13 The lowest energy cluster containing one uranium vacancy and 3 U^{5+} ions (note: this is not a charge neutral cluster). The uranium vacancy is represented by a blue cube and the U^{5+} ions as green spheres. 108

4.14 The energy barrier to migration for a U^{4+} cation migrating into a uranium vacancy in the <110> direction for all calculated cluster morphologies plotted against the morphology stability relative to the most stable arrangement of $\{V_U''''{:}3U_U^{\bullet}\}'$ cluster. The line represents the migration energy for the lowest cluster morphology arrangement minus the relative cluster energy to calculate whether a migration is more or less favourable than that for the most stable cluster. 109

4.15 The energy barrier to migration for a U^{5+} cation migrating into a uranium vacancy in the <110> direction for all calculated cluster morphologies plotted against the morphology stability relative to the most stable arrangement of $\{V_U''''{:}3U_U^{\bullet}\}'$ cluster. The line represents the migration energy for the lowest cluster morphology arrangement minus the relative cluster energy to calculate whether a migration is more or less favourable than that for the most stable cluster. 110

4.16 The lowest energy cluster containing one uranium vacancy and 4 U^{5+} ions (note: this is a charge neutral cluster). The uranium vacancy is represented by a blue cube and the U^{5+} ions as green spheres. 112

4.17 Binding energy of the most stable $\{V_U'''':Cr_U':2U_U^\bullet\}''''$ cluster with various V_U'''' to Cr_U' separations. 115

4.18 The lowest energy morphology of the $\{V_U'''':Cr_U':2U_U^\bullet\}''''$ cluster. 116

4.19 Binding energy of the most stable $\{V_U'''':In_U':2U_U^\bullet\}''''$ cluster with various V_U'''' to In_U' separations. 116

4.20 The lowest energy morphology of the $\{V_U'''':Cr_U':3U_U^\bullet\}''$ cluster. 117

4.21 Binding energies of $\{V_U'''':Cr_U':xU_U^\bullet\}''''^{-x}$ clusters with various increasing numbers of U^{5+} cations. A cubic fit has been made to the four points to understand the approximate value of the number of U^{5+} ions that will give the most bound cluster. 118

4.22 The energy barrier to migration for a Cr^{3+} cation migrating into a uranium vacancy in the <100> direction for all calculated cluster morphologies plotted against the morphology stability relative to the most stable arrangement of $\{V_U'''':Cr_U'2U_U^\bullet\}'$ cluster. 119

4.23 The energy barrier to migration for a Cr^{3+} cation migrating into a uranium vacancy in the <110> direction for all calculated cluster morphologies plotted against the morphology stability relative to the most stable arrangement of the $\{V_U'''':Cr_U'2U_U^\bullet\}'$ cluster. 120

4.24 The lowest energy migration of a Cr^{3+} cation into a vacancy in the $\{V_U'''':Cr_U':2U_U^\bullet\}''$ cluster. Here, the Cr^{3+} ion is shown as a purple sphere and the vacancy as a blue cube. 121

4.25 The energy barrier to migration for a U^{4+} cation migrating away from a chromium substitutional defect in the <110> direction for all calculated cluster morphologies plotted against the morphology stability relative to the most stable arrangement of $\{V_U'''':Cr_U'2U_U^\bullet\}'$ cluster. 122

5.1 Structure of ZrB_2 showing the zirconium atoms as light blue and the boron atoms as dark yellow. The five interstitial sites are shown as red crosses. . . 126

5.2 Convergence of the cut-off energy for use in ZrB_2 calulations. The system energies are relative to the lowest system energy calculated, at 475 eV. . . . 128

5.3 Zirconium interstitial on the (0,0,z) site forming a split interstitial. Zirconium shown in blue and boron in green. 131

5.4 Neutron cross section spectrum of B_5^{10} showing a decrease in capture probability at high neutron energies [191]. 135

5.5 Structure of ZrB_2 showing the zirconium atoms as light blue and the boron atoms as dark yellow. The five interstitial sites are shown as red crosses. . . 139

5.6 Nudged elastic band calculation of the He migration from a $X_{i(\frac{1}{3},\frac{2}{3},0)}$ site to a $X_{i(\frac{1}{2},0,0)}$ site showing the activation energy for He migration to be 0.51 eV. 139

5.7 Process showing the transmutation of a boron atom by a neutron into a lithium and helium atom leaving a vacancy. Lithium will occupy the vacant B site preferentially over He. 141

6.1 The hexagonal closed packed (HCP) structure of beryllium showing three basal layers and the octahedral interstitial (Oc), tetrahedral interstitial (Te), hexahedral interstitial (Hx), trigonal interstitial (Tr) and Non-basal trigonal interstitial positions. 144

6.2 Illustration of convergence of cut-off energy with the Be system showing that 400 eV gives good accuracy of above 0.001 eV. 145

6.3 The cubic $FeBe_5$ intermetallic crystal structure. Showing the Be atoms on the (0,0,0) and $(\frac{5}{8},\frac{5}{8},\frac{5}{8})$ sites (blue) and the Fe atoms half occupying the $(\frac{1}{4},\frac{1}{4},\frac{1}{4})$ sites. 146

6.4 The cubic $FeAlBe_4$ intermetallic crystal structure. Showing the Al atoms on the (0,0,0) site (green), Be atoms at the $(\frac{5}{8},\frac{5}{8},\frac{5}{8})$ sites (blue) and the Fe atoms half occupying the $(\frac{1}{4},\frac{1}{4},\frac{1}{4})$ sites. 147

6.5 The fluorite crystal structure of Be_2C. Be atoms are shown to occupy the $(\frac{1}{4},\frac{1}{4},\frac{1}{4})$ sites (blue) and the C atoms the FCC (0,0,0) sites (grey). 148

6.6 Energy profile for the migration of a Be atom via vacancy mechanism through the basal plane between equivalent lattice sites, with configurations shown above. 152

6.7 Energy profile for the migration of a Be interstitial atom between Tr sites through a NBt site. 154

6.8 Energy profile associated with the migration of a H interstitial defect moving from a Hx site to an Oc site. 158

6.9 Energy profile associated with the migration of the He interstitial defect moving from a Tr site to a Hx site. 159

6.10 Energy profile for the migration of a vacancy moving through the basal plane towards a He_{Be} defect. 160

6.11 Energy variation of the migration of a vacancy moving through the basal plane around a He_{Be} defect. 161

7.1 Image of a $\Sigma 5$ grain boundary in UO_2. The plot shows the interaction energy of the two grain boundaries in the system falling with increases in distance between them. This highlights the importance of using large enough system sizes when investigating grain boundaries. 175

7.2 Change in defect energy of a Schottky trivacancy with distance from a UO_2 <110> grain surface. The plot shows the drive for trivacancies to move towards the surface. 176

7.3 Image removed as instructed by funding body. 178

7.4 Twin in beryllium created using the program 'GBStudio'. 184

A.1 Summary of the Kröger-Vink notation used throughout this thesis to describe defects. 185

Chapter 1

Introduction

- “The Italian navigator has just landed in the new world. The earth was not as large as he had supposed, so he arrived earlier."

- “Were the natives friendly?"

- “Everyone landed safe and happy."

Telephone conversation between Arthur H. Compton and James B. Conant.

December 2nd, 1942 [1].

1.1 Nuclear Power

1.1.1 Introduction

Supervised by Enrico Fermi and Leo Szilard, under an abandoned sports ground stand at the University of Chicago, a young scientist removed a cadmium coated control rod from Chicago Pile 1 allowing the first artificial fission chain reaction to begin [2, 3]. The scientists looked on, Fermi carefully monitoring the neutron activity from the un-shielded pile containing 400 tons of graphite, 6 tons of uranium metal and 50 tons of uranium oxide (see Figure 1.1 [4]). Thirty minutes passed before the neutron absorbing cadmium

rods were pushed back in, gently bringing the first man-made fission reaction to an end. Mankind had harnessed fission.

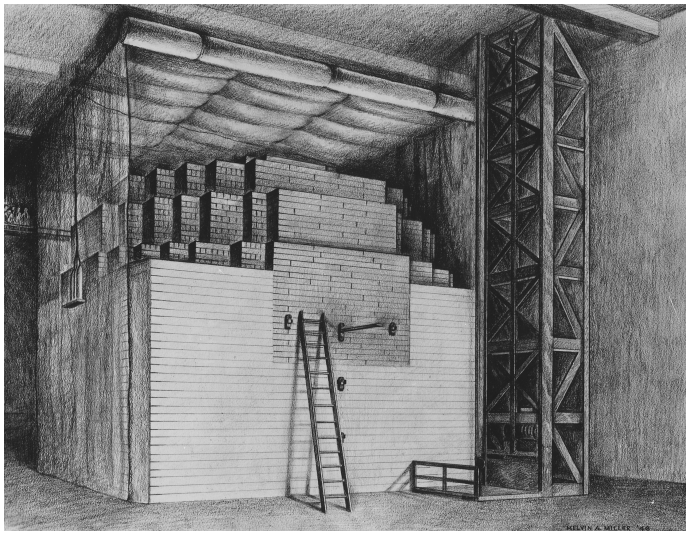


Figure 1.1: Chicago Pile 1 - Drawing showing the graphite and blocks surrounding the uranium core. The cadmium control rods are shown to be inserted horizontally into the pile [4].

Of course, this first controlled fission reaction was the preliminary step to creating the first un-controlled man-made fission reaction [5], the atomic bomb. The first piles were used to breed uranium into plutonium, used as the fissionable material in fission bomb tested at Alamogordo Bombing and Gunnery Range in New Mexico (now White Sands Missile Range). However, once the fog of war passed in the early years of the 1950's, the lessons learned from CP-1 and the plutonium breeding piles used for the Manhattan Project allowed scientists to build the first nuclear reactor capable of producing electricity, the Experimental Breeder Reactor I (EBR-I) [2, 6]. At 1.50 pm, December 20$^{\text{th}}$ 1951, four 200 watt light-bulbs hung in a line shining with nuclear generated electricity. Reactors now can produce 1400 MW each - enough to light 7 million of the original bulbs.

The first generation of nuclear power reactors around the globe were designed not only to produce electricity but also produce plutonium for military purposes [2]. This somewhat limited the useful designs of the reactors and steered design onto two main paths, gas and water cooled reactors with solid fissile fuel. On the 27$^{\text{th}}$ August 1956 (exactly 29 years before the author was born), Calder Hall power station was opened by Queen Elizabeth II [7, 8]. It was a MAGNOX design reactor (named after the magnesium alloy used as a fuel

cladding material [2]) used not only for power but also to breed plutonium for weapons. (Interestingly, plutonium is given the symbol Pu, where it should by, ordinary convention, take the spymbol Pl. Pu was given as a joke by Seaborg as it was difficult to work with and "Peee-euggh!" just fitted the element's character better [9]).

British designs were focused on power and plutonium production, while the US Navy (in particular Captain Hyman Rickover) was looking to nuclear power as the way to propel and power submarines quietly through the water for large distances without surfacing [10]. Both water based reactors and sodium cooled reactors were considered (by Westinghouse and General Electric respectively). Two competing light water reactors were deemed potentially suitable for power production: the pressurised water reactor (PWR) and the boiling water reactor (BWR). Although both are viable reactor types for generating electricity, the PWR is easily scaled [2] and therefore was chosen as the main power source for the United States and subsequently Great Britain's submarine fleet [10, 11]. After military development, the PWR design was converted into a purely commercial power reactor and built first at Shippingport Atomic Power Station [12] (under the eyes of the by then Admiral Hyman Rickover).

Since Rickover's development of nuclear energy in the USA, parallel to other nuclear nation's efforts, the nuclear power industry has strived to improve safety and efficiency (Rickover's safety standard was impressive and stands firm as some of the key safety practice implementations still used in the industry today). This thesis aims to take a small step forward focused on some material behaviour used for future nuclear energy fuels. Much more can be done and should be done with regards to improving safety and efficiency. The nuclear industry is constantly evolving having to face new challenges and incorporate new technology (as is the case with any other industry). This chapter intends to introduce a variety of subjects related to fuels and nuclear materials as a foundation to the remainder of the work.

1.1.2 Light Water Reactor Design

Reactors using water to cool and moderate nuclear reactors make up the majority of power reactors globally. There are two main types of electricity generating light water reactor (LWR); the boiling water reactor (BWR) and pressurised water reactor (PWR). Both designs will now be discussed.

A schematic of the PWR design is shown in Figure 1.2. PWR designs have a number of

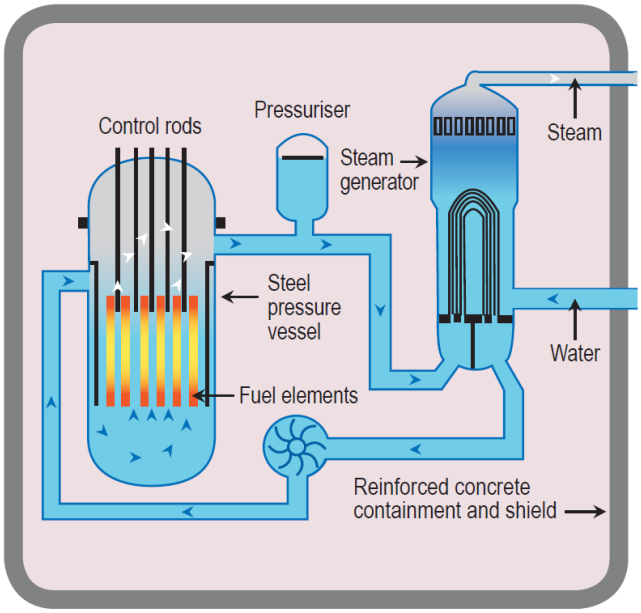


Figure 1.2: Pressurised water reactor design - Reactor containment is shown housing the reactor itself, containing the fuel, and the steam generator. The components outside of the reactor containment are used to convert the steam generated in the containment to useful electricity (Taken from [13]).

safety features intrinsically linked with the design [2, 12, 14]:

- The PWR has a two loop design with one loop taking heat away from the reactor and the other driving the turbine generators (linked together by a heat exchanger). The design reduces the radiological contamination of the electricity generators (compared to a one loop design) by containing the majority of activated material within the preliminary loop and therefore within the containment building (or nuclear island).
- Due to the change in neutron moderating properties of water compared to steam,

increases in power and temperature will produce a negative feedback response as the water boils (reducing the neutron moderation) and thereby lowering the fission rate (and subsequently the temperature of the coolant). This is called the negative void coefficient [15]. However, excessive heating and boiling is dangerous as heat transfer away from the fuel will be reduced, causing fuel element damage.

- The design of the reactor and the neutron behaviour within it mean that control rods can enter the fuel from above (unlike BWR reactors [2]) and therefore can fall under gravity when the electromagnets lose current under emergency conditions, shutting the fission reaction down. Allowing the control rods to fall down involves a simpler mechanism that has fewer potential points of failure compared to a system that drives the control rods upwards into the reactor vessel.

- Modern designs such as the Westinghouse AP1000 [16] incorporate internal condensation and natural recirculation of water vapour within the containment structure. In the event of a loss of coolant accident from the reactor, cooling will continue passively, preventing a core melt-down.

The BWR design is also a simple design (simpler than the PWR), employing one loop [2, 13]. Steam is generated by the heat of the nuclear fuel and is transported to electricity generators, cooled and then passed back into the reactor as water to produce steam again [2]. This simple design has a slightly better efficiency than the PWR, however, the electricity generators are in contact with activated water from the reactor and therefore their components will in turn become activated, needing to be replaced more frequently and requiring additional shielding [12]. Due to the intrinsic design of the BWR, it cannot 'load follow' as easily as the PWR (it cannot increase and decrease power as quickly). The steam generated in the reactor vessel also causes some corrosion issues that would not be prevalent in the PWR design as steam presents a more corrosive environment. The operating pressures of a BWR are, however, lower than a PWR (as the name suggests) and therefore, in this aspect, it is safer [12].

Both PWR and BWR designs can experience the same kind of accident scenarios including

loss of coolant accidents (LOCAs). This is where the water in the reactor vessel is lost or stops flowing, allowing the fuel temperatures to rise [3], causing ballooning of the fuel elements and possible rupture of fuel into the vessel. This can lead to reactions of the fuel with the water and in extreme situations fuel melting. A type of LOCA was the main problem with the General Electric designed BWRs at Fukushima in 2011 after the devastating earthquake caused a tsunami that swept away the backup generators used to power the pumps [17]. Good design, understanding of materials and careful reactor operation can significantly reduce the likelihood of serious accidents like Fukushima occurring again.

1.1.3 Other Current Reactor Designs

There are a number of other reactor designs being used and built around the world at the time of writing. Reactors of note include the AGR (advanced gas reactor), RBMK (reaktor bolshoy moshchnosti kanalniy), CANDU (Canadian deuterium uranium) [2] and Fast Breeder Reactors (FBR) [18] such as that being built in Kalpakkam, India (see Figure 1.3, due to begin operation by the end of 2011). All reactor types 'breed' to some degree (converting fertile isotopes to fissile isotopes), in the case of UO_2 fuel in PWR/BWR designs, fertile U_{92}^{238} is converted to fissile Pu_{94}^{239} but the FBR is able to convert more fertile material to fissile material than ordinary 'thermal' fission reactors, and therefore increase the efficiency of the fuel [2, 18] and minimise the long lived radioisotopes. Thorium, relatively abundant in India will be able to be used in these fast reactors [19] breeding U_{92}^{233}, able to be used as a fissile fuel in conventional reactors. Table 1.1 gives a summary of the fuel types, coolants, power outputs and fuel enrichments of some of the current reactors, including the PWR and BWR.

Future reactor types are based on the FBR designs with Pb and gas coolants being used instead of the liquid Na [2]. There are also advancements of the AGR design such as the Very High Temperature Reactors (VHTR), which can be fuelled conventionally (using fuel assemblies) or by a pebble bed arrangement where the fuel is circulated in graphite spheres (see [20] for example). The likely coolant for the VHTR is the inert gas helium [2].

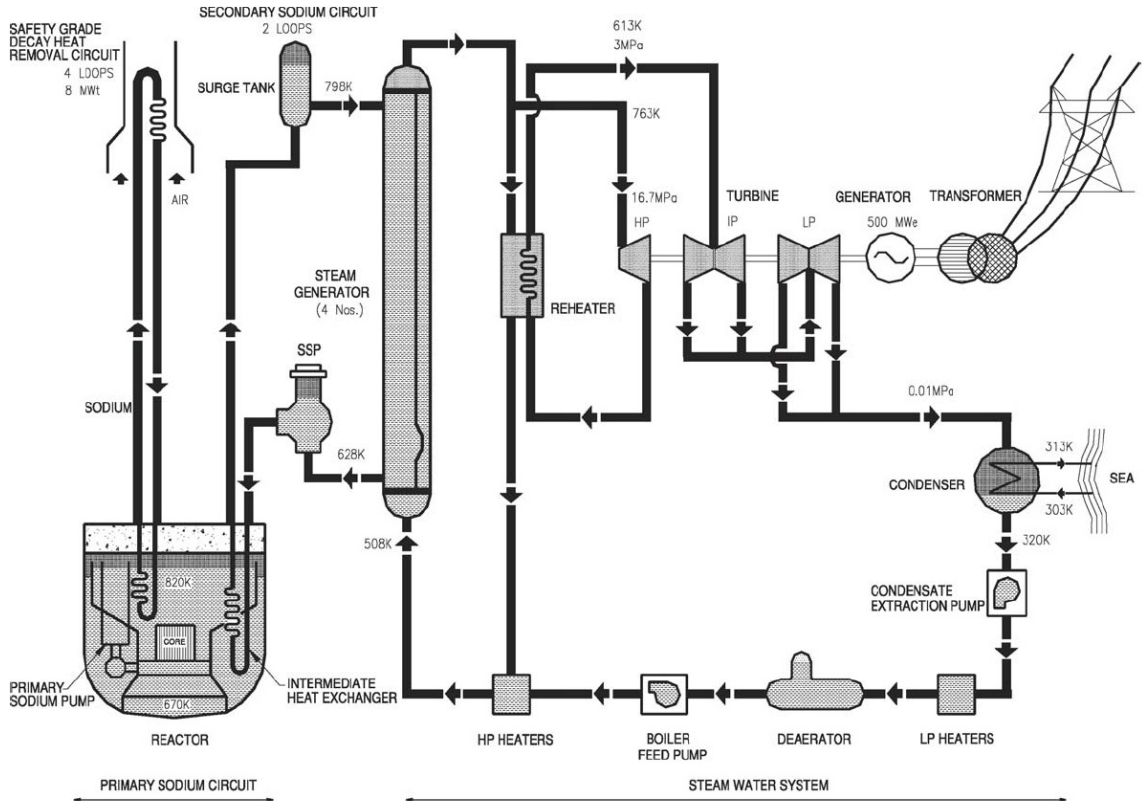


Figure 1.3: Prototype fast breeder reactor flow diagram. The sodium circuits and steam circuits are labelled (Taken from [18]).

Table 1.1: Comparison of Current Reactor Designs (Taken from [2, 18]).

Reactor	Power (MWe)	Fuel	Coolant	Moderator	Enrichment (%)
LWR-PWR	1150	UO_2 / MOX	H_2O	H_2O	3-4.5
LWR-BWR	1200	UO_2	H_2O	H_2O	2-4.5
AGR	660	UO_2 / MOX	CO_2	Graphite	2.5-3.6
CANDU	870	UO_2	D_2O	D_2O	Natural
RBMK	1500	UO_2	H_2O	Graphite	2
FBR	500	Mixed Oxide/Carbide/ Metallic	Liquid Na	None	>20 PuO_2

1.2 Nuclear Fuel

1.2.1 Introduction

A fission reaction that releases energy requires fissile isotopes of elements. Fissile isotopes have an even proton number and an odd total mass for example U_{92}^{235}. When a neutron impacts with this nucleus, it becomes unstable and breaks up, producing fission products [21, 51, 22] and energy due to a slight loss in the total mass. The fission process is described in detail in Section 1.2.3.

In the first reactors both metal and ceramic fuels were used. In Britain, MAGNOX reactors were fuelled with uranium metal (unenriched) [2]. Metal fuels generally have higher thermal conductivity than the ceramic fuels but the uranium has a much lower melting temperature of 1405 K [23, 80] compared to UO_2 (which has a melting temperature of 3138 ± 15 K [24, 80]). More importantly, the metal goes through two crystal structure phase transitions, $\alpha \rightarrow \beta$ (orthorhombic to tetragonal) and $\beta \rightarrow \gamma$ (tetragonal to body-centred cubic) at 935 K and 1045 K respectively resulting in a volume increase (at high pressures a $\alpha \rightarrow \gamma$ transition can take place with the α-β-γ triple point at 3.6±0.2 G Pa at 1080 K) [23, 25]. These phase transitions both reduce the stiffness and increase the Poisson's ratio of the metal, both un-desirable property changes [2]. It is for this reason ceramic fuels (mainly UO_2 but also mixed U/Pu oxide 'MOX' fuel) are now used in most modern BWR and PWR reactors [2, 51, 26].

UO_2 is the most common ceramic fuel used, although other uranium containing ceramics have been considered including: UC [27], UC_2 [28], UN [27], U_3O_8 [29], U_3Si [30] and U_3Si_2 [30] (of the two silicides U_3Si_2 is preferred as it does not go through the same $\alpha \rightarrow \beta$ as pure uranium does, however, both have a transition to the γ phase at about 1350 K [32]). These fuels have some advantageous properties over UO_2. Foremore, UC and UN have higher thermal conductivities. Nevertheless, the production of UC and UN fuels are difficult and oxidation of the fuel makes them less economically viable at the time of writing.

1.2.2 UO_2 Fuel Fabrication

As discussed in section 1.2.1, UO_2 is the most widely used fuel type for commercial nuclear power generation. There are a number of pellet processing routes but the majority of light water reactor fuel production proceeds as follows [2]: Uranium extraction and purification → Enrichment → Conversion to oxide → Shaping → Sintering → Cladding application. Each of these steps will now be discussed in more detail.

Uranium Extraction

Uranium can be extracted from a number of uranium containing ores. These include uranite (UO_2) [31], pitchblende (U_3O_8/U_3O_7) [31], coffinite ($U(SiO_4)_{1-x}(OH)_{4x}$) [33] and brannerite (UTi_2O_6) [34]. The ores are extracted by mining and the rock is milled into a uniform particle size before undergoing a chemical treatment specific to the ore, to produce "yellowcake" [31], a powder with a high U_3O_8 content. Figure 1.4 illustrates the global uranium resources, which total 2438100 tU that are economically viable (less than $80 per kg) taken from a WNA report [31].

The extraction process is outlined in Figure 1.5. The U_3O_8 is then enriched when required or sent for palletisation.

Enrichment

Enrichment is required for the majority of reactor types. Notable exceptions are the CANDU reactor and the MAGNOX type reactors. Enrichment increases the molar fraction of the fissile isotope U_{92}^{235} from the natural fraction ($\sim$0.7 %) to a higher fraction (reducing the molar fraction of U_{92}^{238}). The level of U_{92}^{235} enrichment is categorised in the following ways [2]:

- Slightly enriched uranium (SEU) - 0.9-2 % U_{92}^{235}.

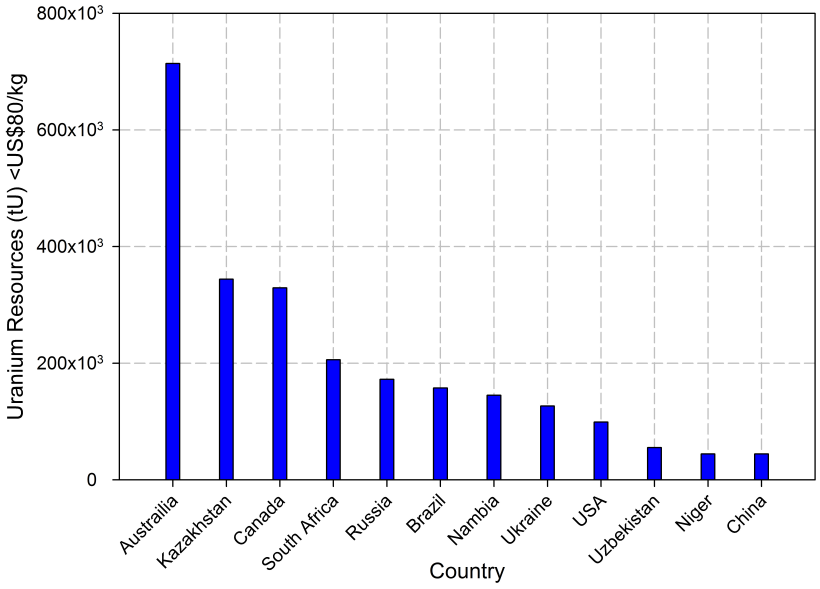


Figure 1.4: Economical uranium global resources (OECD/NEA Reasonably Assured Resources Category). Total resources are 2438100 tU. It should be noted that some countries not shown here have known uranium resources (e.g. Pakistan, India and Czech Republic). Adapted from [31].

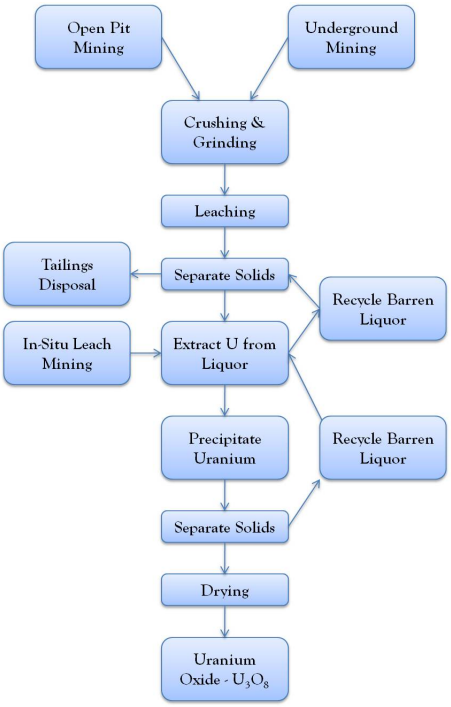


Figure 1.5: Extraction process detailing the various steps to producing U_3O_8 for further processing. Adapted from [31].

- Low-enriched uranium (LEU) - <20 % U_{92}^{235}. Commonly used in LWRs (though only enriched to 3-5 % [3]).
- Highly enriched uranium (HEU) - >20 % U_{92}^{235}. Can be used in fast reactors, which can require an enrichment of about 20 % [18].

The enrichment process is quantified in terms of 'separation works units' (SWU) [2, 12]. A SWU is one separation process per kg of material. To process 100 kg of natural uranium to LEU approximately 61 SWU are required [35]. The efficiency of a separation technique will vary the degree of enrichment per SWU.

There are a number of methods used for isotope enrichment for uranium. The most established methods are the gaseous diffusion and centrifuge techniques. Most of the methods require the uranium to be in the form of uranium hexafluoride (UF_6). As fluorine only has one stable isotope the UF_6 molecules containing U_{92}^{235} will always be lighter than those containing non-fissile U_{92}^{238}.

Conversion to Oxide

The enriched uranium (usually in the form of uranium hexafluoride) is then transported in canisters to the conversion plant where the uranium is converted to UO_2 via various reactions [2]. Conventionally these conversion processes are split into two types, wet and dry routes [2]. Wet routes are more commonly used globally and each process type yields a different UO_2 powder type. The two common wet routes are named after the intermediate compounds; ammonium diuranate (ADU) and ammonium uranyl carbonate (AUC). A dry route used by British Nuclear Fuel Limited (BNFL) is known as the integrated dry route (IDR) [2].

The first process in the IDR route is the reaction of the uranium hexafluoride with steam to produce the first intermediate uranium containing compound [36, 2].

$$UF_6 + 2H_2O \rightarrow \ UO_2F_2 + 4HF \tag{1.1}$$

The HF is removed allowing another reaction with water producing UO_3:

$$UO_2F_2 + H_2O \rightarrow \ UO_3 + 2HF \tag{1.2}$$

The UO_3 is then reduced with hydrogen producing the UO_2 powder ready for pelletisation:

$$UO_3 + H_2 \rightarrow \ UO_2 + H_2O \tag{1.3}$$

The IDR that BNFL uses produces a near stoichiometric powder (see section 1.2.4). However, the morphology of the powder particles is such that a free flowing material is not produced, which causes some processing issues [2]. Free flowing powders are preferred as transport of the material is more simple as it can flow from one processing area to another.

The ADU and AUC routes are the wet routes used by the majority of fuel manufacturers to produce the UO_2 powder [2, 37]. Both use nitric acid and water. Each route can also use the residues left over from previous process, increasing the efficiency of the wet routes with respect to the IDR [37]. The AUC route, as used by Westinghouse Electric Sweden AB [38], is now discussed in more detail:

The uranium hexafluoride is vaporised and reacted with aqueous ammonium hydroxide and ammonium carbonate forming ammonium uranyl carbonate solid which can then be filtered away (leaving a yellow powder)[2, 37].

$$UF_6 + 5H_2O + 10NH_3 + 3CO_2 \rightarrow \ (NH_4)_4UO_2(CO_3)_3 + 6NH_4F \tag{1.4}$$

The compound is then transferred to a fluidised-bed reduction furnace and supplied with steam and hydrogen gas at $\sim$925 K allowing the ammonium-uranyl carbonate to reduce to UO_2 whilst forming the other reaction products [2],

$$(NH_4)_4UO_2(CO_3)_3 + H_2 \rightarrow \ UO_2 + 3CO_2 + 4NH_3 + 3H_2O \tag{1.5}$$

The UO_2 powder is then stored in hoppers ready for pelletisation and sintering. The

uranium dioxide powder is stored slightly oxidised ($UO_{2.16}$) to prevent further oxidation to U_3O_8 during storage, detrimental to pelletisation. The powder produced is made up of a polycrystalline material with a high density of internal porosity (see micrograph in Figure 1.6). The molar composition of the powder is important when considering the sintering

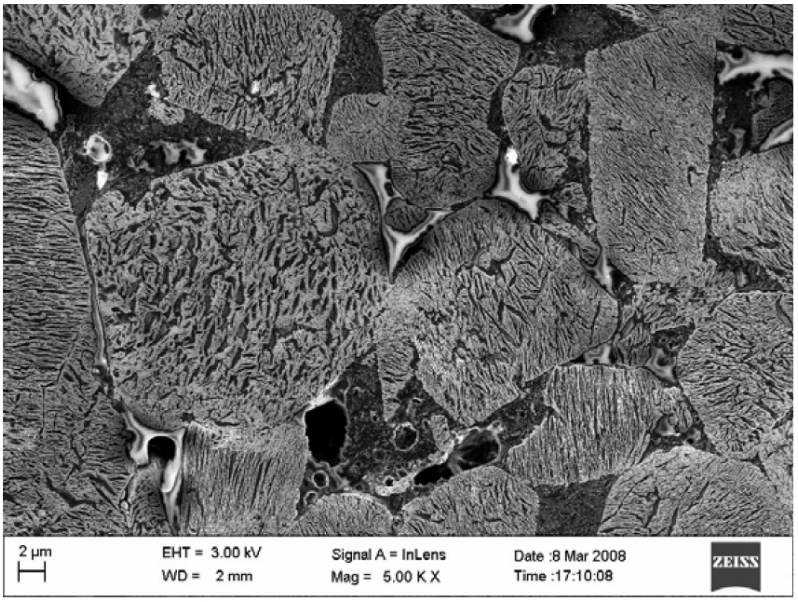


Figure 1.6: Micrograph showing the polished cross section of a number of UO_2 powder particles produced by the AUC route at Westinghouse Electric Sweden (Taken by Hans Bergvist and Wubeshet Sahle at KTH, Sweden).

behaviour and in turn the in-reactor properties of the fuel. As will be highlighted through this work, stoichiometry plays a key role in a number of atomistic mechanisms resulting in large changes in bulk behaviour.

Shaping and Sintering

After the UO_2 powder has been produced, the material is processed into a pellet. Powders can be transformed into a bulk solid by sintering methods, of which there are a number of types. These include putting the powder under pressure, leading to the removal of porosity (by hot isostatic pressing for example). The process is performed at higher temperatures in order to increase the rate of atomic diffusion and as a result, the sintering process [2].

Before sintering, the powder is pressed and shaped in to what is termed a 'green body'

[39]. Green bodies have high porosity but a near correct shape. Light water reactor fuel is usually a simple cylinder type form, as shown in Figure 1.7, however, annular fuel is common also and is used extensively in Britain's AGRs [2].

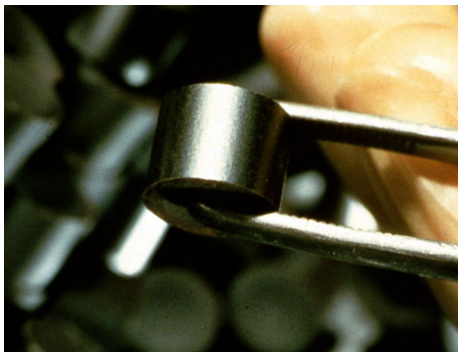


Figure 1.7: Light water reactor UO_2 fuel pellet.

Sintering simply involves the binding of powder grains to each other with material moving from the separate grains to the neck, the area where the two grains bind [40]. Sintering reduces the porosity and changes the mechanical properties of the solid [2, 41]. The driving force for the process to occur is the decrease in the free energy of the surfaces, forming more stable grain boundaries and larger crystal grains. Figure 1.8 illustrates the mechanisms for sintering, showing the binding of two spherical powder particles.

The mechanisms allowing sintering include [2, 42, 43]:

- Viscous flow (η) - Material is transported from the bulk of the grain to neck regions. High temperatures lead to lower viscosities and therefore more transport will occur.
- Gas diffusion (D_g) - Material is transported from grain surface to the neck through the porosity. Higher temperatures will lead to more gas being evolved and therefore more gas transport will take place.
- Evaporation/condensation (Δp) - Material moves from grain surface to neck regions through the porosity. Lower sintering vapour pressures will lead to more vapour being produced and therefore more evaporation and condensation.
- Surface diffusion (D_s) - Material is transported from the grain surface to the neck

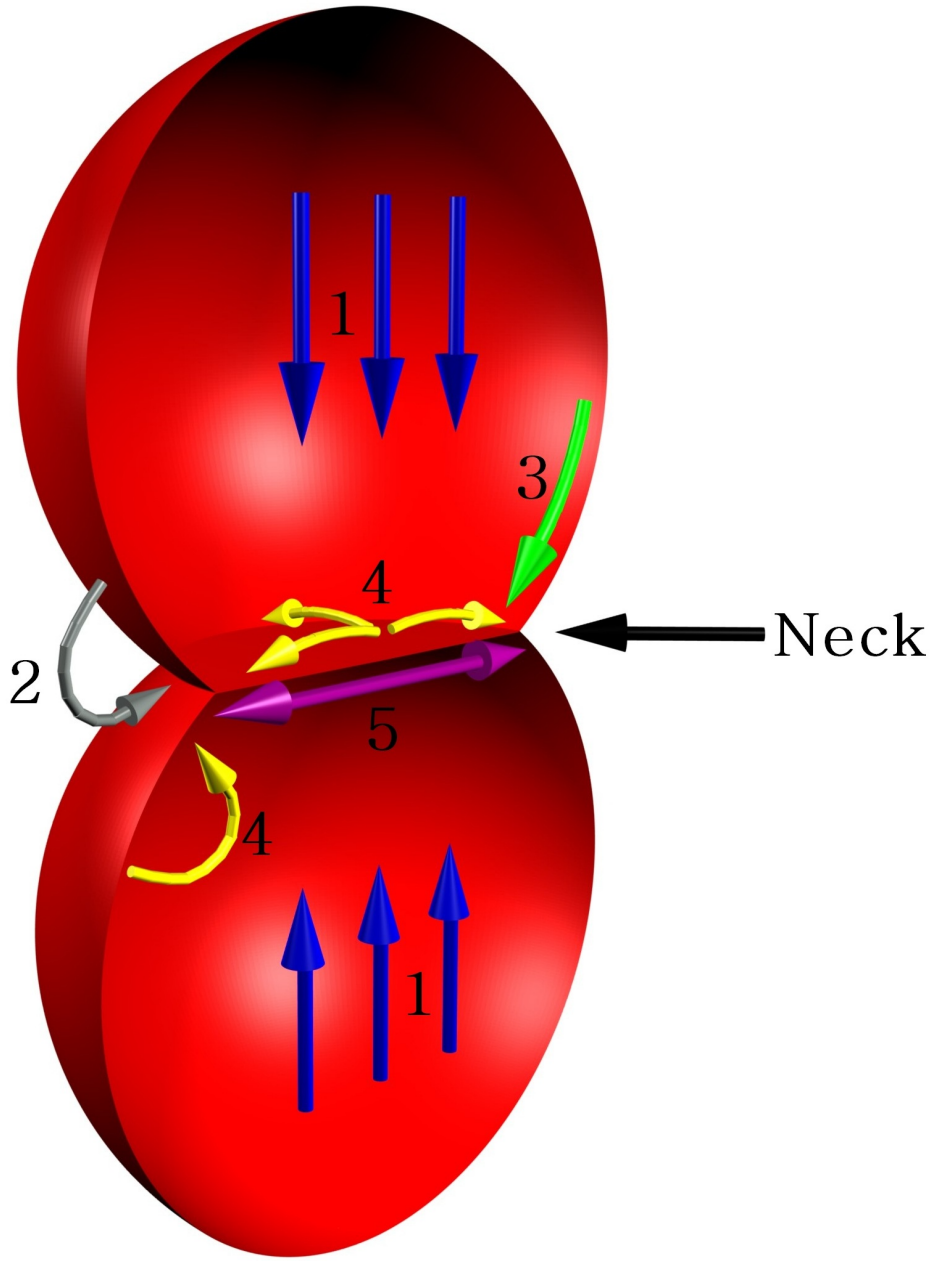


Figure 1.8: Various material transport processes possible during sintering illustrated with two spherical particles after necking. The processes are: **1.** Viscous flow (η) **2.** Gas diffusion (D_g) , evaporation/condensation (Δp) **3.** Surface diffusion (D_s) **4.** Lattice diffusion between the grain boundary or grain surface to the neck (D_l) **5.**Ġrain boundary diffusion (D_g). Adapted from [43].

over the grain surfaces. Higher temperatures will allow more diffusion and therefore more sintering will occur. D_s will also be effected by surface morphology.

- Lattice diffusion (D_l) - Movement of atoms from grain boundaries and surfaces through the bulk material to the neck. Enhanced by high temperatures. Changes in bulk properties due to dopants and stoichiometry changes will have an affect on the D_l.

- Grain boundary diffusion (D_g) - Material transported down the grain boundaries to the neck. Enhanced by increased temperature and dependent on grain boundary morphology.

- Plastic deformation - This is the movement of material due to external forces (i.e. pressure), because UO_2 is usually sintered at atmospheric pressure this is an unimportant mechanism.

Both the increase in the diffusion coefficient of atoms in the powder's bulk surface and the increase in the volatility of a powder's grain surfaces will increase the rate of sintering. Only processes that involve surface diffusion (i.e. D_s, Δp and D_g) will have an effect on the densification of the material [2, 44].

Control of the sintering atmosphere is of high importance [40, 45]. UO_2 can easily change in stoichiometry depending on the oxygen partial pressure and temperature [45]. An example atmosphere used by manufacturers is hydrogen gas with additions of CO_2. The CO_2 is added in varying amounts and acts as an atmospheric oxidiser.

Once the pellet has been produced, the cladding can be applied and a fuel assembly is produced [2]. The fuel assemblies are then transported from the fuel manufacturing plant to the reactor for use. Common cladding materials are low alloy zirconium and stainless steels [2]. Beryllium and silicon carbide based composites are also being considered for future cladding materials [2, 46].

1.2.3 In-Reactor Fuel Behaviour

Fission processes in the fuel create energy (E) by converting small amounts of mass (m) in the way predicted by Einstein's famous equation $E = \Delta mc^2$ where 'c' is the speed of light [47]. The energy is released as thermal, kinetic and electromagnetic radiation [48, 49]. An example of a fission reaction is illustrated in Figure 1.9.

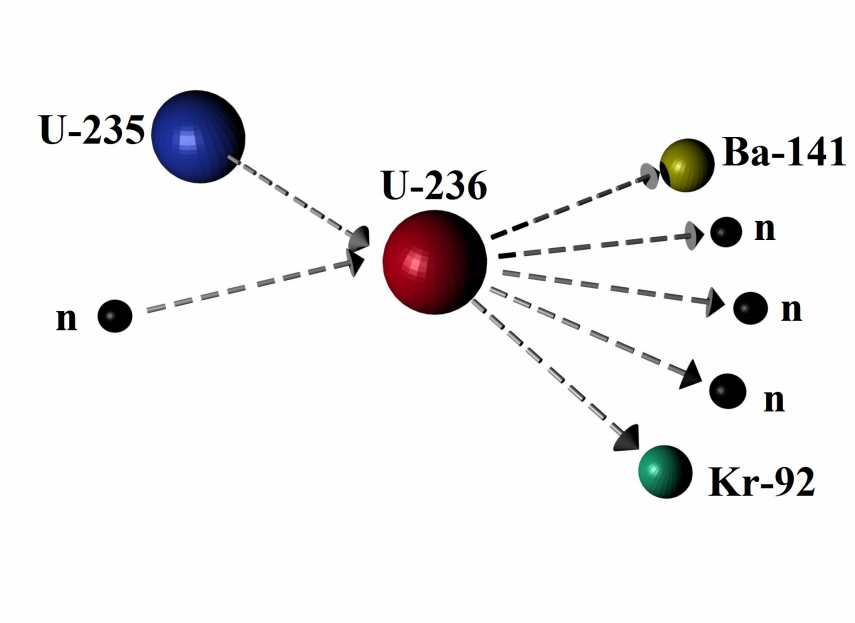


Figure 1.9: Fission reaction showing a U_{92}^{235} atom reacting with a neutron to produce three neutrons and two different fission products, Ba_{56}^{141} and Ke_{36}^{92}.

A neutron produced from the fission process can go on and produce another fission event, hence maintaining the fission chain reaction [50]. Heat is produced as the fission products move through the fuel's crystal lattice, creating damage, which then recovers to an extent [51]. Each fission product will form a cascade of fission products. The Kinchin-Pease model is a simple description of this process [52], which simply states that an atom given enough energy to displace it from its lattice site will move and transfer its energy to other atoms through a cascade.

Fission Products

A fission event will usually insert two lighter nuclei into the fuel lattice (termed fission products) [51, 21, 22, 53] and also produce both free neutrons and γ-rays [49, 54, 55] (sometimes three fission products are produced, termed a 'ternary fission' process [56]). Fission products in UO_2 can be classified into three categories depending on how they behave: noble gases (e.g. Kr, Xe), non-volatile elements (e.g. Zr, Ba, Ce, Sr) and volatile elements (e.g. Cs, I, Te) [51, 57]. A typical fission yield is shown in Figure 1.10.

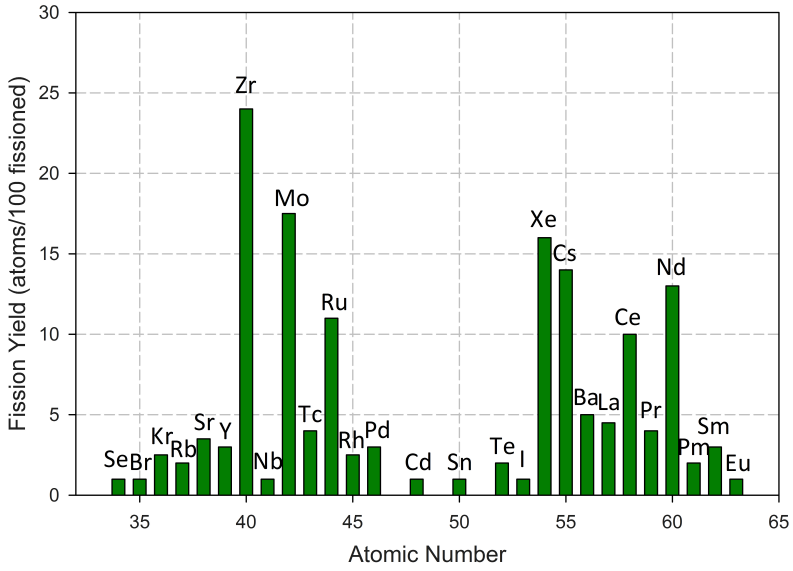


Figure 1.10: Typical fission yield after 2.9 % FIMA [51]

Each of the three types of fission product will behave differently within the pellet over the fuel's lifetime. The noble gases are insoluble in the UO_2 lattice and form bubbles within the UO_2 grains, swelling the fuel or migrating to the grain boundaries and subsequently the rod free volume, causing a detrimental effect to the thermal conductivity of the fuel rod [21, 22, 57, 62]. It is therefore critical to understand noble gas migration processes, in order to produce a complete fuel performance code. The processes for gas release are detailed in the following section.

The volatile elements are also of high importance. The production of iodine and caesium both contribute to the highly detrimental effects of stress corrosion cracking; problematic

in both stainless steel and zirconium based cladding [57, 51]. The species react with the metal thereby initiating cracks and enhancing their growth [63]. Additives are added to some UO_2 based fuels to absorb or prevent the volatile elements interacting with the clad material. One such doped fuel uses additives of Al_2O_3 and SiO_2 to form an alumino-silicate type glassy phase within the fuel that is reported to be proficient at reducing the effect of caesium and iodine on the cladding [21]. Dopants are discussed in more detail in section 1.2.5.

The non-volatile elements either stay in solution within the UO_2 lattice (having effects on the overall diffusivity of the bulk and other properties) or form precipitates within the grain and at grain boundaries [21, 57]. These precipitates have an effect on the mechanical properties of the material. Figure 1.11 shows a scanning electron micrograph of average burnup UO_2, clearly showing metallic precipitates (light spots) [64].

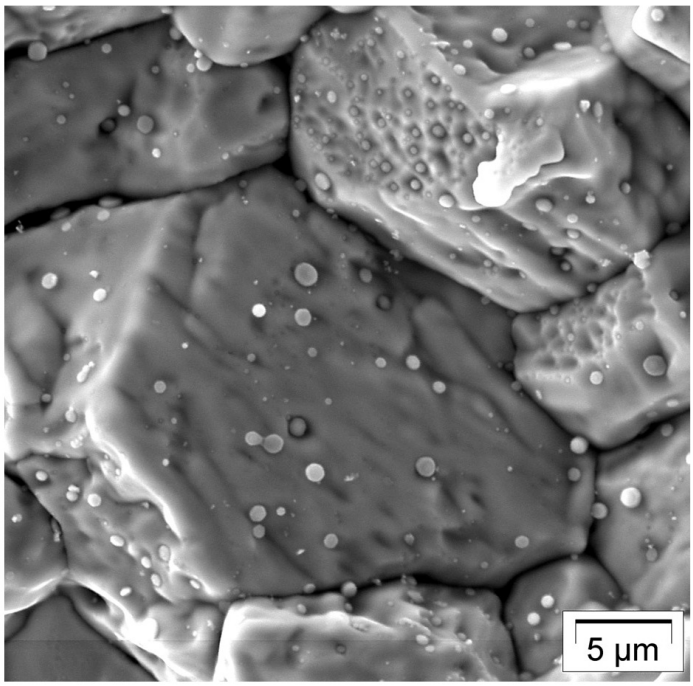


Figure 1.11: Metallic precipitates (light spots) on the grain boundaries of MOX fuel [64]

When in solution (but not necessarily in thermal equilibrium), the non-volatile elements are accommodated as point defects and in defect clusters [61]. An example of such a

mechanism is the solution of the common trivalent cation fission product Nd^{3+}. The Nd^{3+} ion is accommodated at a uranium site, while charge neutrality is maintained by oxidising a uranium ion to U^{5+} (the Nd^{3+} and U^{5+} average charge is 4+, the same charge as the uranium cations in UO_2). These defects can form a cluster which can be written as $\{Nd'_U{:}U^{\bullet}_U\}^{\times}$ in Kröger-Vink notation [65] which is used throughout this thesis (further reactions analogous to this are discussed in more detail in subsequent chapters and in detail in Appendix A).

Fission Gas Release

Xe and Kr produced in the UO_2 crystal lattice are released to the rod free volume via a number of routes. The gases are released from the grains to the grain boundaries by either thermal or athermal processes [66]. Athermal release of gases from the grains to the grain boundaries is, as the name suggests, mostly temperature independent [67]. The fission gases produced during a fission event move in a ballistic manner through the lattice and come to a rest after the energy has been dissipated to the surrounding material. If initiated near the grain boundaries gas may come to rest at the grain boundary instead of in the UO_2 lattice [68]. If gas comes to rest within the crystal, subsequent fission events causing crystal damage and species re-location may allow further migration of the gas atom to the grain boundary. In fuel codes, the athermal release can be approximated to assume total release from a volume of crystal near a grain boundary (typically $\sim$10 μm deep) [69].

In the remaining crystal xenon and krypton diffuse by thermal migration [51, 67, 69, 70], in that there is a temperature dependence on the movement of the gases related to defect migrations within the UO_2 ceramic [51, 21, 62]. Thermal migration is only a determining factor for fission gas release at moderate to high fuel temperatures, when the activation energies for defect migration can be easily overcome. Thermal migration is discussed fully in the point defects section later in this chapter.

Once at the grain boundaries, the fission gases form intergranular lenticular bubbles [70]. As these bubbles grow they interlink until all the bubbles are connected allowing gas to

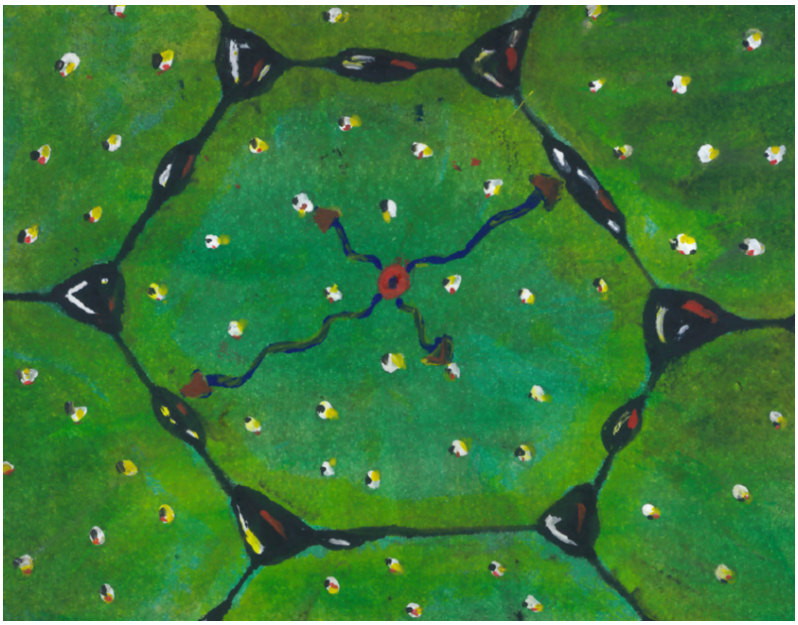


Figure 1.12: Painted schematic of fission gas release. The fission gas species (red) can be seen to be trapped at either an internal gas bubble (intragranular) shown in white or at a grain boundary bubble (intergranular) shown in black.

flow freely into the rod free volume [71]. Once the gas is released, the intergranular porosity collapses to some degree and intergranular bubble growth can begin again [71]. Figure 1.13 shows a micrograph of a grain boundary with interlinking intergranular porosity (taken from [71]).

Increasing the distance or the time that fission gases take to reach the grain boundaries will reduce the volume of fission gas released from the grain boundaries [38, 73, 70]. The increase in distance can be achieved by making fuel with a larger grain size (see the sintering section) or slowing the diffusion of the fission gases in the grains, both of which are results of fuel doping [38, 74, 75]. By limiting the fission gas release, the thermal conductivity of the rod free volume will be maintained to a greater extent and pressures in the rod will rise at a slower rate than in standard fuel [38].

Intragranular Gas Bubbles

Fission gases can either be released to the rod free volume (through the growing and interconnection of intergranular bubbles) or trapped in intragranular bubbles within the

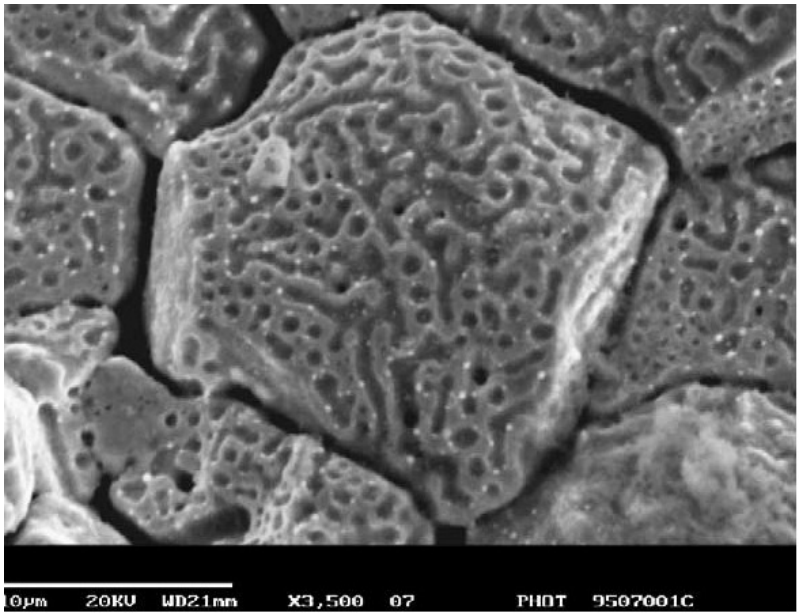


Figure 1.13: Micrograph showing the interlinked porosity that develops as fission gas is released from the grains to the grain boundary in polycrystalline UO_2 (taken from [71]).

UO_2 grains [68, 76, 72]. These bubbles trap the gases and only a small proportion of the gas is resolved back into the UO_2 [68, 77]. Increasing the number and size of intragranular bubbles will therefore decrease the volume of fission gas released to the rod free volume [68, 70]. A micrograph showing intragranular bubbles is presented in Figure 1.14.

In accident scenarios, increased numbers of intragranular bubbles may be an issue. At high pressure, any rapid increase in temperature will cause the bubbles to exert more pressure on the surrounding material. In extreme conditions this could cause fuel fragmentation [78], releasing much of the gas into the rod free volume thereby rapidly increasing the pressure on the cladding. This increase in clad pressure may cause the rod to balloon (causing fuel lift-off which will increase the fuel temperature further causeing an un-desirable positive feedback response) and eventually even rupture [79].

1.2.4 Effects of Stoichiometry

The uranium-oxygen phase diagram is shown in Figure 1.15. Uranium is often stored as the oxide U_3O_8 due to its stability in normal atmospheric oxidising conditions, and

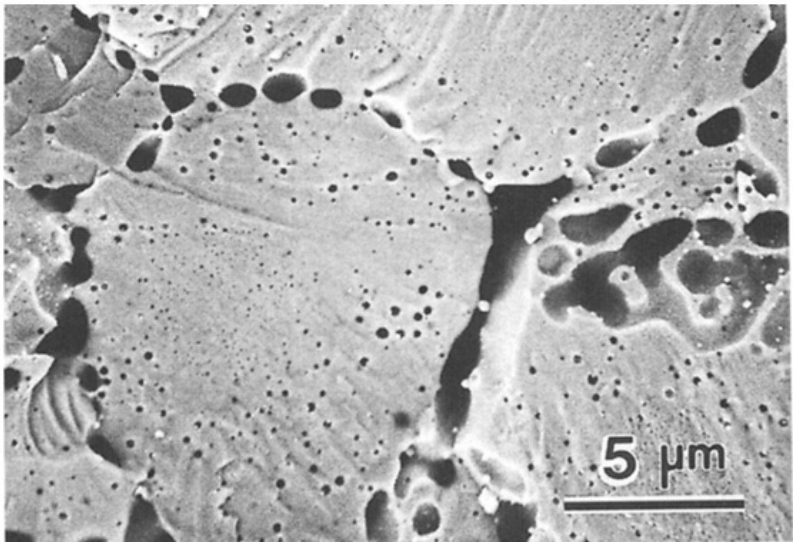


Figure 1.14: Intragranular bubbles in UO_2 irradiated to 23 GWd/t. The intragranular bubbles are near spherical. Also shown are intergranular bubbles around the grain boundaries (taken from [72]).

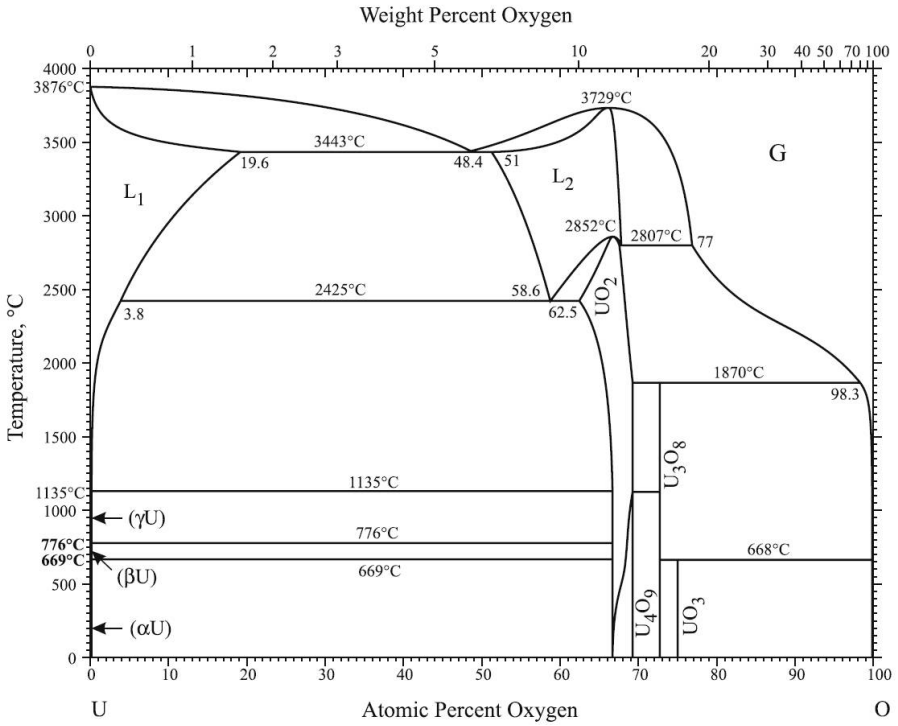


Figure 1.15: The Oxygen-Uranium system phase diagram by Okamoto [80].

then reduced before the sintering stage of manufacture [2]. The stoichiometry is known to vary in the fuel, but remains slightly hyperstoichiometric (UO_{2+x}) [2, 61] during most fuel manufacture processes. In Figure 1.15 the small area between 66 wt.% and 69 wt.% is the range of UO_2 to UO_{2+x}. Hypostoichiometric UO_{2-x} is shown to only exist at high temperatures [40] forming a two phase material at lower temperatures [80]; reduction of UO_2 to UO_{2-x} is energetically unfavourable and rarely encountered within the fuel cycle [2]. The IDR, ADU and AUC routes mentioned in section 1.2.2 produce an oxide powder with an O/U ratio of 2.05, 2.03-2.17 and 2.06-2.16 respectively, all hyperstoichiometric [2].

Cation diffusion in UO_2 is important and determines many of the creep, gas release and sintering properties of the fuel [40]. Any variation in the cation diffusion will have a marked effect on these processes [40, 75]. Figure 1.16 shows a diagram taken from reference [61] that indicates how cation diffusion varies with O:M ratio. This Arrhenius number relates

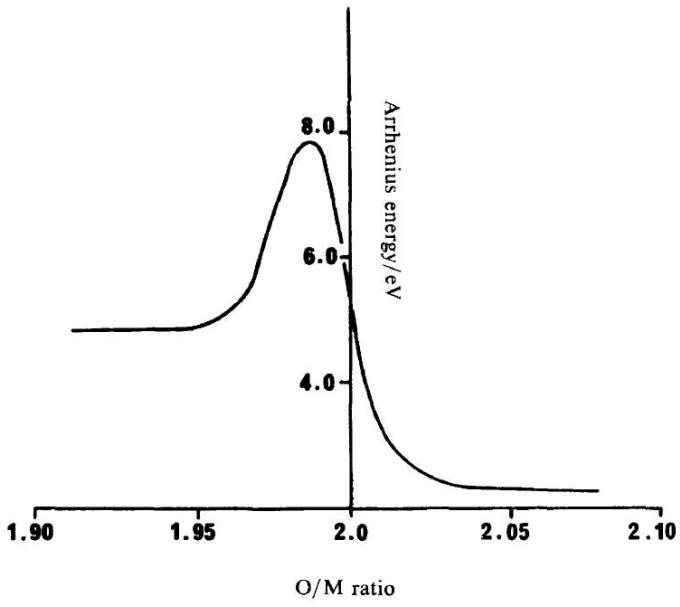


Figure 1.16: The change in Arrhenious energy for the migration of cations with stoichiometry in UO_2 taken from [61].

to Fick's law, detailed in section 1.4, where larger energy values result in lower diffusivity of the specific species within the solid.

The solubility and charge state of defects and fission products in UO_2 is also predicted

to vary with the stoichiometry of the host lattice [51, 62]. It has been suggested that Xe might even exist in the Xe^{+} and Xe^{2+} charge states in UO_{2+x} but that this would not be possible in UO_2 and UO_{2-x} [62]. Further predictions are consistent with the stability of I^{+} and I^{2+} in UO_{2+x} [51, 21, 22]. Varying charge states therefore result in different solubilities.

The creep rate in polycrystalline UO_2 fuels has been shown to increase linearly with oxygen excess (i.e. hyperstoichiometry) [81, 61, 82]. This will be linked with the increased cation diffusion predicted by Catlow [61] in Figure 1.16.

The stoichiometry of fuel is known to vary during burn-up [57, 81]. Burn-up replaces tetravalent uranium ions with lower valency ions, often forming metallic precipitates and leaving the remaining oxygen in the UO_2 solution, which in turn increases the stoichiometry [21, 57]. Oxygen diffuses up the temperature gradient towards the centre of the pellet and is reported to be gettered to some extent by clad materials including Zr based clads, forming the oxide ZrO_2 and other phases in the Zr-O system. A slight hyperstoichiometry is still reported near the rim of the pellet but not necessarily at the rim. Kleykamp [57] presents some results for a mixed oxide fuel used in a FBR. The fuel had the compositions $^{238}U_{0.7}\,^{239}Pu_{0.3}O_{1.97}$ and $^{235}U_{0.7}\,^{239}Pu_{0.3}O_{1.97}$ taken to 9 and 24 at. % burn-up respectively. The O:C molar ratio (where 'C' is the cation concentration) of both fuels fuel was shown to increase [57].

1.2.5 Dopants in UO_2

Dopants can be added to the fuel to improve the manufacturing processing and in-reactor performance [38, 82, 74, 83, 84]. One such dopant will be discussed in section 1.2.6, Gd_2O_3, which is in solid solution with the UO_2 and is used to control fuel burn-up. A number of studies have shown that Gd_2O_3 is highly soluble in UO_2 and forms a solid solution by oxidising uranium ions to 5+ to balance the 3+ of the Gd cation [85].

Other than controlling burn-up, dopants can be used to control the density of fuel pellets

(important especially in AGR fuel where high densities are required) and increasing grain sizes in sintered fuel, improving fission gas release behaviour in reactor [2]. Additives such as CONPOR [86] or U_3O_8 [12] are used to control densities (the theoretical density of UO_2 is $10.96\,g/cm^3$). CONPOR is a pore former that results in pores of a well controlled size and homogeneous distribution that improves fission gas retention.

Other dopants in UO_2 fuel include:

- Cr_2O_3 - Used to enlarge the ceramic's grain size, increase the as-manufactured pellet density and enhance creep. Increasing grain-size will decrease the fission gas release rate of a fuel pellet. However, the solubility of the oxide in UO_2 is low with varying solubilities quoted [38, 82, 74].

- Al_2O_3 - Used with Cr_2O_3 to enhance the grain growth characteristics. The oxide is reported to be insoluble in UO_2 to any measurable degree [38, 87, 88].

- Er_2O_3 - Used as a neutron absorber, having a lower neutron cross section in comparison to Gd [89] allowing the absorption of neutrons to be tailored to the pellet's position in the fuel rod more finely.

- TiO_2 - Increases the grain size and thermal conductivity of UO_2 allowing higher burn-ups as the pellet centre temperatures will be lower [84].

- Nb_2O_5 - Improves structural properties such as increasing creep and acts as a grain size enlarger. The oxide is highly soluble in UO_2 [90].

- SiO_2 - Increases grain size in UO_2 by modifying the grain boundaries and forming a low-melting-point-eutectic that melts during sintering [88].

One focus of this work is to investigate the mechanisms and effects of chromium (III) oxide doping in UO_2. The following subsection will highlight the previous work.

Cr_2O_3 in UO_2

Cr_2O_3 is added to UO_2 to increase the grain size in the pellet, increasing the distance fission gases have to diffuse before reaching the grain boundary, where they are released [38]. Cr_2O_3 also increases the as-manufactured pellet density.

Killeen reports results of UO_2 doped with Cr_2O_3 [74, 75]. His conclusions include:

- The doped fuel has a grain size 7 times larger than the undoped fuel (initial grain size before irradiation of 52 μm compared with 6 μm and a final grain size after irradiation of 71 μm in comparison to 10.2 μm).
- The porosity of the doped fuel differs from the undoped UO_2. The interlinkage and shape of the intergranular pores in the doped fuel are far less obvious than in the undoped samples studied and are highly linked. This leads to extensive grain-face porosity which will give more swelling than in undoped fuel, reducing the effect of the larger grains. The fuel is predicted to be more 'friable', that is, more likely to fracture and spall when un-restrained.
- Segregation of the Cr to the grain boundaries has been observed using scanning electron microscope analysis.
- The diffusion rate of gas products in the fuels is shown to have increased.

$$\mathrm{D}^{\mathrm{UO_2}}(1465\,^{\circ}\mathrm{C}) = 1.3 \times 10^{-20} \pm 0.2 \times 10^{-20}\,\mathrm{m}^2/\mathrm{s} \tag{1.6}$$

$$\mathrm{D}^{\mathrm{Cr\,Doped}}(1500\,^{\circ}\mathrm{C}) = 6.0 \times 10^{-20} \pm 0.4 \times 10^{-20}\,\mathrm{m}^2/\mathrm{s} \tag{1.7}$$

Leenaers *et al.* published an article on the use of Cr_2O_3 as a dopant in UO_2 with varying Cr_2O_3 concentrations and using various sintering atmospheres [82]. The conclusions given are as follows:

- The solubility limit of Cr_2O_3 in UO_2 varies with the oxygen partial pressure during sintering. Higher oxygen partial pressures give higher Cr_2O_3 solubility.

- A decrease in the lattice parameter of the UO_2 crystal has been observed, with increasing Cr_2O_3 concentration.

- Whether the Cr resides as an interstitial species or a substitutional species could not be deduced but it is assumed that it is an interstitial species with an accompanying oxidation of U^{4+} to U^{5+} (NB. this is not likely as the interstitial species will be positive and, if interstitial, would reduce the surrounding lattice).

Arborelius *et al.* produced an article on the sintering and irradiation behaviour of fuel doped with Cr_2O_3 (1000 ppm), a fuel doped with Cr_2O_3 and Al_2O_3 (referred to as ADOPT for Advanced Doped Pellet Technology containing 500 ppm Cr_2O_3 and 200 ppm Al_2O_3) and a fuel doped with Cr_2O_3 and MgO (1000 ppm and 100 ppm respectively) [38]. The conclusions and main findings are outlined here:

- The fabricated density of the Al_2O_3 and Cr_2O_3 doped pellets is greater than the standard UO_2 pellet. The standard density was found to be 96.0 % of theoretical density while the Cr_2O_3 doped density was 97.3 % and the Cr_2O_3 with Al_2O_3 doped material was 97.4 %; both dopants lead to increased pellet density. The density in the MgO-Cr_2O_3 doped pellet was also found to be 97.4 %.

- The heat capacity of the ADOPT pellet was measured using a differential scanning calorometer and no obvious differences were found compared to the standard pellet.

- The melting temperatures of the ADOPT pellets did not vary significantly from the standard pellet.

- No changes in thermal diffusivity were found between the ADOPT and standard pellet.

- Due to the increased fabricated density, the pellet-clad gap closed earlier and showed an approximate 0.1 % higher axial rod growth for the ADOPT pellet in comparison to the standard pellet.

- The viscoplasticity of the ADOPT pellet is greater compared to standard UO_2 increasing the pellet clad interaction properties.

Kashibe and Une [88] investigated the effect of the dopants Cr_2O_3, Al_2O_3, SiO_2 and MgO on diffusional release of Xe :

- Of the 239 ppm Cr_2O_3 added, 47 % of it was measured to be retained. (The 121 ppm Al_2O_3 retention was lower at 27 %).
- The stoichiometry of the Cr_2O_3 and Al_2O_3 doped pellets were seen to be lower than the standard UO_2 falling from 2.004 to 2.002 O:M ratio.
- The diffusion coefficient for the Cr_2O_3 doped fuel was about three times larger than the standard pellet at high temperatures ranging from 1770-1870 K. The following relationship was given:

$$\mathrm{D}^{\mathrm{UO_2}}(\mathrm{m^2 s^{-1}}) = 1.7 \times 10^{-12} \mathrm{e}^{\frac{-235(\mathrm{kJ\,mol^{-1}})}{\mathrm{RT}}} \tag{1.8}$$

$$\mathrm{D}^{\mathrm{Cr_2O_3}}(\mathrm{m^2 s^{-1}}) = 1.5 \times 10^{-10} \mathrm{e}^{\frac{-293(\mathrm{kJ\,mol^{-1}})}{\mathrm{RT}}} \tag{1.9}$$

- Al_2O_3 was shown to have negligible solubility in UO_2.

The experimental studies suggest that there are some conflicts and unclear results from the past work on Cr_2O_3 doped fuels. Important differences involve the solubility limit, thermal diffusivity and effects of stoichiometry. This will be one focus for this thesis.

1.2.6 Controlling Fuel Burn-Up

The reactivity of normal nuclear fuel changes and degrades over the life-time of the energy source in the reactor [2, 91]. As fuel burns, the overall neutronic properties of the fuel core vary and control of the neutrons is important in keeping the core critical (essentially the number of neutrons being produced by the total fission and decay events in the core

over a set time period is equal to the number that are being used to initiate further fission events). Failing to control the fission process will result in either a transient fission event or fission processes in the core stopping, both undesirable events under normal operating conditions.

Control rods are used to control the overall neutronic flux of the reactor [91]. Usually manufactured from elements and isotopes with high neutron cross sections such as silver, boron, cadmium and hafnium [91, 92]. Common control rod materials for pressurised water reactors include silver-indium-cadmium rods (80% Ag, 15% indium and 5% Cd) encased in stainless steel cladding and boron containing compounds [2, 12]. Common boron compounds used for neutron control are high-boron stainless steels and boron carbide [2]. The boron has to be enriched in the B_5^{10} isotope, due to its preferable neutron cross section over the more abundant B_5^{11} isotope [12, 93].

Boric acid is often added to the coolant of pressurised water reactors [94], limiting the reactivity of the fuel, enabling a more even and manageable burn up of the fuel [3, 94].

Burnable absorbers (often referred to as burnable poisons due to their neutron poisoning effect) are added to the fuel rod to control the burn-up of fuel [2, 85]. These burnable absorbers can be added to nuclear fuels as pellet coatings or as additives (e.g. solid solutions or secondary phases) within the fuel pellet itself. The use of pellets with burnable absorbers can be preferable as individual pellets or areas that would usually have high reactivity and neutron fluxes within a reactor can be easily targeted and controlled [91] without the use of the control rods.

Gadolinium oxide (Gd_2O_3) is often used as a burnable absorber [85, 95], added to the fuel during the pelletisation phase and it is therefore described as an additive or dopant. Gd_{64}^{157} has a neutron cross-section of ~254,000 barn for thermal neutrons [96], very high, and absorbs a neutron to become Gd_{64}^{158}, an unstable isotope that decays via a number of intermediate steps, with products that possess much smaller neutron cross-sections. Over time, the Gd within the fuel is burned away, allowing the less reactive, older fuel to be used without any intentional poisoning effects [96].

Boron in the form of zirconium diboride has been used as a neutron absorber on both PWR and BWR fuels [89]. It is, unlike Gd_2O_3, added as a coating on individual pellets by a process of plasma deposition [89]. The B_5^{10} isotope in the ZrB_2 coating absorbs a neutron and transmutates. Equation 1.10 shows the reaction that occurs:

$$B_5^{10} + n \rightarrow \ He_2^4 + Li_3^7 \tag{1.10}$$

Helium and lithium are produced [89] and have much lower neutron cross-sections than the boron. The behaviour of these transmutation products within the ZrB_2 material is important and the focus of Chapter 5 in this thesis.

1.3 Nuclear Applications of Beryllium

Beryllium (Be) occurs in sparse concentrations, not only on earth (2.8 ppm [97]), but throughout the universe in comparison to similar sized elements that are commonly produced by stellar fusion such as hydrogen, helium, lithium, carbon, nitrogen and oxygen. This is because the isotope of Be produced in the triple alpha process (see Figure 1.17), where two He_2^4 atoms combine to create a Be_4^8, is an unstable isotope that has a half life of $3{\times}10^{-16}$ s [98, 99, 100]. It either combines with another He to produce carbon or decays away to the constituent He_2^4 nuclei. Beryllium is also produced by the process of cosmic ray spallation nucleosynthesis whereby oxygen and nitrogen are impacted in the upper atmosphere of the earth by solar radiation, which produces Be_4^7 and Be_4^{10} [101] that have half lives of 52.28 days [102] and 1.5 million years respectively [103] (see equation 1.11).

$$O_8^{16} + p \rightarrow \ Be_4^7 + Be_4^{10} + \beta^+ \tag{1.11}$$

Beryllium has only one stable isotope that is not seen to decay [104], Be_4^9. Be is therefore considered a monoisotopic element having only one stable isotope [105]. Interestingly, it the only monoisotopic element (there are 26 in total) with an even number of protons.

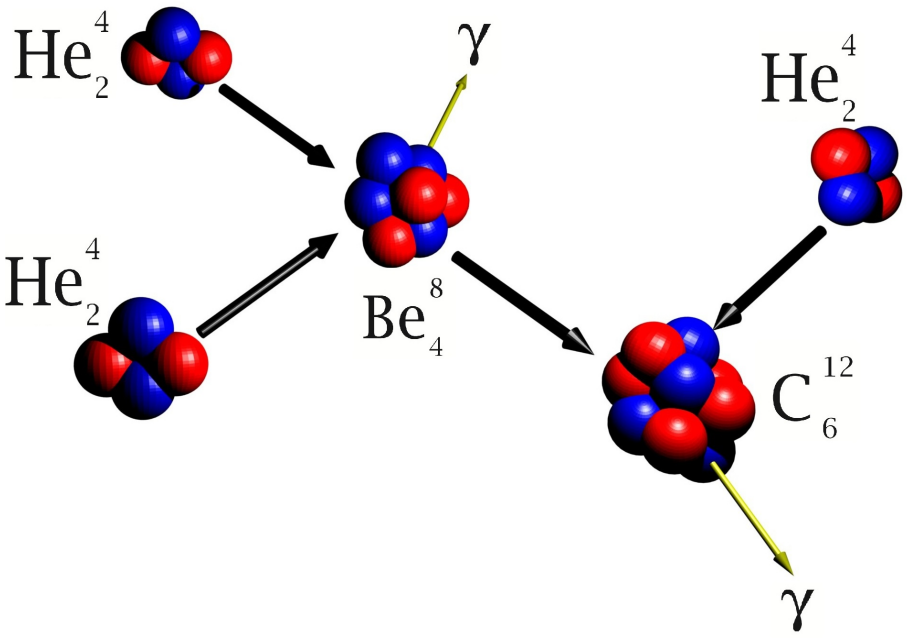


Figure 1.17: The triple alpha nucleosynthesis process showing the fusion of He_2^4 nuclei to first produce Be_4^8 and then the C_6^{12} nucleus.

Beryllium's Neutronic Properties

$Be_4^{10/9}$ can be used both as a neutron reflector [106] (and has a key role as a neutron source [107, 108]) or a neutron multiplier [109]. A neutron can be absorbed into the Be_4^{10} nucleus, forming an unstable nucleus that will release two neutrons leaving the stable Be_4^9 isotope. The reaction is shown in equation 1.12:

$$Be_4^{10} + n \rightarrow \ Be_4^9 + 2n \tag{1.12}$$

When combined with a high alpha emitter, such as Pu_{94}^{239}, the Be_4^9 isotope acts as a neutron source [107], important not only in the nuclear industry but also research [111], medicine [112] and petroleum exploration [113]. A reaction involving the absorption of an alpha particle to produce a neutron is shown below in equation 1.13.

$$Be_4^9 + He_2^4 \rightarrow \ C_6^{12} + n \tag{1.13}$$

Beryllium can play a key role in nuclear reactors, reflecting and moderating neutrons, improving the reactor efficiency [106]. It has a high scattering cross section for high-energy neutrons and therefore slows them into a thermal neutron regime, ideal for initiating fission [109]. Beryllium is highly transparent to the thermal neutrons and is therefore an excellent candidate for either a fission or fusion cladding material [114].

Beryllium's use in ITER

The current International Thermonuclear Experimental Reactor (ITER) design uses a 1 cm thick layer of beryllium as the plasma facing section of the 'first wall' as a protection against the high temperatures and high neutron fluxes in the torus [110, 109]. As the Be will degrade over time (activated with tritium) and non-normal conditions will put the plasma into contact with the blanket wall, it has been designed to be modular with easily replicable parts 1.5m^2 in area. The tokomac design and position of the Be is shown in Figure 1.18.

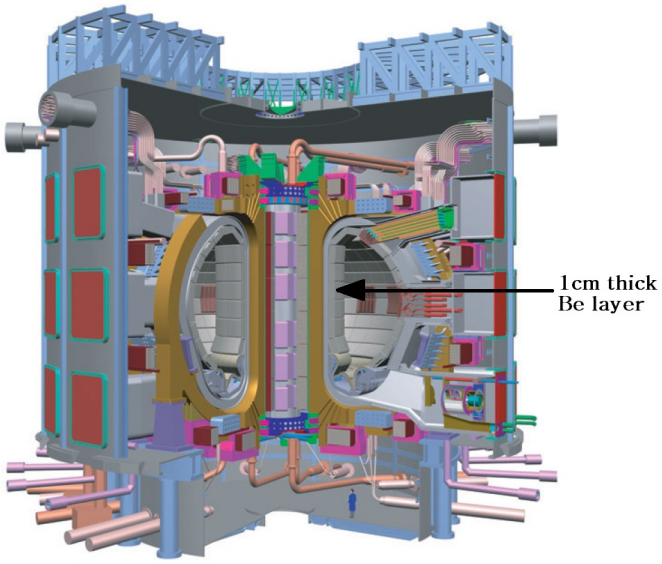


Figure 1.18: Design for the ITER tokomak fusion reactor. The Be layer on the blanket layer is highlighted. Taken from [110].

1.4 Atomic Theory

Atoms can bond together in a regular, long range order forming a crystal [115, 116]. Metallic, ionic and covalent bonded elements and combinations of elements can form crystals. The crystal structure will depend on the bonding and determines a number of features of a material: thermal conductivity, stiffness, electrical conductivity, isotropy and the defects that can exist within it.

Although bonding describes what a perfect material is like and how it behaves, defects are present in most crystalline solid structures and can define some interesting and useful properties of a material. The following section will introduce crystal defects.

1.4.1 Point Defects in Crystalline Solids

There are many types of defect in crystalline materials. Grain boundaries, surfaces, dislocations, stacking faults and point defects; are all variations from the perfect crystal [117, 118].

In a crystal lattice, a point defect is a type of imperfection in the order of the atoms and probably the most simple to describe [118]. An extra atom in the crystal lattice will create an interstitial defect while a missing atom will produce a vacancy; both are point defects. The concentration, bonding and transport of these defects will affect how the material behaves electronically and mechanically. The formation of point defects also eludes to some interesting material properties including varying accommodation of non-stoichiometry.

The concentration of point defects is linked to the temperature in the solid [119]. The formation of a point defect requires energy, increasing the configurational energy of the system. The thermodynamic equilibrium concentration of defects is described by the Ahrrhenius equation:

$$\mathrm{C_T} = \mathrm{C_0 exp}(-\frac{\mathrm{E_f}}{\mathrm{k_B T}}) \tag{1.14}$$

Where C_T is the concentration of defects at a given temperature 'T', C_0 is the defect

concentration within the material at 0 K and k_B is the Boltzmann constant.

Equation 1.14 can be derived as follows. The change in the Gibbs free energy of a solid due to the formation of n point defects, ΔG, is given by:

$$\Delta G = nE_f - T\Delta S \tag{1.15}$$

Where E_f is the formation energy of the defect, T is the temperature and S is the entropy of the system. Minimising the free energy of the system with respect to the number of defects will provide an expression giving the concentration of defects.

$$\frac{\delta \Delta G}{\delta n} = E_f - k_B T \left(\ln \frac{N-n}{n} \right) = 0 \tag{1.16}$$

Given (for small defect concentrations):

$$\frac{n}{N-n} \rightarrow \frac{n}{N} = e^{-\frac{E_f}{k_B T}} \tag{1.17}$$

The theoretical concentration at 0 K (not a practically attainable temperature) is therefore zero. Because entropy variation apart from the configurational entropy is ignored a pre-exponential term (C_0) is required giving Equation 1.14.

The two main types of intrinsic defect are Schottky and Frenkel defects in materials investigated in this thesis [120, 121]. Both produce vacancies, but by different routes. Schottky disorder is the spontaneous production of a vacancy or a neutral vacancy cluster (in ionic ceramics both anions and cations are removed leaving an overall neutral charge) with the material removed by forming new solid.

A metal such as Be can form the following Schottky defect:

$$Be_{Be} \rightarrow V_{Be} + Be\,(\text{solid}) \tag{1.18}$$

A Schottky defect in a material such as UO_2 involves an entire unit of UO_2 being removed

and incorporated in new solid:

$$U_U^{\times} + 2O_O^{\times} \rightarrow V_U'''' + 2V_O^{\bullet\bullet} + UO_2\,(\text{solid}) \tag{1.19}$$

It can be seen that the point defects in the ceramic are charged but the overall charge remains neutral. The individual defects are likely to cluster forming the $\{V_U'''':2V_O^{\bullet\bullet}\}^{\times}$ neutral tri-vacancy cluster [122]. Stronger binding energies between the individual defects will result in a larger proportion of defect clusters being present within the material.

Frenkel disorder produces a vacancy and an interstitial species as an atom is displaced from its normal site, forming a defect pair [123]. In UO_2 the Frenkel has the lowest energy and therefore occurs most readily [124]. Equation 1.20 shows how oxygen Frenkel disorder in UO_2 is produced.

$$O_O^{\times} \rightarrow V_O^{\bullet\bullet} + O_i'' \tag{1.20}$$

These Frenkel defects are produced in fission cascades [125]. In ionic crystals the defects (vacancy and interstitial) will be oppositely charged and therefore have a Coulombic attraction to each other [126, 123].

1.4.2 Transport in Crystalline Solids

For the migration of atomic species through a solid to occur, there needs to be a suitable path available for the defect [127]. As the defect moves from an initial to final state it must overcome the energy barrier to migration [128, 127]. This is illustrated in Figure 1.19 which shows the migration of an interstitial species (red) from one site to another, and the energy of the system as this migration occurs. The higher the energy barrier to diffusion (E_m), the less likely the migration step will occur. The energy to overcome the migration barrier comes from the lattice (thermal and phonon energy). The thermal contribution to diffusion can be described in the Arrhenius equation [123]:

$$D_T = D_0 e^{-\frac{E_m}{k_B T}} \tag{1.21}$$

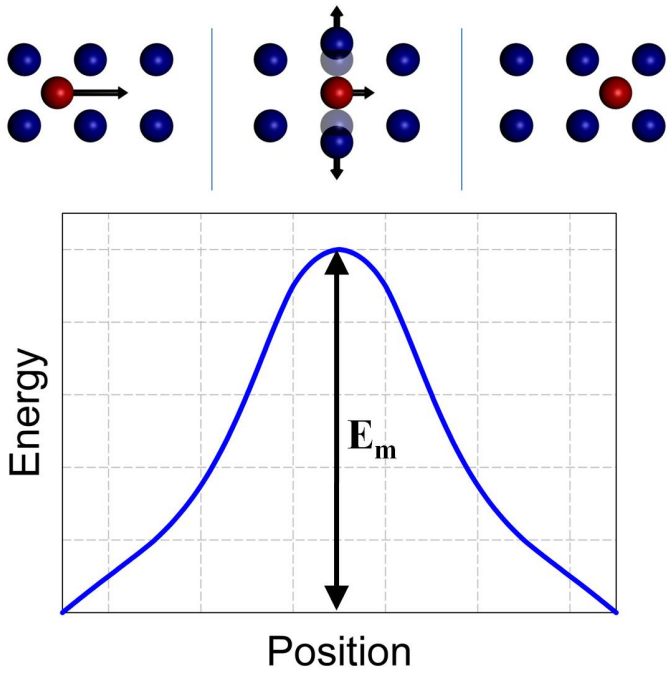


Figure 1.19: Illustration of an interstitial migration showing how the energy may change as the migrating species moves through the crystal showing the energy barrier to migration (E_m).

Where D_T is the diffusion (m^2sec^{-1}) at temperature T, D_0 is the diffusivity pre-exponential term that contains all of the entropic and hop frequency (dependent on defect co-ordination and defect morphology) for the migration to overcome the migration energy barrier (E_m) [123].

1.5 Aims of this Work

The aim of the research reported in this thesis is threefold:

- To gain greater understanding into the behaviour of extrinsic cations, dopants in UO_2 and UO_{2+x} are studied to understand their effect on the atomic scale processes within the UO_2 structure. This includes solution mechanisms of dopants and fission products in Chapter 3 and the effects of the dopants on transport properties in Chapter 4. Understanding the behaviour of trivalent and other dopants in UO_2, will

eventually contribute towards higher burn-up fuel and more effective fuel codes can be produced, increasing the efficiency of fuels in power reactors.

- In Chapter 5, work has been carried out to understand the stoichiometric properties and He and Li in ZrB_2. These properties relate to the ZrB_2 manufacturing processes and ZrB_2 being used as a fuel neutron poison. In carrying out this investigation on ZrB_2, a number of useful properties have been highlighted that have an impact in aerospace research.

- Chapter 6 presents research that gives greater understanding to the intrinsic properties of Be and a number of Be containing compounds and intermetallics. The likely defect processes that occur in Be are investigated extensively for the first time. These properties will be related to its use as a plasma facing material in the ITER fusion program. Important extrinsic defect properties will also be investigated in this regard.

The next chapter introduces the methodology used to carry out this research. The reader will notice that a variety of techniques have been used, which are tailored to each system and simulation type.

Chapter 2

Calculation Methods

"It is a mistake to think you can solve any major problems just with potatoes."
- Douglas Adams from *Life, the Universe and Everything* [129]

2.1 Introduction to Atomic Scale Simulations

Various atomic scale simulation methods are used in this thesis to predict the behaviour of materials. Crystal lattices can be modelled using classical simulation methods with empirical type atomic interactions or by quantum mechanical methods, such as density functional theory (DFT). Both approaches can be used to predict materials phenomenon such as defect populations, defect cluster morphology and binding energies, diffusion processes, solubilities of extrinsic species and non-stoichiometric deviations.

The techniques that have been used here and the methodology used to predict specific material behaviours are outlined in this section. The seemingly simple empirical potentials method is the first to be tackled.

2.2 Empirical Potentials

2.2.1 Introduction

The models that involve empirical simulations in this work use the simplified Born model of solids as the basis for the atomic description of a crystal lattice. Each ion or atom interacts with all others in the system and an energy that quantifies this interaction is derived. All simulations using empirical potentials employed the Buckingham pair type interaction to model the pairwise short-range interactions and the simple Coulombic interaction to model the long-range charge interactions. The sum of the short-range and long-range interactions gives the lattice energy $E_{lattice}$ as shown in equation 2.1.

$$E_{lattice} = \sum_{i,j>i} \left(\frac{q_i q_j}{4\pi\epsilon_0 r_{ij}} + A_{ij} e^{\frac{-r_{ij}}{\rho_{ij}}} - \frac{C_{ij}}{r_{ij}^6} \right) \tag{2.1}$$

By going through the terms individually, it is possible to understand the implications and shortcomings of this potential form. The first term in the summation involves the charges 'q' on atoms 'i' and 'j'. The product of q_i and q_j will be negative for oppositely charged ions and positive for like-charged ions. In this convention, a negative energy suggests an attractive interaction. The other terms in the Coulombic interaction are ϵ_0 which is the permittivity of free space (-8.85418782 $\times$ $10^{-12} N^{-1} m^{-2} C^2$) and r_{ij} the distance between the two interacting ions. Figure 2.1 illustrates the Coulombic interaction between like-charged and oppositely charged ions.

As the separation between two oppositely charged ions decreases, the Coulombic energy becomes increasingly negative, suggesting the ions will have the lowest energy when r_{ij}=0. This is un-realistic and a short-distance term is required. The short-distance term takes the Buckingham form and is given by the combination of the second and third parts of the summation in equation 2.1.

The Buckingham pair interaction is parametrised for each pair of ions. These parameters are A_{ij}, ρ_{ij} and C_{ij}. Both A_{ij} and ρ_{ij} describe the electronic repulsion of the ions' electrons

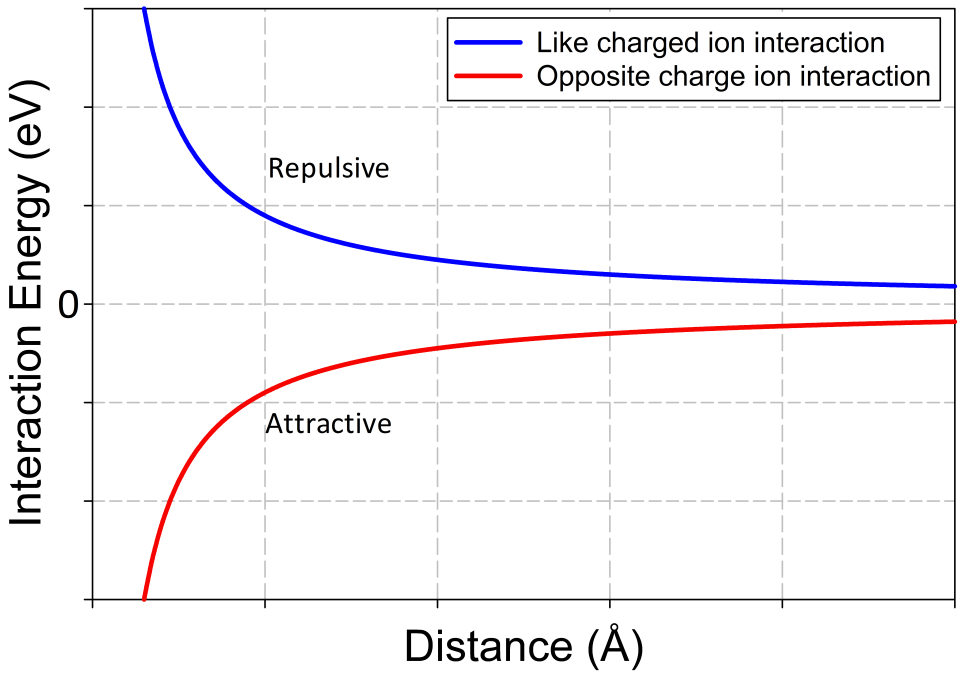


Figure 2.1: Varying interaction energy due to Coulombic interactions of like-charged ions (blue) and oppositely charged ions (red) as a function of the interionic separation distance, r_{ij}, described by the first expression in equation 2.1.

and is related to the ionic radius of each atom. The C_{ij} term is used to describe the attractive van der Waal's forces that act between pair interactions but depend strongly on the relative polarisability of the species. The C_{ij} term can be calculated (using equation 2.2 where the 'α' terms are the polarisabilities of the ions and the 'P' terms are the effective number of electrons). Alternatively, it can be fitted when producing an empirical potential.

$$C_{ij} = \frac{\frac{3}{2}\alpha_i\alpha_j}{\sqrt{\frac{\alpha_i}{P_i}}\sqrt{\frac{\alpha_j}{P_j}}} \tag{2.2}$$

The interaction energy as a function of the inter-atomic separation, as dictated by the Buckingham potential, is shown in Figure 2.2. The O^{2-}-O^{2-} which has a non-zero C_{ij} term and U^{4+}-O^{2-} ion pair potential C_{ij} value is zero. It should be noted that at very small separations, potential forms with a non-zero 'C' term become attractive in an unphysical manner and additional terms may be needed if atoms are being forced into close proximity as may occur in a radiation cascade.

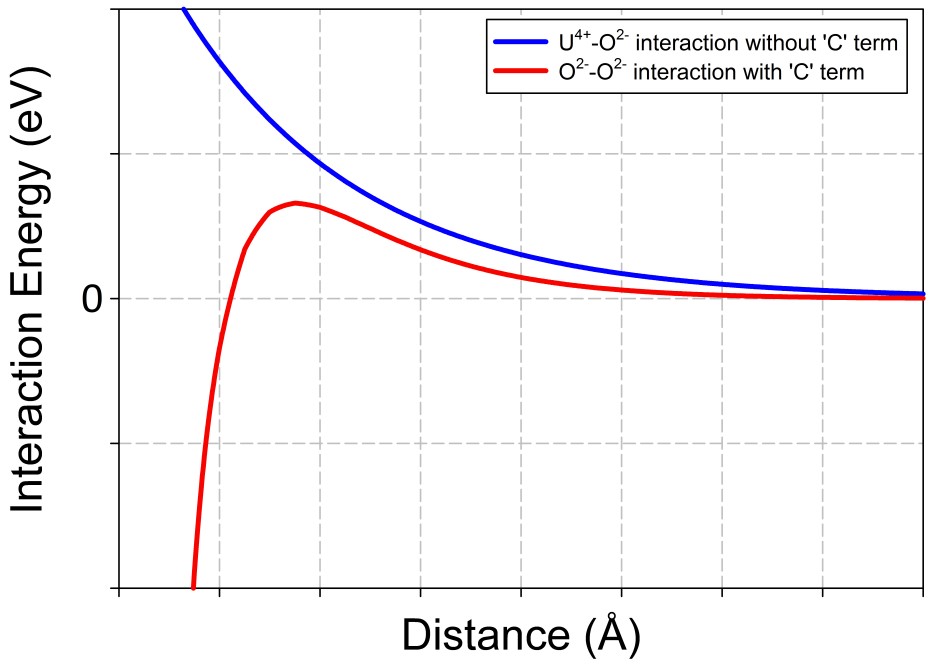


Figure 2.2: Interaction energy as a function of the interionic separation due to the Buckingham pairwise interactions between U^{4+} and O^{2-} ions (blue) and O^{2-} and O^{2-} ions (red) as described by the second and third parts of equation 2.1. The O^{2-}-O^{2-} interaction includes a 'C' term whilst for the U^{4+}-O^{2-} the 'C' term is zero.

The summation of the Coulombic and Buckingham terms gives the overall interaction between all ion pairs. The Buckingham potential parameters used throughout this work are reported in Table 2.1.

Table 2.1: Buckingham potential parameters used throughout this work.

Interaction	A (eV)	ρ (Å)	C (eV Å^6)	Reference
O^{2-}-O^{2-}	9547.9600	0.219160	32.00	[130]
U^{5+}-O^{2-}	2386.4200	0.341100	0.00	[131]
U^{4+}-O^{2-}	1761.7750	0.356421	0.00	[132]
Ru^{4+}-O^{2-}	1215.7800	0.344100	0.00	[133]
Mo^{4+}-O^{2-}	1223.9700	0.347000	0.00	[134]
Zr^{4+}-O^{2-}	1502.1100	0.347700	5.10	[135]
Am^{4+}-O^{2-}	1763.0875	0.353947	11.37	
Np^{4+}-O^{2-}	1762.3100	0.356300	11.71	
Ce^{4+}-O^{2-}	1809.6800	0.354700	20.40	[136]
Pu^{4+}-O^{2-}	1762.8400	0.354200	11.48	[137]
Th^{4+}-O^{2-}	1070.2200	0.398800	0.00	
Al^{3+}-O^{2-}	1120.0400	0.312500	0.00	[138]
Cr^{3+}-O^{2-}	1313.1800	0.316500	0.00	[138]
Dy^{3+}-O^{2-}	1807.6800	0.339300	18.77	[136]
Eu^{3+}-O^{2-}	1925.7100	0.340300	20.59	[135]
Fe^{3+}-O^{2-}	1414.6000	0.312800	0.00	[138]
Gd^{3+}-O^{2-}	1885.7500	0.339900	20.34	[135]
In^{3+}-O^{2-}	1495.6500	0.332700	4.33	[138]
La^{3+}-O^{2-}	2088.8900	0.346000	23.25	[135]
Nd^{3+}-O^{2-}	1995.2000	0.344300	22.59	[135]
Pr^{3+}-O^{2-}	2055.3500	0.343800	23.95	[136]
Sm^{3+}-O^{2-}	1944.4400	0.341400	21.25	[135]
Y^{3+}-O^{2-}	1766.4000	0.338490	19.43	[135]
Mg^{2+}-O^{2-}	1284.3800	0.299690	0.00	[136]
Zn^{2+}-O^{2-}	529.7000	0.358100	0.00	[136]
Cd^{2+}-O^{2-}	951.8800	0.348560	0.00	[136]
Sr^{2+}-O^{2-}	682.1700	0.394500	0.00	[136]
Ba^{2+}-O^{2-}	905.7000	0.397600	0.00	[136]

An empirical description of a crystal lattice is simple and the simplistic nature neglects some key physics. It is important to understand what is omitted so simulations can be steered to negate the inaccuracies.

- The Buckingham description works best for highly ionic systems. Crystals with high covalent or metallic bonding should use different potential forms to the Buckingham pair type. Covalent systems can use many-body formalisms whilst metallic systems may use an embedded atom many body type of interaction.

- The Buckingham potential is isotropic, therefore systems and ion-ion interactions with strong directional bonding will not be accurately replicated. Three or four body descriptions of inter ionic interaction may be better suited to such systems.

- Charge transfer in systems is difficult to implement. For example, during migrations the charge on a specific ion may change but the charge is fixed in the simulation. Quantum mechanical simulations would be better suited to a situation like this although charge transfer models are currently being developed [139].

- The polarisability of ions is not treated in the Buckingham or Coulombic interactions. The Shell model (see section 2.2.2) can be used with the Buckingham potential to account for this.

- The ions in this thesis use formal charges, i.e. U^{4+} and O^{2-}. Covalency will reduce the effective values of these charges. A partial charge model can be produced, however, the charges will not be easily transferable between different compositions.

2.2.2 The Shell Model

Polarisation of the ions in a crystal is a significant phenomenon, especially when charged defects and clusters with a dipole are present. In the absence of an external potential the cloud of electrons surrounding an atom (or ion) will be centred on the nucleus. When an external potential acts on an atom, the electron cloud can shift off-centre under the influence of the external field. The shell model mimics the behaviour of the electrons about an ion by having a charged shell around the central core that is able to be displaced a distance relative to the core, relative to a spring constant 'k', as proposed by Dick and Overhauser. A representation of Dick and Overhauser's model for an individual ion is

illustrated in Figure 2.3. A charge is defined for both the shell and the core. As the shell

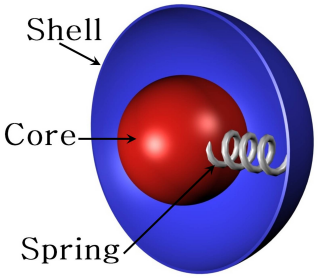


Figure 2.3: The representation of an ion in the Dick and Overhauser shell model [140]. The shell is shown in blue, the core in red and both are attached to each-other with a spring.

represents the electrons, it is usually given a negative charge. The total charge of the core and shell is the charge on the ion. For example, oxygen has a shell charge of -2.04 and a core charge of 0.04 giving an overall charge of -2. When a negative charge is encountered near the ion, the shell will be displaced away from it and visa-versa with a positive charge, as illustrated in Figure 2.4.

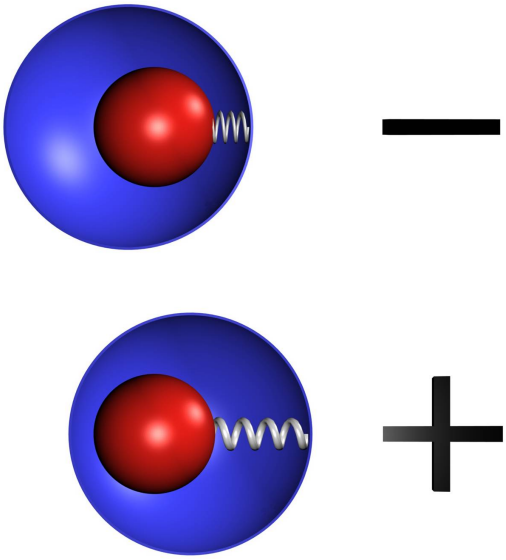


Figure 2.4: Displacement of the shell of an ion due to a point charge. A negative charge will push away the negative shell and a positive charge will attract the negative shell.

The stiffness of the spring constant 'k' will determine the polarisability of the ion. The spring constant for the O^{2-}-O^{2-} potential used throughout this work is $6.3\,\mathrm{eV\,\AA^{-2}}$.

2.2.3 Empirical Potentials Simulations

In this work the General Utility Lattice Program (GULP) code, developed by Julian D. Gale had been used to implement the empirical potential based simulations. GULP has predominantly been used to calculate defect energies and lattice energies and thereby predict lattice structures particularly defect configurations. Further details of the calculations carried out using GULP are given after the discussion of quantum mechanical methods in section 2.4

2.3 Quantum Mechanical Methods

2.3.1 Introduction

The electronic interactions between atoms determine how they are bonded to one another. The most complete description of the electronic structure around a nucleus uses quantum mechanical methods where electrons can be modelled using the non-relativistic, time-independent Schrödinger equation for many electrons reproduced in equation 2.3.

$$\hat{\mathrm{H}}\Psi(\mathbf{R_I}, \mathbf{r_i}) = \mathrm{E}\Psi(\mathbf{R_I}, \mathbf{r_i}) \tag{2.3}$$

This states that the wavefunction of the system 'Ψ' (this is the quantum state of a system of particles) operated on by the Hamiltonian operator '$\hat{\mathrm{H}}$' (containing the kinetic and potential energy contributions of the ion-electron system) is equal to the total energy 'E' of the system multiplied by the same wave-function for all ion positions '$\mathbf{R}_\mathrm{I}$' and electron positions '$\mathbf{r}_\mathrm{i}$'.

Understanding of the Hamiltonian operator is key to understanding the power of the Schrödinger equation. It can be split into a number of parts:

$$\hat{\mathrm{H}} = \overbrace{\hat{T}_N + \hat{T}_e}^{\hat{\mathrm{H}}^\mathrm{T}} + \overbrace{\hat{V}_{Ne} + \hat{V}_{NN} + \hat{V}_{ee}}^{\hat{\mathrm{H}}^\mathrm{V}} \tag{2.4}$$

where the 'T' terms refer to the kinetic energy of the nuclei (T_N) and electrons (T_e) while the 'V' terms describe the potential energy between the nuclei with other nuclei ($\hat{V}_{NN}$), electrons with other electrons ($\hat{V}_{ee}$) and between nuclei and electrons ($\hat{V}_{Ne}$). Both the kinetic and potential parts of the Hamiltonian can be split into the following two expressions:

$$\text{Kinetic} \rightarrow \hat{H}^{T} = -\sum_{I} \frac{\hbar^2}{2M_I} \nabla^2_{R_I} - \sum_{i} \frac{\hbar^2}{2m_i} \nabla^2_{r_i} \tag{2.5}$$

$$\text{Potential} \rightarrow \hat{H}^{V} = \sum_{I,J} \frac{Z_I \, Z_J \, e^2}{2|\mathbf{R_I} - \mathbf{R_J}|} + \sum_{i,j} \frac{e^2}{2|\mathbf{r_i} - \mathbf{r_j}|} - \sum_{I,i} \frac{Z_I e^2}{|\mathbf{R_I} - \mathbf{r_i}|} \tag{2.6}$$

The masses of a nucleus and electron in the system are denoted as 'M_I' and 'm_i', ∇ is the Laplacian differential operator related to a function in Euclidean space and 'e' is the charge on one electron. The atomic numbers of the 'i^{th}' and 'j^{th}' nuclei are given as 'Z_I' and 'Z_J'. As the number of electrons and ions in a system increases, the complexity of the Hamiltonian escalates considerably. Because of the complexity some approximations are required to implement the Schrödinger equation for useful systems. One of these approximations is the Born-Oppenheimer approximation [141].

2.3.2 Born-Oppenheimer Approximation

The Born-Oppenheimer approximation simplifies the Hamiltonian operator considerably, allowing the electronic and nuclear energy relaxations to be treated separately and linked with an exchange function.

Simply put, the mass of the electrons is far smaller than the mass of a nucleus. As the momenta of the nuclei and electrons will be of the same order, one can assume that the electrons move much faster than the nuclei, therefore the electrons respond almost instantaneously compared to nuclear motion. The approximation states that the nuclei are completely stationary providing an external force on the electrons. By treating the ionic nuclei as stationary, a ground state for the electron wave-functions can be found and the forces on the nuclei can be calculated, allowing a separate and simpler nuclei only step to be carried out thereafter.

Equation 2.4 can be modified, taking account of the Born-Oppenheimer approximation by simply removing the terms that do not involve the electrons interactions:

$$\hat{\mathrm{H}}_{\mathrm{e}}(\mathbf{r};\mathbf{R}) = \hat{\mathrm{T}}_{\mathrm{e}}(\mathbf{r}) + \hat{\mathrm{V}}_{\mathrm{Ne}}(\mathbf{r};\mathbf{R}) + \hat{\mathrm{V}}_{\mathrm{ee}}(\mathbf{r}) \tag{2.7}$$

Combining equations 2.5 and 2.6 together, but only including the electronic terms gives:

$$\hat{\mathrm{H}}_{\mathrm{e}}(\mathbf{r};\mathbf{R}) = -\sum_{\mathrm{i}} \frac{\hbar^2}{2\mathrm{m}_{\mathrm{i}}} \nabla^2_{\mathrm{r_i}} + \sum_{\mathrm{i,j}} \frac{\mathrm{e}^2}{2|\mathbf{r_i} - \mathbf{r_j}|} - \sum_{\mathrm{I,i}} \frac{\mathrm{Z_I e}^2}{|\mathbf{R_I} - \mathbf{r_i}|} \tag{2.8}$$

The $\hat{\mathrm{T}}_{\mathrm{N}}$ and $\hat{\mathrm{V}}_{\mathrm{NN}}$ terms in equation 2.4 can then be treated in a separate calculation and subsequently added to the electronic terms.

2.3.3 Implementing the Born-Oppenheimer Approximation

Hatree [142] and Hartree-Fock [143] methods employ the Born-Oppenheimer approximation to calculate the energy of a system. The Hartree model approximates the wavefunction as a product of non-interacting particles (known as the Hartree approximation). The Hartree-Fock methodology is an improvement on the Hartree method owing to its incorporation of the Pauli exclusion principle, however both neglect to include true electron-electron interactions, treating each electron's movement as if it were in a mean field of other electrons [144].

Kohn and Sham formulated a different approach to understanding the energy of a system using the Schrödinger equation and the Born-Oppenheimer approximation. The method uses the theorem that one can minimise the energy of a system by relating it to the density of electrons [145] by simply varying the density of the electrons over all densities for any number of electrons. This is density functional theory.

The electrons in the Kohn-Sham formulation are not interacting but because the density is considered, the electrons behave as if they were interacting (an improvement on the

Hartree-Fock formalism) [145]. The fictitious electrons wavefunction (Ψ^*) is related to the actual electron wavefunction Ψ by the Kohn-Sham Hamiltonian:

$$\mathrm{E[n(\mathbf{r})]} = \langle \Psi^* | \hat{\mathrm{H}}_{\mathrm{KS}} | \Psi \rangle \tag{2.9}$$

The Hamiltonian operator ($\hat{\mathrm{H}}_{\mathrm{KS}}$) takes the kinetic and potential energy terms for the electrons and the external potential into consideration and relates them both to the electron density of the system. Equation 2.9 can be expanded splitting the electronic and external terms as in equation 2.10:

$$\mathrm{E[n(\mathbf{r})]} = \langle \Psi^* | \hat{\mathrm{T}}_{\mathrm{e}} + \hat{\mathrm{V}}_{\mathrm{e}} | \Psi \rangle + \int \mathrm{V_{ext}}(\mathbf{r}) \mathrm{n}(\mathbf{r}) \mathrm{d}\mathbf{r} \tag{2.10}$$

where $\mathrm{V_{ext}}$ is the external potential acting on the electrons and $\hat{\mathrm{V}}_{\mathrm{e}}$ is the potential due to the electrons explicitly modelled in the system.

When solved for a single electron-like particle equation 2.10 can be described as:

$$\left[-\frac{\hbar^2}{2\mathrm{m_e}} \nabla_{\mathrm{r}}^2 + \mathrm{V_{eff}}(\mathbf{r}, \mathrm{n}(\mathbf{r})) \right] \phi_{\mathrm{i}}(\mathbf{r}) = \epsilon_{\mathrm{i}} \phi_{\mathrm{i}}(\mathbf{r}) \tag{2.11}$$

The effective potential energy component '$\mathrm{V_{eff}}$' contains not only the external and electronic potential energy terms ($\mathrm{V_{ext}}$ and $\mathrm{V_e}$) but also a term linking them, the exchange-correlation function '$\mathrm{V_{XC}}$' such that:

$$\mathrm{V_{eff}} = \mathrm{V_e} + \mathrm{V_{XC}} + \mathrm{V_{ext}} \tag{2.12}$$

All of the terms in equations 2.11 and 2.12 are derivable exactly apart from the exchange-correlation function that is not known. A number of approximations have been made for the $\mathrm{V_{XC}}$ term, two of which are detailed in the following section.

Exchange Correlation Details

There have been a number of functional forms developed for estimating the energy associated with the exchange-correlation. The exchange correlation estimates the physics that governs the density of electrons around the nucleus of an ion. The local density approximation is the most simple of these and compares the electron density at a point in the system of interest to the uniform electron gas [146] as expressed in equation 2.13 that gives the approximation for a charge density '$\mathrm{n}(\mathbf{r})$' at a point '$\mathbf{r}$':

$$\mathrm{E}_{\mathrm{XC}}^{\mathrm{LDA}}[\mathrm{n}] = \int \mathrm{n}\epsilon_{\mathrm{XC}}^{\mathrm{uniform}}[\mathrm{n}(\mathbf{r})]\mathrm{d}\mathbf{r} \tag{2.13}$$

Where $\epsilon_{\mathrm{XC}}^{\mathrm{uniform}}[\mathrm{n}(\mathbf{r})]$ is the exchange-correlation energy per electron-like particle in the uniform electron gas. This approach ignores the influence of the highly non-uniform nature of charge densities around an ion. As a consequence the generalised gradient approximation (GGA) [147] was formalised to account for this.

The GGA method for estimating the exchange-correlation functional involves a directional term '$\nabla\mathrm{n}$' and is formed in a similar manner to the LDA shown in equation 2.14.

$$\mathrm{E}_{\mathrm{XC}}^{\mathrm{GGA}}[\mathrm{n}] = \int \mathrm{f}(\mathrm{n}, \nabla\mathrm{n})\mathrm{d}\mathbf{r} \tag{2.14}$$

GGA is a marked improvement over LDA but is more computationally intensive due to the increased complexity. Neither method offers a complete description of the exchange correlation energy and although GGA includes more physics, some systems are better described by LDA [148] meaning that each system should be considered in a case-by-case manner.

Plane Waves

Many DFT computational methods express the the wave-function as the sum of plane-waves. For periodic systems, implementing Bloch's theorem [149] can significantly simplify

a calculation. The Bloch theorem is shown in equation 2.15:

$$\Psi_{\mathrm{n,k}}(\mathbf{r}) = \mathrm{u_n}(\mathbf{r})\,\mathrm{e}^{i\mathrm{kr}} \tag{2.15}$$

The value 'k' refers to the wave-vector representing the position in reciprocal lattice space; the Brillouin zone. The wave-function can be expressed as:

$$\Psi_{\mathrm{n,k}}(\mathbf{r}) = \sum_{\mathrm{k}} \Psi_{\mathrm{n,k}}(\mathbf{r}) \tag{2.16}$$

This in turn is expanded as a plane wave basis set giving the following function as a function of the reciprocal lattice vectors 'g' of the supercell.

$$\Psi_{\mathrm{n,k}}(\mathbf{r}) = \sum_{\mathrm{g}} \mathrm{c}_{i,\mathrm{k+g}}\mathrm{e}^{i(\mathrm{k+g})\mathbf{r}} \tag{2.17}$$

The sum of the plane waves would be infinite unless the terms are limited to a certain energy value, the cut-off energy $\mathrm{E_{cut}}$. The cut-off energy should be converged for each system and involves increasing the cut-off energy value while calculating the effect on the system energy.

Pseudopotentials and PAW Potentials

Pseudopotentals [150] are used to simplify the DFT calculation further. They are, in essence another approximation, this time assuming that the non-valence electrons are invariant to external influences such as bonding. Pseudopotentials remove the need to carry out all-electron calculations.

Figure 2.5 shows how pseudopotentials and the pseudo wave-functions that are produced by them differ from the all-electron type potential and wave-function. Figure 2.5 shows the importance of using a sensible cut-off radius to produce the pseudopotential. Pseudopotentials do two things: remove core electrons and they modify the core region of the valence electron wavefunctions.

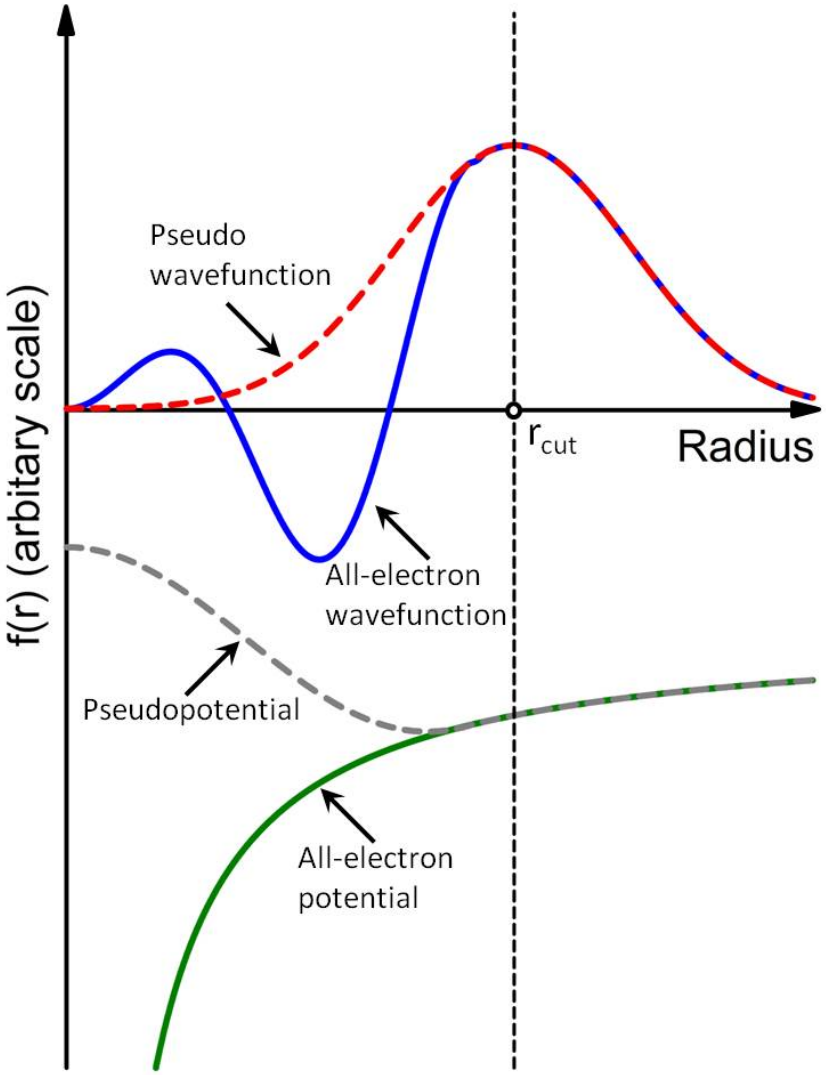


Figure 2.5: Diagram illustrating the difference between the all-electron potential and wave-functions with the pseudopotential and wave-function. The cut-off radius for the pseudopotential is shown. Figure based on that given in [151].

A pseudopotential that considers more valence and near valence electrons explicitly will be more accurate compared to the all-electron calculation. It is essential that a compromise is reached between scientific accuracy and computational expense. Aluminium is given as an example below showing a large core (computationally more simple) and a smaller core (higher accuracy).

$$\text{Al large core} \rightarrow \underbrace{1s^2 2s^2 2p^6}_{\text{core}} 3\text{s}^2 3\text{p}^1 \tag{2.18}$$

$$\text{Al small core} \rightarrow \underbrace{1s^2}_{\text{core}} 2\text{s}^2 2\text{p}^6 3\text{s}^2 3\text{p}^1 \tag{2.19}$$

When dealing with metallic systems and systems where non-valence shells have an effect on the bonding and system within a material, it is usually preferable to use smaller cores, assuming this is computationally feasible.

2.4 Static Calculations

Static calculations have been used throughout this work to calculate defect energies and to understand the thermodynamic equilibria of point defects and defect clusters in crystals.

2.4.1 Supercell Methods

A supercell is a 3-dimensional representation of a portion of a crystal that is repeated through 3-dimensional space using periodic conditions. Leaving one supercell's surface will put you in an equivalent supercell with an identical arrangement of atoms as the adjacent one. The supercell itself can initially be constructed from either an array of primitive unit cells or full unit cells and it is usually these larger cells that are expanded through space into a supercell. The expansion of the UO_2 fluorite structure from both its unit cell and primitive cell is illustrated in Figure 2.6.

The primitive unit cell is the arrangement of atoms that can be placed at each of the lattice points of one of the fourteen Bravais lattices. In the case of the fluorite lattice, the 3 atom

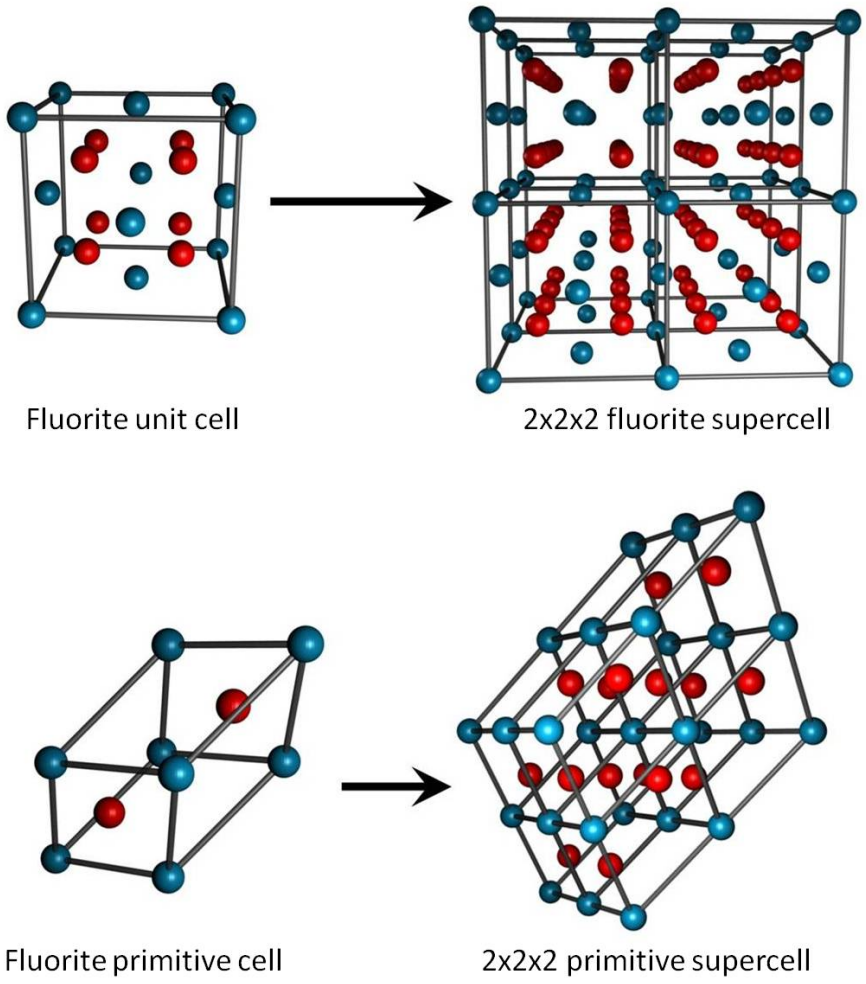


Figure 2.6: The formation of 2×2×2 supercells from primitive and unit fluorite cells.

primitive cell shown in Figure 2.6 fits onto a face centred cubic Bravais lattice to form the unit cell also shown in Figure 2.6 (the complete fluorite space group is $Fm\bar{3}m$).

Defects can be placed within a supercell by changing the arrangement of some atoms. For a single defect, the overall concentration can be varied by varying the size of the supercell. A 1×1×1 fluorite supercell containing 12 atoms with one defect will have a higher concentration of defects in comparison to a 2×2×2 supercell that contains 96 atoms with one defect. Increasing and decreasing the supercell size can give understanding of the stability of defects with varying concentrations.

Due to the nature of supercell calculations, defects are usually charge neutral or charge compensated by defects in the supercell. A uniform charged background field can be added in both DFT codes and empirical potential codes.

In this work, supercell type calculations are used in all defect calculations that employ the DFT approach. Supercell methods were also used with some the empirical potential calculations.

The Perfect Lattice

Minimisation of the energy of a perfect crystal can be achieved using a supercell type method under either constant volume minimisation (where the atom positions are allowed to change but the volume stays constant) or constant pressure conditions (where the cell size and shape can vary under a pre-determined pressure) [152]. Both energy minimisation techniques involve calculating the forces on the atoms at each step. The atoms are then displaced with a proportional distance related to the force. Constant pressure calculations remove the strains on the supercell at each step by adjusting the supercell lattice vectors.

Nudged Elastic Band Method

Static defects can be modelled using the supercell method and migration pathways can be found using the nudged elastic band method (NEB) [153] within a supercell. A defect in

a supercell will change the energy of the system. A stable defect in equilibrium with the system will have a lower energy than one that is not stable. The NEB method measures the energy of the supercell with respect to a species migrating from and to a stable position over a number of nodes (or images). Each node requires an independent supercell calculation but all are linked. At each set of energy minimisations the effective force on the migrating ion in each position is calculated. The ion is then moved at a normal to the vector between the two neighbouring images. The final, energy minimised set of images reveals the lowest energy migration pathway (the minimum energy path). The E_m can be taken to be the maximum energy point on the migration pathway (see Figure 1.19 in section 1.4).

The NEB method has been used in both DFT and empirical calculations in this thesis. For each run, the beginning and final positions of the migrating atom has to be geometrically minimised in two separate prior calculations.

Within GULP [154], the empirical potential code, the intermediate images can be added to the input data explicitly or the code can extrapolate a stated number of images between the initial and final position of the migrating species. The DFT code VASP requires the user to produce a set number of images that can be extrapolated between the initial and final state.

Defect Energy

A number of useful energies can be calculated using supercells. The defect energy is simply the energy difference between a perfect crystal supercell and one that contains the defect or defect cluster i.e.

$$E_{\text{Defect}} = E_{\text{Defective Supercell}} - E_{\text{Perfect Supercell}} \tag{2.20}$$

Note: These energies are only components of a complete thermodynamic process and are not physically significant on their own.

In a supercell there can be problems related to the boundary conditions and the defect and

the defect volume (the volume of a crystal lattice affected by the defect) interacting with its periodic image in adjacent supercell (this problem is addressed by the Mott-Littleton method [155] in the next section). Larger supercells reduce the interaction between defects in neighbouring supercells and therefore give defect energies better related to defect energies tending to the infinite dilute limit.

Incorporation Energies

The incorporation energy [152] is similar to the calculation of the defect energy, however, the defect is being incorporated into a perfect or defective lattice; specifically on to a vacant site an interstitial site or into a cluster of vacancies.

$$E_{\text{Incorporation}} = E_{\text{S.C. With Incorporated Atom}} - E_{\text{S.C. Without Incorporated Atom}} - E_{\text{Atom at Infinity}} \tag{2.21}$$

The energy of an atom at infinity is zero when using an empirical description of a system. However, in a quantum mechanical description of a system the atom has a self energy due to election-nucleus and electron-electron interactions giving the atom a specific structure when it is in a non-interacting environment.

The incorporation energy gives important information about the behaviour of defects in defective systems. That is, indicative of the preference for one site over another. They are, however, still not complete from a thermodynamic point of view. An example would be in a system with high Schottky disorder (having a high concentration in vacancies). The energy change of the system when defects are placed onto these various vacancy sites will help us understand how Schottky disorder will effect the solubility of the incorporated defect.

The same boundary issues that are present when calculating the defect energy are present when calculating the incorporation energy. Larger supercell sizes increase the accuracy while the Mott-Littleton methodology can also be used within the GULP code when using empirical methods.

2.4.2 The Mott-Littleton Method

By removing the periodic boundaries associated with the supercell methods, defects can be studied in the dilute limit without a defect in an adjacent cell. Calculations of isolated defects employ the Mott-Littleton methodology [155].

The Mott-Littleton method involves centring a defect in a set of concentric spheres where the energies of the atoms are calculated in a number of ways with the 'best' description employed in the region immediately surrounding the defect as the relaxation (the movement of ions to reduce the overall system energy) will be greatest in this region.

In the inner-most region, termed 'region I', the system is relaxed explicitly. The radius for this sphere is defined as an input parameter. The surrounding volume is termed region IIa (where the radius is also defined), and is a boundary layer between region I and region IIb, the outermost layer (see Figure 2.7).

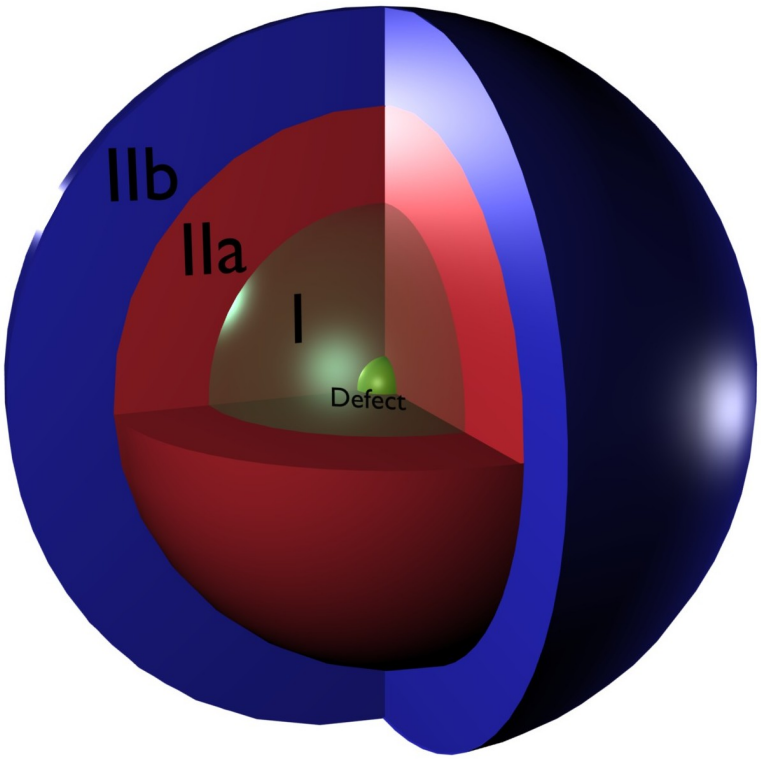


Figure 2.7: Illustration of the two region approach used to carry out Mott-Littleton defect energy calculations. The defect in the centre (light green) is surrounded by three concentric spheres, region I (green), region IIa (red) and region IIb (blue).

Atoms in region IIb are said to have a weak enough interaction with the defect that they are treated with a continuum method involving the ions' charges and the distance away from the centre of region I to calculate the (polarization) response energy of the lattice away from the defect, EP.

$$P = \frac{V_C q r}{4\pi |r|^3}(1 - \frac{1}{\epsilon^0}) \tag{2.22}$$

'r' is the distance of the atom from the centre of region I, 'q' is the charge on the ion, 'P' is the polarisation of the atom, V_C is the volume of the unit cell and ϵ^0 is the static dielectric constant of the crystal.

The ions in region IIa also use the Mott-Littleton approximation but the interactions between the ions in region IIa and I are treated explicitly. The region sizes need to be large enough for the approximations to be valid. For each system the region sizes should be optimised. Figure 2.8 shows an example minimisation of the region I size for an oxygen vacancy in UO_2.

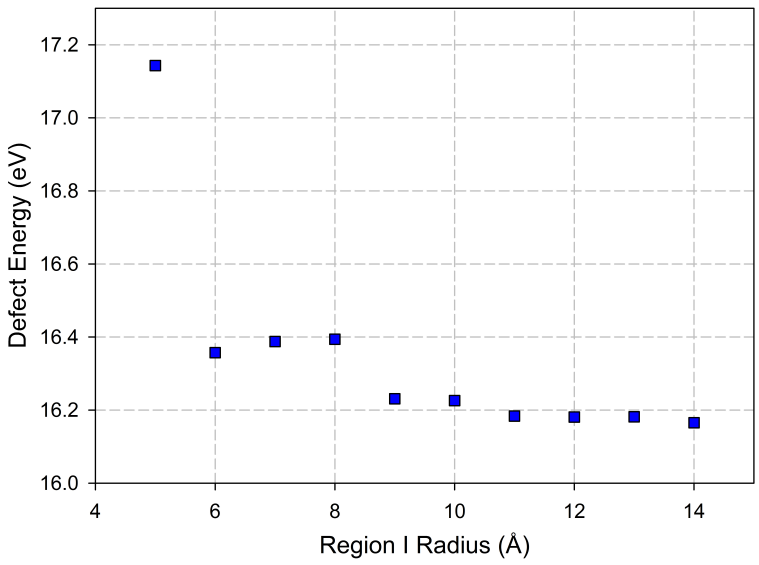


Figure 2.8: Example of how a defect energy will vary with region I size. Here the region II radius is varied around an oxygen vacancy in UO_2. In these calculations the region IIa radius was kept constant at 34 Å.

Calculation of Defect Energy

The defect energy (E_d) can then be calculated by adding the energy of the ions in region I, and the energy of ions in regions IIa and the response energy of region IIb where the energies are a function of the atoms' displacement from their lattice sites. Usually the Mott-Littleton energy of region IIa is calculated for all atoms in one simple calculation. As region IIb extends to infinity, the energy of region IIb has to be approximated to have harmonic order and the energy of the region is a quadratic function of the displacements predicted by the Mott-Littleton approximation (affected by regions I and IIa). The defect energy can therefore be calculated as shown in equation 2.23.

$$E_d = E_{region\ I}(r) + E_{region\ IIa}(r,\zeta) - \frac{\zeta}{2}\frac{\delta E_{region\ IIa}(r,\zeta)}{\delta\zeta}|_{\zeta=\zeta_e} \tag{2.23}$$

Where ζ are the displacement vectors of the ions in region II, ζ_e are the equilibrium displacement vectors and r is the distance. Notice how the dependence of energy on region IIb has been removed.

Transition State Finder

In the GULP program, transition states can be found by using the so-called RFO method, within the Mott-Littleton framework. RFO actually stands for the optimisation technique, 'Rational Functional Optimisation', and the transition finder is an implementation of this minimiser that allows the inverse Hessian matrix to be searched to obtain the eigenvalues and eigenvectors. Transition points are special in that they only have one negative eigenvalue. The overall migration energy barrier can be obtained by taking the energy of a RFO transition calculation away from a simple Mott-Littleton calculation of the starting arrangement for each migration.

$$\mathrm{E_m} = \mathrm{E_{transition}} - \mathrm{E_{defect}} \tag{2.24}$$

Care must be taken into the placement of the migrating ion when carrying out an RFO calculation as it is difficult to visualise the entire energy landscape (as is the case with the NEB method).

Lattice energies, defect energies and incorporation energies can be used for a number of predictions including solution energies and stoichiometry changes. Each will be detailed in the results chapters.

Approximating Defect Concentrations

When reaction, defect and solution energies are discussed in the following chapters they will generally be enthalpies and as such do not have entropic terms included. Nevertheless, these energies can be used to calculate the approximate equilibrium concentrations when considering something like the following reaction:

$$\mathrm{A} + \mathrm{B} \rightarrow \ \mathrm{C} + \mathrm{D} \tag{2.25}$$

Where the energy of the reaction is ΔG. The equilibrium constant 'K' can be expressed as:

$$\mathrm{K} = \frac{[\mathrm{C}][\mathrm{D}]}{[\mathrm{A}][\mathrm{B}]} \tag{2.26}$$

and 'K' can be expressed in the Arrhenius form:

$$\mathrm{K} = \exp\left(\frac{-\Delta \mathrm{G}}{\mathrm{kT}}\right) \tag{2.27}$$

By using the equation

$$\Delta \mathrm{G} = \Delta \mathrm{H} - \mathrm{T}\Delta \mathrm{S} \tag{2.28}$$

Equation 2.27 can be expanded to give:

$$\mathrm{K} = \exp\frac{-\Delta \mathrm{H}}{\mathrm{kT}}.\exp\frac{-\Delta \mathrm{S}}{\mathrm{k}} \tag{2.29}$$

If the change in the entropy of the system can be considered quite small (as it is for most solids compared to the lattice enthalpies [156]), then $\exp\left(\frac{-\Delta S}{k}\right) \approx 1$, the concentration of products compared to reactants can be estimated as:

$$\frac{[C][D]}{[A][B]} \approx \exp\left(\frac{-\Delta H}{kT}\right) \tag{2.30}$$

Defect Relaxation Volumes

Defect relaxation volumes are used to understand the effect of a defect in a crystal on the volume of the crystal. Although supercells can be used to understand the change in volume due to certain neutral defects in a crystal, a method that uses Mott-Littleton type calculations can be used to predict the effect of individual charged defects and defect clusters.

The defect relaxation volume for one defect or defect cluster can be calculated using the following equation:

$$v = \kappa_T V_C \left(\frac{\delta f_v}{\delta V_C}\right)_T \tag{2.31}$$

where κ_T is the isothermal compressibility of the crystal (the inverse of the bulk modulus and therefore a material constant) measured in ÅeV^{-1}, V_C is the volume of the perfect unit cell, measured in Å^3 and $\left(\frac{\delta f_v}{\delta V_C}\right)_T$ is the change in defect formation energy as a function of cell volume at a constant temperature, measured in eVÅ^{-3}. The latter term is calculated by carrying out a series of constant volume Mott-Littleton calculations on a single defect or defect cluster. The lattice parameter is varied by $\pm 1\%$ of the nominal cell volume and the defect energy is plotted against the volume allowing the gradient $\left(\frac{\delta f_v}{\delta V_C}\right)_T$ to be evaluated.

The defect relaxation volume, v, can be used to calculate the change in lattice parameter or volume as a function of defect concentrations by using the following equations:

$$\text{Lattice parameter} = \left[\sum (c_i \times v_i) + V_{UO_2}\right]^{\frac{1}{3}} \tag{2.32}$$

$$\text{Percentage volume change} = \frac{\sum (C_i v_i)}{V_{UO_2}} \times 100 \tag{2.33}$$

In each of the equations the C_i term is the concentration of each defect or defect cluster with the defect volume, v_i. Equations 2.32 and 2.33 are only accurate for cubic systems such as UO_2. Other systems require more complicated expressions.

Chapter 3

Solution of Dopants and Fission Products in Uranium Dioxide

"It doesn't matter how beautiful your theory is, it doesn't matter how smart you are. If it doesn't agree with experiment, it's wrong."
- Richard P. Feynman [157].

3.1 Introduction

Trivalent oxides are added to uranium dioxide fuel to improve their in-reactor performance by manipulating the microstructure and the neutronic response of the fuel. Examples include gadolinium (Gd) used as a 'burnable poison' [158] and chromium (Cr) added as a grain size enlarger and also to increase the as-manufactured pellet density [74]. Mixed oxide fuels are often manufactured by mixing the sesquioxide of a minor actinide or plutonium with UO_2 (e.g. Am_2O_3 with UO_2). The purpose of this study is to develop an atomic scale understanding of how such trivalent dopants are accommodated in stoichiometric and hyper-stoichiometric fuel and then understand the effects of dopants and fission products on the swelling of the lattice.

Trivalent cations are produced in large concentrations as a result of fission processes [51]. As with the dopant sesquioxides, it is important to understand how these fission products will behave within the fuel, staying in solution or forming precipitates (possibly forming nucleation sites for further fission products).

Isovalent and aliovalent cations' effect on the lattice volume are also investigated. When combined with a fission product inventory, the overall effect of fission products as burnup progresses on lattice volume can be ascertained and compared to experimental data.

3.2 Solution Energies of Trivalent Oxides into UO_2

In this section the solution of trivalent cations into the uranium dioxide lattice is discussed. Solution into both UO_2 and UO_{2+x} is considered, allowing a comparison between the mechanisms that can proceed in both. Special attention is given to the behaviour of Cr_2O_3 due to its use as a dopant in some advanced fuels [82, 38].

3.2.1 Trivalent Cation Solution into Stoichiometric UO_2

Solution of trivalent oxides into fluorite crystal systems have been modelled in the past; a predominant example being Y_2O_3 solution into ZrO_2. As the formal charge of the sesquioxide cation is one less than the cation in the fluorite ZrO_2 compound (Zr having a "4+" charge and Y having a "3+" charge), a -1 charge defect will be produced when the trivalent cation resides on the tetravalent site. To maintain charge neutrality a positive defect is required, the form of which will vary depending on the solution mechanism. We begin by assuming that the solution of trivalent ions creates oxygen vacancies (equation 3.1) or trivalent interstitial ions (equation 3.2) that are well in excess of those available through intrinsic disorder processes whilst maintaining charge neutrality (a suitable approximation for even low extrinsic concentrations). The two mechanisms are described here using

Kröger-Vink notation [65],

$$T_2O_3 + 2U_U^{\times} + O_O^{\times} \rightarrow \ 2T_U' + V_O^{\bullet\bullet} + 2UO_2 \tag{3.1}$$

$$2T_2O_3 + 3U_U^{\times} \rightarrow \ 3T_U' + T_i^{\bullet\bullet\bullet} + 3UO_2 \tag{3.2}$$

A compensation mechanism similar to equation 3.1 has been reported for Y_2O_3 in CeO_2 [159]. Reactions analogous to equation 3.2 are currently the assumed solution mechanism for Cr_2O_3 solution in UO_2 [82].

Solution energies for the simple reactions given in equations 3.1 and 3.2 are calculated using empirical potentials using GULP, by taking the total energy of the reactants away from the products. Equation 3.1 solution energies would be calculated by taking the energy for a unit of T_2O_3 away from the energy of a unit of UO_2, plus the defect energies of two T_U' and one $V_O^{\bullet\bullet}$ defects. The solution energies for a range of trivalent cations were calculated for reactions 3.1-3.2, in order to establish the variation of solution energy with cation radius. In all cases, constituent defect energies were calculated using the Mott-Littleton approach (with the radii of region I and region IIa 13 Å and 34 Å respectively). Initially, all of the defects are treated as individual defects (i.e. they are not interacting with each other). Clustered defects are considered subsequently.

Figure 3.1 reports the solution energies for trivalent oxides into UO_2, treating all the constituent defects. It can be seen that both mechanisms give positive solution energies for all trivalent cations entering uranium dioxide. Before continuing, it is important to note that both equation 3.1 and 3.2 result in defects of opposite charge. Consequently, there will be Coulombic attractions between defects resulting in the formation of defect clusters and a reduction in the solution energy. Of course, there are a number of different possible defect arrangements (configurations) of the clusters that must be investigated in order that the most stable cluster is identified.

The stable clusters were identified by carrying out a range of calculations, arranging the constituent defects in all possible arrangements within a unit cell and identifying the lowest

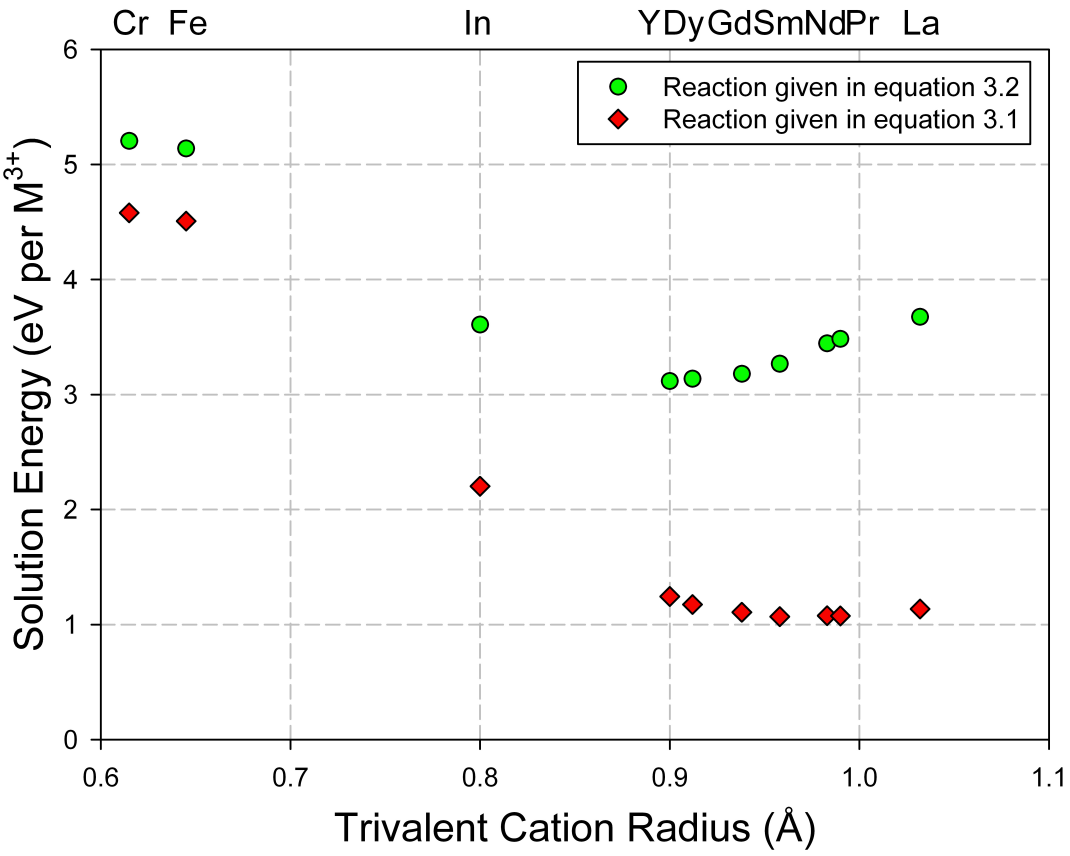


Figure 3.1: Showing the variation in solution energy with oxygen vacancy and trivalent interstitial defect compensation mechanisms given in equations 3.1 and 3.2 when defects are treated as isolated.

defect energy cluster using the classical Mott-Littleton method.

In the case of the oxygen vacancy cluster $\{V_O^{\bullet\bullet}{:}2T_U'\}^{\times}$, the oxygen vacancy was calculated to always reside in a second nearest neighbour position with respect to the M^{3+} substitutional ions as shown in Figure 3.2 (this behaviour was identified previously for trivalent ions in ZrO_2 [160] and CeO_2 [156]). It can be seen that the two T_U' defects sit in a nearest neighbour position with respect to each other. One would intuitively expect these oppositely charged defects to attract each other enough to sit in a nearest neighbour position. Previous work in CrO_2 [156] and ZrO_2 [160] showed that this was due to a strain effect on the lattice due to the defect.

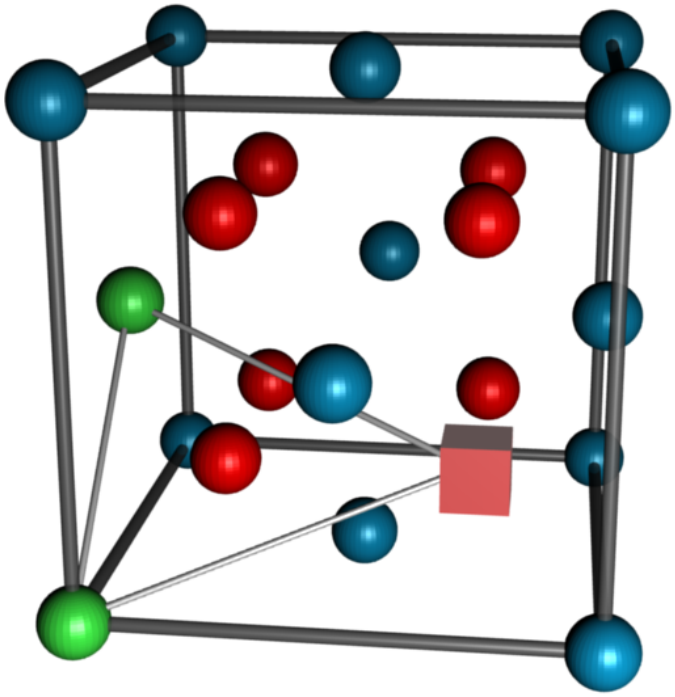


Figure 3.2: Oxygen vacancy cluster that is predicted to form, accommodating two trivalent cations. The red cube represents the vacant oxygen ($V_O^{\bullet\bullet}$) and the green spheres represent the trivalent cations residing on a uranium site (T_U').

The cluster that incorporates a trivalent interstitial ion in UO_2, the $\{3T_U'{:}T_i^{\bullet\bullet\bullet}\}^{\times}$ cluster, has also been investigated. The lowest energy arrangement involves all the M_U' species in nearest neighbour sites with respect to the $T_i^{\bullet\bullet\bullet}$ defect ion as illustrated in Figure 3.3.

The solution energies for the defects when they are considered as clustered defects is

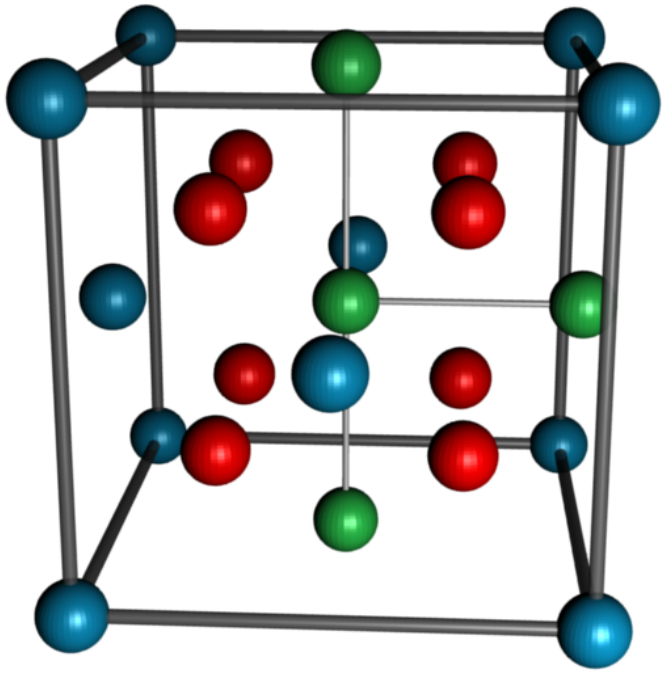


Figure 3.3: Uranium interstitial cluster that is predicted to form, accommodating four trivalent cations. The green spheres represent the trivalent cations, with the central trivalent cation being the $(\frac{1}{2},\frac{1}{2},\frac{1}{2})$ interstitial site.

illustrated in Figure 3.4. Cluster formation is shown to be more energetically favourable compared to isolated defects by comparing the solution energies presented in Figures 3.1 and 3.4. The binding energy of each of the clusters can be ascertained by calculating the difference in solution energies. The binding energies for the oxygen vacancy clusters is presented in Figure 3.5. It is evident that the binding energy of the clusters increases with decreasing trivalent cation size, that is, the smaller trivalent cations will bind more readily.

Irrespective of trivalent ion size the results suggest that cations are accommodated via the oxygen vacancy compensation mechanism (equation 3.1). Furthermore, the solution energies are all positive indicating limited solubility in the stoichiometric lattice. Larger cations are shown to have smaller solution energies into UO_2, the minimum energy being associated with a radius near Gd^{3+}.

The solution energy for Cr_2O_3, via oxygen vacancy compensation, is 9.15 eV (assuming isolated defects). This energy is high and suggests that the extent of solution will be very small. Consequently, it is first necessary to establish if the reaction stated in equation 3.1

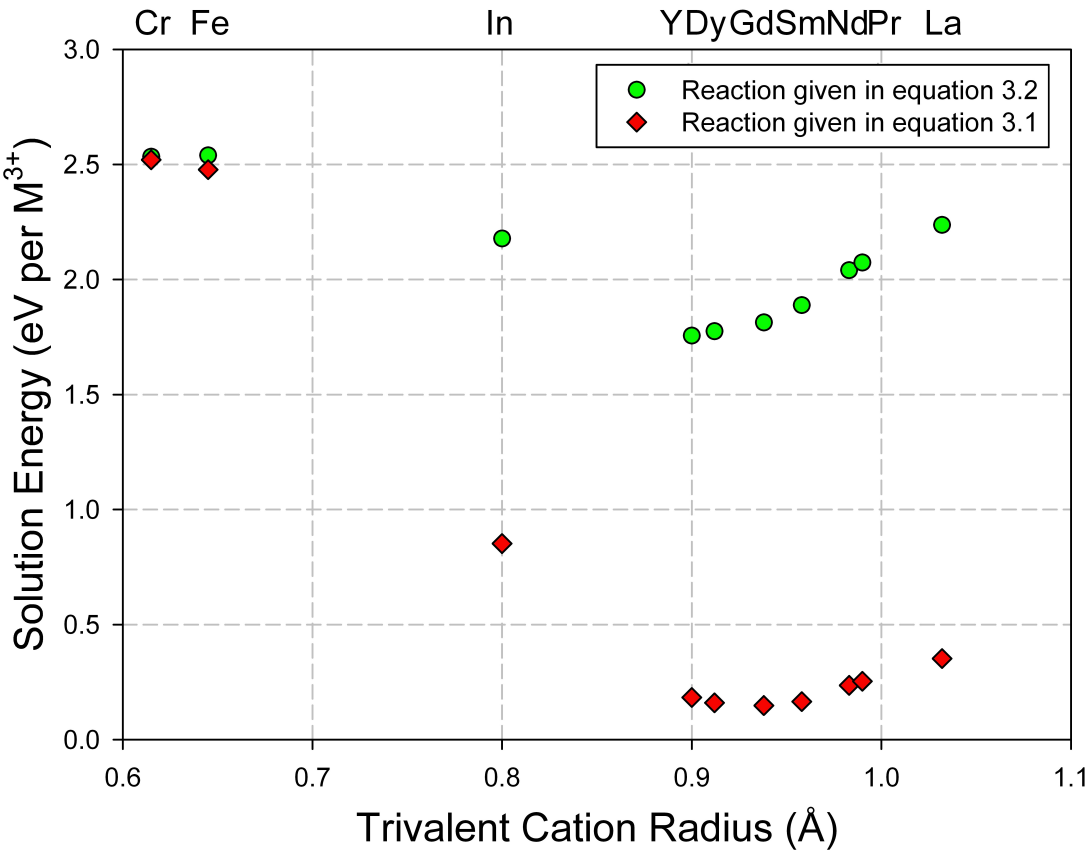


Figure 3.4: Showing the variation in solution energy with oxygen vacancy and trivalent interstitial defect compensation mechanisms given in equations 3.1 and 3.2 when defects are treated as clustered.

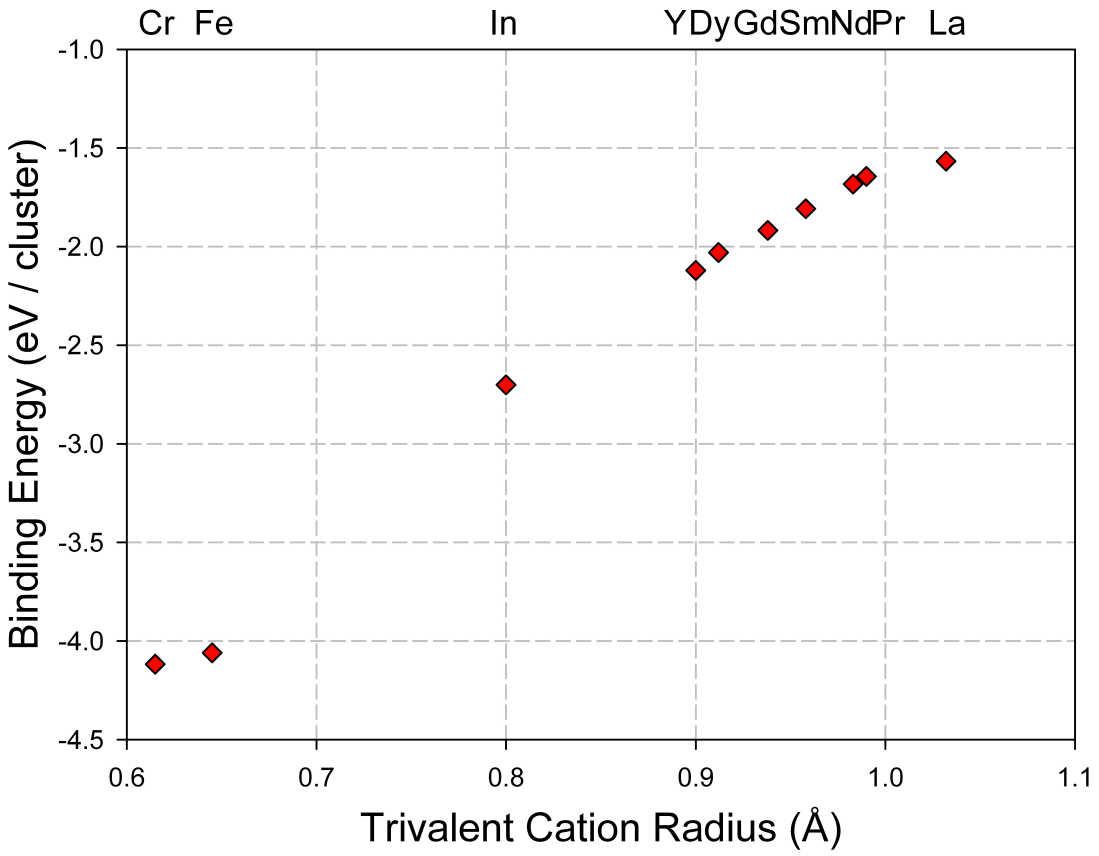


Figure 3.5: Binding energy of the constituent defects that make up the $\{2T'_U{:}V^{\bullet\bullet}_O\}^{\times}$ cluster for a range of trivalent cations. The smaller cations are more bound (i.e. with a greater negative energy).

or the UO_2 dominant intrinsic defect reaction (the oxygen Frenkel [161]) gives rise to the majority of oxygen vacancies. The total oxygen Frenkel reaction (equation 3.3 and shown in Figure 3.6) is 8.32 eV (using the present potential set).

$$O_O^{\times} \rightarrow O_i'' + V_O^{\bullet\bullet} \tag{3.3}$$

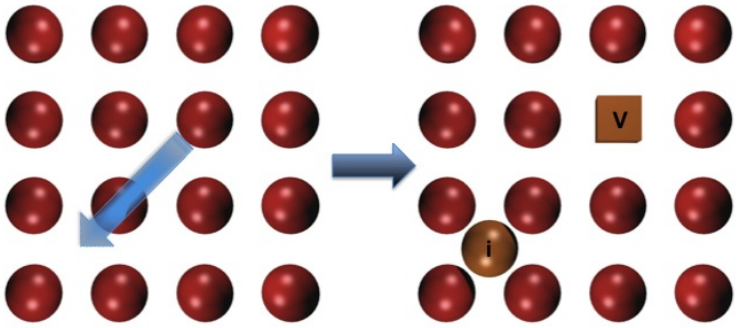


Figure 3.6: Schematic of the formation of an oxygen Frenkel defect pair (both defects shown on the left in orange, the vacancy as a cube and interstitial as a sphere.

Thus, if it is the controlling oxygen vacancy reaction (which will imply $[O_i'']$=$[V_O^{\bullet\bullet}]$), the equilibrium vacancy concentration will be given by:

$$[V_O^{\bullet\bullet}] = e^{\frac{-\Delta H_{Fr}}{2kT}} = e^{\frac{-4.16}{kT}} \tag{3.4}$$

Conversely, if the solution reaction is dominant, electroneutrality is maintained by $2[Cr_U']$ = $[V_O^{\bullet\bullet}]$ and it follows that,

$$[Cr_U']^2[V_O^{\bullet\bullet}] = e^{\frac{-\Delta H_{sol}}{kT}} \tag{3.5}$$

$$\Rightarrow [V_O^{\bullet\bullet}] = \sqrt[3]{4}\, e^{\frac{-\Delta H_{sol}}{3kT}} = \sqrt[3]{4}\, e^{\frac{-3.05}{kT}} \tag{3.6}$$

Given that $\Delta H_{Fr}/2 > \Delta H_{sol}/3$ when Cr_2O_3 is considered, the oxygen vacancy concentration is dominated by the Cr_2O_3 solution mechanism.

It is possible that defect cluster formation might lower the solution energy sufficiently

to give rise to higher concentrations of Cr in the UO_2 lattice. In this case, the solution reaction becomes,

$$Cr_2O_3 + 2U_U^{\times} \rightarrow \{2Cr'_U : V_O^{\bullet\bullet}\}^{\times} + UO_2 \tag{3.7}$$

so that the concentration of clusters in the lattice will be given by

$$[\{2Cr'_U : V_O^{\bullet\bullet}\}^{\times}] = e^{\frac{-\Delta H_{cluster}}{kT}} \tag{3.8}$$

where the solution energy assuming cluster formation, $\Delta H_{cluster}$= 5.1 eV. Since each cluster results in the accommodation of two Cr^{3+} ions on uranium lattice sites, the concentration of Cr^{3+} ions at lattice sites is therefore equal to $2\,e^{\frac{-\Delta H_{cluster}}{kT}}$. However, since $\Delta H_{sol}/3 < \Delta H_{cluster}$, it follows that isolated Cr^{3+} ions dominate the solution of Cr_2O_3 in the stoichiometric lattice, commensurate with a low solubility of Cr_2O_3 in stoichiometric UO_2.

Now, turning to Gd_2O_3, the isolated solution energy is 2.2 eV whereas the cluster solution energy is 0.3 eV. Thus, for Gd^{3+}, $\Delta H_{sol}/3 > \Delta H_{cluster}$ and consequently, solution is dominated by $\{2Gd'_U{:}V_O^{\bullet\bullet}\}^{\times}$ clusters. Furthermore, such a small solution energy implies a high degree of solid solubility commensurate with previous experimental observations [162]. For trivalent ions of intermediate size, both isolated and cluster mechanisms will be important. Figure 3.7 presents the changes in drive to form defect clusters over isolated defects as a function of trivalent cation radius. It can be seen that trivalent cations smaller than and including In^{3+} preferentially enter the UO_2 lattice as isolated defects.

The results so far have shown that all sesquioxides have a positive solution energy into stoichiometric UO_2, larger cations being more soluble with respect to smaller cations. All trivalent species enter by forming oxygen vacancy defects similar to those observed for Y_2O_3 solution in ZrO_2. Solution has been found to be dominated by the extrinsic species and not intrinsic defect processes. The larger cations will form defect clusters whereas smaller cations are more likely to form isolated defects, meaning that the oxygen vacancies will not necessarily associate themselves with the smaller substitutional trivalent cations. In the forthcoming section solution into a non-perfect lattice is considered, specifically

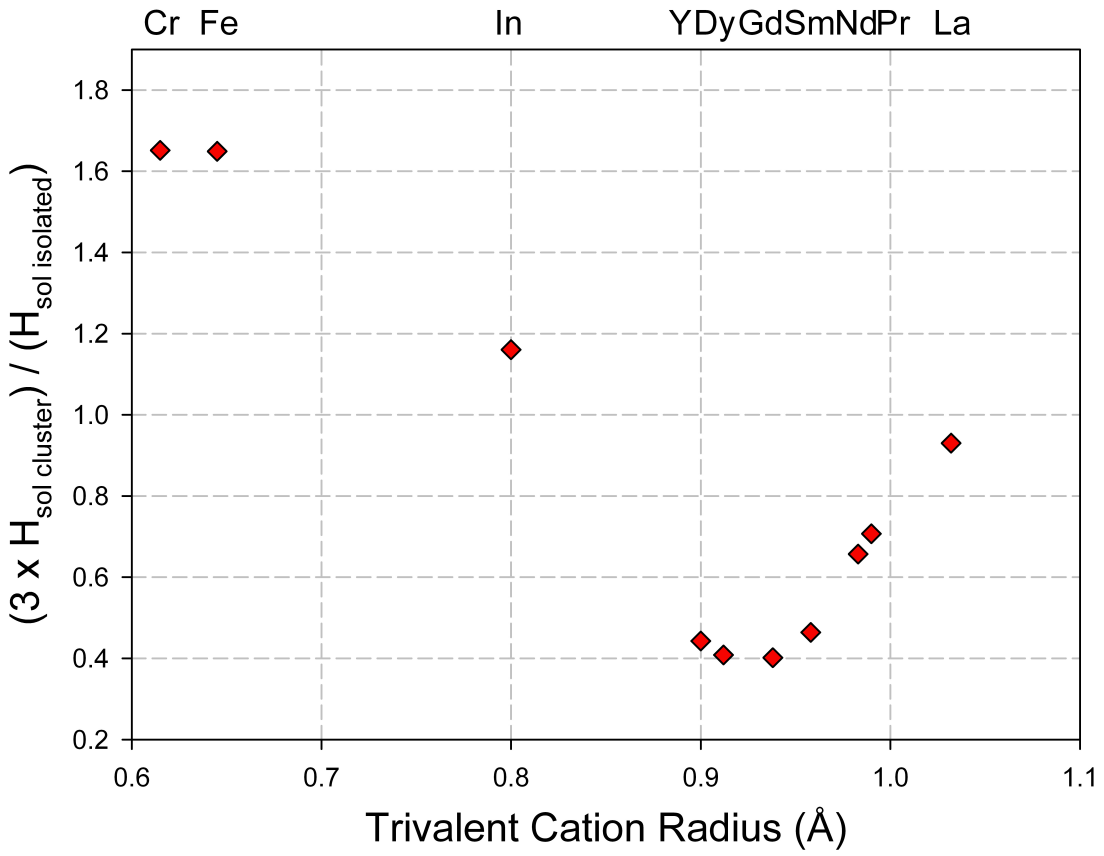


Figure 3.7: The drive for the defects produced during solution to cluster forming the $\{2T'_U{:}V^{\bullet\bullet}_O\}^{\times}$ cluster. Cations that have values lower than 1.0 are predicted to form clusters while trivalent cations above are predicted to enter UO_2 by forming isolated defects.

looking at the changes in solution mechanism and magnitude in UO_{2+x}.

3.2.2 Reaction into Hyper-stoichiometric UO_2

When UO_{2+x} is formed, oxygen interstitials are assumed to preferentially be produced [163], however uranium vacancies will also accommodate the hyper-stoichiometry. The following equation can be used to calculate which defect is most favourable:

$$U_U^{\times} + 2O_i'' \rightarrow V_U'''' + UO_2 \tag{3.9}$$

The potential set used in this study gives a negative reaction energy of -2.2 eV for this reaction when all defects are treated as separated species, suggesting that uranium vacancies are most stable. Even if this is just an artefact of the empirical nature of the potentials, since the oxygen Frenkel equilibrium (equation 3.3) must be maintained, a decrease in the $V_O^{\bullet\bullet}$ concentration will follow. Maintenance of the Schottky equilibrium,

$$U_U^{\times} + 2O_O^{\times} \rightarrow \ V_U'''' + 2V_O^{\bullet\bullet} + UO_2 \tag{3.10}$$

then implies that there is an increase in the V_U'''' concentration and therefore V_U'''' defects can be considered more relevant in UO_{2+x} than for stoichiometric UO_2.

Thus, given a degree of hyper-stoichiometry UO_{2+x}, T_2O_3 sesquioxides may be accommodated via the following reactions. First, taking advantage of the increase in oxygen interstitial concentration:

$$T_2O_3 + O_i'' + 2U_U^{\times} \rightarrow \ 2T_U' + 2UO_2 \tag{3.11}$$

Second, via the uranium vacancy excess:

$$V_U'''' + 3U_U^{\times} + 2T_2O_3 \rightarrow 4T_U' + 3UO_2 \tag{3.12}$$

In both cases, U^{5+} ions are already in evidence in the hyper-stoichiometric lattice as charge

compensating species and it is these species that charge compensate the trivalent T'_U ions. As the defects are oppositely charged, the morphology of the defect cluster was investigated and it was found that the two defects preferentially sit in a nearest neighbour position to each other forming the $\{T'_U{:}U^{\bullet}_U\}^{\times}$ dimer as illustrated in Figure 3.8.

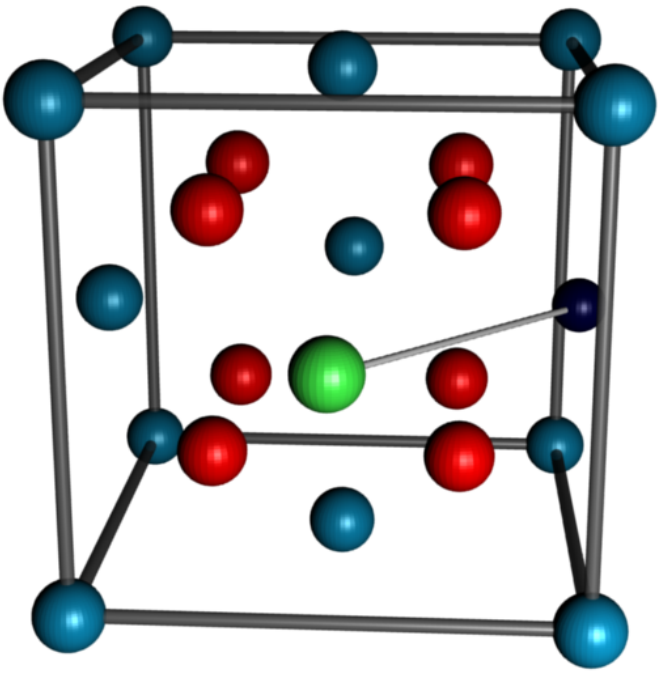


Figure 3.8: Uranium 5+ cluster that may form, accommodating a trivalent cation. The navy blue sphere represents the oxidised uranium ($U^{\bullet}_U$), the green sphere represents a trivalent cation sitting on a uranium site (T'_U).

The solution energy of Cr_2O_3 and that of other trivalent cations into hyper-stoichiometric UO_2 has been calculated. Figure 3.9 presents the trivalent oxide solution energies in UO_{2+x} for both mechanisms 3.11 and 3.12 when the species are considered clustered within the urania lattice. Irrespective of the mechanism of accommodation of non-stoichiometry, by O''_i or V''''_U, solution energies follow the same trend where increasing the M^{3+} cation size reduces the solution energy to a minimum around Gd^{3+} before increasing again very slightly. Furthermore, all solution energies are negative when removing oxygen interstitials. This means that as long as there is hyper-stoichiometry available in the form of oxygen interstitials, solution of M_2O_3 will proceed to completion. Solution beyond x in UO_{2+x} will be subject to the mechanisms of stoichiometric UO_2 (with the positive solution energies

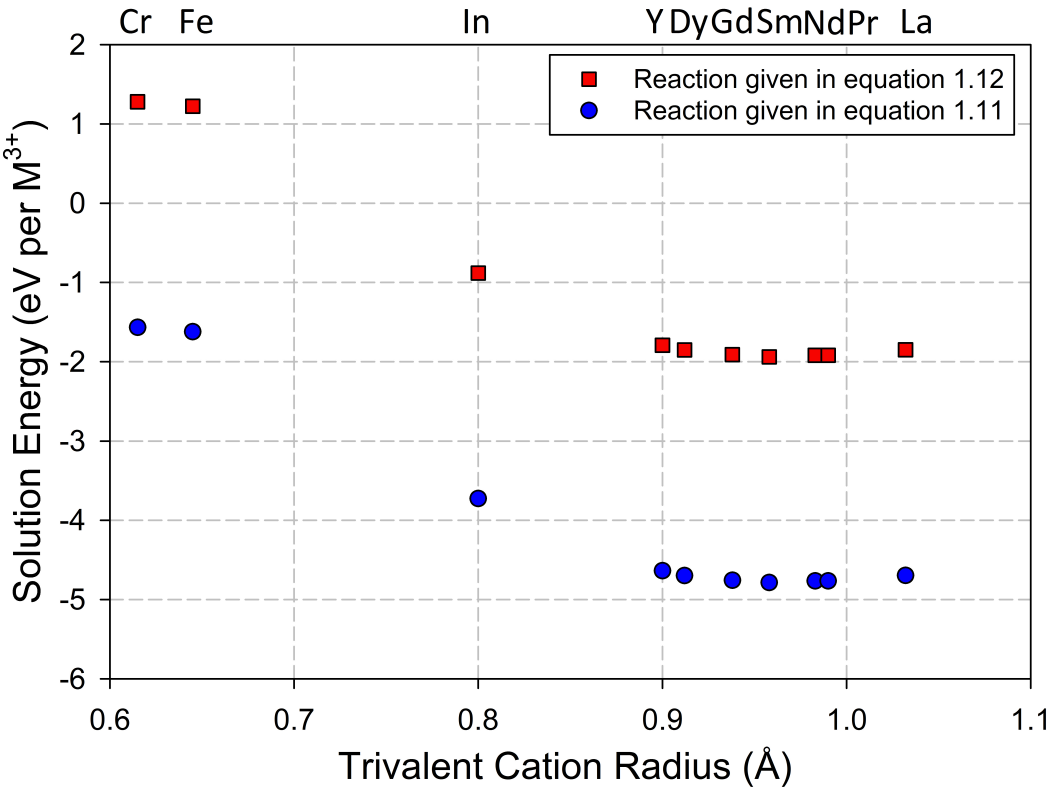


Figure 3.9: Showing the variation in solution energy of various trivalent metal oxides into UO_{2+x} as a function of cation radius. Both reactions involving hyperstoichiometry in the uranium dioxide lattice compensated by oxygen interstitials (equation 3.11) and uranium vacancies (equation 3.12) are considered.

reported in Figure 1). Thus, for small ions such as Cr^{3+}, the solution limit is controlled by the degree of non-stoichiometry (for all but minute values of x). For species such as Gd^{3+}, which is highly soluble in UO_2, the additional extent of solution in UO_{2+x} will be far less pronounced.

3.2.3 Validation of Chromium Charge State

Oxides of chromium exist with varying oxidation states commonly from "2+" to "4+". The "3+" charge state has been used through this study. To justify this DFT and simple empirical calculations using published ionization energies have been used and are presented in this section.

The $\{Cr'_U{:}U^{\bullet}_U\}^{\times}$ cluster was investigated using DFT. The simulation was achieved by placing a chromium ion in a 96 atom UO_2 cell and allowing the structure to relax electronically and geometrically. It was found that if the charge of one uranium ion was fixed at 5+ for 15 self consistency steps during the first electronic relaxation, the lowest energy ground state would be reached. In this situation the charge on the Cr ion was found to be "3+" with one uranium ion being oxidised to a 5+ charge. Crucially, the system reported a 0.9 eV lower energy than when the charge on the Cr was confined to be 4+. This result suggests that the non-charge transfer empirical model involving a Cr^{3+} ion is suitable for modelling the solution of Cr in the UO_2 system.

Another method to check that the charge on the Cr ions remains constant is to use the empirical potentials to calculate the energy for reaction 3.13. If the reaction is positive, the reaction is predicted to be un-favourable. The reaction is illustrated in Figure 3.10.

$$Cr'_U + U^{\bullet}_U \rightarrow \ Cr^{\times}_U + U^{\times}_U \tag{3.13}$$

The energy required for the reaction to proceed is 0.8 eV, suggesting that via the classical method Cr will exist in the "3+" charge state in UO_2 consistent with the DFT+U cal-

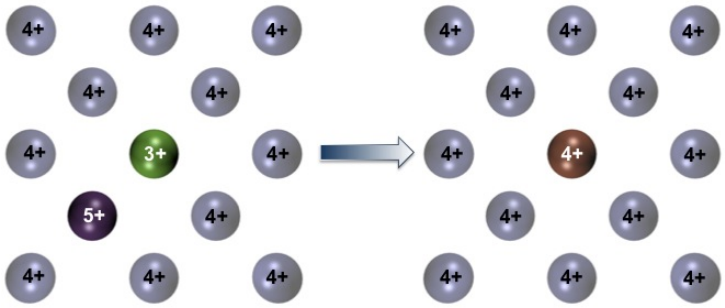


Figure 3.10: Illustration of reaction 3.13. On the left, a Cr^{3+} cation is charge balanced by a U^{5+} cation to maintain an overall "4+" charge in the lattice. On the right, the Cr takes on a "4+" charge and no longer needs to be charge balanced by another defect.

culations (Note: since the classical defect energies assume a fixed charge state, here the electronic contribution to the change in charge states must be accounted for by including the electronic ionization energies: $Cr^{3+} \rightarrow Cr^{4+}$; the 4^{th} ionization potential = 49.1 eV and $U^{4+} \rightarrow U^{5+}$, the 5^{th} ionization potential = 45.7 eV [164]).

3.3 Defect Relaxation Volumes in Uranium Dioxide

This chapter has thus far described the solution characteristics of trivalent oxides into UO_2 and has provided understanding of whether a particular trivalent oxide will form a solid solution as is the case with larger trivalent cations, such as Gd^{3+}, or be highly insoluble and more likely form a secondary phase, such as Cr^{3+}. These predictions are now advanced to understand the possible changes in the volume of the crystal due to the incorporation of defects including the studies trivalent cations. Defect volumes predict the change in volume of a unit cell as a function of defect concentration. By comparing results from previous (experimental) published work to the predictions presented here, one can validate solution mechanisms and also suggest what microstructural changes may be observed with varying concentrations of each extrinsic defect type. Defect relaxation volume calculations may also give some insight into the interaction of intrinsic and extrinsic defects and also to the dopant/fission-product cation interactions with fission gases.

The results have been divided into three main sections that report tetravalent, trivalent

and divalent extrinsic defects' effect on the UO_2 lattice. In each section a table giving the defect relaxation volume is presented and compared to experimental data. All these volumes can be used together to predict the magnitude of swelling/contraction of the UO_2 crystal lattice associated with the concentration of extrinsic defects with a simple relationship such as:

$$\text{Percentage Volume Change} = \frac{\sum(\mathrm{C_n} v)}{\mathrm{V_{UO_2}}} \times\ 100 \tag{3.14}$$

where '$\mathrm{V_{UO_2}}$' is the unit cell volume of UO_2 (in $\mathrm{\AA}^3$) and '$\mathrm{C_n}$' is the concentration of the extrinsic defect in atomistic percent and 'v' is the defect relaxation volume.

The change in average lattice parameter can be predicted using:

$$\text{Lattice Parameter} = \sum \left(\frac{v}{|v|} \times (\mathrm{C_i} \times |v|)^{\frac{1}{3}} \right) + \mathrm{a_{UO_2}} \tag{3.15}$$

where $\mathrm{a_{UO_2}}$ is the lattice parameter of pristine UO_2. Given the lattice parameter or volume changes due to extrinsic defects (fission products or dopants) and a knowledge of the proportion (inventory) of each element in solution (derived from the fuel history, largely burnup) an explicit connection with fuel swelling can be made.

3.3.1 Tetravalent Cations

Although this chapter has so far focused on trivalent cations entering the UO_2 lattice, here tetravalent oxides ("4+" cation containing binary oxides) are considered. Late in the fuel lifetime there are high concentrations (∼5 at.% [51]) of the tetravalent cations Zr^{4+}, Mo^{4+}, Ru^{4+} and Ce^{4+} whilst Am^{4+}, Np^{4+} and Pu^{4+} will also be present in small but not insignificant concentrations (∼0.6 at.% [51]). The swelling arising from the introduction of the minor actinides is also of interest for the development of mixed oxide fuels such as $(Am,U)O_2$ and $(Pu,U)O_2$ [165, 166]. These isovalent species simply substitute onto

uranium cation sites, in both UO_2 and UO_{2+x}, via the following reaction:

$$MO_2 + U_U^{\times} \rightarrow M_U^{\times} + UO_2 \tag{3.16}$$

The defect relaxation volumes of Ru, Mo, Zr, Ce, Am, Np and Pu are shown in Figure 3.11. As might be anticipated, as the dopant cation radius (Shannon [167]) is decreased, the contracting effect on the UO_2 lattice is increased. Ions such as Np and Pu exhibit a limited contracting effect on the lattice where as Ru and Mo, the smaller of the tetravalent cations studied, have a larger effect.

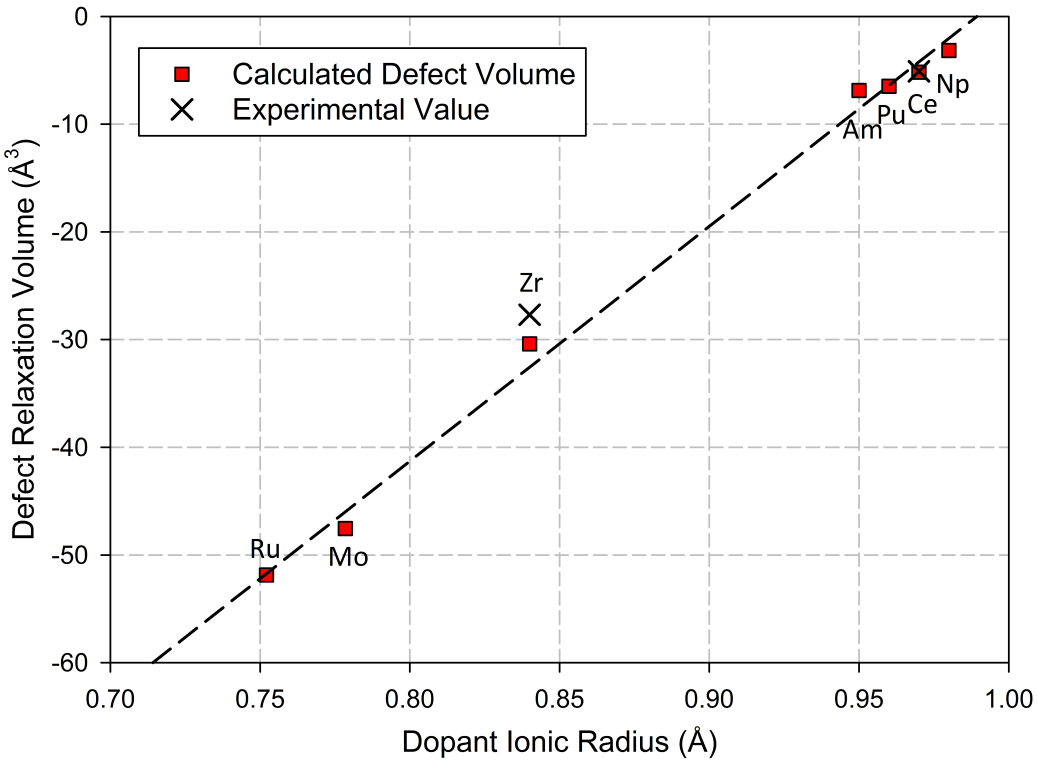


Figure 3.11: Variation in defect relaxation volume for tetravalent cations in UO_2 as a function of their ionic radius.

Experimental data for both Zr [168] and Ce [169] are included in Figure 3.11 and show that the experimental values are comparable with the predicted values. An overall trend

for the defect relaxation volume for tetravalent defects is given by (R^2=0.996):

$$v = 218.1\, r - 215.7 \tag{3.17}$$

where 'r' is the tetravalent cation radius (co-ordination number 8). This relationship can be used to predict the defect relaxation volumes for tetravalent ions not considered in this work. Thorium for example, which has a radius of 1.03 Å is predicted to have a defect relaxation volume of positive 9.5 $Å^3$.

Table 3.1: Defect relaxation volumes of tetravalent cations accommodated in UO_2

Impurity	Calculated Defect Volume, v ($Å^3$)	Experimental Defect Volume, v ($Å^3$)
Ru	-51.85	-
Mo	-47.55	-
Zr	-30.40	-27.7 [168]
Am	-6.88	-
Pu	-6.50	-
Np	-3.16	-
Ce	-5.18	-5.1 [169]

3.3.2 Trivalent Cations

Trivalent oxides are produced in high concentrations as fission products and as already discussed, trivalent oxides are added to UO_2 to improve the in-pile performance [38, 74].

The accommodation of aliovalent trivalent cations into uranium dioxide is not as simple as that of isovalent tetravalent cation incorporation. In particular, the substitution of a trivalent cation at a site usually occupied by a tetravalent species results in the formation of a T'_U defect (where the dash indicates a net charge of -1). Consequently it is necessary to charge compensate by either an oxygen vacancy, $V_O^{\bullet\bullet}$ (where the two dots indicate a double positive charge) or a U^{5+} species, $U_U^{\bullet}$ as already discussed. The opposite charges of T'_U and $V_O^{\bullet\bullet}$ or T'_U and $U_U^{\bullet}$ means there is an energy advantage for them to form neutral defect clusters. Below are the two charge neutral defect cluster reactions that were previously established as responsible for the accommodation of trivalent cations in UO_2 and UO_{2+x}:

- Oxygen vacancy cluster (in UO_2) - $\{V_O^{\bullet\bullet} : 2T_U{}'\}^\times$ via:

$$T_2O_3 + O_O^\times + 2U_U^\times \rightarrow \{V_O^{\bullet\bullet} : 2T_U'\}^\times + 2UO_2 \tag{3.18}$$

- Uranium 5+ mediated cluster (in UO_{2+x}) - $\{U_U^\bullet : T_U{}'\}^\times$ via:

$$T_2O_3 + O_i'' + 2U_U^\bullet + 2U_U^\times \rightarrow 2\{U_U^\bullet : T_U'\}^\times + 2UO_2 \tag{3.19}$$

It was established that for all but the very lowest defect concentrations the defect clusters are dominant over isolated charged defects in Section 3.2.1. Hence, it is appropriate to consider only clusters as only these concentrations of defects result in observable changes.

The simulation results of the two cluster reactions are compared with experimental data for Cr^{3+} [82], Y^{3+} [170], Dy^{3+} [171], Gd^{3+} [172], Eu^{3+} [170], Sm^{3+} [173], Nd^{3+} [170], Pr^{3+} [174] and La^{3+} [175] and are reported in Table 3.2.

Table 3.2: Defect volumes for trivalent cations accommodated in UO_2 (via oxygen vacancy compensation, equation 3.18) and UO_{2+x} (via U^{5+} ion compensation, equation 3.19). Neutral defect cluster formation is assumed in each case.

Impurity	UO_2 Defect Volume, v (Å^3)	UO_{2+x} Defect Volume, v (Å^3)	Experimental Volume, v (Å^3)
Cr	-26.11	-52.58	-27.7 [82]
Fe	-44.3	-53.33	-
In	-22.76	-35.34	-
Y	-1.10	-19.38	-23.9 [170], -2.6[170], -21.0 [170]
Dy	-0.09	-17.09	3.75 [171], -5.33 [176]
Gd	5.26	-13.21	-15.6 [170]
Eu	3.60	-13.44	-13.2 [170]
Sm	10.79	-7.12	0.00 [173]
Nd	13.02	-2.56	-6.23 [170]
Pr	16.40	-1.64	-1.78 [174], 18.08 [174]
La	21.71	3.33	9.2 [175]

In Section 3.2.1 it was predicted that the initial solution of trivalent cations occurs by taking up any oxygen excess (hyperstoichiometry) resulting in a negative solution energy

. Solution will proceed in this manner (producing the $\{U_U^{\bullet}:T_U'\}^{\times}$ clusters) until the excess of oxygen is exhausted. Beyond this, solution will proceed by forming $V_O^{\bullet\bullet}$ defects (i.e. via the stoichiometric mechanism).

Table 3.2 reports that the experimental results agree well with either the result for UO_2 or UO_{2+x}. Exceptions to this are Sm, La and Dy which have experimental defect volumes in-between the two predicted values, consistent with solution proceeding by consuming the excess oxygen and then proceeding by producing oxygen vacancies, forming an averaged defect relaxation volume (the defect relaxation volume for Nd does not match well to the experimental data).

Taking Pr^{3+} as an example, one can see that the experimental defect volumes [174] match closely for both UO_2 and UO_{2+x} calculated results. From the X-ray diffraction (XRD) experimental data of Yamashita *et al.* [174], it is evident that there are two regimes of behaviour; as solution increases the uranium dioxide lattice parameter initially decreases (when in a vacuum) or shows a slight increase (when in a He atmosphere). This behaviour is then followed by an increase once a certain quantity of Pr has been added (v=18.08). This is entirely consistent with the calculated defect relaxation volumes in Figure 3.12. In the first regime, the reaction shown in equation 3.19 dominates while in the second regime, the reaction given in equation 3.18 is seen to proceeds (as the excess oxygen in the lattice has been removed by the initial Pr^{3+} additions).

XRD data for Y^{3+} solution is similar to Pr^{3+}. Ohmichi *et al.* [170] clearly discuss this behaviour taking results from [177], showing two different lattice parameter variations with Y^{3+} content under different oxygen potential environments, one forming $(U_{1-x}, Y_x)O_{2-\frac{x}{2}}$, which is consistent with the formation of oxygen vacancies (UO_2) and the second forming $(U_{1-x},Y_x)O_2$, which is consistent with the formation of oxidized uranium ions (UO_{2+x}). Again, it is clear that there is a strong dependence of defect relaxation volume on the oxidation state of the material.

For Cr^{3+}, the experimental defect relaxation volume matches closely with the defect volume for hyper-stoichiometric uranium dioxide. The relative insolubility of Cr_2O_3 in UO_2 with

respect to other trivalent oxides has been discussed in Section 3.2.1 where it was predicted that it will only be soluble in significant amounts given oxygen excess, resulting in solution by forming Cr'_U and $U^{\bullet}_U$ defects. The concentration of Cr_2O_3 added by Leenaers [82] is small and therefore consistent with Cr^{3+} forming oxidised uranium defect clusters (equation 3.19) as proposed here.

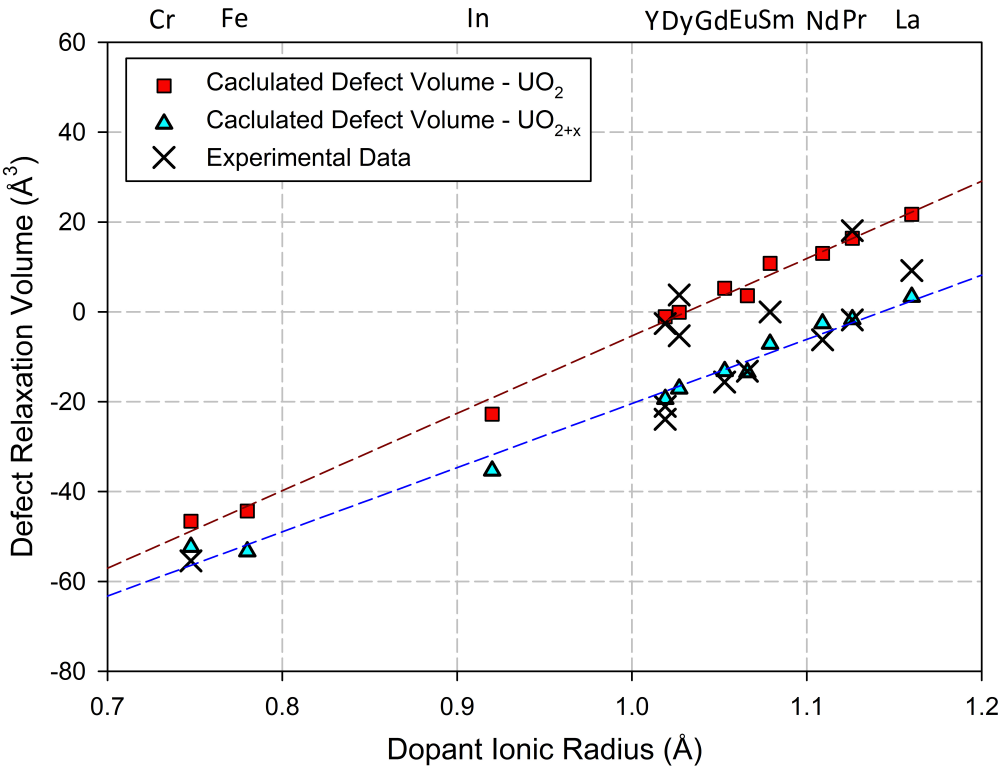


Figure 3.12: Defect volumes for trivalent cations accommodated in UO_2 (via oxygen vacancy compensation, equation 3.18) and UO_{2+x} (via U^{5+} ion compensation, equation 3.19). Neutral defect cluster formation is assumed in each case.

Interestingly the difference in defect relaxation volume between UO_2 (Equation 3.18) and UO_{2+x} (Equation 3.19), shown in Figure 3.12, increases as a function of dopant radius. This is because in UO_{2+x} the U^{5+} ion itself has a negative volume, which is better at compensating for the larger dopant cations.

3.3.3 Divalent Cation

Divalent cations are produced in a significant concentrations as fission proceeds in UO_2 nuclear fuel. Both Sr and Ba are examples of divalent fission products [131, 57, 51, 53]. Mg is important as MgO has been considered as the matrix for an inert matrix fuel and is therefore also considered in this study.

In a manner similar to trivalent cations, divalent cations require charge compensating defects to be accommodated within UO_2 or UO_{2+x}. Two different reactions have been identified as possible, analogous to those suggested in section 3.3.2 for trivalent cations. The clusters considered are:

- Oxygen vacancy cluster - $\{V_O^{\bullet\bullet} : D_U{''}\}^{\times}$ (in UO_2):

$$DO + U_U^{\times} + O_O^{\times} \rightarrow \{D_U'' : V_O^{\bullet\bullet}\}^{\times} + UO_2 \tag{3.20}$$

- Uranium 5+ mediated cluster $\{2U_U^{\bullet} : D_U{''}\}^{\times}$ (in UO_{2+x}):

$$DO + 2U_U^{\bullet} + O_i'' + U_U^{\times} \rightarrow \{D_U'' : 2U_U^{\bullet}\}^{\times} + UO_2 \tag{3.21}$$

D_U'' being a divalent cation on a uranium site. Defect volumes for divalent cations are reported in Figure 3.13 and Table 3.3. Experimental data, with which to compare, is available for only Sr^{2+}. As with trivalent cation accommodation, the experimental defect volume for Sr^{2+} corresponds strongly with one of the predicted defect volumes, in this case with UO_{2+x}. This would be consistent with solution of Sr^{2+} proceeding by taking up any excess stoichiometry available, forming the $\{2U_U^{\bullet}:D_U{''}\}^{\times}$ cluster. Further additions of Sr^{2+} may exhaust the excess oxygen, then forming the $\{V_O^{\bullet\bullet}:D_U{''}\}^{\times}$ defect cluster thereafter.

Table 3.3: Defect relaxation volumes of divalent cations accommodated in UO_2 andUO_{2+x}.

Impurity	UO_2 Defect Volume, v (Å^3)	UO_{2+x} Defect Volume, v (Å^3)	Experimental Volume, v (Å^3)
Mg	-18.74	-25.69	-
Zn	-10.46	-21.55	-
Cd	5.71	-13.41	-
Sr	27.62	-3.15	-3.2 [178]
Ba	50.00	7.75	-

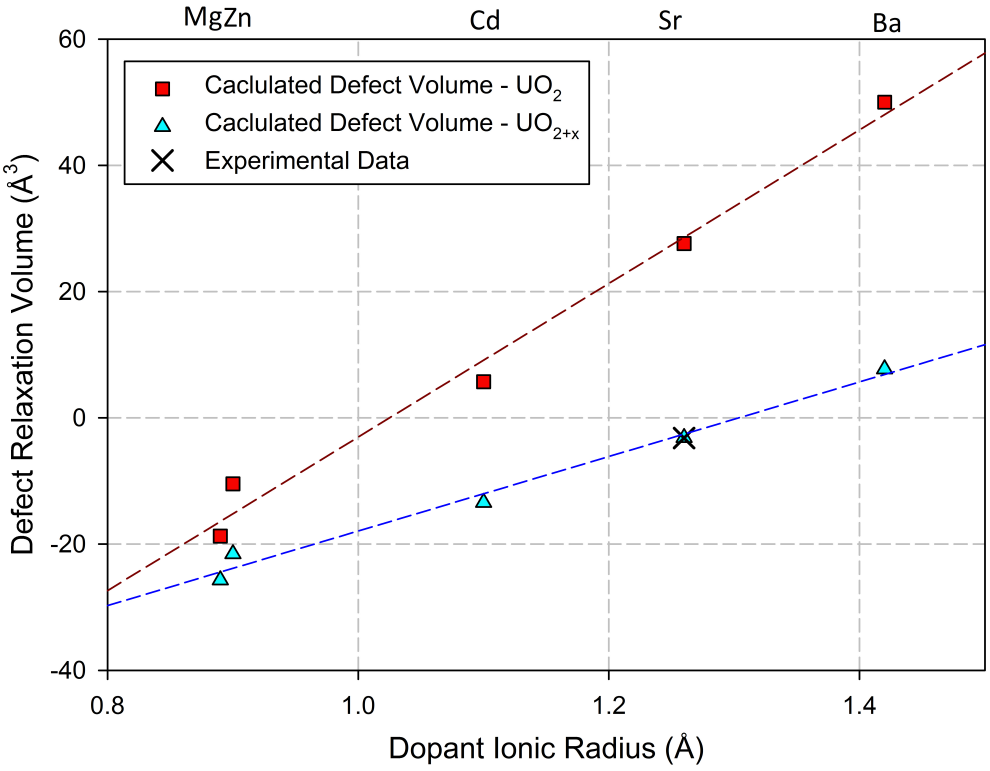


Figure 3.13: Defect volumes for divalent cations accommodated in UO_2 (via oxygen vacancy compensation, equation 3.20) and UO_{2+x} (via U^{5+} ion compensation, equation 3.21). Neutral defect cluster formation is assumed in each case.

3.3.4 Lattice Parameter Variation with Burnup

The change in lattice volume due to the accommodation of soluble dopants, resulting from a given burnup can now be predicted and compared to experimental data. This is subject to a number of assumptions - not least of which is that the inventory of dopants are all accommodated in the lattice rather than in a secondary phase precipitate (see Kleykamp [57] for a discussion of grey phase precipitate experimental studies and Grimes and Catlow [51] for modelling predictions). Each dopant does have a solution limit but these are not usually well established. Nevertheless, by predicting the inventory of a typical PWR UO_2 fuel as a function of burnup one can establish the limiting concentration and use equation 3.14 to calculate the predicted volume. Data from FISPIN 7A has been used [58], including specifically the significant fission products: Sr, Ba, Y, La, Pr, Nd, Sm, Eu, Gd, Dy, Zr and Ce. The results are plotted in Figure 3.14 and compared to experimental data from Une *et al.* [59] and Davies and Ewart [60] (both are obtained from XRD data after annealing of irradiated fuel), which suggest only a small change in volume as burnup progresses. This suggests that the data of Une *et al.* is consistent with solution in stoichiometric UO_2. Conversely, the present data suggests as a distinct decrease in cell volume when the lattice is oxidised to UO_{2+x}. Thus, the data from Davies and Ewart appears to agree better with the accommodation of fission products by taking up some excess oxygen (equations 3.19 and 3.21).

The clear difference in value change between stoichiometric and hyper-stoichiometric materials has implications because the rim of a pellet in a typical PWR fuel pellet is nearer stoichiometry (due to the zirconium cladding gettering oxygen and oxygen migrating up the thermal gradient [179]) than the centre of the pellet. Thus, measurable changes in lattice parameter are not expected to be observed in the rim: the stoichiometric composition means that a UO_2 grain accommodating a significant inventory of fission products will appear to have the same lattice parameter as a dopant free UO_2 grain.

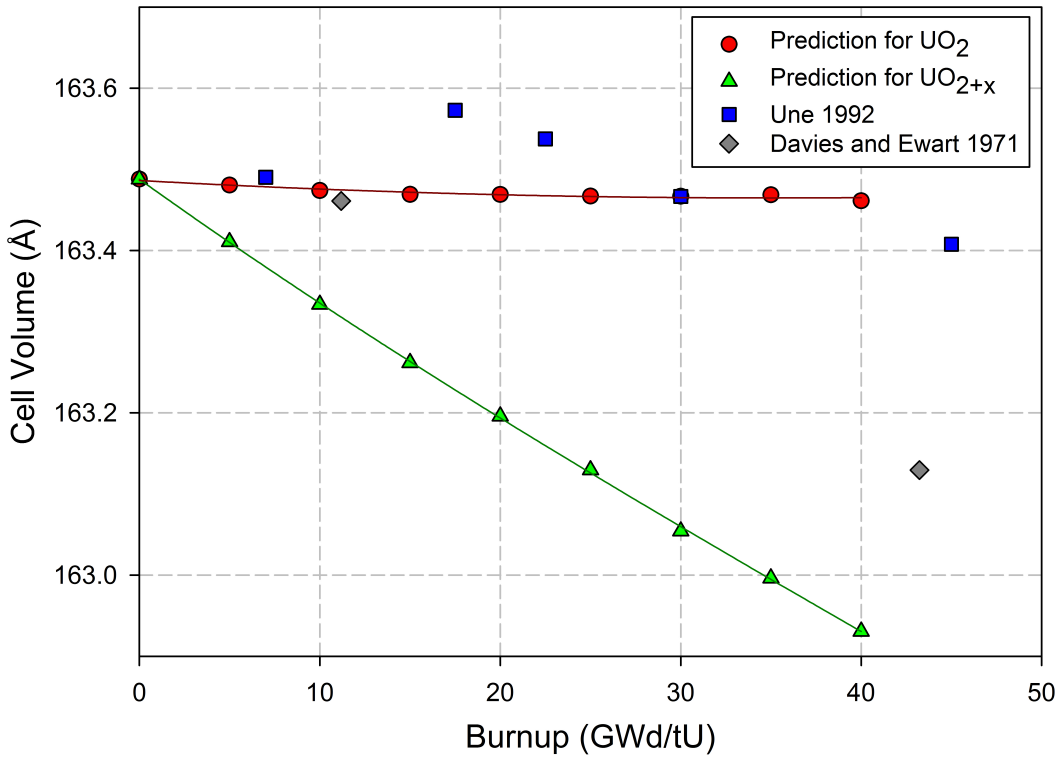


Figure 3.14: Variation of UO_2 unit cell volume with burnup due to fission products using concentrations from [58], compared to data from Une *et al.* [59] and Davies and Ewart [60].

3.4 Summary

Simulations have been carried out to establish the mechanism of solution for a range of trivalent oxides in UO_2 and UO_{2+x}. A strong dependence on cation radius was predicted in both cases. For UO_2, a bound oxygen vacancy cluster $\{2M'_U{:}V^{\bullet\bullet}_O\}^\times$ provided the preferred solution mechanism for all but the smallest trivalent cations (e.g. Cr^{3+}), where isolated defects are preferred. In UO_{2+x}, all trivalent cations form stable clusters with U^{5+} ions (i.e. $\{M'_U{:}U^{\bullet}_U\}^\times$), that are present as charge compensating species for the hyper-stoichiometry.

In UO_2, Gd_2O_3 and other large trivalent cation oxides were found to be much more soluble than small cations, which is in agreement with currently available data [162]. The solution energies all become negative when hyper-stoichiometric UO_{2+x} is considered, which corresponds to a dramatic change in solubility of Cr^{3+} and other small cations but not for Gd^{3+} and other larger cations. This is a consequence of a change in solution mechanism whereby the trivalent substitutional species can consume defects made available through hyper-stoichiometry. The solution mechanism predicted here for Cr_2O_3 accommodation contradicts that previously assumed [82].

The solubility limit of the smaller cation containing sesquioxides such as Cr_2O_3 is controlled by the oxidation state of the uranium dioxide, that is, the amount of Cr^{3+} that can enter solution is highly dependent on the degree of hyper-stoichiometry. Conversely, larger cations such as Gd^{3+}, being already highly soluble in UO_2, are not much more stable in UO_{2+x} and as such their solubility is not greatly changed by the degree of hyper-stoichiometry.

DFT calculations have shown that chromium will maintain its "3+" charge within UO_2, charge compensated by an adjacent uranium ion in a 5+ charge state.

Subsequently, calculations were carried out to provide a catalogue of defect volumes associated with the accommodation of divalent, trivalent and tetravalent cations in uranium dioxide. The individual effect of each dopant is predicted and used alongside a fission product inventory code, to predict the overall change in volume of of the lattice. Following

previous work in this chapter, solution mechanisms in stoichiometric UO_2 require oxygen vacancy charge compensation defects to be formed for aliovalent dopants. Conversely, in hyperstoichiometric UO_{2+x}, these charged dopants take advantage of the excess oxygen and are charge compensated by U^{5+} ions. Again, following previous work, the charged dopants and their charge compensating defects form neutral defect clusters, upon which the volume calculations are based. Where experimental data is available, the predictions are in good agreement.

While this is a suitable method of predicting the change in lattice parameter of uranium dioxide, care must be taken when considering high concentrations of fission products as each cation will have a concentration limit. Comparison to experimental data for the overall lattice volume change (swelling) is therefore limited here to modest burnups. Once the solution limits of each dopant are established as a function of stoichiometry, it will be possible to extend the current model to higher burnups, assuming equilibrium is maintained. However, this may not necessarily be the case. For example, Cr^{3+} is only soluble in UO_{2+x}. As the lattice moves towards a stoichiometric composition, it must be accommodated by oxygen vacancy compensation. This is possible because oxygen vacancies are fast diffusion species in the fluorite lattice. Conversely, Cr^{3+} ions will be much slower moving species. The result, at least initially upon stoichiometry changes will be an expansion of the lattice volume (see Figure 3.12), until Cr^{3+} ions are expelled from the lattice and equilibrium is re-established. As a consequence, fuel performance codes may eventually take into account such changes in fuel volume over their whole life-times.

Results also suggest that the lattice parameter in stoichiometric fuel, as seen near the fuel rim, will not vary to any great extent from the nominal UO_2 lattice parameter. This questions earlier studies that have described the high burn up structure crystals as 'clean' whereas dopants could be present but accommodated via a different compensation mechanism to the more oxidised inner pellet material, resulting in a near zero volume expansion.

Results have suggested that as Cr^{3+} is released from solution either by displacement of fission products or changes in stoichiometry, an increase in lattice parameter will be evident.

As a consequence, fuel performance codes may wish to take into account a slight increase in fuel volume over the life-time of Cr_2O_3 doped fuels.

In summary, the work presented has given some useful trends and indications into how cations will effect the volume of the UO_2 lattice. Further work on this subject should include the effect of further clustering of the cations to ascertain whether this will have an impact on the crystal swelling presented in this work. The solution limits of the extrinsic cations should also be further examined with relation to the formation of 'grey phases' and more complex precipitates than the simple sesquioxides considered in this work.

Chapter 4

Effect of Trivalent Cations on the Transport Processes In Uranium Dioxide

"Anyone who has never made a mistake has never tried anything new."
- Albert Einstein [180].

4.1 Introduction

The previous chapter was primarily focused on gaining an understanding of where and how trivalent cations are accommodated in the uranium dioxide crystal lattice. This work is now extended to predict how key defect transport processes are modified in the presence of trivalent cations in the urania lattice.

The mechanism for fission gas release has been the focus of numerous studies with the primary goal of improving fuel code predictions [181, 182, 73, 183]. Being able to reliably predict rates of fission gas release will allow fuel to be used more efficiently and safely. One way to achieve this is via an improved mechanistic understanding of the processes involved,

eventually allowing unexpected behaviour and environments to be as well predicted as the standard situations.

It has been shown that once in solution, fission gases are likely to migrate via a uranium vacancy mechanism [184]. This will be limited by uranium vacancy migration [161] and there are a number of studies suggesting an activation energy for this type of release [161].

In this chapter, the effect of trivalent cations in solution on vacancy migration in UO_{2+x} is studied, to gain an understanding of the impacts of dopants and fission products on the diffusion kinetics (and therefore release) of xenon. The dopant oxide Cr_2O_3 in UO_{2+x} is considered in detail, discussing the change in thermally activated diffusion and how it relates to the expected fission gas retention due to the larger grain size.

4.2 Migration Processes

Two possible mechanisms are considered for the migration of trivalent species in UO_2: *i*) a sequential diffusion process where a vacancy is bound to a trivalent cation and moves through the UO_2 lattice via sequential re-arrangement of a $\{V_U'''':M_U'\}^{\times}$ cluster (bound by oxidised uranium defects, $U_U^{\bullet}$) illustrated in Figure 4.1, or *ii*) a capture release mechanism

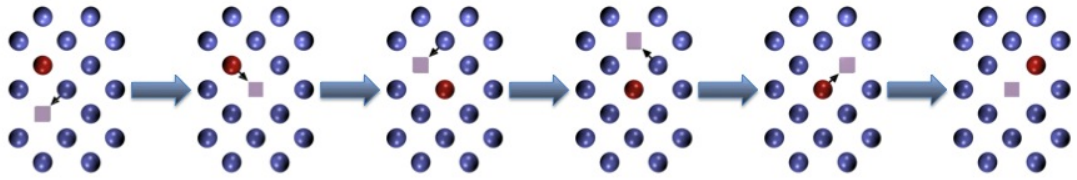


Figure 4.1: Diffusion of a species (red sphere) by a sequential movement of a vacancy (box) in a (100) FCC plane of UO_2.

where the uranium vacancy is captured by the trivalent cation, the trivalent cation migrates into the vacancy and the new vacancy is released into the bulk (illustrated in Figure 4.2).

The effect of trivalent doping on vacancy diffusion in UO_2 will be linked with mechanisms *i*) and *ii*). Any enhancement of migration compared to undoped UO_2 will lead to an

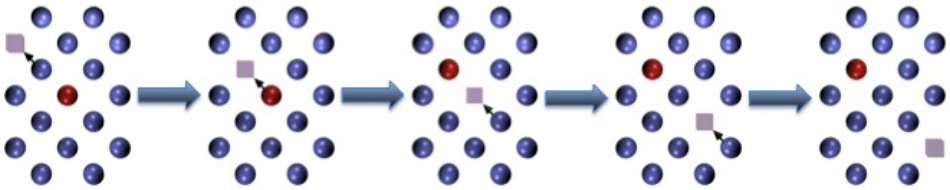


Figure 4.2: Diffusion of a species (red sphere) by the capture then release of a vacancy (box) in a (100) FCC plane of UO_2.

increase in vacancy diffusivity. If *i*) dominates, the vacancy diffusivity will be the same as the largest migration barrier step in the sequential migration but if *ii*) dominates, vacancy diffusion will be more complicated as the thermodynamic drive for a vacancy to move towards the trivalent cation will need to be considered as well as the migration barriers.

4.3 Uranium Vacancy Cluster Morphology and Migration

In the previous chapter it was discussed that chromium and iron cations will only enter UO_2 in significant concentrations with an associated hyperstoichiometry. In this regard, hyperstoichiometric UO_{2+x} is considered. This section investigates vacancies and trivalent cations accommodated in the lattice by forming U^{5+} charge compensating defects, i.e. $\{V''''_U{:}4U^{\bullet}_U\}^{\times}$ for vacancies and $\{V''''_U{:}T'_U{:}5U^{\bullet}_U\}^{\times}$ for vacancies bound to substitutional trivalent cations (T). Initially, we consider the migration of vacancies in hyperstoichiometric fuel, UO_{2+x}.

To understand the morphology of these clusters a series of Mott-Littleton calculations have been carried out to identify the arrangement that gives the lowest defect energy. For both the $\{V''''_U{:}4U^{\bullet}_U\}^{\times}$ and the $\{V''''_U{:}T'_U{:}5U^{\bullet}_U\}^{\times}$ cluster, the vacancy was placed in the centre of a 2×2×2 supercell and the other defects arranged around it (the 2×2×2 supercell is part of a larger 4×4×4 supercell). After the lowest energy cluster morphology is determined for each cluster, the cluster morphology that gives the lowest migration energy for U^{4+}, U^{5+} and Cr^{3+} is determined by carrying out a series of RFO calculations (see Methodology, Chapter 2).

First considering the uranium vacancy, the number of U^{5+} defects was increased from 0 to 4 so it is possible to understand how they associate themselves with the vacancy. 31 calculations were carried out for the single U^{5+} cation (2×2×2×4=32, corresponding to the number of uranium sites in a 2×2×2 supercell minus the uranium vacancy site). 930 calculations are required to find the lowest energy cluster for 2 U^{5+} and one uranium vacancy (31×30); 26,970 calculations were carried out to find the lowest energy cluster for a vacancy with 3 U^{5+} cations (31×30×29). Four U^{5+} cations would need 755,160 calculations, excessive for the purpose of this study and a number of assumptions have therefore been made to study this system in a more computationally convenient manner, discussed subsequently in this chapter. Information from calculations with 1, 2 and 3 U^{5+} cations have been used to inform on the behaviour of vacancies surrounded by 4 U^{5+} cations.

For each migration mechanism the migration energy barrier for the lowest energy cluster has been calculated. In addition, the metastable arrangements for each cluster is investigated to determine if a lower total energy migration is possible (added cluster energy plus migration energy barrier) and therefore more favourable. First, it is necessary to consider the barrier associated with a U^{4+} ion moving into an isolated vacancy in the absence of U^{5+} cations.

4.3.1 0 × U^{5+} Cations

RFO calculations were used to calculated the migration energy barrier for a U^{4+} cation in the absence of any charge balancing U^{5+} cations. The migration barrier for the U^{4+} cation in the <110> direction was found to be 6.99 eV. It should be now noted that the migration of a U^{4+} ion in the <100> direction was found to proceed with an energy of 12.01 eV, much higher than the barrier to migration in the <110> direction. The following, more complex calculations will only consider migrations in the <110> direction.

4.3.2 1 × U^{5+} Cation

When one U^{5+} cation is considered it will bond with a vacancy in to a nearest neighbour position. Figure 4.3 illustrates the lowest energy cluster along with the migration of a U^{4+} cation. Post migration the cluster is symmetrically identical. The barrier for the migration

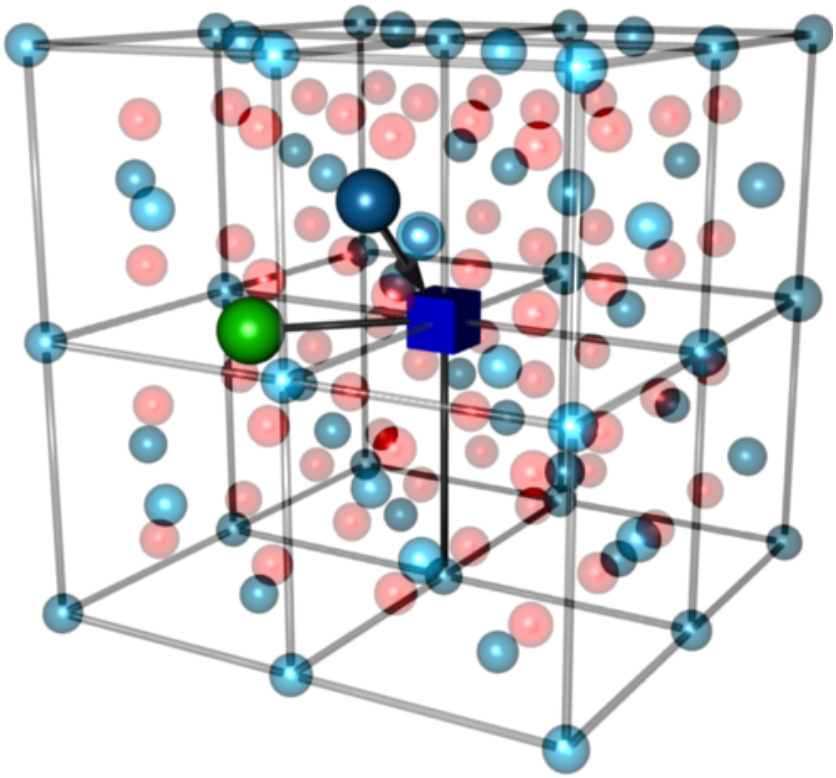


Figure 4.3: The lowest energy cluster containing one uranium vacancy and one U^{5+} ion (note: this is not a charge neutral cluster). The uranium vacancy is represented by a blue cube and the U^{5+} ion as a green sphere. The migrating U^{4+} cation is represented by a solid blue sphere.

of the U^{4+} cation in the arrangement illustrated in Figure 4.3 is 6.77 eV. However, Figure 4.4 reports a cluster that is 0.65 eV less stable than this can be formed, which provides an energy barrier 0.12 eV lower than that associated with the most stable cluster arrangement. The arrangement that gives the smallest migration barrier for a U^{4+} cation into a vacancy, charge compensated by just one U^{5+} cation is illustrated in Figure 4.5. The U^{4+} cation is migrating away from the the U^{5+} cation in the <110> direction leaving the vacancy and the U^{5+} cation in a nearest neighbour position to each other. It is clear that more energy is needed to create the lowest migration energy cluster, is larger than the reduction

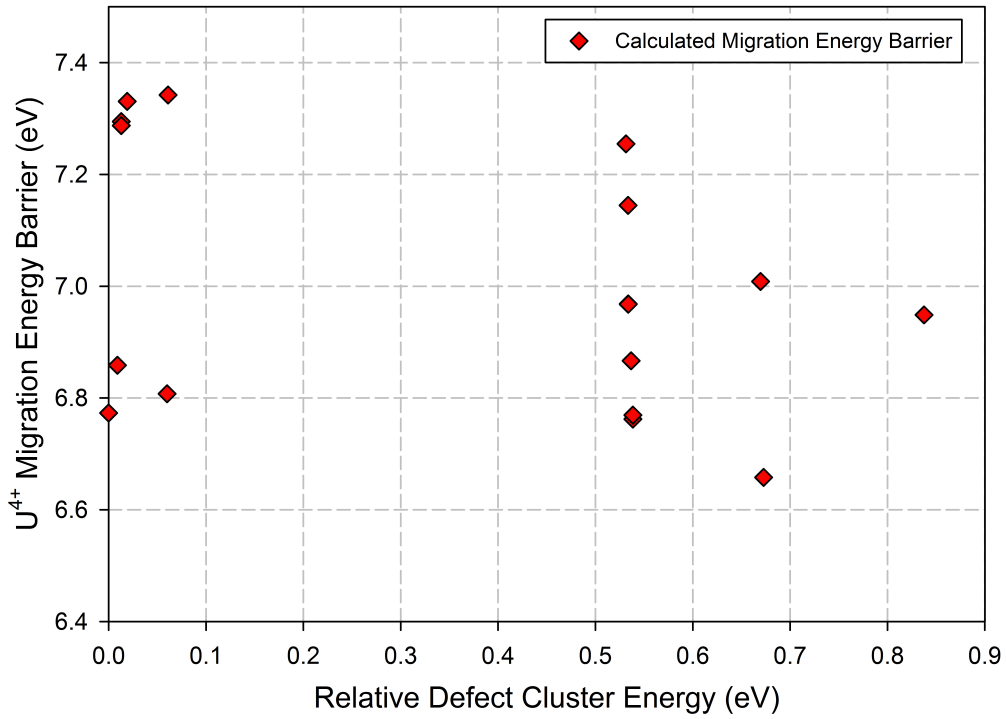


Figure 4.4: The energy barrier (eV) to migration for a U^{4+} cation migrating into a uranium vacancy in the <110> direction for all calculated cluster morphologies plotted against the cluster stability relative to the most stable arrangement of $\{V_U''''{:}U_U^{\bullet}\}''''$ cluster.

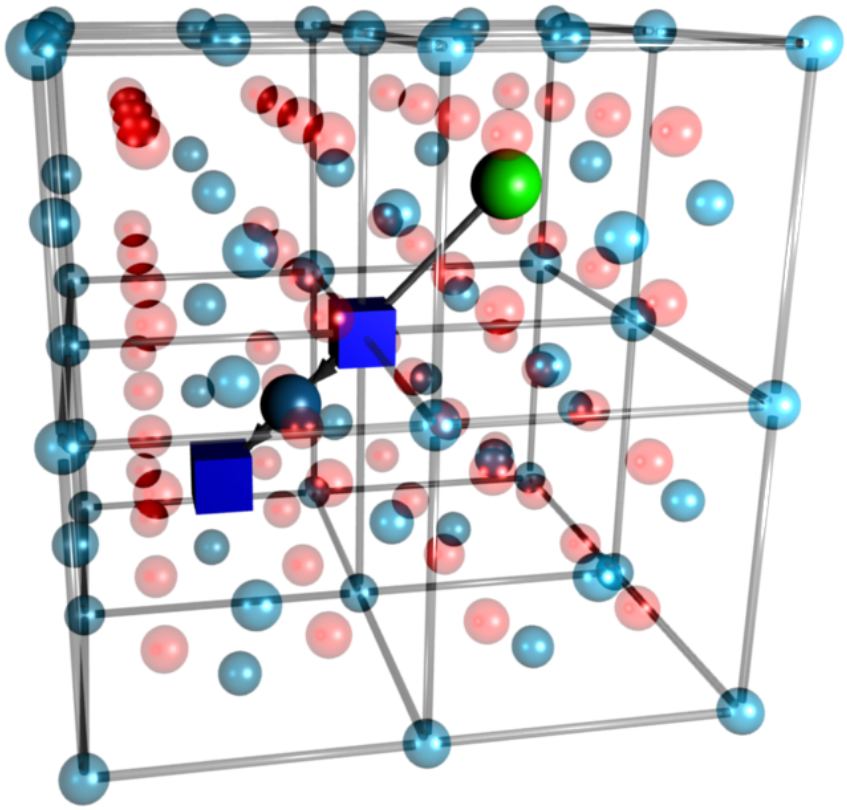


Figure 4.5: The cluster morphology that produces the smallest barrier to migration that contains two uranium vacancies, one migrating U^{4+} cation and 1 U^{5+} ion. The uranium vacancy is represented by a blue cube and the U^{5+} ion as a green sphere. The migrating U^{4+} cation is represented by a solid blue sphere half way between uranium lattice sites.

in the energy barrier meaning the transition will be less favourable. Figure 4.4 reports no migration processes where sum of the formation energy of a metastable cluster (i.e. compare to the most stable arrangement) and the migration barrier is smaller than the migration barrier for the ground state arrangement.

Migration of the U^{5+} species in the <110> direction proceeds with a energy barrier to migration of 9.5 eV, significantly higher th an for U^{4+} cations. U^{4+} ions are therefore expected to migrate into vacancies far more readily than U^{5+} cations.

At this point it is pertinent to review the properties of the U^{5+} species. It has often been described as a small polaron [26] that is, an electronic hole localised on a single uranium ion. Furthermore, the hole can hop between uranium ions with an activation energy between equivalent sites that has been estimated to be 0.1 eV [26]. This is substantially smaller than the difference between the activation energies for migration of a U^{4+} and U^{5+} ions. Consequently, for an U^{4+} ion to migrate into a vacancy, the U^{5+} cations are likely to re-arrange themselves, possibly during the U^{4+} migration, to lower the energy barrier to migration. This will be further tested below when considering two U^{5+} ions in the system. For a U^{5+} ion to migrate, it is likely that the ion will accept an electron from another ion, become a U^{4+} cation and allow it to migrate with a lower energy. After the migration, the cation may or may not release the electron to become a U^{5+} cation again, depending on the local $\{V_U''''{:}U_U^{\bullet}\}'''$ cluster geometry.

This section has considered a cluster with a total charge of 3-, as the negatively charged vacancy is only partly charge balanced by one U^{5+} cation. Next, we consider the vacancy with 2 U^{5+} cations.

4.3.3 2 × U^{5+} Cations

When two U^{5+} ions are considered, the energetically most favourable configuration is that in which they both sit in nearest neighbour positions to the vacancy but since they repel each-other due to Coulombic interactions, they therefore form the cluster shown in

Figure 4.6 where they sit in a 2nd nearest neighbour position to each-other (in the <100> direction). The lowest energy of U^{4+} ion migration in a <110> direction associated with

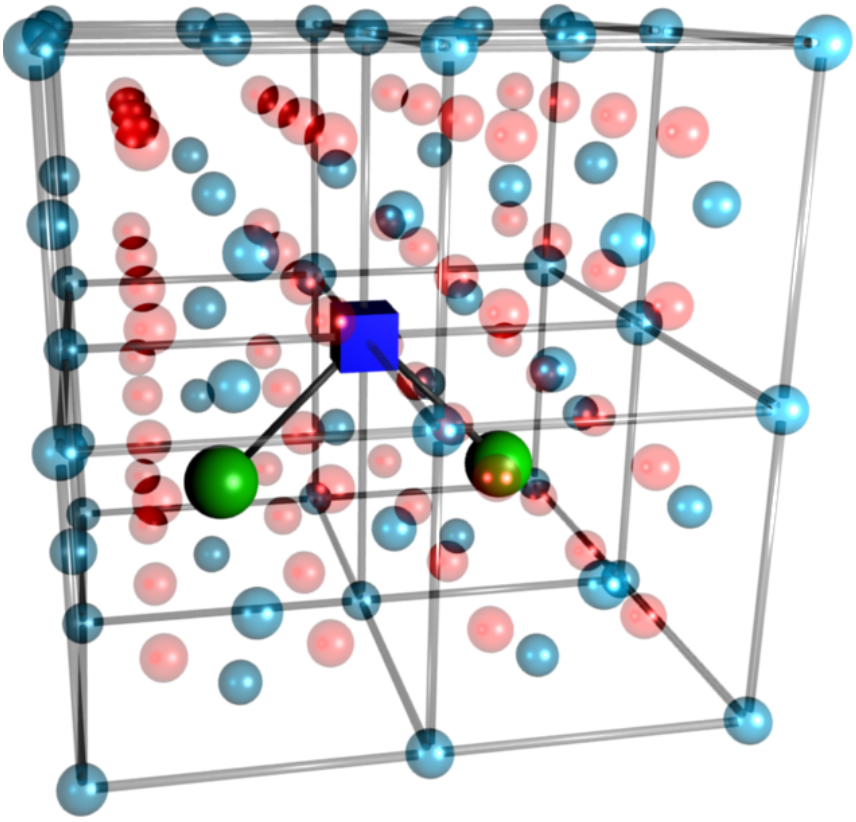


Figure 4.6: The lowest energy cluster containing one uranium vacancy and 2 U^{5+} ions (note: this is not a charge neutral cluster). The uranium vacancy is represented by a blue cube and the U^{5+} ions as green spheres.

this cluster is 6.53 eV. The migration is illustrated in Figure 4.7.

Figure 4.8 reports all of the migration energy barriers for a U^{4+} cation as a function of cluster stability relative to the lowest energy cluster illustrated in Figure 4.6. The arrangement of U^{5+} cations that gives the lowest energy migration for a U^{4+} cation is illustrated in Figure 4.9 (it is 0.73 eV less stable that the lowest energy arrangement of U^{5+} cations). The energy barrier for U^{4+} migration associated with this cluster is 6.42 eV, which is 0.23 eV lower than when only one U^{5+} cation was considered. For this migration to proceed the system must gain 0.73 eV in energy but the migration barrier only falls by 0.11 eV and is therefore unfavourable with respect to the lowest energy arrangement of the $\{V''''_U{:}2U^{\bullet}_U\}''$ cluster.

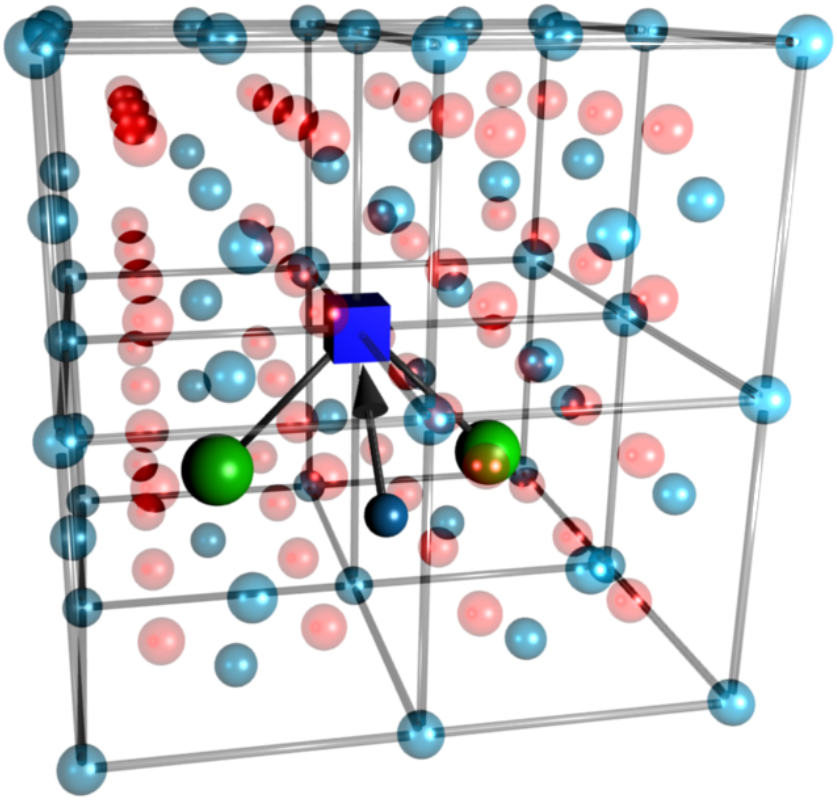


Figure 4.7: This is the cluster that will facilitate the migration of a U^{4+} ion to migrate into a vacancy with the lowest total energy. The uranium vacancies are represented by a blue cube and the U^{5+} ions as green spheres.

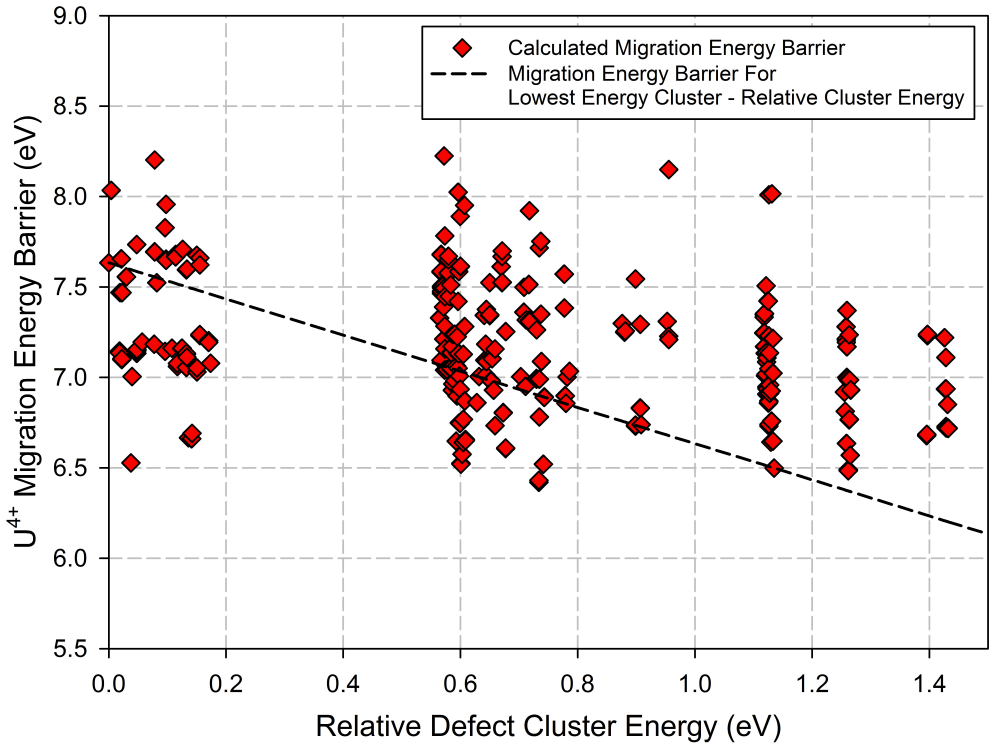


Figure 4.8: The energy barrier to migration for a U^{4+} cation migrating into a uranium vacancy in the <110> direction for all calculated cluster morphologies plotted against the morphology stability relative to the most stable arrangement of $\{V_U''''{:}2U_U^{\bullet}\}''$ cluster. The line represents the migration energy for the lowest cluster morphology arrangement minus the relative cluster energy to calculate whether a migration is more or less favourable than that for the most stable cluster.

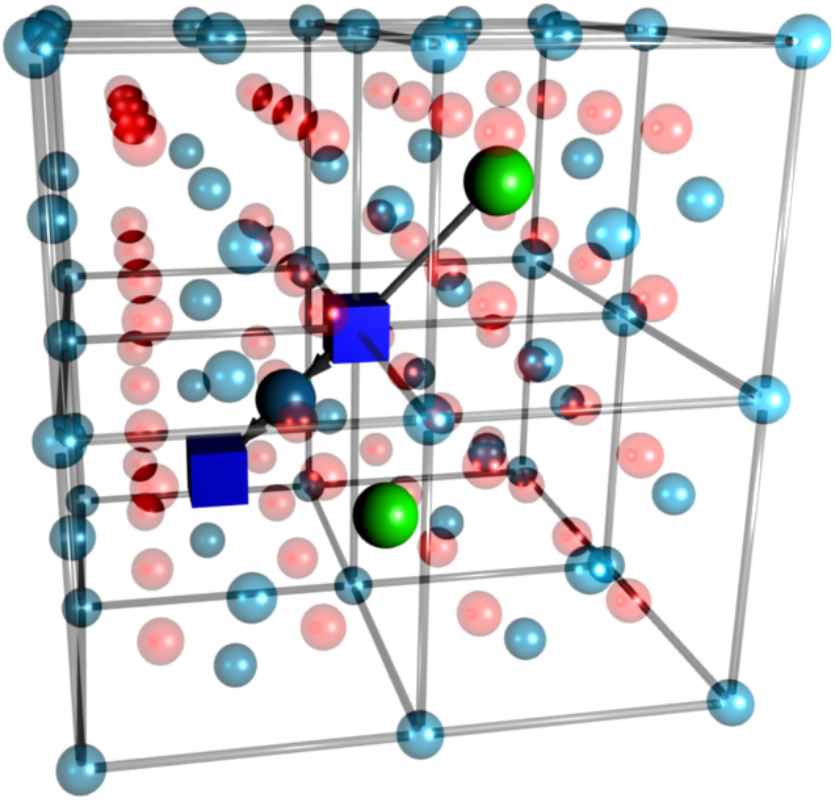


Figure 4.9: The cluster that will allow the migration of a U^{4+} ion to migrate into a vacancy with the lowest energy with two U^{5+} ions in the cluster. The uranium vacancies are represented by a blue cube and the U^{5+} ions as green spheres. The migrating U^{4+} ions is represented by a solid dark blue sphere.

The energy barrier for one of the U^{5+} cations to migrate from the lowest energy morphology is found to be 9.29 eV. However, the lowest total energy migration required involves a metastable cluster. The lowest migration arrangement of cations is illustrated in Figure 4.10 and is 0.90 eV less stable than the cluster shown in Figure 4.6. Similar to the U^{4+}

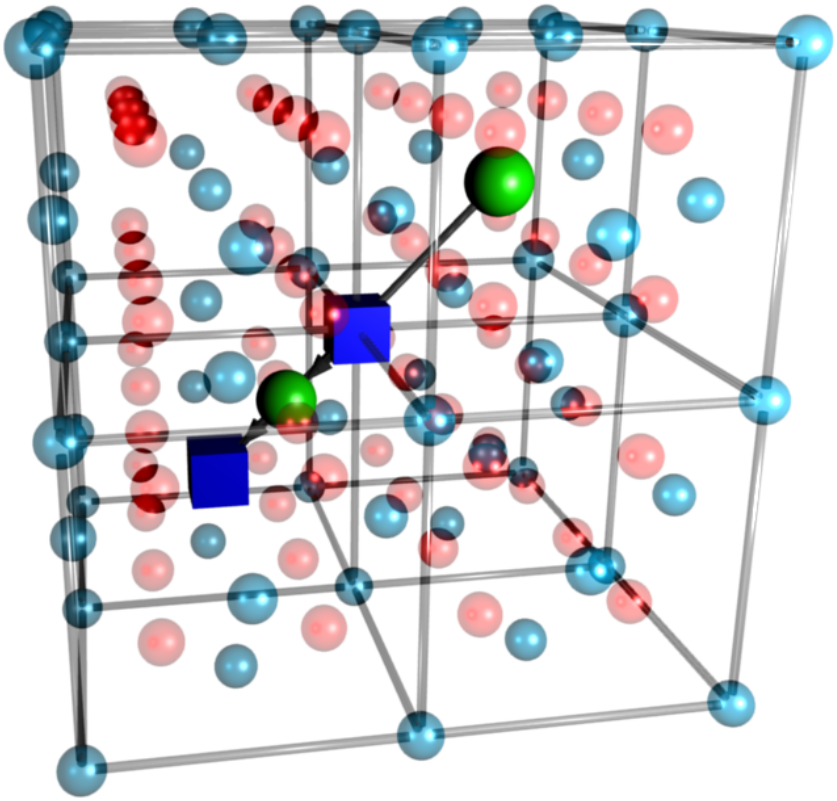


Figure 4.10: The cluster that will facilitate the migration of a U^{5+} ion into a vacancy with the lowest energy. The uranium vacancies are represented by a blue cube and the U^{5+} ions as green spheres.

migration, the lowest energy migration will not occur often due to the energy penalty in forming the cluster. Instead, a more stable cluster that will still enable migration to proceed readily will be more likely. All of the migration energies are given as a function of the relative cluster stability in Figure 4.11. One such migration process is illustrated in Figure 4.12 and has an energy barrier of 8.67 eV but is only 0.05 eV less stable than the stable cluster. The barrier to migration is still significantly higher than U^{4+} migration and therefore a cation that is initially a U^{5+} cation will gain an electron to become U^{4+} and migrate as discussed earlier in this chapter.

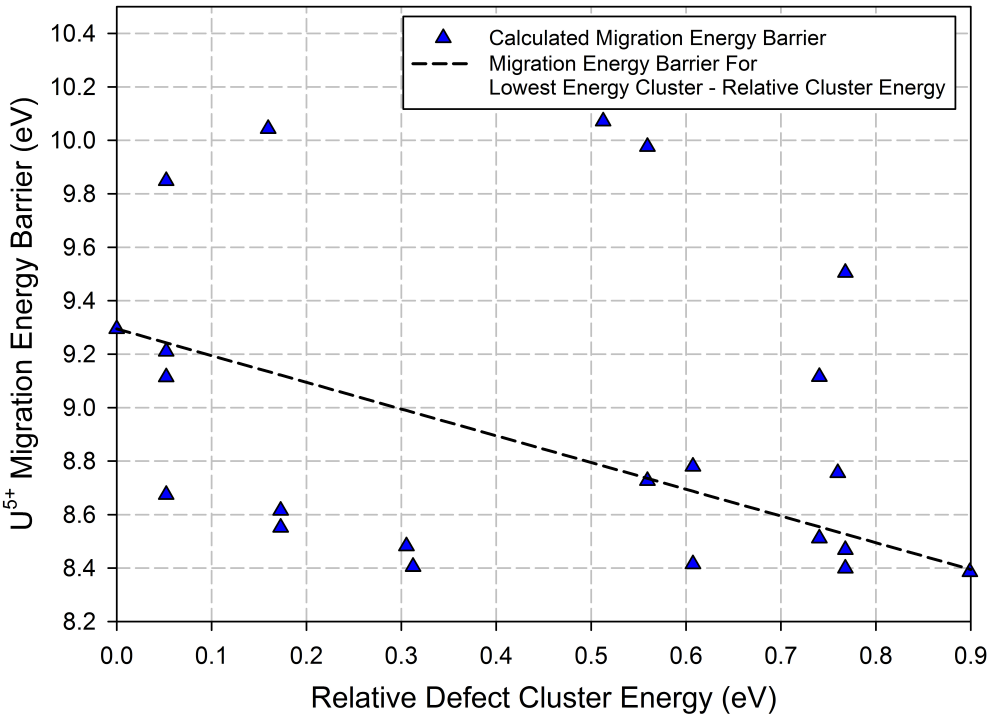


Figure 4.11: The energy barrier to migration for a U^{5+} cation migrating into a uranium vacancy in the <110> direction for all calculated cluster morphologies plotted against the morphology stability relative to the most stable arrangement of $\{V_U''''{:}2U_U^{\bullet}\}''$ cluster. The line represents the migration energy for the lowest cluster morphology arrangement minus the relative cluster energy to calculate whether a migration is more or less favourable than that for the most stable cluster.

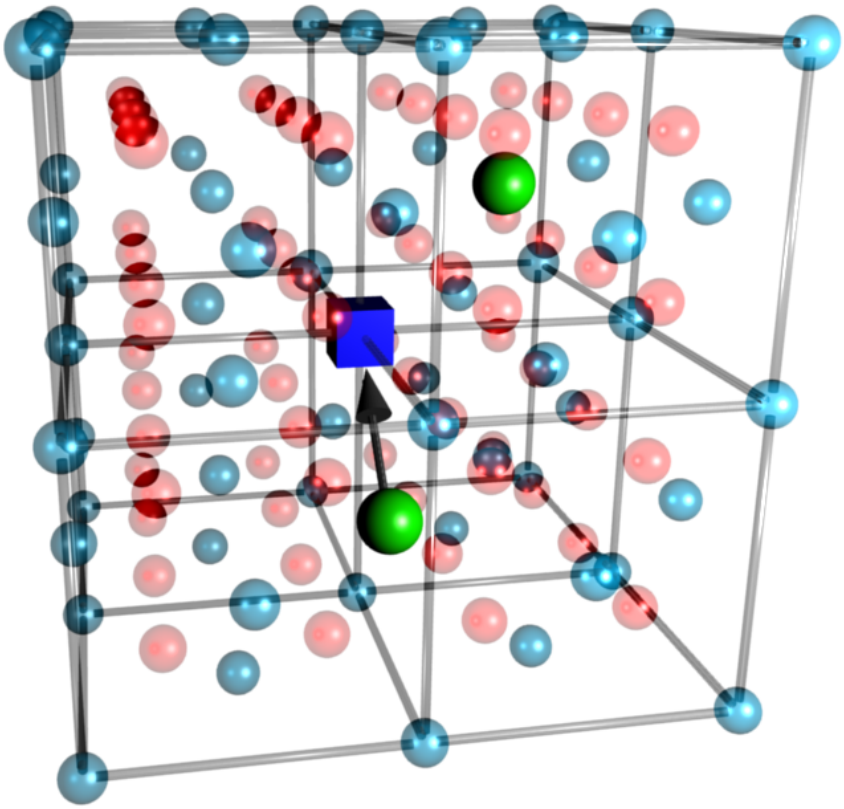


Figure 4.12: The cluster that will allow the migration of a U^{5+} ion to migrate into a vacancy with a low energy and an morphology close to the ground state morphology. The uranium vacancies are represented by a blue cube and the U^{5+} ions as green spheres.

4.3.4 3 × U^{5+} Cations

Three U^{5+} cations are now considered bound to the uranium vacancy and, once again, it is found that in the most stable cluster they all bind in a nearest neighbour position, but with an arrangement that allows maximum distance of the U^{5+} ions from each other (see Figure 4.13). Figure 4.14 reports that this cluster will give a migration energy barrier of 7.13 eV.

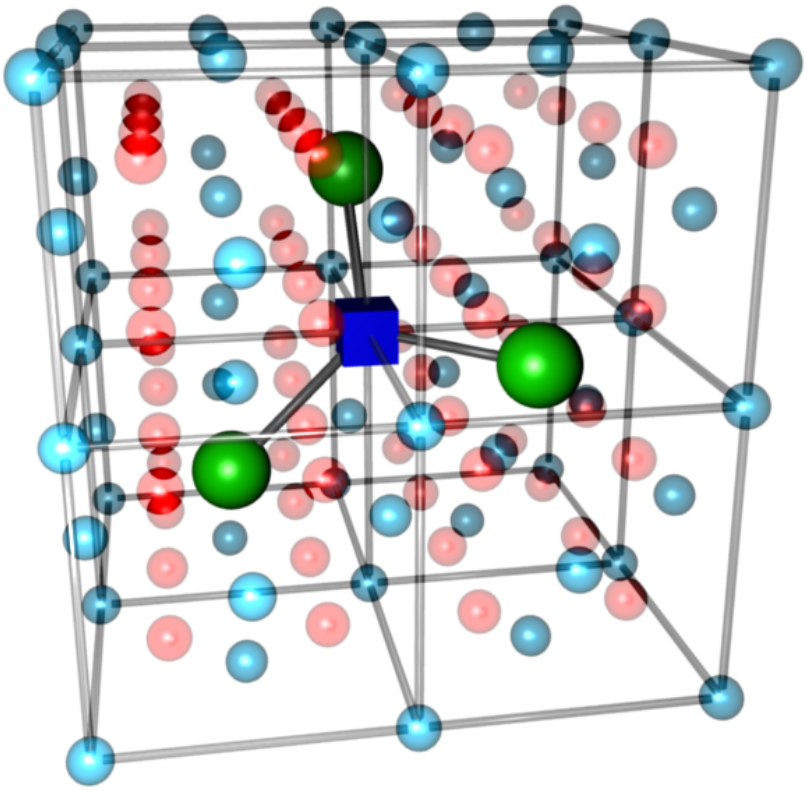


Figure 4.13: The lowest energy cluster containing one uranium vacancy and 3 U^{5+} ions (note: this is not a charge neutral cluster). The uranium vacancy is represented by a blue cube and the U^{5+} ions as green spheres.

There is a cluster with only a slightly higher energy of 0.05 eV that gives a migration energy barrier of 6.01 eV, markedly lower than the migration involving the most stable cluster. Interestingly, the migration energy is lower than that for a vacancy associated with 0, 1 or 2 U^{5+} cations. Furthermore, Figure 4.14 shows that there are a few different clusters that provide migration barriers close to 6 eV. There are many others that provide a lower overall barrier than the most stable cluster, even once their relative lower stability is taken into account.

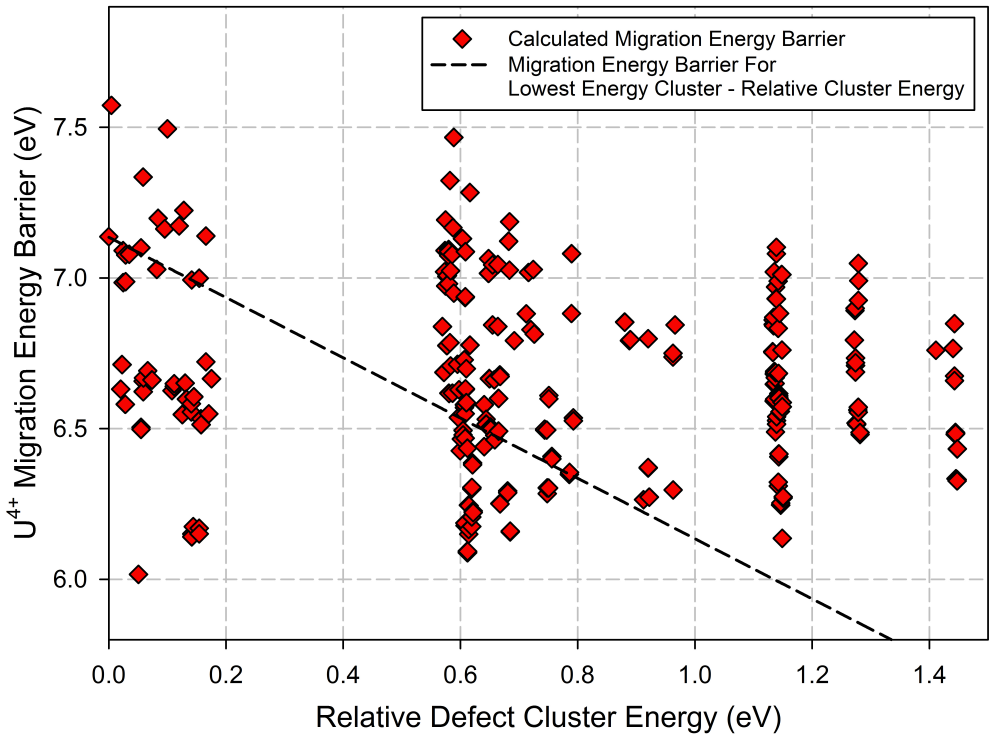


Figure 4.14: The energy barrier to migration for a U^{4+} cation migrating into a uranium vacancy in the <110> direction for all calculated cluster morphologies plotted against the morphology stability relative to the most stable arrangement of $\{V_U''''{:}3U_U^{\bullet}\}'$ cluster. The line represents the migration energy for the lowest cluster morphology arrangement minus the relative cluster energy to calculate whether a migration is more or less favourable than that for the most stable cluster.

When migration of a U^{5+} into the vacancy of a $\{V_U'''':3U_U^\bullet\}'$ cluster is considered there is once again a spread of migration energy barriers for the different clusters. Figure 4.15 reports the migration energies associated with a U^{5+} ion migration for a range of different clusters. It is clear that there is a large spread in the data and that clusters near the

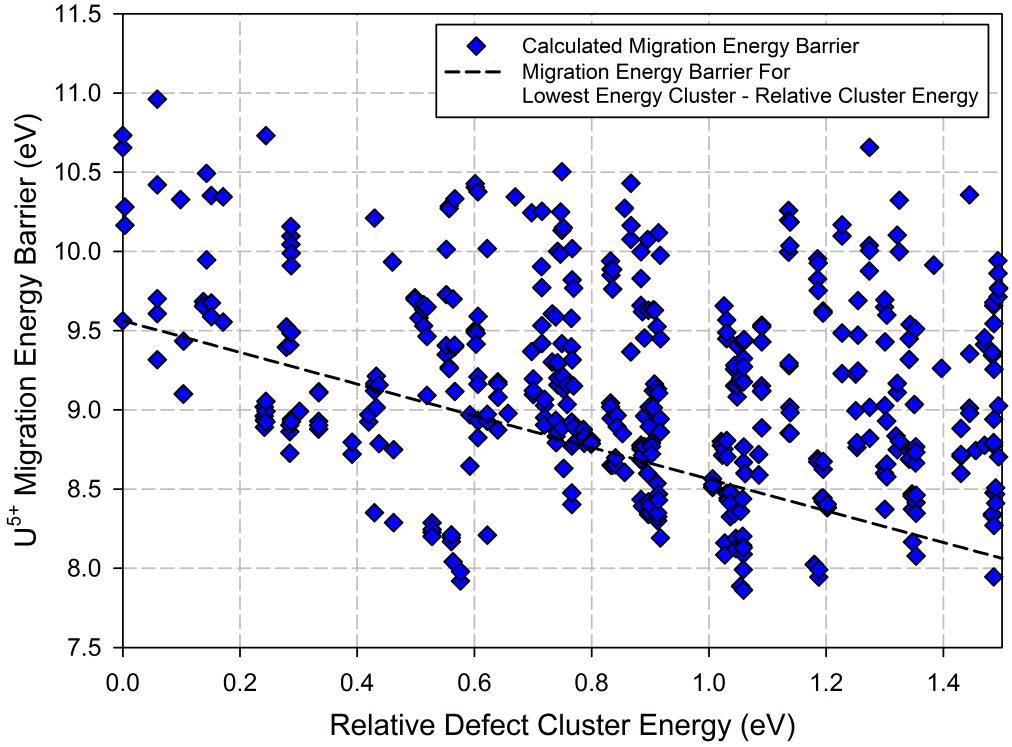


Figure 4.15: The energy barrier to migration for a U^{5+} cation migrating into a uranium vacancy in the <110> direction for all calculated cluster morphologies plotted against the morphology stability relative to the most stable arrangement of $\{V_U'''':3U_U^\bullet\}'$ cluster. The line represents the migration energy for the lowest cluster morphology arrangement minus the relative cluster energy to calculate whether a migration is more or less favourable than that for the most stable cluster.

ground state arrangement of the $\{V_U'''':3U_U^\bullet\}'$ cluster do not have a significantly lower migration energy barrier. It follows that migration of vacancies will still be dominated by U^{4+} migration.

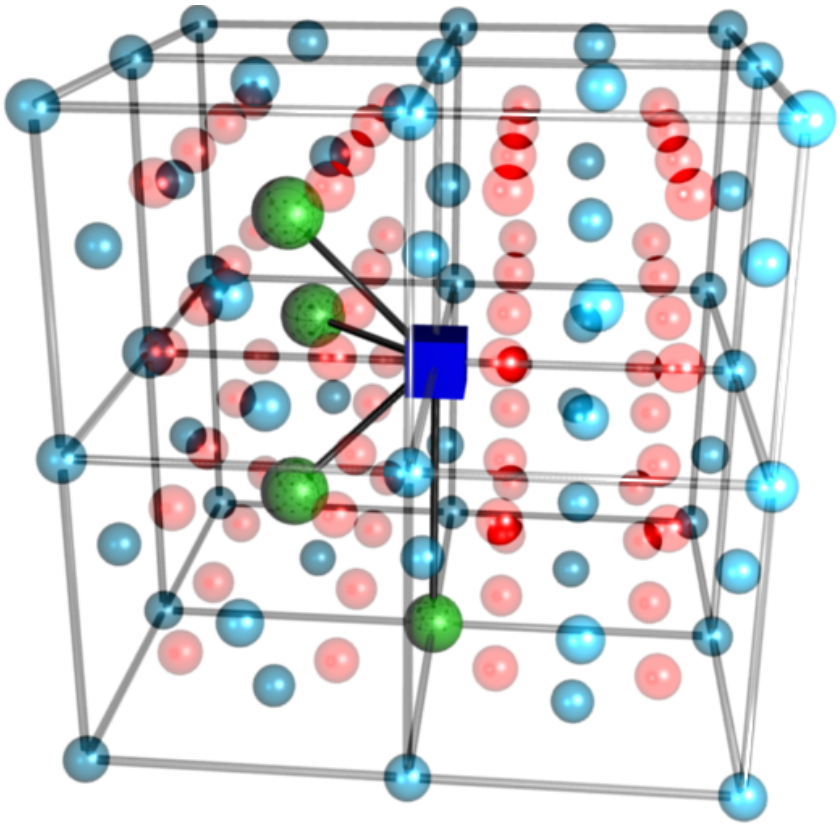
The complexity of V_U'''' migration in UO_2 when the vacancy is charge balanced by U^{5+} cations is clearly very complicated. Results suggest that instead of having a simple migration through UO_2, as the U^{5+} cation is able to hop to a different sites readily (as it can be considered a small polaron), the number of potential migration mechanisms is large

and metastable arrangements of the various part charged compensated clusters appear to be more favourable for facilitating migration than the most respective stable cluster arrangement.

4.3.5 4 × U^{5+} Cations

If four U^{5+} cations were to be considered, too many calculations would be required to calculate the lowest energy configuration in this 4×4×4 supercell (more than 750,000 separate calculations). As one of the U^{5+} was found to sit in a nearest neighbour position to the vacancy for all other clusters (1 to 3 U^{5+} ions) an assumption has been made to simplify the calculation, by keeping one of the U^{5+} cations in the nearest neighbour position allowing the lowest energy cluster to be formed by the other 3 U^{5+} ions (this involves 24,360 calculations, although the full 755,160 calculations are still required for the migration calculations and are therefore not included in this study). The lowest energy cluster morphology is shown in Figure 4.16. Three U^{5+} take up nearest neighbour positions to the vacancy and one takes up the 2^{nd} nearest neighbour position. This is not the intuitive arrangement of U^{5+} cations as one of the U^{5+} cations takes up a nearest neighbour position to two other nearest neighbour U^{5+} cations. This may be due to strain effects on the lattice or may be an artefact of the empirical potentials used in this study (see further work section). There are 24 other arrangements of U^{5+} cations within 0.3 eV of the lowest energy structure shown in Figure 4.16.

Although the migration energy for the vacancy has not been calculated for 4×U^{5+} cations in the vacancy cluster, the trend suggests that the energy could be lower still than when 3 U^{5+} cations are considered. This should be investigated further (see future work section) but for this study, the relative effects will allow a qualitative comparison of how dopants and fission products will change the vacancy diffusion characteristics of UO_{2+x}.



/

Figure 4.16: The lowest energy cluster containing one uranium vacancy and 4 U^{5+} ions (note: this is a charge neutral cluster). The uranium vacancy is represented by a blue cube and the U^{5+} ions as green spheres.

Table 4.1: Summary of uranium cation migration energies (eV) into a V_U'''' balanced by U^{5+} cations. All migration processes processes are for U^{4+} ions migrating into a vacancy as opposed to U^{5+} as these were found to be universally lower.

Number of U^{5+} Ions	Lowest Stable Cluster Mediated Migration Energy	Lowest Metastable Cluster Mediated Migration Energy(*Relative Cluster Energy*)
0	6.99	-
1	6.77	6.65 (*0.65*)
2	6.53	6.42 (*0.73*)
3	7.13	6.01 (*0.05*)

4.3.6 Summary of Uranium Vacancy Migration in Undoped UO_{2+x} and Future Work Required

Section 4.3 has highlighted the complexity of uranium ion migration via V_U'''' defects in UO_2, when charge balanced by U^{5+} cations. We can form a number of conclusions from the results presented so for but there is a great deal of future work required to fully establish uranium vacancy diffusion in UO_2.

It is clear from the calculations that U^{5+} migration is higher energy compared to U^{4+} migration. For a U^{5+} ion to migrate it first needs to take up an electron to become a U^{4+} ion, which is possible as the U^{5+} ions behave like small polarons. This trend is likely to be the same for the neutral $\{V_U'''':4U_U^{\bullet}\}^{\times}$ cluster, although further work should be carried out to confirm this.

The association of multiple U^{5+} cations changes the barrier for migration of U^{4+}. A number of lower energy processes are possible when various metastable clusters are present. It is likely that the trend will be the same for the neutral $\{V_U'''':4U_U^{\bullet}\}^{\times}$ cluster. Work needs to be carried out to understand whether the migration barrier rises as another U^{5+} ion is associated with the cluster or falls (as was the case with each progressive addition of U^{5+} cations from 0 to 3).

The diffusion of V_U'''' species in UO_{2+x} has been shown to be complex. This work is a step in the direction of being able to correctly predict the effective migration of U^{4+} via vacancies. It also allows some qualitative comparison to the vacancy migration in the presence of trivalent cations as will be discussed next.

4.4 Trivalent Cation and Vacancy Cluster Morphology

Now that there is a reasonable understanding of the arrangement of U^{5+} cations around a single vacancy and the vacancy diffusion characteristics, the next step is to understand the morphology of a cluster that contains a vacancy and a trivalent cation bound with

varying numbers of U^{5+} cations. The calculations were carried out in a similar manner to the investigation into the morphology of the cluster consisting of a vacancy and U^{5+}, with the vacancy being defined as a constant and the U^{5+} cation positions varied in order to identify the lowest energy arrangement.

To calculate the lowest energy arrangement of the trivalent cation, the vacancy and the varying number of U^{5+} cations, the trivalent cation was placed in a nearest neighbour position with respect to the vacancy but then moved away sequentially to a 4^{th} nearest neighbour position, at each step all of the arrangements of U^{5+} cations were considered.

The investigation of a V_U'''' with a substitutional trivalent cation were carried out with 0 to 2 U^{5+} species in the cluster. Further additions of U^{5+} cations are too computationally intensive to consider at this time.

4.4.1 Binding of Trivalent Cations To Vacancies

For migration of the trivalent cation to occur via a vacancy mechanism, the trivalent species must be able to associate itself with a vacancy, either taking up a 1^{st} nearest neighbour position (allowing migration in the <110> direction) or a 2^{nd} nearest neighbour position (allowing migration in the <100> direction). If a species does not easily take up one of these positions, either by it being the most stable site or by it being a site that is a preferable metastable site, it is unlikely that migration of the trivalent species will occur via a vacancy mediated mechanism.

When two U^{5+} cations are present, the $\{V_U'''':T_U':2U_U^{\bullet}\}''$ cluster is formed (where 'T' is a trivalent cation). Consideration of a range of T^{3+} ions shows that only Fe and Cr are bound to the vacancy in a position that will allow migration of the species into the vacancy (i.e. the 1^{st} or 2^{nd} nearest neighbour position). Both Cr and Fe preferentially occupy the 2^{nd} nearest neighbour position. This is reported in Figure 4.17. The binding energy was calculated by considering the following equation:

$$V_U'''' + 2U_U^{\bullet} + T_U' \rightarrow \{V_U'''' : T_U' : 2U_U^{\bullet}\}''' \tag{4.1}$$

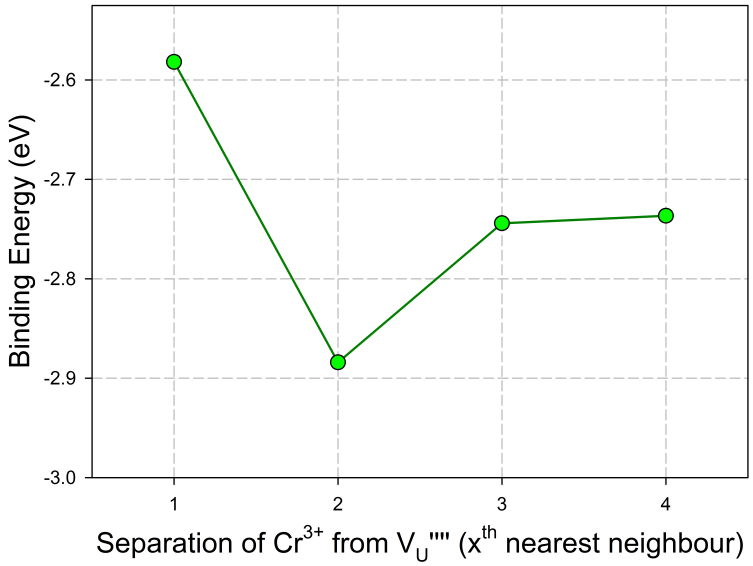


Figure 4.17: Binding energy of the most stable $\{V_U''''{:}Cr_U'{:}2U_U^\bullet\}'''$ cluster with various V_U'''' to Cr_U' separations.

The lowest energy cluster morphology for the $\{V_U''''{:}Cr_U'{:}2U_U^\bullet\}''$ cluster is illustrated in Figure 4.18.

Cations larger than Fe^{3+} are not preferentially bound to the vacancy in a nearest neighbour position. More specifically, they do not preferentially occupy a 1st, 2nd or 3rd nearest neighbour position with respect to the uranium vacancy. In the series of calculations carried out only interactions up to the 4th nearest neighbour where considered and this (4th neighbour) is the most stable position for trivalent species larger than (and not including) Fe^{3+}. The same trend was seen for the clusters involving one U^{5+} cation and no U^{5+} cations. The binding energies of an In^{3+} cation, a V_U'''' and $2U_U^\bullet$ at various V_U'''' and In_U' separations is reported in Figure 4.19.

Further detailed calculations are now limited to the chromium cation. The lowest energy cluster morphology was investigated for the $\{V_U''''{:}Cr_U'{:}3U_U^\bullet\}''$ cluster. The 2nd nearest neighbour position is once again the most stable arrangement and is illustrated in Figure 4.20. This cluster morphology is similar to the cluster incorporating a vacancy and 3 U^{5+} cations without the trivalent cation (see Figure 4.13), orientated with one of the U^{5+} cations in the nearest neighbour position to both the vacancy and the Cr substitutional cation.

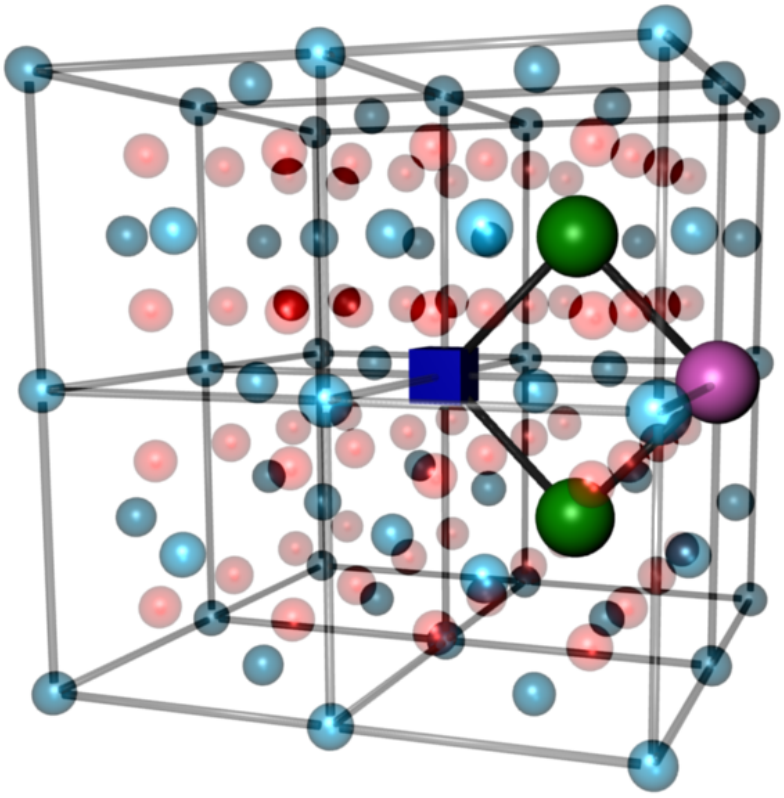


Figure 4.18: The lowest energy morphology of the $\{V_U'''':Cr_U':2U_U^\bullet\}''''$ cluster.

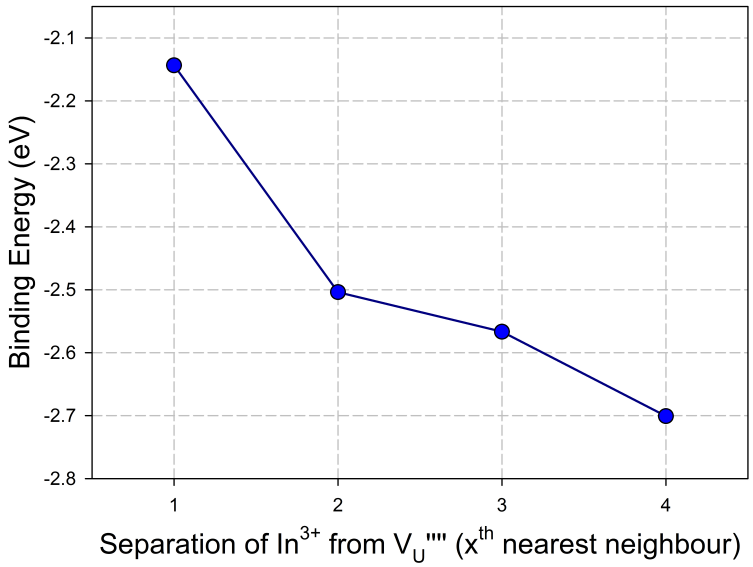


Figure 4.19: Binding energy of the most stable $\{V_U'''':In_U':2U_U^\bullet\}''''$ cluster with various V_U'''' to In_U' separations.

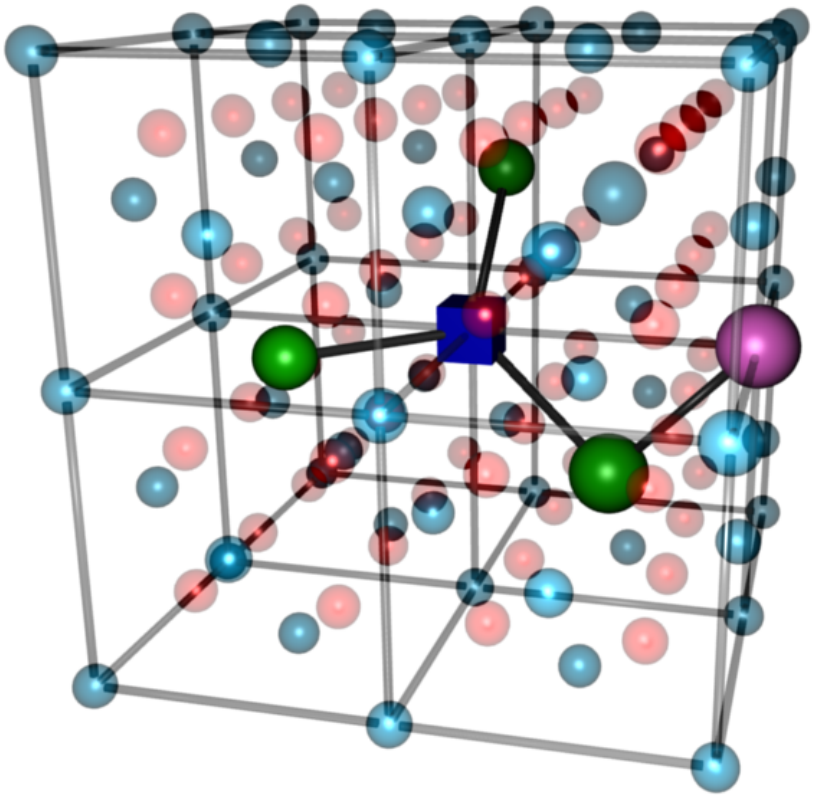


Figure 4.20: The lowest energy morphology of the $\{V''''_U{:}Cr'_U{:}3U^{\bullet}_U\}''$ cluster.

The binding energy for the $\{V_U'''':Cr_U':3U_U^\bullet\}''$ cluster was found to be -1.83 eV. Figure 4.21 reports the binding energies of the $\{V_U'''':Cr_U':xU_U^\bullet\}''''^{-x}$ with values of 'x' from 0 to 3. The

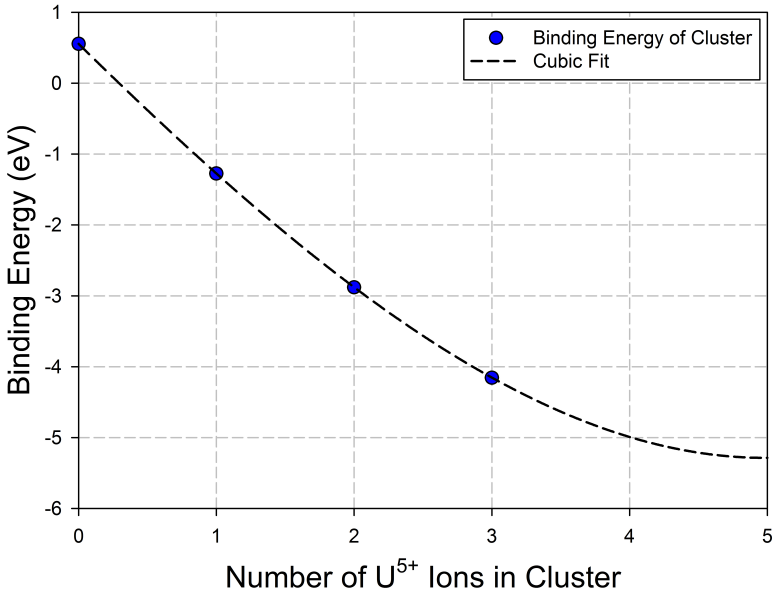


Figure 4.21: Binding energies of $\{V_U'''':Cr_U':xU_U^\bullet\}''''^{-x}$ clusters with various increasing numbers of U^{5+} cations. A cubic fit has been made to the four points to understand the approximate value of the number of U^{5+} ions that will give the most bound cluster.

calculated binding energies fall as a function of x, with each step less than the previous. The cluster with the lowest binding energy is expected to be the charge neutral cluster that contains five U^{5+} ions as there will maximise the net Coulombic interactions between the constituent defects. Interestingly, a cubic fit to the four data points shows a minimum near 5 U^{5+} cations as would be expected (note: the physical relevance of the cubic fit is not established and may be a coincidence). The morphology of the $\{V_U'''':Cr_U':5U_U^\bullet\}^\times$ cluster has not been investigated due to the large number of possible configurations and hence calculations it would require.

4.4.2 Diffusion of Cr^{3+} in UO_{2+x} Fuel

The diffusion of Cr^{3+} is now considered in more detail due to its importance as a fuel dopant (further work should be carried out to understand Fe^{3+} migration). As Cr^{3+} ions occupy the 2^{nd} nearest neighbour position to the vacancy for all calculated morphologies,

migration of the Cr^{3+} cation in the <100> direction is first considered. Cr^{3+} migration is required for a coupled vacancy to proceed. The migration energies plotted against relative cluster energies are presented in Figure 4.22. It can be seen that all migration energies

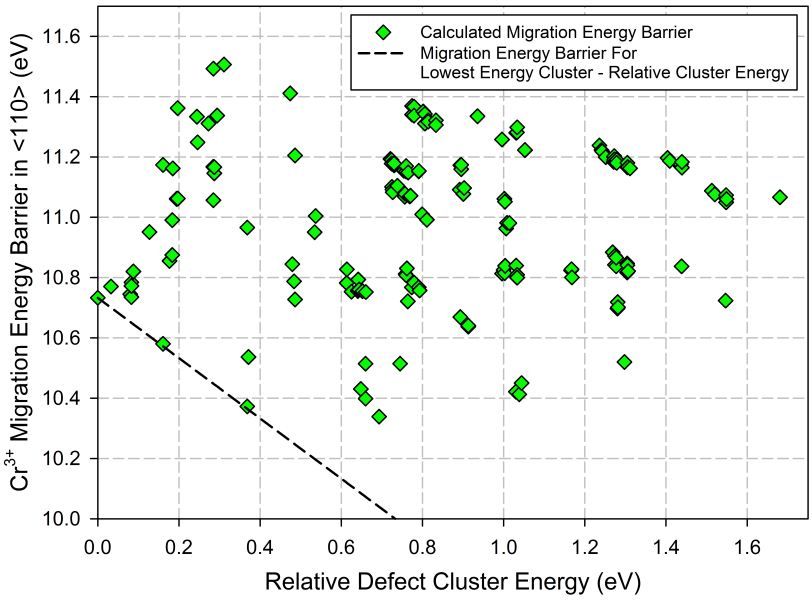


Figure 4.22: The energy barrier to migration for a Cr^{3+} cation migrating into a uranium vacancy in the <100> direction for all calculated cluster morphologies plotted against the morphology stability relative to the most stable arrangement of $\{V_U''''{:}Cr_U'2U_U^{\bullet}\}'$ cluster.

are very high, the barrier for the lowest energy arrangement being 10.73 eV. This indicates that migration of the Cr^{3+} cation will be a high energy process and therefore slow even compared to that of U^{4+}.

Knowing that migration of Cr^{3+} in the <100> direction is unfavourable, migration from the metastable 1st nearest neighbour position is considered as it is the only other simple migration route. The migration energies of the Cr^{3+} ions into the vacancy in the <110> are plotted against their relative cluster stability in Figure 4.23. It can be seen that the migration energy is substantially lower from the 1st nearest neighbour position with the most stable cluster giving a migration energy barrier of 3.18 eV. It can be seen that there are no metastable arrangements of the defects that will give a lower combined relative cluster energy and migration energy. The stable cluster and migration of the Cr^{3+} in the

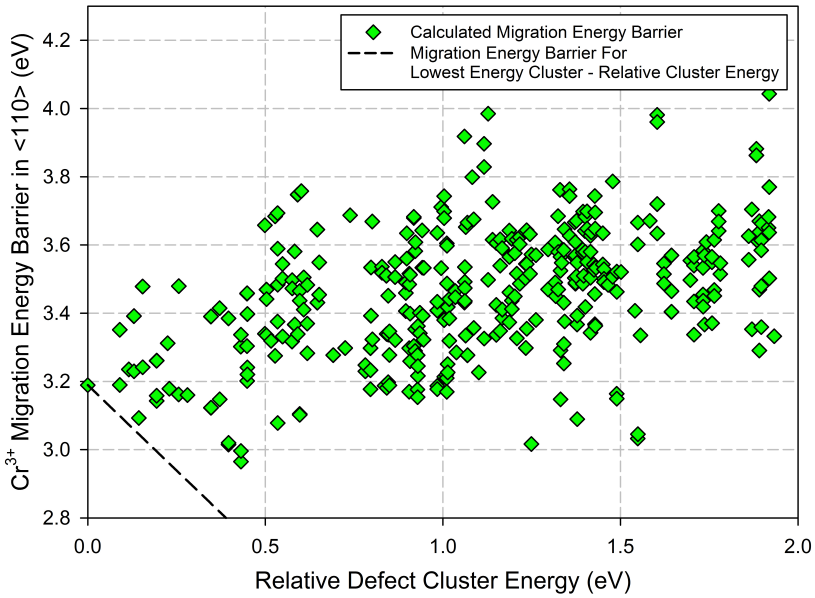


Figure 4.23: The energy barrier to migration for a Cr^{3+} cation migrating into a uranium vacancy in the <110> direction for all calculated cluster morphologies plotted against the morphology stability relative to the most stable arrangement of the $\{V''''_U{:}Cr'_U 2U^{\bullet}_U\}'$ cluster.

<110> direction is illustrated in Figure 4.24.

For migration from the 1st nearest neighbour position to occur, the vacancy must migrate from the 2nd nearest neighbour position. Calculations suggest that the migration energy barrier for this process will be 6.52 eV, as reported in Figure 4.25. This is slightly lower than the lowest bulk migration in energy barrier value for vacancy migration in undoped UO_2, indicating that if this is the limiting step for migration, the overall energy for migration of Cr^{3+} will be very slightly higher than for a U cation in undoped fuel. It can therefore be noted that Cr^{3+} may be transported through the lattice at roughly the same rate as U^{4+} cations. More complex concerted migration mechanisms may prove to be energetically preferable for Cr^{3+} transport and the present result may be an artefact of the non-charge neutral clusters that the current calculations have been limited to considering. Both concerns should be addressed properly in future investigations.

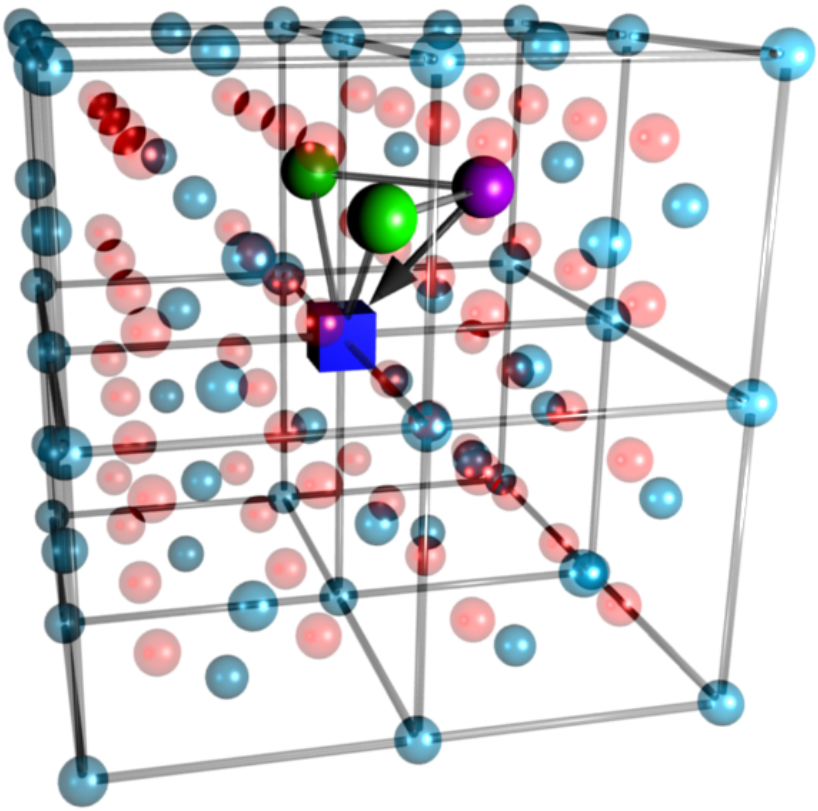


Figure 4.24: The lowest energy migration of a Cr^{3+} cation into a vacancy in the $\{V_U''''{:}Cr_U'{:}2U_U^{\bullet}\}''$ cluster. Here, the Cr^{3+} ion is shown as a purple sphere and the vacancy as a blue cube.

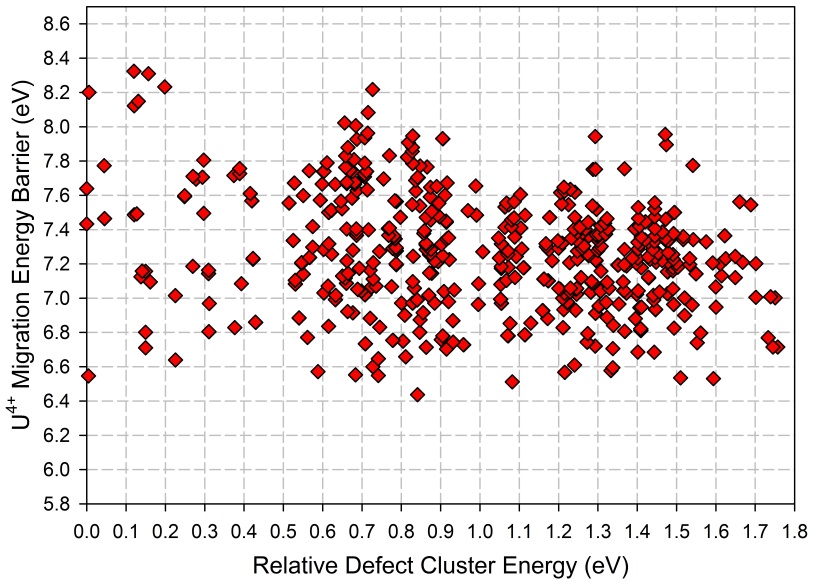


Figure 4.25: The energy barrier to migration for a U^{4+} cation migrating away from a chromium substitutional defect in the <110> direction for all calculated cluster morphologies plotted against the morphology stability relative to the most stable arrangement of $\{V''''_U{:}Cr'_U 2U^{\bullet}_U\}'$ cluster.

4.4.3 Summary of Trivalent Cation Migration and Effect on Vacancy Migration

This chapter has highlighted the complexity of uranium ion migration via uranium vacancies. The complexities inherent in the understanding of the Cr^{3+} cation transport and that for larger trivalent cations is significant. The influence of trivalent cations on vacancy migration in hyperstoichiometric fuel is also very complex. Although a great deal of further work is required for a full understanding of vacancy migration in doped hyperstoichiometric fuel, a number of key conclusions can be made.

For the large trivalent cations (In^{3+} and larger), a key finding is that there is an energy penalty for vacancies to be associated with the trivalent cation (in a 1^{st} to 4^{th} nearest neighbour position). Since vacancies are required to facilitate transport through a vacancy mechanism, this means that these larger cations will migrate through the UO_2 lattice at a lower rate than U^{4+} ions. Burn-up indicators such as Nd^{3+}, Pr^{3+} and Y^{3+} will therefore not move far from where they are initially produced via fission processes allowing a good

indication of the burnup at a specific local environment. Burnup indicators provide key tools when carrying out post-irradiation examinations on fuel.

When considering the smaller trivalent cations Cr^{3+} and Fe^{3+}, calculations suggest that vacancies will preferentially occupy in a 2^{nd} nearest neighbour position. This gives the possibility for a coupled mechanism for vacancy migration and transport of trivalent cation migration through the UO_{2+x} lattice. Calculations focused on the fuel dopant Cr^{3+} suggest that migration of the Cr^{3+} cation from the 2^{nd} nearest neighbour directly into the vacancy (<100>) are all high energy relative to conventional V''''_U migration (<110>). For migration of the Cr^{3+} cation to proceed with a lower migration energy barrier, the vacancy needs to migrate to a nearest neighbour position to the Cr^{3+} ion. The migration energy barrier for the vacancy from a 2^{nd} to 1^{st} nearest neighbour position is only slightly higher than for vacancy migration in un-doped UO_2 indicating that this mechanism will allow Cr^{3+} to diffuse through the UO_{2+x} lattice at approximatally the same rate as that for U^{4+} cations.

Chapter 5

Point Defects and Transmutation Products in Zirconium Diboride

'There is nothing so stable as change."
- Bob Dylan [185].

5.1 Introduction

Zirconium diboride (ZrB_2) is used as a burnable absorber, applied as a 10 μm coating on advanced PWR and BWR fuel pellets. The ceramic has an extremely high melting temperature of approximately 3300 K [186] and for this reason the material falls under the category of an ultra-high-temperature ceramic (UHTC).

The high melting temperature and relatively low density of ZrB_2, coupled with good mechanical properties, make the material ideal for uses other than as a neutron poison in nuclear reactors; in the aerospace industry, ZrB_2 has been used in designs for the leading edges of hypersonic control surfaces and other key, high temperature components [186].

The properties of ZrB_2 have been investigated in this chapter and give relevant information to the behaviour of the UHTC within fission reactors, taking into account transmutation

products, and intrinsic defects including variations in stoichiometry and defect processes. The stoichiometry of ZrB_2 has also been investigated to help understand what variations can be accommodated and in doing so aid in the manufacture of the ceramic.

5.2 Structure of ZrB_2

ZrB_2 has a hexagonal structure with the P6mmm space group consisting of alternating layers containing zirconium and boron. When in the primitive unit cell, the lattice vectors are a≡b=3.17 Å and c=3.53 Å as experimentally determined by Fahrenholtz and Hilmas [187]. The Zr atoms reside at the (0,0,0) site and the B atoms occupy the $(\frac{1}{3},\frac{2}{3},\frac{1}{2})$ sites. A total of five symmetrically distinct interstitial sites were identified in the ZrB_2 structure, two in the Zr layer, $(\frac{1}{2},\frac{2}{2},0)$ and $(\frac{1}{2},0,0)$, two in the B layer, $(\frac{1}{2},0,\frac{1}{2})$ and $(0,0,\frac{1}{2})$, and one site in-between the two layers $(0,0,z)$. The structure of ZrB_2 and the interstitials sites are illustrated in Figure 5.1.

All of the atom sites and interstitial sites are labelled in Table 5.1 showing the Wyckoff sites and the species that take up the site. The number of the Wyckoff position relates to the number of equivalent sites in the unit cell while the letter is simply the ordering of the interstitial sites.

Table 5.1: Symmetrically distinct sites within the P6mmm space group showing the position (multiplicity and Wyckoff letter), symmetry, coordinates and what occupies the site within ZrB_2.

Position	Symmetry	Coordinates			Species at Site
1 a	$6/mmm$	0,0,0			Zr atom
1 b	$6/mmm$	$0,0,\frac{1}{2}$			Interstitial
2 c	$\bar{6}m2$	$\frac{1}{3},\frac{2}{3},0$	$\frac{2}{3},\frac{1}{3},0$		Interstitial
2 d	$\bar{6}m2$	$\frac{1}{3},\frac{2}{3},\frac{1}{2}$	$\frac{1}{3},\frac{2}{3},\frac{1}{2}$		B atom
2 e	$6mm$	$0,0,z$	$0,0,\bar{z}$		Interstitial
3 f	mmm	$\frac{1}{2},0,0$	$0,\frac{1}{2},0$	$\frac{1}{2},\frac{1}{2},0$	Interstitial
3 g	mmm	$\frac{1}{2},0,\frac{1}{2}$	$0,\frac{1}{2},\frac{1}{2}$	$\frac{1}{2},\frac{1}{2},\frac{1}{2}$	Interstitial

ZrB_2 is highly covalent and the system can be appropriately modelled using DFT. The

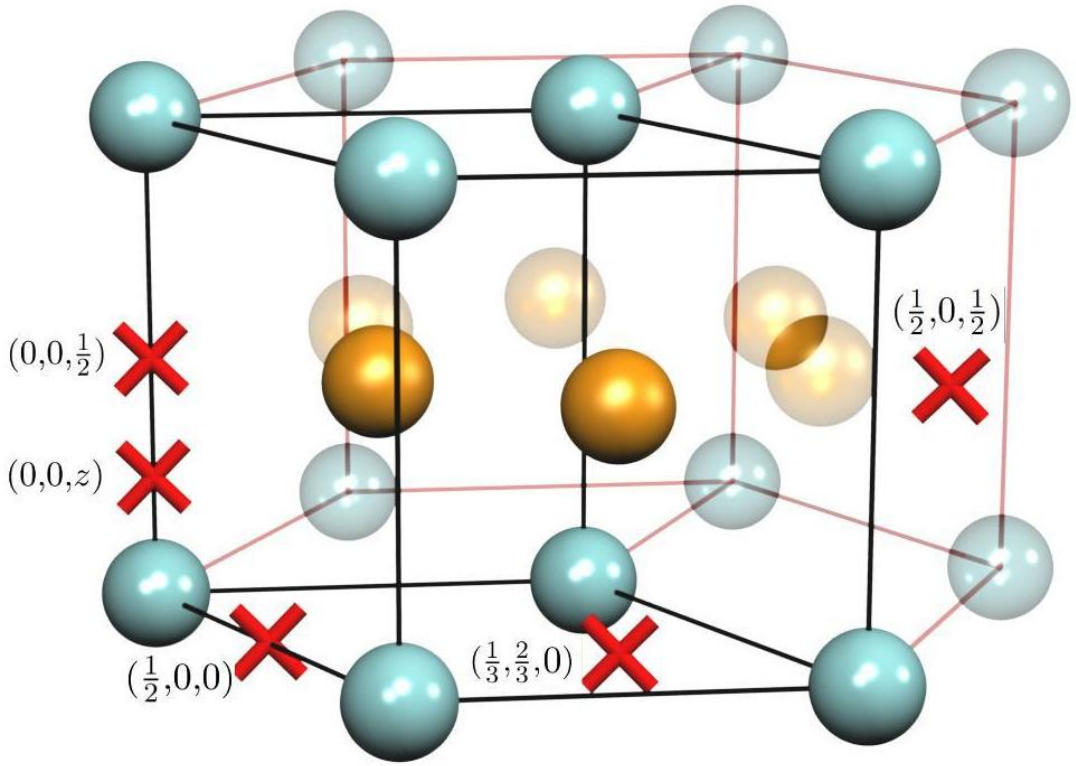


Figure 5.1: Structure of ZrB_2 showing the zirconium atoms as light blue and the boron atoms as dark yellow. The five interstitial sites are shown as red crosses.

material possess graphite-like sp^2 bonds such that the directional σ bonds between B atoms are fully occupied but the π orbitals are available to accept charge from the Zr atoms in the adjacent layers.

5.3 Computational Details

The choice of exchange-correlation functional was determined by comparison. The VASP package comes with a collection of good psuedopotentials and PAW potentials. Table 5.2 presents the lattice constants for each of the functionals available in the VASP package and previous DFT work on ZrB_2 and compares them to experimental data.

Table 5.2: Comparison of lattice vectors with exchange-correlation functionals in ZrB_2.

Exchange Functional	a (Å)		c (Å)		Reference
Experimental	3.169		3.531		[188]
LCAO	3.183	(0.5%)	3.546	(0.6%)	[189]
TB-LMTO	3.197	(0.9%)	3.561	(1.1%)	[189]
GGA-PBE	3.167	(-0.1%)	3.542	(0.5%)	[189]
LDA	3.127	(-1.3%)	3.490	(-0.9%)	[189]
PAW-PBE	3.175	(0.2%)	3.558	(1.0%)	Present Work
PAW-LDA	3.126	(-1.4%)	3.514	(-0.9%)	Present Work
PAW-GGA	3.174	(0.2%)	3.564	(1.15%)	Present Work

The PAW-PBE exchange functional was chosen for this work as it described the lattice parameters adequately.

For DFT calculations the cut-off energy and the k-point grid need to be converged to give accurate results with tractable computational use. The cut-off energy to be used was determined by carrying out a number of simple electronic relaxations of a primitive unit cell at a number of different energies. The convergence results are presented in Figure 5.2.

425 eV was determined as the lowest cut-off energy to give a convergence of greater than 0.001 eV accuracy and was therefore taken as the minimum cut-off energy to be used in

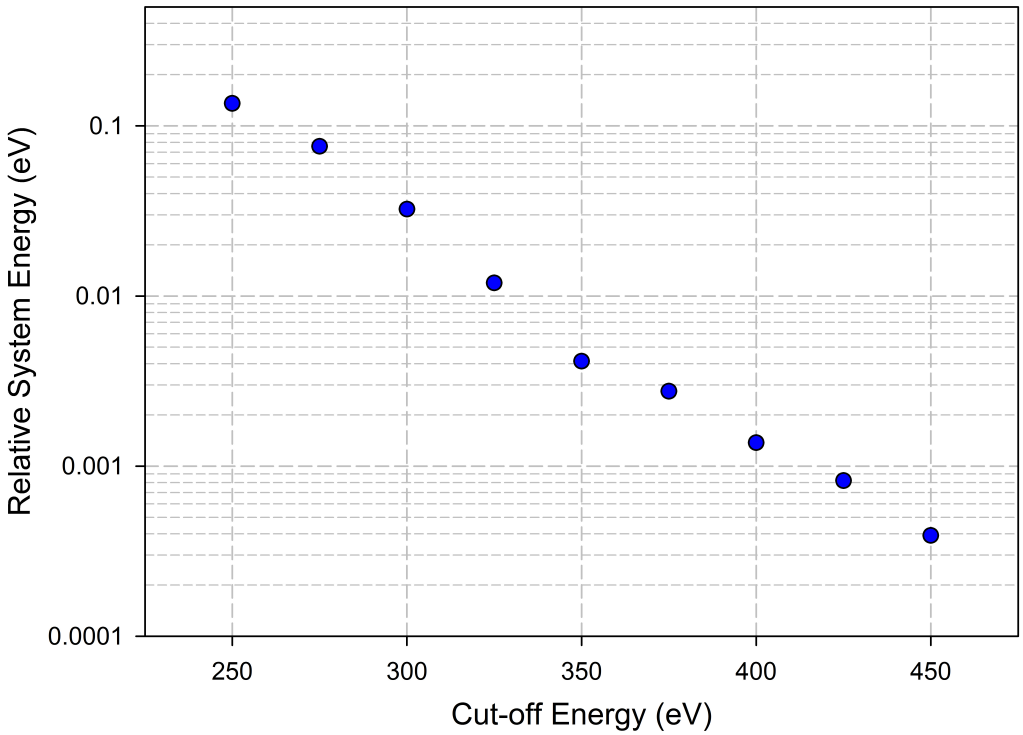


Figure 5.2: Convergence of the cut-off energy for use in ZrB_2 calulations. The system energies are relative to the lowest system energy calculated, at 475 eV.

the calculations on ZrB_2. A γ-centred sampling of the Brillouin zone was utilised in the calculations with a k-point spacing of approximately $0.04\,\text{Å}^{-1}$. Spin polarisation of the species was considered.

A 4×4×3 supercell containing 144 lattice sites was used for defect energy calculations as this was judged to be the largest sized supercell to carry out calculations given the computational restraints. The supercell is asymmetric as the c lattice vector is larger than the a and b vectors. The defect calculations were carried out at constant pressure with stopping criterion for the electronic self-consistancy steps of $1\times10^{-4}\,\text{eV}$ and an ionic relaxation convergence stopping energy of $1\times10^{-3}\,\text{eV}$.

A 2×2×2 supercell was used for quantum mechanical molecular dynamics calculations due to the increased computational load of the calculations. A time step of 1 fs was judged to be suitable. The QMD simulations were carried out at constant volume after relaxing the strains on the supercell. The strains were relaxed by running a series of simulations at different cell volumes to highlight the lattice constants that provide the minimum external pressure on the supercell.

Nudged elastic band (NEB) calculations were carried out to fully understand the migration pathway of any species that were found likely to migrate from the defect calculations. The start and end points for each migration were identified from static calculations.

5.4 Intrinsic Defect Processes of ZrB_2

The intrinsic defect processes of ZrB_2 are discussed in this section. Point defects are initially discussed and then understanding is progressed to identify the dominant defect processes and variation in stoichiometry.

5.4.1 Point Defects in ZrB_2

Isolated defects and defect clusters have had their energies calculated using the method outlined in chapter 2. Defect energies were calculated by finding the difference in energy between an isolated defect and a perfect supercell, taking the energy of the defect species at infinite separation in to account. The defect energies are reported in Table 5.3. The anti-site, Frenkel and Schottky defect energies are also reported. (Note: the formation energy of ZrB_2 with respect to B (-6.68 eV per atom in solid B) and Zr, -8.48 eV per atom in α-Zr) was determined to be 9.62 eV)

Table 5.3: Intrinsic ZrB_2 defect energies calculated in a 4×4×3 supercell.

Defect	Notation	Type	Defect Energy (eV)
Boron Vacancy	V_B	-	9.65
Zirconium Vacancy	V_{Zr}	-	11.66
Boron Interstitial	B_i	$(0,0,\frac{1}{2})$	-0.63
		$(\frac{1}{2},0,0)$	-0.01
		$(\frac{1}{3},\frac{2}{3},0)$	0.53
		$(\frac{1}{2},0,\frac{1}{2})$	14.59
		$(0,0,z)$	30.99
Zirconium Interstitial	Zr_i	$(0,0,\frac{1}{2})$	8.96
		$(\frac{1}{2},0,0)$	7.39
		$(\frac{1}{3},\frac{2}{3},0)$	7.40
		$(\frac{1}{2},0,\frac{1}{2})$	32.85
		$(0,0,z)$	5.58
Boron on Zirconium Site	B_{Zr}	-	5.42
Zirconium on Boron Site	Zr_B	-	9.11
Antisite pair	$\{B_{Zr}: Zr_B\}$	Bound	8.17
		Separated to Infinity	12.13
Boron Frenkel Defect	$\{B_i: V_B\}$	Bound	8.45
		Separated to Infinity	9.02
Zirconium Frenkel Defect	$\{Zr_i: V_{Zr}\}$	Bound	18.79
		Separated to Infinity	19.05
Schottky Trivacancy	$\{V_{Zr}: 2V_B\}$	Bound	31.40
		Separated to Infinity	30.96

We can use Table 5.3 to appreciate that boron interstitials are over 0.6 eV more stable in the $(0,0,\frac{1}{2})$ position compared to the other studied interstitial sites. This is a large

preference for one site and in contrast to Zr which is less stable by, 3.4 eV at the $(0,0,\frac{1}{2})$ site. Zr preferentially occupies the $(0,0,z)$ site, displacing a Zr onto an adjacent interstitial site in the <001> direction, forming a split interstitial (shown in Figure 5.3).

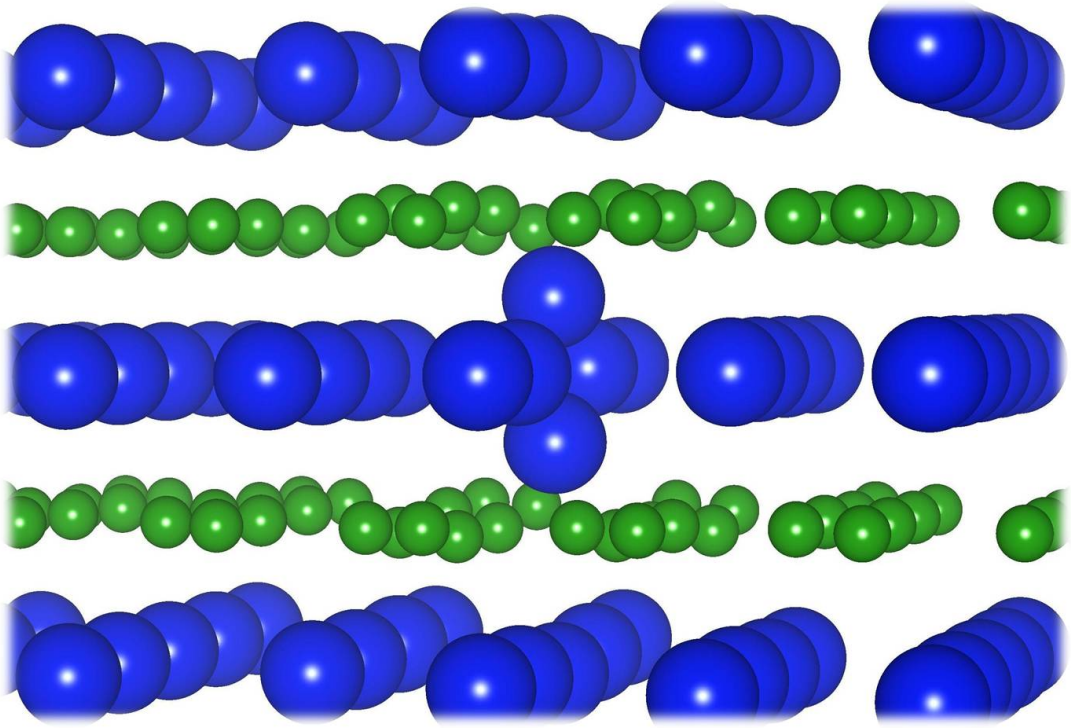


Figure 5.3: Zirconium interstitial on the $(0,0,z)$ site forming a split interstitial. Zirconium shown in blue and boron in green.

Both anti-site defect energies are high and therefore would be unlikely to form. The binding energy for the anti-site defect pair was calculated to be 3.96 eV, a considerable attractive energy, although the high defect energy of the defect would render the concentration of anti-site pairs low.

The Schottky trivacancy defect energies, both clustered (31.40 eV) and separated (30.961 eV) are very high. Unusually, the clustered energy is less favourable in comparison to the separated defects dso this provides an interesting exception. The extremely high energy suggests that Schottky defects will be very unlikely to form. At 3000 K, the concentration of Schottky defects will be:

$$[2V_B + V_{Zr}] = e^{\frac{-30.961}{kT}} \approx 1 \times 10^{-53} \tag{5.1}$$

where 'k' is Boltzmann's constant and 'T' is the temperature.

When considering the Frenkel energies, the first point of interest is that the defect energies are considerably lower than the Schottky energy. Further, the boron Frenkel reaction has a lower energy than the zirconium Frenkel reaction by about 10 eV. The calculations predict that both the zirconium and boron Frenkel prefer to be bound defects as the bound energies are lower energy than the isolated defect energies. Although the boron Frenkel energy is lower and therefore more likely to form, it still has a significant magnitude and as such the concentration of boron vacancies and interstitials will be rather low. Using the standard laws of mass analysis one can calculate the concentration of boron interstitials:

$$[B_i] = [V_B] = e^{-\frac{4.51}{kT}} \tag{5.2}$$

At a modest fuel pellet rim temperature of 700 K, the equilibrium concentration of either boron vacancies or interstitials due to Frenkel disorder will be 3.441×10^{-33}, which is very small compared with the defects that will be formed due to the B_5^{10} transmutation (see equation 1.10 in section 1.3). It is however possible that the bound intrinsic Frenkel defect clusters may play a role in the trapping of the transmutation products Li and He. This can be considered unlikely by considering Table 5.3 where the defect energies are either very slightly negative or very positive (compared with the total defect process energy). As such, intrinsic defect clusters will exhibit an even smaller concentration than the isolated intrinsic defects (due to a reduction in configurational entropy of a cluster compared with isolated defects). Consequently, intrinsic defect sites will not provide important trap sites for He or Li.

5.4.2 Variation of Stoichiometry of ZrB_2

Alternative trap sites may be present in the ZrB_2 crystal if the material was able to vary with stoichiometry, either during manufacture or in reactor. Non-stoichiometry may be formed by either excess boron or excess zirconium. Variations in stoichiometry can be

formed through anti-site defects, vacancies or interstitial mediated processes. In the case of B excess, the three reactions that can occur are:

$$B_{(s)} \rightarrow B_i \tag{5.3}$$

$$B_{(s)} + \frac{1}{2}Zr_{Zr} \rightarrow \frac{1}{2}V_{Zr} + \frac{1}{2}ZrB_2 \tag{5.4}$$

$$B_{(s)} + \frac{1}{3}Zr_{Zr} \rightarrow \frac{1}{3}B_{Zr} + \frac{1}{3}ZrB_2 \tag{5.5}$$

The total energies for these processes are: 7.01 eV, 0.43 eV and 4.45 eV, respectively. The energy for the V_{Zr} mediated process (equation 5.4 is considerably lower and can be quantitatively assessed by the mass action equation [190] corresponding to:

$$[V_{Zr}] = e^{-\frac{0.43}{2kT}} \tag{5.6}$$

At a temperature of 700 K the Zr vacancy concentration will be 2.95×10^{-2}, a significant concentration. This suggests that ZrB_2 may deviate from the stoichiometric composition ZrB_2 to ZrB_{2+x} in the presence of excess B by forming Zr vacancies.

In the case of Zr excess (a possibility due to the proximity of the fuel pellet to the zirconium based alloy), the following three reactions involve the addition of Zr from its solid, analogous to that described for B:

$$Zr_{(s)} \rightarrow Zr_i \tag{5.7}$$

$$Zr_{(s)} + 2B_B \rightarrow 2V_B + ZrB_2 \tag{5.8}$$

$$Zr_{(s)} + \frac{2}{3}B_B \rightarrow \frac{2}{3}Zr_B + \frac{1}{3}ZrB_2 \tag{5.9}$$

The total energies for these processes are: 15.88, 2.93 and 6.27 eV, respectively. These energies are higher than the boron excess energies. The lowest reaction is given by equation

5.8 and the concentration of V_B will be:

$$[V_B] = e^{-\frac{2.93}{2kT}} \tag{5.10}$$

At 700 K the boron vacancy concentration will be 2.83×10^{-11}, extremely low. This suggests that the ZrB_2 system is very unlikely to vary from stoichiometry to form $Zr_{1+x}B_2$ to any extent that is significant compared with the Li or He concentration that would be formed due to the B transmutation reaction.

The results suggest that ZrB_2 will not accommodate any significant deviation from stoichiometry with excess Zr but excess B will be accommodated to a much greater degree. This has implications for the fabrication of ZrB_2, which would have to ensure a processing route that maintained a strict control of zirconium to avoid producing a non-homogeneous, two-phase material but excess B can be accommodated. Given that ZrB_2 has a potential use as an ultra-high temperature ceramic, the presence of a second phase would degrade the high-temperature stability of the ceramic. In avoiding secondary phase formation by manufacturing ZrB_2 with a slight boron excess, the mechanical properties of the material may reduce, having implications for its use as a structural ceramic. Understanding the changes in mechanical properties with deviation in stoichiometry would be useful future work.

5.5 Helium and Lithium Defects in ZrB_2

Helium and lithium are produced as products of the transmutation of B_5^{10} when a neutron is absorbed. B_5^{10} is better at absorbing slower 'thermal neutrons' as illustrated in Figure 5.4. These are the thermal neutrons that unless absorbed, can go on to initiate a fission event.

Once produced via the transmutation, the He and Li atoms or ions can then remain within the ZrB_2 crystal lattice or be released from the solid phase to the surrounding environment.

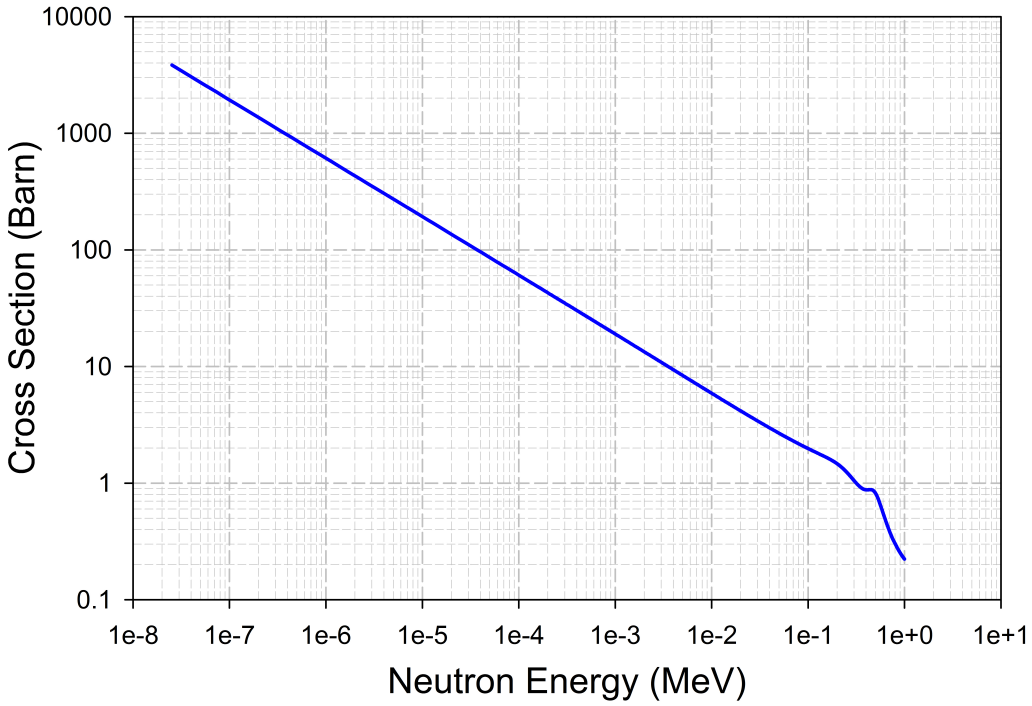


Figure 5.4: Neutron cross section spectrum of B_5^{10} showing a decrease in capture probability at high neutron energies [191].

Understanding where these extrinsic defects reside and the release characteristics of the products is important, especially for He, as any He released into a fuel pin will increase the internal rod pressure and will need to be accounted for during fuel design and by predictive fuel performance codes.

5.5.1 Accommodation of He and Li

The incorporation energies of He and Li were calculated at a variety of pre-existing sites to understand whether there was a preference for each of the species to occupy a specific site. Incorporation energies assume incorporation from infinity as isolated atoms. The results are shown in Table 5.4.

The incorporation of Li as an interstitial is most favourable at the $(0,0,\frac{1}{2})$ site (as with the intrinsic B_i defect), whereas He atoms preferentially occupy $(\frac{1}{3},\frac{2}{3},0)$ with $(0,0,\frac{1}{2})$ being the least favourable site. In all cases the highly reactive Li atom is $\sim$5 eV more stable in

Table 5.4: He and Li incorporation energies in ZrB_2.

Defect	Notation	Li Incorporation Energy (eV)	He Incorporation Energy (eV)
Defect on B vacancy	X_B	-1.871	4.039
Defect on Zr vacancy	X_{Zr}	-4.145	0.882
Defect on existing trivcancy	X_{ZrB_2}	-4.223	0.725
(0,0,$\frac{1}{2}$) interstitial	$X_{i(0,0,\frac{1}{2})}$	3.707	6.060
($\frac{1}{2}$,0,0) interstitial	$X_{i(\frac{1}{2},0,0)}$	4.487	5.927
($\frac{1}{3}$,$\frac{2}{3}$,0) interstitial	$X_{i(\frac{1}{3},\frac{2}{3},0)}$	4.377	5.418
($\frac{1}{2}$,0,$\frac{1}{2}$) interstitial	$X_{i(\frac{1}{2},0,\frac{1}{2})}$	7.112	8.848

a vacancy or vacancy cluster site than the inert He atom. This results in Li preferentially occupying a boron site (i.e. Li_B) when in direct competition with a He ion, as is likely during a B_5^{10} transmutation event. The nuclear reaction and other ballistic events will cause lattice damage and more potential trap sites for the transmutation products. However, the high formation energies of intrinsic defects mean that there is a strong driving force for any damage to anneal and remove the potential trap sites. Therefore, despite the high trapping energy for Li at a Zr site, the low concentration of Zr vacancies (when the material is stoichiometric) will result in the Li mostly being occupied at V_B sites. This is partly demonstrated by the reaction:

$$Zr_i + Li_{Zr} + B_B \rightarrow Zr_{Zr} + Li_B + B_i \tag{5.11}$$

for which the energy is 13.5 eV indicating a strong preference for Li_B defects.

When excess boron is present, there will be an increase in concentration of V_{Zr} defects that may trap more Li. However, as the boron is transmutated away, a more stoichiometric material will begin to form, reducing the concentration of V_{Zr}.

To consider complete equilibrium, one needs to understand the state of the He and Li when not in the ZrB_2 lattice. In doing so, one can convert the simple incorporation energies in table 5.4 into solution enthalpies. Converting He incorporation energies into

solution enthalpies is simple as He is an inert gas with little or no bonding to other He atoms leaving the incorporation energies practically identical to the solution enthalpies. He will therefore have positive solution enthalpies in ZrB_2 (i.e. He is insoluble in ZrB_2 under equilibrium conditions) and, if diffusion processes allow, it will therefore be released into the rod free volume adding to the He inventory (used as a filler gas within PWR fuel). For Li, the situation is much more complex as Li can form a number of different compounds out of the ZrB_2 crystal including oxides. It would be reasonable to consider a Li-U-O type oxide through a reaction with the UO_2 fuel. Such reactions have associated enthalpies that are much less (and sometimes negative, for example Li insertion into U_3O_8 [192]) than the energy to remove Li from the ZrB_2 lattice (i.e. the reverse of the incorporation energy, 1.87 eV) and as a consequence there is no thermodynamic driving force for Li to be removed. The rate of release of He and Li from ZrB_2 will depend on the magnitude of the migration activation energy (when considering thermal diffusion processes), that is the kinetics.

5.5.2 Transport of He and Li Through ZrB_2

A number of migration processes have been studied that will permit transport of Li or He species through the ZrB_2 lattice. The key reactions and energies are reported in Table 5.5.

Table 5.5: He and Li diffusion Mechanism energies in ZrB_2 where X is either Li or He

Reaction	Li Reaction Energy (eV)	He Reaction Energy (eV)
$X_{Zr} \rightarrow X_i$	8.522	4.536
$X_B \rightarrow X_i$	6.248	1.379
$X_{Zr} \rightarrow X_B$	2.274	3.157
$X_{i(0,0,\frac{1}{2})} \rightarrow X_{i(\frac{1}{2},0,0)}$	0.780	-0.133
$X_{i(\frac{1}{3},\frac{2}{3},0)} \rightarrow X_{i(\frac{1}{2},0,0)}$	0.110	0.509

There is a very low energy difference between the two lowest energy Li interstitial sites; 0.11 eV. This suggests that there is a potential low energy migration pathway for Li diffusion in the zirconium layer. However, the energy to remove a Li from a vacancy B site is

a considerable 6.25 eV meaning that once trapped at a vacancy (produced during a transmutation event) the interstitial migration of Li will only be of importance during radiation assisted annealing. Alternative diffusion mechanisms involving V_B may occur, however, as the concentration of boron vacancies is very low their contribution to Li transport will not be significant. Consequently, Li transport in a near pristine lattice will be limited, however, radiation induced Li diffusion may occur.

A potential low-energy diffusion path has been identified for He in Table 5.4 (0.51 eV) is between the two basal plane interstitial sites. This diffusion process will provide a continuous diffusion pathway in that the migrating species will move into a symmetrically identical site at the end of the migration process with relation to its original position. These energy differences do not take into account the total barrier to diffusion, just the difference between the two sites and as such the activation energies need to be calculated to understand He thermal diffusion fully.

Quantum mechanical molecular dynamical calculations were carried out to try and establish the migration of He within the lattice and investigate if the barrier to migration was surmountable at a typical in-pile temperature of the ZrB_2 layer on the periphery of a fuel pellet, i.e. 700 K. Even over the very short time periods possible to investigate using QMD (1 ps), diffusion of He from the ($\frac{1}{3}$,$\frac{2}{3}$,0) site through the ($\frac{1}{2}$,0,0) site to an adjacent ($\frac{1}{3}$,$\frac{2}{3}$,0) site was observed, with He travelling in the <100> direction. Three images of the diffusion path are shown in Figure 5.5.

Nudged elastic band (NEB) calculations were then carried out on this migtation pathway and the activation energy was found to be nearly equal to the energy difference of the He interstitial between the two sites (0.51 eV). A plot of how the energy varies with image number for the diffusion of He in ZrB_2 can be found in Figure 5.6. The results shows that the ($\frac{1}{2}$,0,0) site is practically the saddle point for a migrating He atom rather than a true local minimum. This low activation energy combined with the high temperatures experienced by ZrB_2 as a pellet coating would be commensurate with the rapid transport of He out of the ZrB_2 crystal lattice.

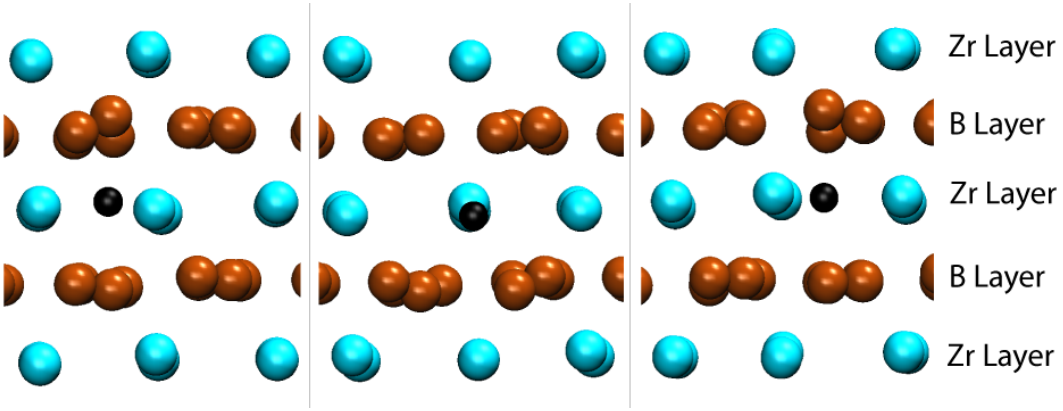


Figure 5.5: Structure of ZrB_2 showing the zirconium atoms as light blue and the boron atoms as dark yellow. The five interstitial sites are shown as red crosses.

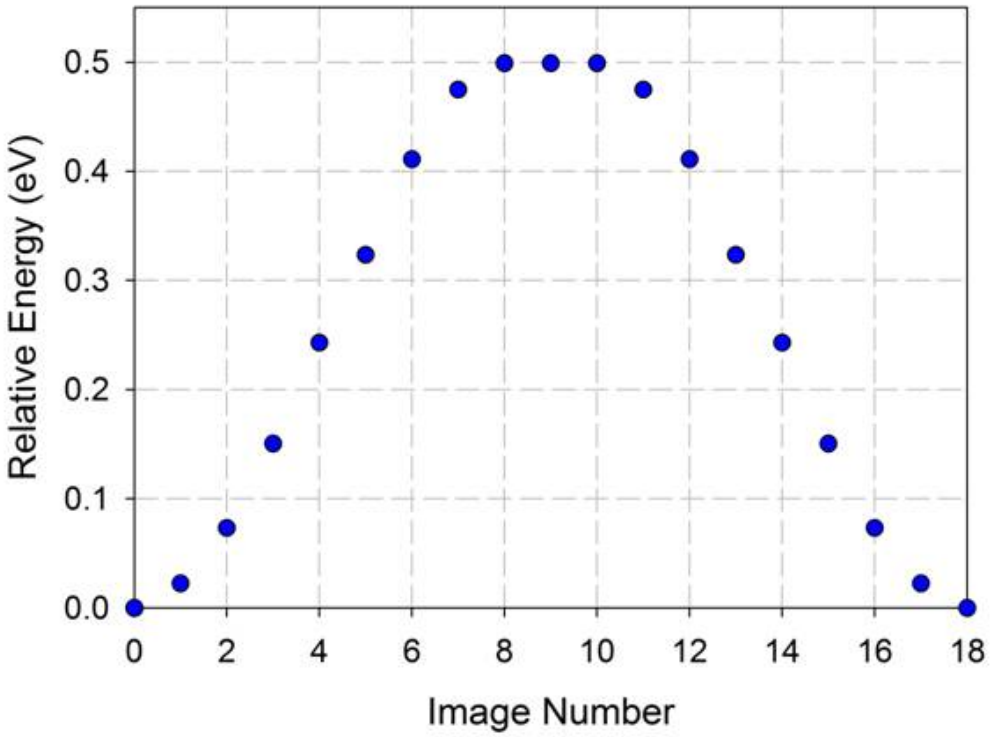


Figure 5.6: Nudged elastic band calculation of the He migration from a $X_{i(\frac{1}{3},\frac{2}{3},0)}$ site to a $X_{i(\frac{1}{2},0,0)}$ site showing the activation energy for He migration to be 0.51 eV.

5.6 Summary

The defect energy calculations indicate that the intrinsic processes in ZrB_2 are high energy and as such intrinsic defect concentrations will be very much lower than the concentration of He and Li species formed through the transmutation of B under neutron irradiation. Calculations also suggest that non-stoichiometry involving Zr excess will be very small but B excess can be accommodated to some degree and the Zr vacancies produced may contribute to the accommodation of Li or He species until the B excess is exhausted through transmutation reactions. The most important site for the accommodation of He or Li will be the vacant boron site formed as a consequence of transmutation in stoichiometric ZrB_2. The lack of appreciable Zr excess non-stoichiometry possible means that ZrB_2 must be processed with special attention to the Zr:B molar ratio to avoid secondary phase formation. It is important to note that as the transmutation of B in ZrB_2 proceeds under neutron irradiation, an overall excess of Zr will manifest and secondary phase formation will occur if equilibrium conditions are attained.

Incorporation energies suggest that Li is much more stable at V_B sites than He and as such will preferentially occupy these sites. Furthermore, once a Li atom occupies a B interstitial site (or a Zr site), there is a large energy penalty to move it to an interstitial site necessary to transport it through the ZrB_2 lattice. Transport would have to occur via a V_B mediated process, although the excess V_B concentration is very small. Furthermore, the driving force for the Li to form compounds external to the ZrB_2 lattice is low. It therefore seems that the Li will be retained in the ZrB_2 lattice.

All He incorporation energies within ZrB_2 are unfavourable and high, so providing the driving force for He to be removed from the lattice. He will preferentially occupy a Zr vacancy, but as these are of such low concentration, He will occupy an interstitial site as direct competition over the B vacancies with Li will result in Li occupying the sites (see Figure 5.7). The lowest energy interstitial site is ($\frac{1}{3}$,$\frac{2}{3}$,0) and a low-energy continuous diffusion pathway was found between ($\frac{1}{3}$,$\frac{2}{3}$,0) sites through a ($\frac{1}{2}$,0,0), which essentially acts as the saddle point. The activation energy is 0.51 eV, indicating that He will be mobile at

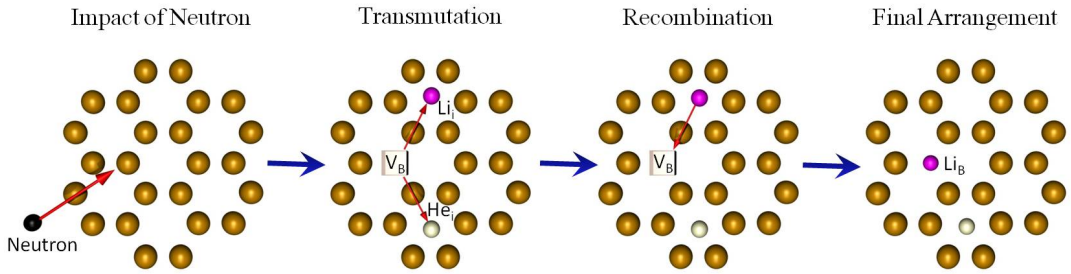


Figure 5.7: Process showing the transmutation of a boron atom by a neutron into a lithium and helium atom leaving a vacancy. Lithium will occupy the vacant B site preferentially over He.

typical fuel surface temperatures.

Chapter 6

Defects and Transport Processes in Beryllium

"Disobedience, the rarest and most courageous of the virtues, is seldom distinguished from neglect, the laziest and commonest of the vices."
- George Bernard Shaw [193].

6.1 Introduction

Beryllium has a number of extremely interesting and useful material properties, already outlined in section 1.3. These have led to its use as a neutron multiplier, neutron reflector and an ionising radiation window material. The light group II metal is relatively scarce in the earth's crust and is normally isolated from a mineral such as beryl ($Be_3Al_2(SiO_3)_5$), bertrandite ($Be_4Si_2O_7(OH)_2$) or chrysoberyl ($BeAl_2O_4$). This atomic scale study of the material will attempt to demonstrate why beryllium may prove important and effective as a material from which to construct components for use in high neutron flux environments. The common alloying elements and impurities found in Be metal alloys are also investigated.

6.2 Structure of Beryllium and the Intermetallics $FeBe_5$, $FeAlBe_4$, Be_2C and $MgBe_{13}$

Before presenting the results in this chapter, the crystal structures of beryllium and the intermetallics studied are introduced. For each crystal structure, the calculation details are outlined. Special care is taken in understanding the HCP crystal structure, appreciating that there are a number of equivalent interstitial sites in, what at first glance, seems a simple system.

6.2.1 Beryllium

Be metal has a hexagonal closed packed crystal structure and exhibits space group $P6_3/mmc$, with a lattice constant of $a = 2.29\,\text{Å}$ and c/a ratio of 1.57 [194].

The Be atoms in the perfect lattice reside at the $(\frac{1}{3}, \frac{2}{3}, \frac{3}{4})$ sites. There are five interstitial sites, two within the basal plane and three in non-basal plane positions [195]. Within the basal plane the trigonal interstitial (Tr) site is at $(0,0,\frac{1}{4})$ and the hexahederal site (Hx) is at $(\frac{1}{3},\frac{1}{3},\frac{1}{4})$. The non-basal octahederal site (Oc) is at $(0,0,\frac{1}{2})$ and the tetrahederal (Te) site is at $(\frac{1}{3}, \frac{2}{3}, \frac{5}{8})$. There is also a non-basal trigonal interstitial site (NBt) on each face of the tetrahedra. The beryllium structure and the five interstitial sites are illustrated in Figure 6.1.

Beryllium is a metallic system and can be modelled appropriately using *ab-initio*-like methods such as density functional theory (DFT). There have been a number of previous studies of Be that have used DFT, employing various exchange-correlation functionals [196, 197]. For example, Allouche *et al.* [196] used the generalized gradient approximation (GGA), which closely reproduced the Be crystal structure. Further, de Bas *et al.* have shown that the GGA-PBE functionals accurately reproduce the bandwidth of Be, experimentally found to be $11.1\pm0.3\,\text{eV}$ and predicted to be $11.13\,\text{eV}$. A number of studies concerning the behaviour of hydrogen in Be have been carried out [196, 194] and, for example, the

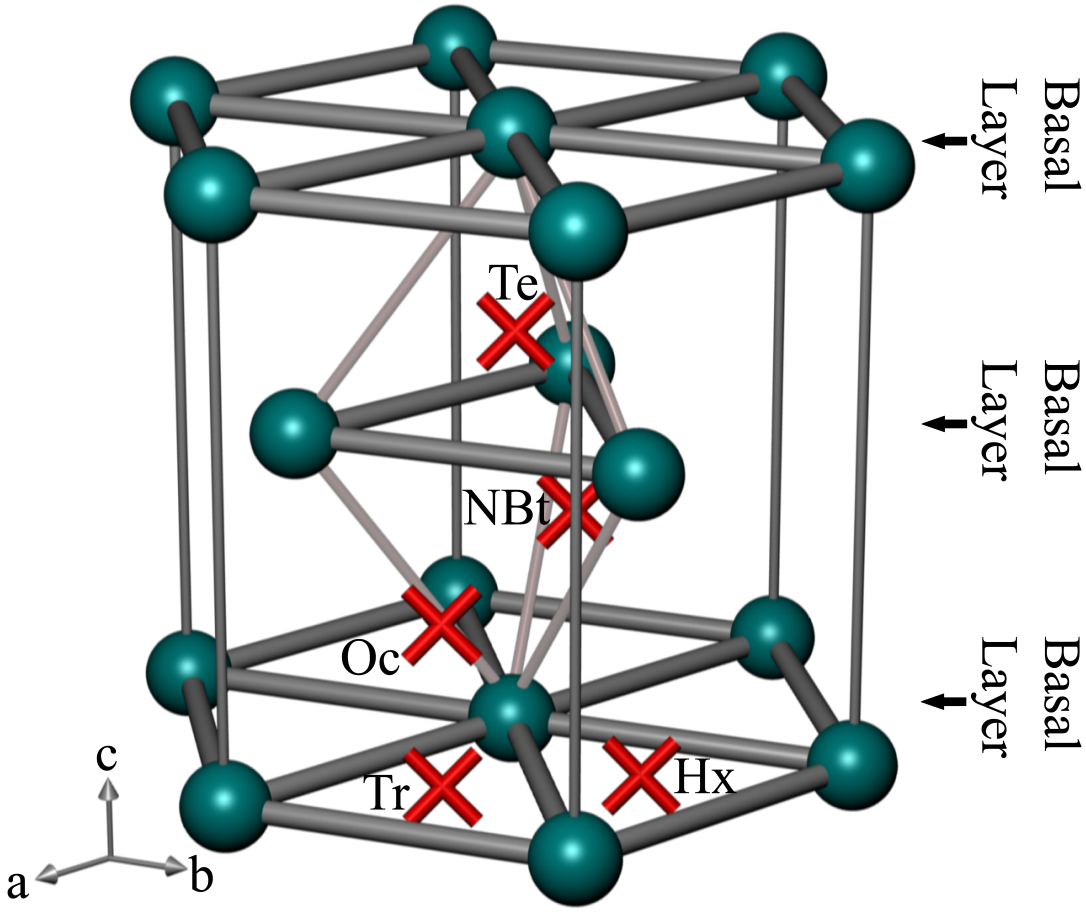


Figure 6.1: The hexagonal closed packed (HCP) structure of beryllium showing three basal layers and the octahedral interstitial (Oc), tetrahedral interstitial (Te), hexahedral interstitial (Hx), trigonal interstitial (Tr) and Non-basal trigonal interstitial positions.

barrier for migration of hydrogen as an interstitial has been calculated by previous DFT calculations to be 0.41 eV [196].

In this work, ion-electron interactions have been described using the projector-augmented wave (PAW) method [198] and the GGA-PBE exchange-correlation functional [148] with a cut-off energy of 400 eV for the Be in this work. The cut-off energy was converged to 0.001 eV. Figure 6.2 illustrates the cut-off convergence.

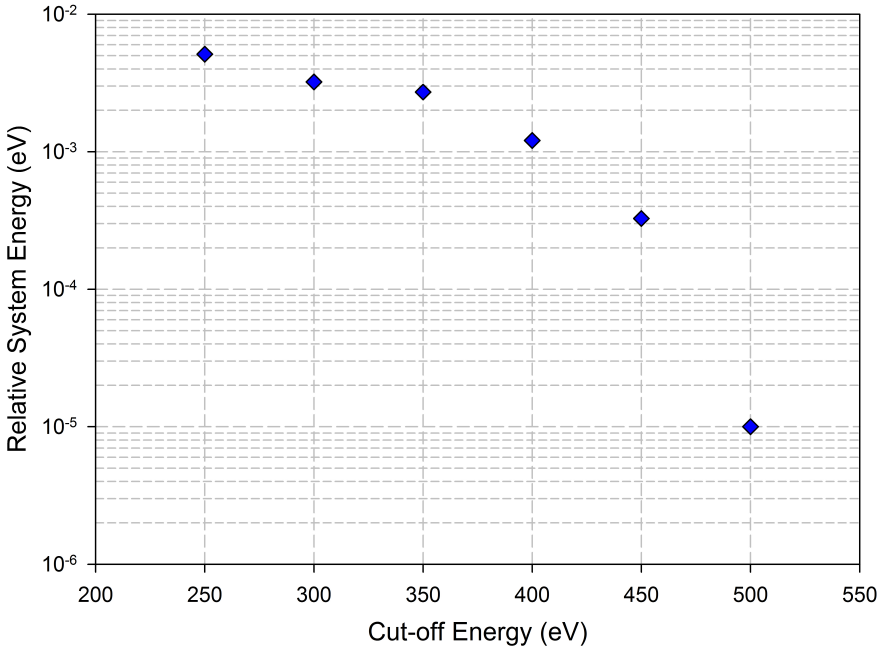


Figure 6.2: Illustration of convergence of cut-off energy with the Be system showing that 400 eV gives good accuracy of above 0.001 eV.

Be was modelled using a γ-centred sampling of the Brillouin zone (ideal for a hexagonal system [199]) with a 6×6×6 k-point grid. A 5×5×4 supercell (made from the primitive cell) containing 200 lattice sites was used for the defect calculations, whilst a smaller 4×4×3 supercell, containing 96 atom sites, was used for some defect migration calculations due to computational limitations but also to demonstrate the degree of convergence of the larger cell in defect energy.

6.2.2 Fe-Al-Be Intermetallics

The intermetallic $FeBe_5$ has been studied in detail in this chapter. It has a very interesting structure based on the $Fd\bar{3}m$ space group: Be atoms reside on a face-centred cubic sublattice sites (0,0,0) with Fe half occupying the tetrahederal sites $(\frac{1}{4},\frac{1}{4},\frac{1}{4})$. The Be atoms occupy the $(\frac{5}{8},\frac{5}{8},\frac{5}{8})$ sites, thereby forming four Be tetrahedra accounting for the remaining tetrahederal sites. The structure is shown in Figure 6.3 with the main interstitial sites: $(\frac{1}{2},\frac{1}{2},\frac{1}{2})$ and $(\frac{1}{4},\frac{1}{2},\frac{1}{2})$.

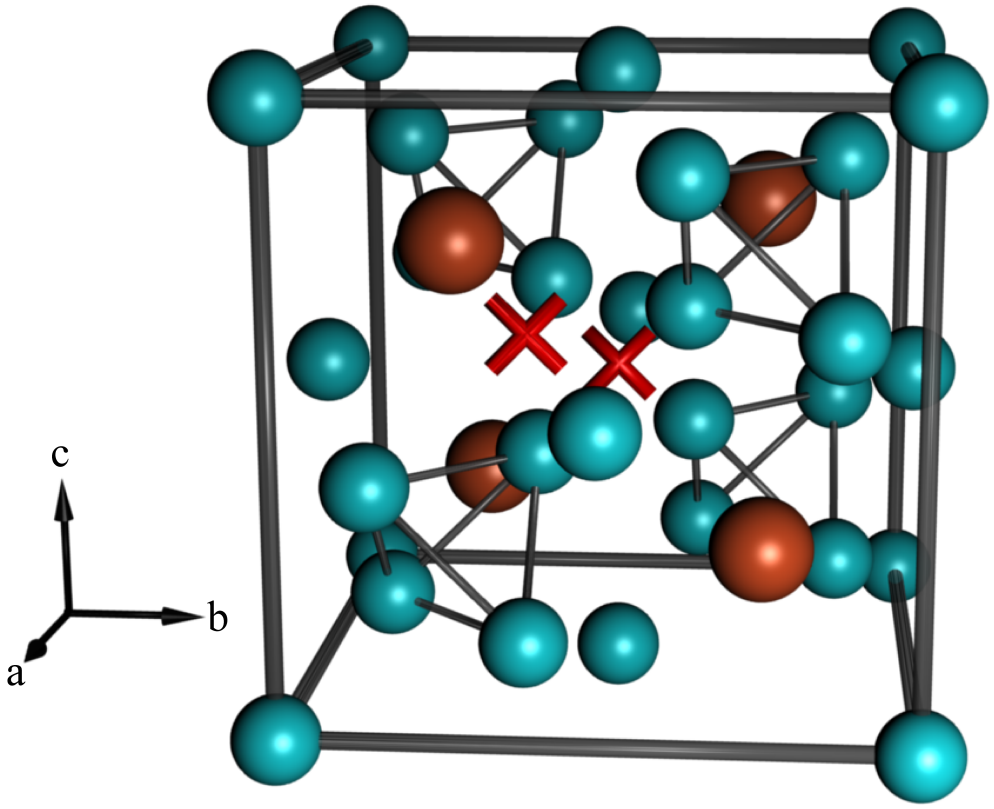


Figure 6.3: The cubic $FeBe_5$ intermetallic crystal structure. Showing the Be atoms on the (0,0,0) and $(\frac{5}{8},\frac{5}{8},\frac{5}{8})$ sites (blue) and the Fe atoms half occupying the $(\frac{1}{4},\frac{1}{4},\frac{1}{4})$ sites.

Aluminium is known to be insoluble in beryllium and no known intermetallic has been reported in the Al-Be binary system. Al does however form an intermetallic in the Fe-Al-Be ternary system, the possible structure of which has been determined more explicitly in this work. Two different structures have been considered in the past: the $(Al,Fe)Be_5$ intermetallic, with the same structure as Figure 6.3 and the $FeAlBe_4$ intermetallic which

is similar structure, however the FCC sites are occupied by Al atoms instead of Be. This structure is shown in Figure 6.4 with the main interstitial sites $(\frac{1}{2},\frac{1}{2},\frac{1}{2})$, $(\frac{1}{2},\frac{1}{2},\frac{1}{4})$ and $(\frac{1}{4},\frac{1}{2},\frac{1}{2})$ (one more than the $FeBe_5$ intermetallic).

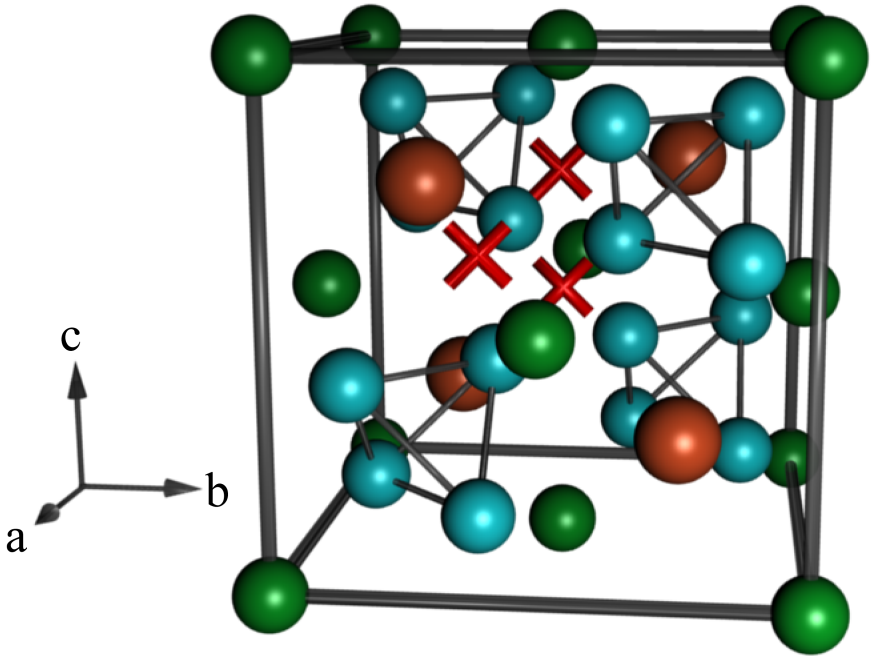


Figure 6.4: The cubic $FeAlBe_4$ intermetallic crystal structure. Showing the Al atoms on the (0,0,0) site (green), Be atoms at the $(\frac{5}{8},\frac{5}{8},\frac{5}{8})$ sites (blue) and the Fe atoms half occupying the $(\frac{1}{4},\frac{1}{4},\frac{1}{4})$ sites.

Both $FeBe_5$ and $FeAlBe_4$ were modelled using the GGA-PBE exchange-correlation functional as used for pure Be. The same cut-off energies and k-point densities were used and were shown to give an excellent reproduction of the lattice constants reported by previous work (shown in Table 6.1).

Table 6.1: Comparison of calculated lattice constants with data from experimental studies.

System	Calculated Lattice Constant (Å)	Experimental Lattice Constant (Å)
$FeBe_5$	5.83	5.875 [200]
$FeAlBe_4$	6.00	6.06 [201]

6.2.3 Be_2C

Beryllium carbide is an ultra-hard, ultra-high temperature ceramic used throughout the aerospace industry for high-end applications. It is also produced as a secondary phase when Be is alloyed with carbon. Be_2C has the fluorite $Fm\bar{3}m$ structure with the C atoms residing at the (0,0,0) FCC sites and the Be atoms at the $(\frac{1}{4},\frac{1}{4},\frac{1}{4})$ sites. The Be_2C structure is illustrated in Figure 6.5.

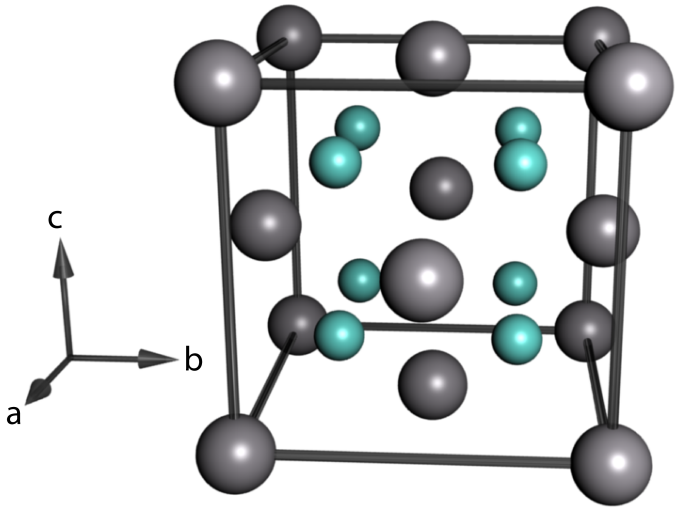


Figure 6.5: The fluorite crystal structure of Be_2C. Be atoms are shown to occupy the $(\frac{1}{4},\frac{1}{4},\frac{1}{4})$ sites (blue) and the C atoms the FCC (0,0,0) sites (grey).

6.2.4 $Be_{13}Mg$

The $Be_{13}Mg$ intermetallic is brittle and acts as a superconductor at low temperatures [202]. It exhibits a structure with the $Fm\bar{3}c$ space group where the Mg atoms sit at the $(\frac{1}{4},\frac{1}{4},\frac{1}{4})$ sites and the Be atoms sit at the (0,0,0) and $(0,\frac{57}{500},\frac{9}{50})$ sites [202]. The unit cell (used for calculations in this work) has a cubic lattice parameter of 10.165 Å and contains 8 Mg atoms and 104 Be atoms.

6.3 Intrinsic Defect Processes of Beryllium

This section begins by presenting the various defects that can form in beryllium and highlights the most stable defects. This is followed by a discussion of how the dominant defects are transported through the bulk. By understanding the stable defects and their transport processes a number of significant predictions can be made.

6.3.1 Defect Formation Energies

The energy to form an intrinsic defect is that required to remove an atom to infinity or introduce an atom native to the host lattice from infinity (forming a Be vacancy or interstitial defect respectively). The defect energy is determined by calculating the energy of the perfect supercell containing 200 Be atoms ($E_{\text{defective cell}}$) multiplied by the ratio of the numbers between the defective cell ($N_{\text{defective cell}}$) and the perfect cell ($N_{\text{perfect cell}}$) and removing the energy from the defective supercell energy ($E_{\text{defective cell}}$).

$$E_{\text{defect}} = E_{\text{defective cell}} - \left(\frac{N_{\text{defective cell}}}{N_{\text{perfect cell}}} \times E_{\text{perfect cell}} \right) \tag{6.1}$$

Defect energies are reported in Table 6.2, along with values (in brackets) calculated using the smaller 96 atom cell. The differences in energies determined using the 5×5×4 and 4×4×3 cell sizes are small indicating that defect energies have converged sufficiently with respect to cell size to offer useful thermodynamic low concentration limiting values.

The Schottky disorder reaction (equation 6.2) is the energy to form a Be vacancy plus the lattice energy of Be.

$$Be_{Be} \rightarrow V_{Be} + Be\,(\text{lattice energy}) \tag{6.2}$$

The Schottky energy is reported in Table 6.2.

Interstitial defects can be produced as a result of anti-Schottky reactions.These reactions involve an interstitial defect being created from the perfect lattice as described by the

following equation:

$$\mathrm{Be\,(lattice\ energy)} \rightarrow \mathrm{Be_i} \tag{6.3}$$

The energies of various anti-Schottky reactions are also reported in Table 6.2, the lowest energy begin associated with the formation of an interstitial atom occupying a basal trigonal site (Tr).

Table 6.2: Intrinsic Be defect formation energies calculated using a 5×5×4 supercell (values calculated using a 4×4×3 supercell are reported in brackets).

Defect	Notation	Type	Defect Energy (eV)	
Vacancy (Schottky)	V_{Be}	-	1.09	(1.26)
Interstitial (Anti-Schottky)	Be_i	Oc	5.06	(5.24)
	Be_i	Te	5.14	(5.26)
	Be_i	NBt	4.77	(4.91)
	Be_i	Hx	5.67	(6.00)
	Be_i	Tr	4.01	(4.27)
Frenkel Reaction	$\{Be_i{:}V_{Be}\}$	Bound	5.08	(5.15)
	$Be_i + V_{Be}$	Separated to ∞	5.10	(5.54)

By comparing Schottky and anti-Schottky energies, it is clear that the Schottky reaction is dominant. Consequently, using the law of mass action [190] the intrinsic vacancy concentration in Be will be given by;

$$[V_{Be}] = e^{\frac{-1.09}{kT}} \tag{6.4}$$

where $[V_{Be}]$ is the Be vacancy concentration, k is Boltzmann's constant and T is the temperature (in K). The concentration of vacancies at 1000 K, resulting from Schottky disorder, is 3.21×10^{-6}. Applying the law of mass action to equation 6.3 to calculate the Be interstitial concentration $[Be_i]$ due to anti-Schottky reactions yields:

$$[Be_i] = e^{\frac{-4.01}{kT}} \tag{6.5}$$

At 1000 K the concentration of interstitial defects will be 6.21×10^{-21}, much smaller than the concentration of vacant Be sites. Thus, it is clear that the concentration of intrinsic

defects in Be is small but completely dominated by vacancies, as might be expected in a close packed atomically dense material. Intrinsic migration processes could therefore be expected to be dominated by a vacancy mechanism (in the absence of interstitials formed through, for example, radiation damage).

Finally, combining the Schottky and anti-Schottky reaction results in the Frenkel disorder reaction (equation 6.6). However, in addition to treating the two defects as separated to infinity they may form a bound defect pair (i.e. the cluster $\{V_{Be}{:}Be_i\}$) at a third nearest neighbour site (calculations suggest that third neighbour is necessary to prevent spontaneous recombination). The results of the calculations are reported in Table 6.2.

$$Be_{Be} \rightarrow V_{Be} + Be_i \tag{6.6}$$

The binding energy of the vacancy to the interstitial is simply the difference in energy between a bound defect cluster and the individual defects. This energy, at the third nearest neighbour, is 0.03 eV, an exceptionally low energy, which suggests that Frenkel pairs hardly interact in this configuration (although this study does not discount possible stronger interactions in configurations beyond third neighbour due to alignment).

6.3.2 Migration Activation Energies of Intrinsic Defects

Be Vacancy Migration

The migration of intrinsic defects will now be discussed. Migration processes can be split into two categories: (i) transport within the basal plane between nearest neighbour sites and (ii) a non-basal plane pathway between nearest neighbour sites. The energy variation along the migration trajectory in the basal plane for the movement of a vacancy, shown in Figure 6.6, reveals an energy barrier (E_m) of 0.72 eV with a saddle point corresponding with the Tr interstitial site (calculated using NEB, see section 2.4). E_m for non-basal vacancy migration is 0.89 eV; this is only 0.17 eV higher, which implies that the transport of Be vacancies will only be modestly anisotropic at elevated temperatures.

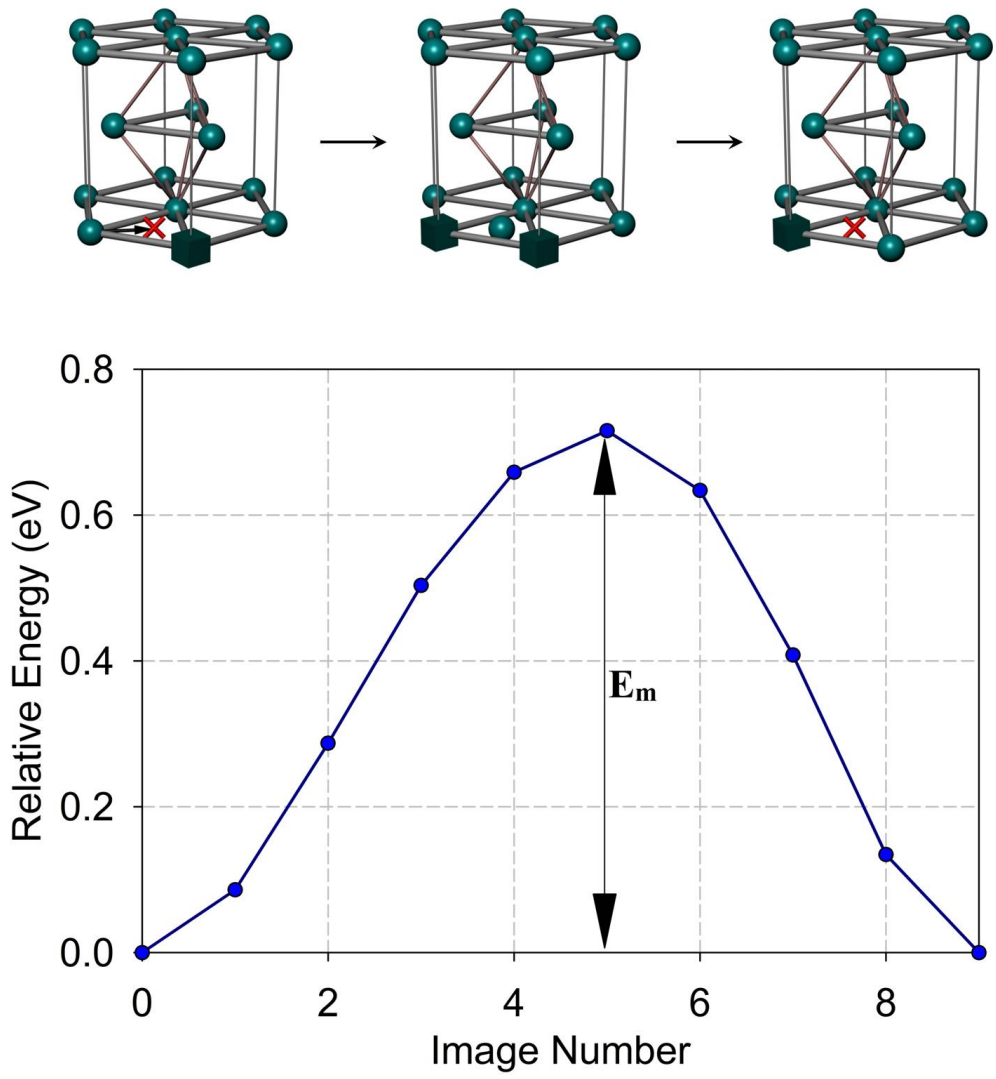


Figure 6.6: Energy profile for the migration of a Be atom via vacancy mechanism through the basal plane between equivalent lattice sites, with configurations shown above.

Be Interstitial Migration

Now considering the Be interstitial migration, three possible migration processes have been examined all involving the lowest interstitial defect energy site, the Tr site, since it is considerably lower in energy compared to the other interstitial sites and transport would therefore be expected to involve this site.In addition, as Tr sites are not contiguous, the migration pathway must pass through another interstitial site.

A simple migration pathway has been identified between trigonal sites (Tr) through the octahederal (Oc) site resulting in migration along the *c*-axis. The activation energy for this process was calculated to be 0.99 eV. Another simple migration mechanism may occur through the basal plane from a Tr site through a Hx site (the saddle point) to an adjacent Tr site. The activation energy for this process is 1.72 eV, considerably higher and therefore unlikely to be important. A third migration pathway was identified, in which the Tr Be interstitial atom moves through an NBt site (on another side of the tetrahedron that makes up the Be crystal) to another Tr site, whether on the original basal plane or an adjacent basal plane. This process has an energy of 0.64 eV (shown in Figure 6.7) and is therefore the lowest energy identified interstitial migration mechanism. As such, Be interstitial migration can be said to be isotropic. Because the migration energies for vacancies and interstitials are of the same magnitude, transport processes in Be will be dominated by vacancies due to the higher concentration.

6.4 Extrinsic Defect Processes in Beryllium

Some common alloying elements and impurities associated with beryllium and beryllium alloys are now discussed. The stable sites for each extrinsic species is first calculated followed by understanding the solubility limit of each of the species. Transport of the soluble species is then considered.

To conclude, the intermetallics in the Fe-Al-Be system are discussed in greater detail due to their importance in beryllium containing alloys.

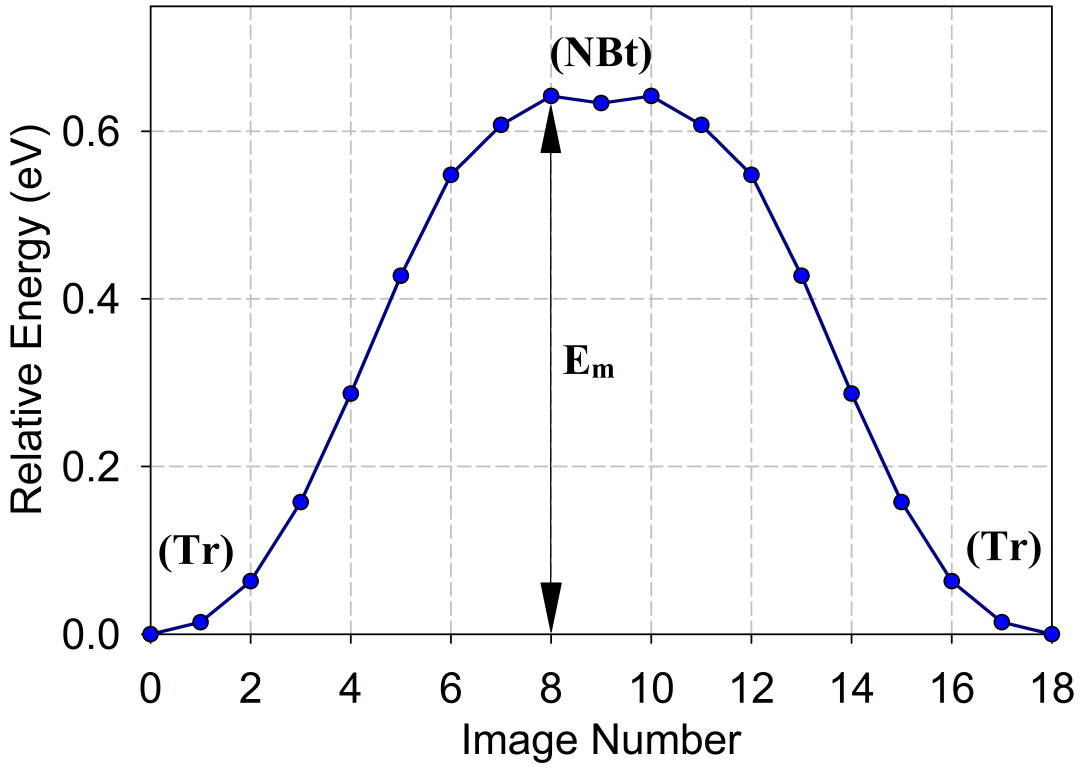


Figure 6.7: Energy profile for the migration of a Be interstitial atom between Tr sites through a NBt site.

6.4.1 Accommodation and solution of defect species in the Be lattice

There has been previous work on the behaviour of H and O in Be [194, 196, 203]. The present study extends this by investigating additional extrinsic defects and their migration processes, namely: hydrogen, helium, oxygen, magnesium, aluminium , iron, carbon and silicon.

The first challenge is to identify the lowest energy site each dopant could occupy. To achieve this, a neutral atom of each element is taken from infinity (i.e. the reference state of the dopant) and placed in the 200 atom supercell, in turn at each of the interstitial sites and then atom positions are relaxed to zero strain. The interstitial dopant (accommodation energy) calculation proceeds as the energy of the supercell with the dopant incorporated, minus the sum of the perfect supercell plus the energy of an isolated dopant atom. In the case of the vacancy, the energy to form the vacancy (the solution site) must also be taken into consideration. Thus, the accommodation energy is the energy of the supercell with the substitutional defect minus the sum of the energy of $(\frac{199}{200}) \times$ energy of the supercell plus the energy of the isolated dopant atom. The accommodation energies reported in Table 6.3 allow the deduction of the relative site stability of the extrinsic defects (though not their equilibrium solution energies). Accommodation energies can also give information on the bonding environment of dopant species in the host lattice.

Table 6.3: Accommodation energies of He, H, O, C, Fe, Al, Mg and Si in Be (eV).

Impurity occupying	He	H	O	C	Fe	Al	Mg	Si
Be vacancy	3.46	0.12	-2.17	-4.03	-5.46	-2.17	0.87	-2.87
Tr interstitial	5.68	-0.06	-2.35	-3.24	-0.81	4.61	7.730	12.04
Hx interstitial	5.47	-0.87	-5.06	-3.62	-0.23	4.29	6.31	3.19
Oc interstitial	6.02	-0.68	-3.69	-4.22	-0.32	5.01	7.71	3.34
Te interstitial	*	*	*	*	-0.95	4.10	6.32	2.60
NBt interstitial	*	*	*	1.63	*	4.09	11.22	*

* Indicates spontaneous relaxation (i.e. no barrier) of the defect to a different interstitial site site.

In order to obtain solution energies from accommodation energies, it is necessary to account

for the reference state of the dopant species. For H and O this will be a gas molecule (H_2 and O_2 respectively), or a solid in the case of C, Fe, Al, Mg or Si. In the case of He, the reference state remains the isolated He atom and thus the accommodation energy is equal to the solution energy. For O and H, the difference is half the respective molecular formation energies. For Al and Si the difference is the Al metal and Si solid atomic dissociation energies (lattice energies) because Be forms simple binary eutectics with Al and Si; there are no intermetallic or intermediate phases [204, 205, 206]. Conversely, C, Mg and Fe do form intermetallics, Be_2C, $Be_{13}Mg$ and $FeBe_5$ respectively [207, 203] and as such these offer suitable end members for the solution models (i.e. the lattice energies of these intermetallics will be used).

A small approximation that is unavoidable is that the solution of interstitial species, being 1 defect atom per 200 Be atoms, is comparable to solution via substitution when the concentration is 1 defect atom per 199 Be atoms.

Table 6.4: Solution energies of He, H from H_2, O from O_2, Fe from $FeBe_5$, Al from Al metal, C from Be_2C, Mg from $Be_{13}Mg$ and Si from Si solid into Be (eV).

Impurity occupying	He	H	O	C	Fe	Al	Mg	Si
Be site	3.46	2.39	-1.14	2.98	-0.09	1.35	2.37	1.74
Tr interstitial	5.68	2.22	-1.33	3.77	4.56	8.14	9.24	16.65
Hx interstitial	5.47	1.40	-4.04	3.39	5.14	7.82	7.82	7.80
Oc interstitial	6.02	1.59	-2.66	2.78	5.05	8.54	9.21	7.95
Te interstitial	*	*	*	*	4.42	7.63	7.82	7.21
NBt interstitial	*	*	*	8.64	*	7.62	11.18	*

* Relaxation of the defect to a different interstitial site site (i.e. no barrier).

6.4.2 Gas Species Hydrogen, Oxygen and Helium

The gaseous species H and O are most stable at interstitial sites, due to strong bond formation with a number of Be atoms (indicated by the negative accommodation energies). Interestingly, O quite clearly preferentially occupies the Hx site, whereas H shows similar preference for both the Hx (lowest energy) and Oc sites. Conversely, He will occupy a Be

vacancy site (despite the energy penalty to form the vacancy compared to zero energy to form an interstitial site). The large positive accommodation energy for He reflects the lack of bond formation as expected from this inert gas atom.

Proceeding to solution energies, while account of the H_2 and O_2 molecular dissociation energies means that solution energies are higher than the corresponding accommodation energies, solution energies are still negative. This indicates that there will be take-up of O from the gas phase into Be unless the activation energies for transport of these species into the lattice (or the barrier to molecular dissociation) is prohibitively high.

Next, the transport of H is considered; this will proceed preferentially via an interstitial process due primarily to the large energy difference between solution of the H at an Hx or Oc site compared to a vacancy site. Starting at the lowest energy Hx site, there is a clear pathway to the second most favourable interstitial site, Oc, over a saddle point, and symmetrically back to an equivalent Hx site in the same basal plane or an equivalent site in an adjacent basal plane. The barrier to migration, shown in Figure 6.8 is only 0.40 eV. The diffusion of H within Be will be isotropic and fairly rapid. The results for H interstitials are in agreement with work carried out by Allouche *et al.* [196] who predicted an activation energy of 0.41 eV for H.

Now Considering the migration of O, we begin by recalling the much higher relative energy of O in the second Oc interstitial site. Thus, even before considering possible saddle points (equivalent to those in Figure 6.8) the energy will be at least 1.38 eV (the difference between the energies of O at the Hx and Oc sites) if the pathway traverses through or at least close to this site, as symmetry would suggest. Once the saddle point was identified the barrier was found to be a very significant 1.63 eV. This is a considerable energy barrier that will substantially limit the transport of O through the Be lattice and provide an effective barrier against internal oxidation.

As discussed above, He will preferentially occupy a vacant Be site but is highly insoluble. However, due to the possibility of incorporating He into Be via radiation damage processes associated with fusion reactors [110], the behaviour of He as an interstitial species is also

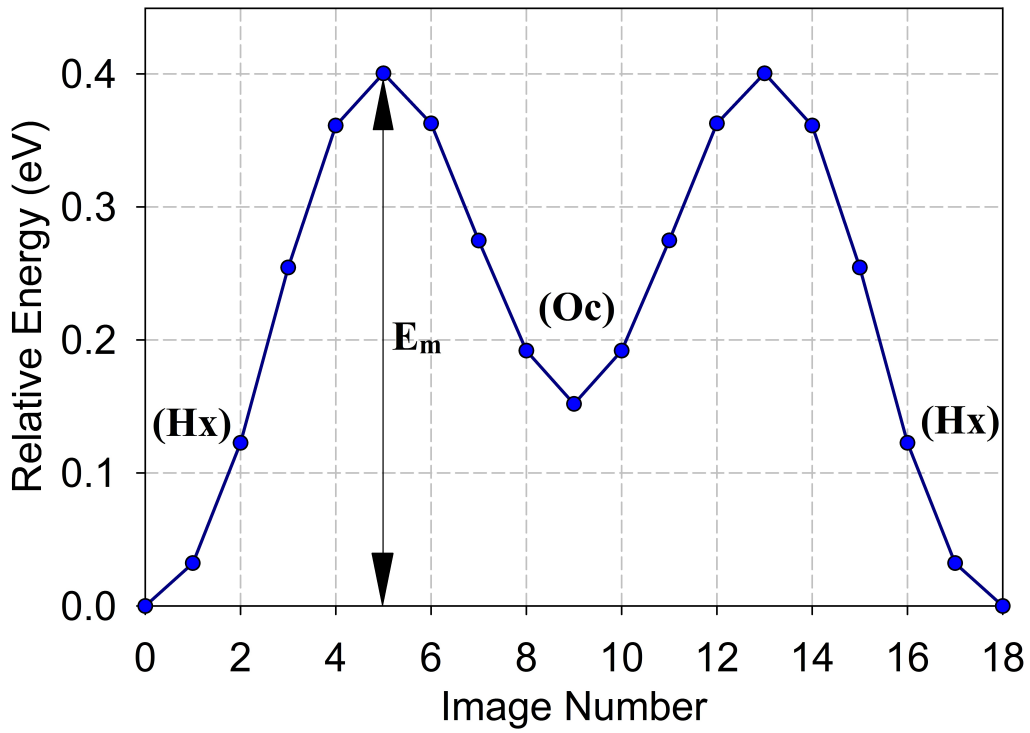


Figure 6.8: Energy profile associated with the migration of a H interstitial defect moving from a Hx site to an Oc site.

discussed. As an interstitial species He will most favourably reside at the Tr site. The Hx site is the next most stable and is also in the basal plane. A simple migration mechanism is possible, with He moving from the Tr site through a Hx site to a symmetrically identical, adjacent Tr site. The migration path is shown in Figure 6.9 and exhibits a migration activation energy, E_m, of 0.25 eV. This small barrier suggests that the diffusion of interstitial He through the Be lattice will be rapid, but this process confines the He to the basal plane. The lowest energy barrier for movement along the c-axis, from the Tr site through an Oc site, is 0.38 eV, ∼50% larger than in the basal plane). He will therefore migrate rapidly but anisotropically as an interstitial species until being released from the system or being trapped at a vacant Be site.

The trapping energy is the difference in energies of two possible sites for the defect to occupy, in the case of He, the trapping energy at a vacancy is 2.01 eV, with respect to the most favourable interstitial site. Given this substantial trapping energy, once trapped a

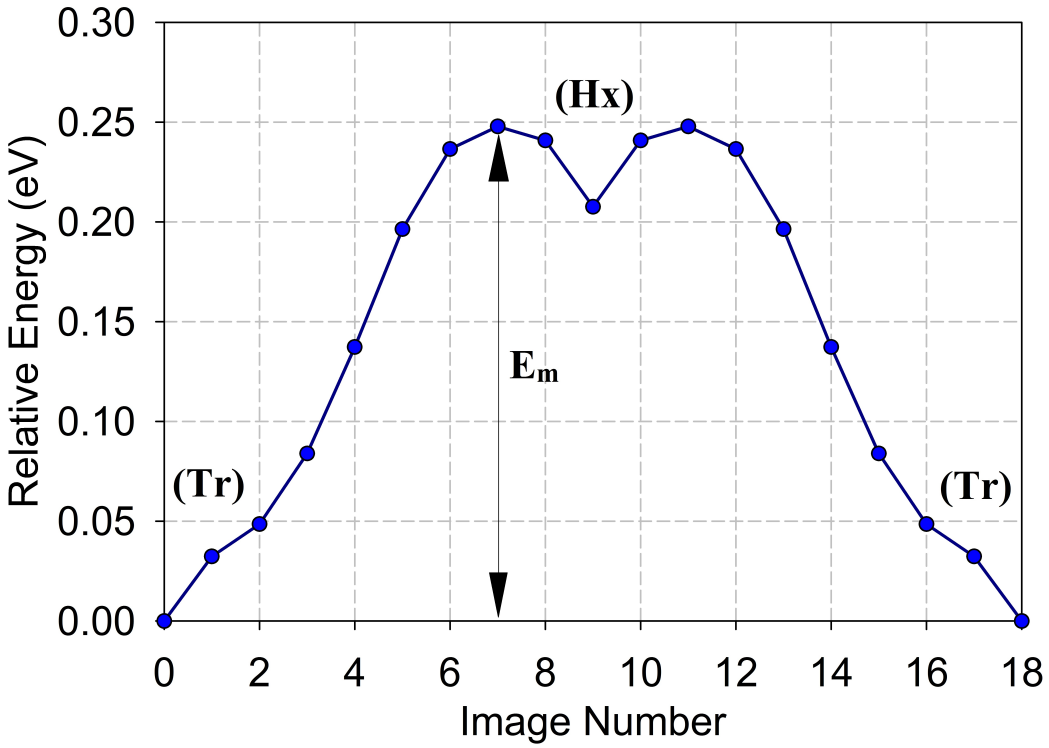


Figure 6.9: Energy profile associated with the migration of the He interstitial defect moving from a Tr site to a Hx site.

He atom would subsequently be transported via a Be vacancy mechanism, so long as the vacancy activation energy is less than the trapping energy.

Transport of He via a vacancy will be facilitated by the association of a second Be vacancy. To identify the rate determining step the following migration barriers are to be considered: (i) of a second vacancy through the Be lattice, (ii) of the second vacancy to the He_{Be} defect to form a $\{V_{Be}{:}He_{Be}\}$ cluster, (iii) re-orientation of the cluster and (iv) ejection of the vacancy that the He atom initially occupied so the He is left occupying a different Be site (i.e. it has moved lattice site). The first step (i) has been established earlier in section 6.3; Be vacancy transport in the basal plane has an activation energy of 0.72 eV. The next step (ii), involves the movement of a Be vacancy from a second nearest neighbour site to a first neighbour (adjacent to the He_{Be} defect) site. The activation energy for this process, E_{m1}, is 0.29 eV and is illustrated in Figure 6.10. Since this is lower than the activation energy for a free vacancy migration, it is not rate determining. Step (iii), reorientation of

the cluster must occur in cases where the migrating species (here He) has to move from its original vacancy site to the newly associated first neighbour vacancy site. However, upon association of the second vacancy, the He atom relaxes so it resides between the two vacant sites and as such there is no barrier for step (iii). Finally, step (iv) is considered, in which

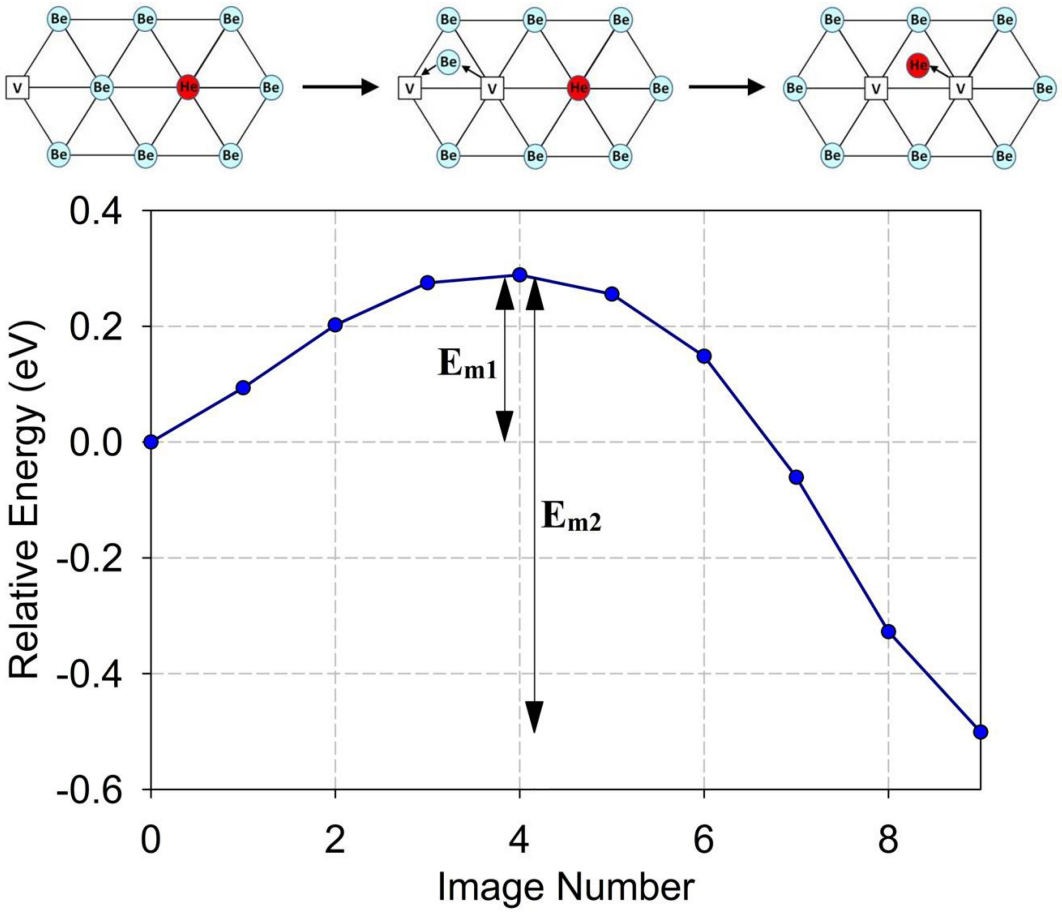


Figure 6.10: Energy profile for the migration of a vacancy moving through the basal plane towards a He_{Be} defect.

a second neighbour Be atom moves into the original Be site that the He atom occupied (now vacant). The activation energy, E_{m2}, is 0.79 eV as illustrated in Figure 6.10 and is rate determining (though it is only modestly higher than that for step (i).

As an alternative to dissociation of the $\{V_{Be}{:}He_{Be}\}$ cluster, it is possible for the cluster to re-orient with one of the vacancies switching between adjacent first neighbour sites (with respect to the site originally occupied by the He atom). This process is illustrated in Figure 6.11. A succession of such steps would lead to He transport. However, the activation energy

for this step is 1.34 eV, substantially greater than the rate determining step of the previous mechanism and therefore it can be discounted.

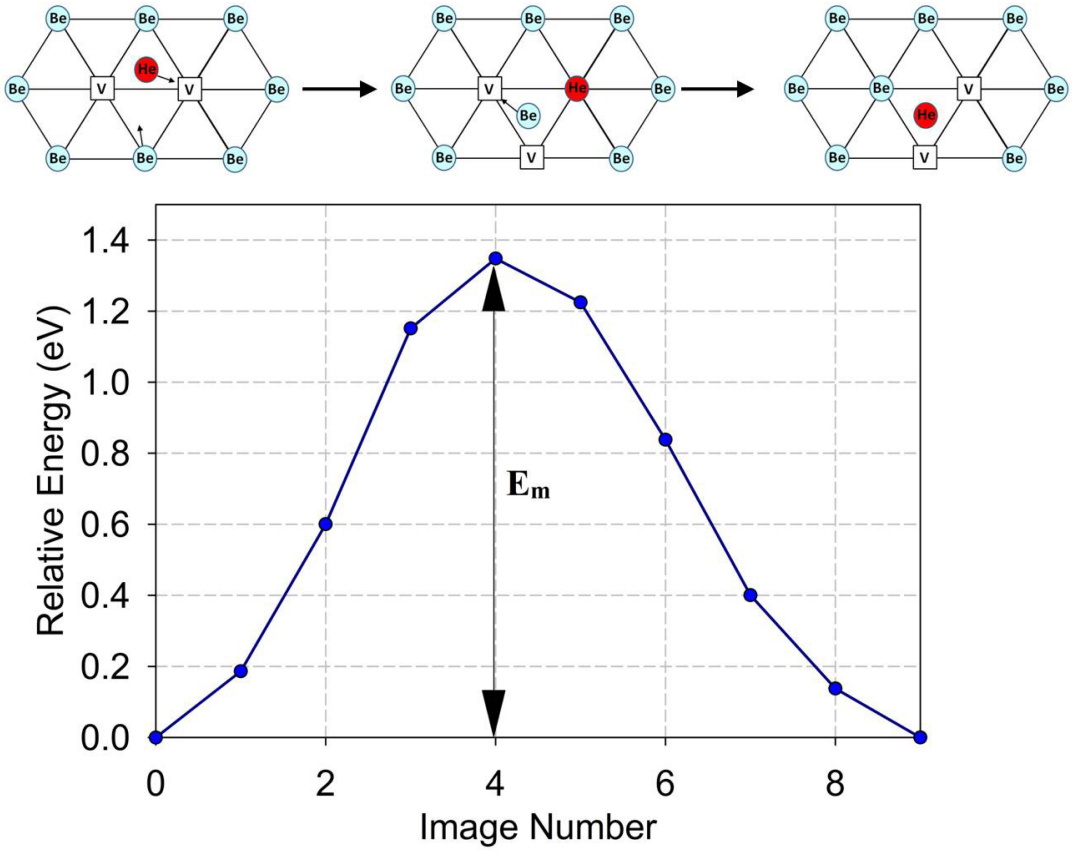


Figure 6.11: Energy variation of the migration of a vacancy moving through the basal plane around a He_{Be} defect.

6.4.3 Carbon in Beryllium

The negative accommodation energies for C (Table 6.3) suggest that if it were inserted into the Be structure it would form a bond if accommodated at both the vacant Be site or a number of different interstitial sites. The most stable site is a Oc interstitial site but only by 0.19 eV over the vacant Be site. When considering solution, the C-Be phase diagram reports a very stable Be_2C intermediate phase [208]. Consequently solution energies (as opposed to accommodation energies) are all large and positive suggesting that C has no driving force to enter the Be structure as an extrinsic species. Activation energies have

therefore not been calculated. The extent of solid solubility for C in Be should be practically zero.

6.4.4 Magnesium in Beryllium

Table 6.3 reports that Mg has high, positive accommodation energies into Be as an interstitial species and still a positive, though smaller energy into a vacant Be site, indicating no significant bond energy. Solution of Mg was calculated from the $Be_{13}Mg$ intermetallic [202]. This leads to very high solution energies (thus activation energies have not been calculated). The solid solubility of Mg in Be should therefore be very small as indicated in the Be-Mg phase diagram [209].

6.4.5 Silicon in Beryllium

In a similar manner to Mg, accommodation of Si in Be as an interstitial species yields large positive energies, indicating no significant bond formation. However, unlike Mg, accommodation of Si at a vacant Be site yields a negative energy, so bond formation does take place. Solution of Si is calculated from its elemental solid as no intermediate phase has been reported for the Be-Si binary system [210]. This leads to strongly positive energies at all solution sites and thus negligible solid solubility is expected. Again, no activation energies have been calculated.

6.4.6 Aluminium in Beryllium

Al has positive accommodation energies into interstitial sites within Be and a negative energy into a vacant Be site (akin to Si). This indicates poor bonding of Al in the Be lattice as an interstitial species and some bonding when it is a substitutional atom. Solution of Al is reported from its elemental solid as there is no reported intermetallic in the Be-Al binary system [211]. All solution energies are high and positive suggesting Al will not

significantly enter into solution in Be, as expected from the binary Be-Al phase diagram [211]. The transport of Al will therefore not be considered further in this work.

6.4.7 Iron in Beryllium

Comparison of accommodation energies for Fe indicates a strong preference for Fe to occupy vacant Be sites, that is, Fe will be accommodated as a substitutional species. The energy is negative indicating strong bond formation. With respect to solution, the binary phase diagram [212] shows the existence of the intermetallic $FeBe_5$. The following simple reaction indicates the stability of $FeBe_5$ with relation to its constituent elements:

$$Fe_{(s)} + 5Be_{(s)} \rightarrow \ FeBe_5 \tag{6.7}$$

The reaction energy is -0.53 eV, consistent with the stability of this intermetallic.

The solution of Fe metal (ferrite) into Be as a substitutional species was found to be slightly negative (-0.09 eV per Fe), which is not as negative as the energy per Fe to form the intermetallic, again consistent with intermetallic formation. The solution energies given in Table 6.4 are therefore with respect to the $FeBe_5$ phase. These energies, both substitutional and interstitial, are positive, however the solution energy with relation to substitutional Fe formation is only 0.44 eV indicating that some solid solubility of $FeBe_5$ within Be metal will be observed which is consistent with the phase diagram of the Fe-Be system [212].

Given the prediction of a strong preference for Fe to be a substitutional species and the relatively small solution energies, transport of Fe through the Be lattice via a vacancy mechanism has been investigated. Equivalent to He migration via vacancies (section 6.4.2), the migration process is considered in terms of four sub-processes (i)-(iv) (the vacancy migration, capture, re-arrangement and release of a vacancy moving a lattice species). The first step involves the free vacancy migration through the lattice (i) which remains constant with an activation energy of 0.72 eV as reported in section 6.3. The migration

of the vacancy from the second nearest neighbour site to the first nearest neighbour site relative to the substitutional Fe defect, step (ii), has a barrier to migration of 0.81 eV. The activation energy for step (iii), where a substitutional Fe migrates across from one vacancy to the other, in the basal plane, is 0.67 eV. Step (iii) could also occur perpendicularly to the basal plane. In this case the activation energy is slightly higher at 0.76 eV. Finally, step (iv), the release of the vacancy from the $\{Fe_{Be}{:}V_{Be}\}$ cluster from the first nearest neighbour site to the second nearest neighbour site, exhibits a migration activation energy of 0.54 eV. In summary, this vacancy capture/release mechanism for Fe migration is therefore limited by the capture of the vacancy from second to the nearest neighbour, that is, step (ii).

An alternative to the vacancy capture/release process is for the second V_{Be} to remain associated with the Fe_{Be} and for the $\{V_{Be}{:}Fe_{Be}\}$ cluster to migrate via a correlated process (somewhat equivalent to that described in Figure 8). Thus, the second captured vacancy moves around the Fe_{Be} defect between nearest neighbour sites. This process has an activation energy of 0.51 eV (which is almost identical to the dissociation of the cluster described by step (iv)). Finally the Fe atom swaps between Be sites as in step (iii) above with an activation energy of 0.67 eV, making this step rate determining once the cluster has formed. However, the $\{V_{Be}{:}Fe_{Be}\}$ cluster must initially be formed and as such, the limiting migration step is once again the capture of the vacancy to the nearest neighbour position. Thus, it seems that both processes will contribute to the transport of Fe in Be.

6.4.8 The $FeAlBe_4$ Intermetallic

While Al might not be soluble in Be, it has been reported as a constituent of the $FeBe_5$ intermetallic, ultimately, forming the intermetallic $FeAlBe_4$ [201]. Conversely, the intermetallic $AlBe_5$ has not been reported. We therefore begin by calculating the energy to form the hypothetical material $AlBe_5$:

$$Al_{(s)} + 5Be_{(s)} \rightarrow \ AlBe_5 \tag{6.8}$$

which is analogous to equation 6.7. This energy is positive (0.58 eV) consistent with this structure not forming. Next, the following reaction is considered:

$$Al_{(s)} + Fe_{(s)} + 4Be_{(s)} \rightarrow \ FeAlBe_4 \tag{6.9}$$

for which the calculated energy is -1.42 eV. The negative energy indicates this is a stable intermetallic in the Fe-Al-Be system, as indicated by Carrabine [201]. Thus, the following reaction of Al metal with the $FeBe_5$ intermetallic is considered. Since Al is highly insoluble in Be metal, the following reaction shows how this intermetallic may form in a system consisting of insoluble Al, Be metal and the $FeBe_5$ intermetallic:

$$Al_{(s)} + FeBe_5 \rightarrow \ FeAlBe_4 + Be_{(s)} \tag{6.10}$$

The calculated energy is -0.89 eV indicating that the reaction will proceed. Therefore, in the presence of excess $FeBe_5$ intermetallic, with respect to reaction 6.10, there will be no Al metal present.

Alternatively, the solution of Al into $FeBe_5$ as a substitutional dopant is considered. In this case, the Al can substitute for Be at two different Be sites ($Be_{(0,0,0)}$ and $Be_{(\frac{5}{8},\frac{5}{8},\frac{5}{8})}$) or at an Fe site ($Fe_{(\frac{1}{4},\frac{1}{4},\frac{1}{4})}$). The solution reactions proceed as follows:

$$Al_{(s)} + Fe_{Fe} \rightarrow \ Al_{Fe} + Fe_{(s)} \tag{6.11}$$

$$Al_{(s)} + Be_{Be(0,0,0)} \rightarrow \ Al_{Be(0,0,0)} + Be_{(s)} \tag{6.12}$$

$$Al_{(s)} + Be_{Be(\frac{5}{8},\frac{5}{8},\frac{5}{8})} \rightarrow \ Al_{Be(\frac{5}{8},\frac{5}{8},\frac{5}{8})} + Be_{(s)} \tag{6.13}$$

The energies for these processes are, -0.31 eV for reaction 6.11, -0.77 eV for reaction 6.12 and 0.87 eV for reaction 6.13. It is therefore predicted that Al will preferentially substitute onto the Be (0,0,0) site, not onto the Fe site as predicted by Rooksby [203]. The (0,0,0) site is the same site as Al occupies in the $AlFeBe_4$ intermetallic [201].

Finally, it is noted that here two limiting cases have been considered: a low concentration

of Al in $FeBe_5$ and the end member of the solution process $FeAlBe_4$. In both cases Al incorporation is shown to be favourable. In future it will be interesting to develop this further and be able to predict equilibrium compositions. For example, in the presence of excess Al, does the reaction proceed completely to $FeAlBe_4$ or to some sub-stoichiometric equilibrium $FeAl_{1-x}Be_{4+x}$ composition?

6.5 Defects in the $FeBe_5$ and $FeAlBe_4$ Intermetallics

The intermetallics that form within the Fe-Al-Be system are of significant engineering importance as Al and Fe are common alloying additions to Be. Some mechanical properties and solution properties of extrinsic species into both $FeBe_5$ and $AlFeBe_4$ are investigated.

6.5.1 $FeBe_5$

The intrinsic defect energies of $FeBe_5$ are shown in Table 6.5. In comparison to Be (Table 6.3), absolute vacancy energies are higher in $FeBe_5$, furthermore, the intrinsic reaction energies, Schottky and Frenkel are of higher energy in $FeBe_5$. Thus, vacancy concentrations will be considerably lower.

Table 6.5: Intrinsic defect energies within $FeBe_5$ (eV).

Defect	Type	Be	Fe
Vacancy	-	6.09/5.44	7.06
Interstitial	$(\frac{1}{2},\frac{1}{2},\frac{1}{2})$	2.85	2.87
	$(\frac{3}{4},\frac{1}{2},\frac{1}{2})$	4.14	2.64
	$(\frac{3}{8},\frac{5}{8},\frac{7}{8})$	*	-3.42
Substitution onto Be	(0,0,0)	-	-2.83
Substitution onto Be	$(\frac{5}{8},\frac{5}{8},\frac{5}{8})$	-	-1.28
Substitution onto Fe		4.59	-

The elastic constants for $FeBe_5$ have also been determined. Table 6.6 reports the elastic moduli of the system. The bulk modulus for $FeBe_5$ was determined to be 100.9 GPa compared to 130 GPa for Be. Table 6.7 reports the energies associated with the various

Table 6.6: Elastic constants (c) and bulk modulus (K) for cubic $FeBe_4$.

Parameter	Value (GPa)
c_{11}	257.2
c_{12}	22.75
c_{44}	119.8
K	100.9

extrinsic defects entering the $FeBe_5$ lattice. Solution of the gases hydrogen, helium and oxygen are compared to their solution into Be. Comparison of solution energies of $FeBe_5$ is

Table 6.7: Solution energies of H_2, He, O_2, Al, C from Be_2C, Mg and Si in $FeBe_5$ (eV).

Impurity occupying	H	He	O	Al	C	Mg	Si
Substitution onto (0,0,0) Be site	1.11	4.28	1.75	-0.77	12.49	0.82	-0.96
Substitution onto $(\frac{5}{8},\frac{5}{8},\frac{5}{8})$ Be site	0.02	4.70	-0.23	0.87	9.26	2.96	-0.35
Substitution onto Fe site	0.30	3.20	0.05	-0.31	11.49	0.79	-0.38
$(\frac{1}{2},\frac{1}{2},\frac{1}{2})$ interstitial	-0.52	7.43	1.00	10.09	12.82	13.50	6.19
$(\frac{1}{2},\frac{1}{2},\frac{3}{4})$ interstitial	-1.00	6.37	-0.82	10.09	14.16	11.70	21.91
$(\frac{3}{8},\frac{5}{8},\frac{7}{8})$ interstitial	-1.69	3.80	1.64	3.02	*	12.36	2.00

made with a 4×4×3 Be supercell, consisting of 96 atoms so that the relative concentrations are similar. Hydrogen has a solution energy of -1.69 eV in $FeBe_5$ as an interstitial species compared with a value of 0.74 eV in Be (in a 4×4×3 supercell). This means that the hydrogen will be gettered by the $FeBe_5$ intermetallic. Helium is also more stable in the $FeBe_5$ intermetallic (3.20 eV in $FeBe_5$ compared to 3.64 eV in the 4×4×3 Be primitive supercell), residing on an Fe site, however, the positive energy still suggests the He is not soluble. Oxygen is less soluble in $FeBe_5$, -0.82 eV, in comparison to -1.67 eV in the 4×4×3 Be supercell. This means there will be no driving force for oxygen to leave the Be lattice to enter the intermetallic.

Silicon has a negative solution energy into the $FeBe_5$ intermetallic unlike solution into Be. This will result in the Si, that normally will sit as an insoluble precipitate, to be incorporated into the Fe-Be intermetallic. The removal of Si precipitates in the Be metal bulk will have useful consequences, cleaning up the lattice and thereby changing the mechanical

behaviour of the material.

6.5.2 $FeAlBe_4$

The elastic constants for $AlFeBe_4$ are reported in Table 6.8. The bulk modulus was determined to be 349.2 GPa, larger than both for Be (130 GPa) and $FeBe_5$ (100.9 GPa).

Table 6.8: Elastic constants (c) and bulk modulus (K) for cubic $AlFeBe_4$.

Parameter	Value (GPa)
c_{11}	557.6
c_{12}	245.0
c_{44}	212.7
K	349.2

The solution of gas species into $AlFeBe_4$ has been investigated in order to compare the solubility of the gases with the $FeBe_5$ phase and Be metal. The results are reported in Table 6.9. Both hydrogen and oxygen have a lower solution energy into the interstitial

Table 6.9: Solution energies of H_2, He and O_2 in $FeAlBe_4$ (eV).

Impurity occupying	H	He	O
Substitution onto Al site	2.15	5.01	1.39
Substitution onto Be site	0.39	4.62	-0.13
Substitution onto Fe site	0.76	3.64	0.55
$(\frac{1}{2},\frac{1}{2},\frac{1}{2})$ interstitial	-0.67	6.91	3.87
$(\frac{1}{2},\frac{1}{2},\frac{3}{4})$ interstitial	-1.19	5.81	-1.27
$(\frac{3}{8},\frac{5}{8},\frac{7}{8})$ interstitial	-1.83	4.48	-0.78

position within $FeAlBe_4$ compared to $FeBe_5$. The change for O_2 solution is particularly significant. He solution remains high and positive suggesting that solution will remain unfavourable.

Of the three studied systems: Be, $FeBe_5$ and $AlFeBe_4$, H will be most stable in the $AlFeBe_4$ crystal phase. In effect, this result suggests that the addition of Al to the Fe-Be system will mean that there is an even greater driving force for the H to be accommodated within

the intermetallic rather than within the Be lattice. This has important engineering implications as the H will be gettered in the intermetallic preventing hydration of the Be that may cause variations of its mechanical properties, compromising the structural integrity of components within systems with high H concentrations.

Oxygen has been found to have a lower solution energy in the $FeAlBe_4$ intermetallic compared to the $FeBe_5$ intermetallic. However, this solution energy is still higher than for O_2 entering the Be metal lattice, resulting in no drive for O_2 to getter in either intermetallic.

Helium, like hydrogen has a lower solution energy in $FeAlBe_4$ compared to $FeBe_5$, however, the energy is still significantly positive, suggesting that it will not be a stable extrinsic defect. All the results for He suggest that, diffusion processes permitting, He will move out of both the Be and intermetallic lattices, to either a grain boundary position, void or out of the system.

6.6 Summary

Intrinsic defect processes in Be metal are all of high energy with a Be vacancy being the dominant defect. Transport of vacancies is close to isotropic with an activation energy of 0.72 eV in the basal plane. Intrinsic Be migration, whilst exhibiting a lower activation energy of 0.64 eV, is not significantly more favourable given the much smaller intrinsic interstitial atom concentration.

These simulations have some interesting implications for radiation damage of Be; as mentioned, Be will be used as a first wall material in fusion reactors [110] and therefore subjected to an enormous neutron flux. Consequently, while the intrinsic defect concentrations are low, there will still be considerable damage leading to the production of vacancies and interstitials. The results presented are encouraging in this regard because there is a significant driving force for defect recombination (high Frenkel energy) and hence damage recovery. Further, the activation energies for vacancy and interstitial transport are not high and fairly isotropic, thus the rate of recombination should be high. Finally, a vacancy

and interstitial pair spontaneously recombine in a second or first nearest neighbour configuration but have almost no interaction at a third neighbour position. While additional simulations should also be carried out, this gives a first indication of the recombination volume.

Turning to extrinsic defects, predicted H solution and migration mechanisms are in agreement with previous studies [196, 194]. It is suggested that atomic H will be transported as an interstitial species and migration will be rapid, having an activation energy of 0.40 eV.

Considering equilibrium, O_2 is soluble in Be exhibiting a solution energy of -4.04,eV at an interstitial site, while also being soluble at a vacant Be site. Furthermore, the difference in vacancy and interstitial accommodation energies (Table 6.3) imply that even if a non-equilibrium process were to provide a population of vacancies for interstitial O atoms to occupy (e.g. created by radiation damage) O atoms would remain an interstitial species (by 2.89 eV). Consequently, the solution properties will not be greatly changed by radiation damage (although ballistic processes could aid migration of O atoms through the lattice). Furthermore, the activation energy for interstitial O transport was predicted to be rather high, 1.63 eV, providing a strong barrier for internal oxidation at low to moderate temperatures. At 1000 K, however, interstitial O would be expected to move on the microsecond time-scale given the size of the migration barrier.

He has been found to be highly insoluble within the Be lattice but the activation energy for interstitial He transport is only 0.25 eV. Consequently, interstitial He introduced into the Be lattice via a high energy (radiation) process will rapidly move through the lattice. It will, however, be strongly trapped by a Be vacancy and is then subject to transport via a Be vacancy mechanism, which requires the association of a second Be vacancy to the He_{Be} defect. It was found that the migration process will be limited by the energy associated with the de-trapping of a Be vacancy from the $\{V_{Be}$: $He_{Be}\}$ cluster, with an activation energy of 0.79 eV. From a radiation damage point of view, while He may become trapped at a Be vacancy, there will be available Be_i species (the damage process proceeds via Frenkel pair formation). Then He may become de-trapped by a migrating Be_i interstitial

($He_{Be} + Be_i \rightarrow Be_{Be} + He_i$ ΔE = -3.1 eV) since the Be_i migration activation energy (0.64 eV) is smaller than the He migration energy via a V_{Be}. Thus, equilibrium and non-equilibrium (damage assisted) processes for He transport through Be will be quite distinct, with the latter offering much lower energy possibilities and beneficial to the removal of the He from the metal. However, cluster formation might alter this conclusion and needs to be considered further.

Iron reacts with Be to form the $FeBe_5$ intermetallic phase and this compound exhibits a fairly small positive solution energy (0.44 eV) in Be and hence it will exhibit some solid solubility. Given the solid solubility of $FeBe_5$ in Be, migration of Fe by a vacancy mechanism was investigated as it was for He in Be. Unlike He, Fe transport can be facilitated by a nearest neighbour coupled migration mechanism in addition to the vacancy capture/release mechanism favoured by He in Be with an activation energy in both cases of 0.81 eV. Overall, it seems transport of extrinsic Fe will be similar to transport of intrinsic Be since both are vacancy mediated and the rate determining processes are of similar energy. Further, since the V_{Be} defect concentration is small at equilibrium, the rate of transport will be low.

Aluminium was found to be insoluble in the Be lattice but soluble in the $FeBe_5$ intermetallic substituting at $Be_{(0,0,0)}$ sites. Solution of Al may proceed until at least the intermetallic $FeAlBe_4$ forms.

Calculations of the solution of He, O_2 and H_2 into both the $FeBe_5$ and $FeAlBe_4$ intermetallics have been carried out. O_2 is not gettered into either of the intermetallics (as the solution energy of O_2 is lower in Be metal compared to both $FeBe_5$ and $FeAlBe_4$). The solution energy of He into both intermetallics is positive as it is in Be metal, however, the solution energy is lower in $FeBe_5$ compared to Be metal. Interestingly, H_2 solution has a negative energy into both $FeBe_5$ and $FeAlBe_4$ and therefore both intermetallics are expected to getter hydrogen and therefore prevent the hydriding of the Be metal. This result is quite significant.

It is also interesting to note that Si has a negative solution energy into $FeBe_5$, substituting

onto any of the lattice sites. This suggests that the presence of the $FeBe_5$ intermetallic will getter any excess Si in the system.

In summary, this work has gone some way towards demonstrating the rich complexity of defect processes in Be and the role of the intermetallics $FeBe_5$ and $FeAlBe_4$. Some species migrate isotropically, such as Be interstitials, whereas other species diffuse anisotropically, such as He. Some dopant species are highly soluble, especially O but also H, whilst others are decidedly insoluble such as C, Mg and Si. Especially for radiation damage studies, much remains to be investigated for this interesting material, particularly with regard to defect cluster formation.

This chapter has introduced the complexities of what, on first appearances, seems a very simple system. Parallels can be drawn with beryllium and other HCP metals such as zirconium, although DFT simulations on Zr will be more computationally expensive due to the increased number of electrons in the system.

Chapter 7

Ongoing and Future Work

"If you don't have to drag yourself off the field exhausted after 90 minutes, you can't claim to have done your best."
- Bill Nicholson, Tottenham Hotspur F.C. Manager 1958-1974 [213].

7.1 Atomic Scale Simulations of Nuclear Fuel

This thesis has contributed to the further understanding of the atomic scale behaviour of trivalent cations and their effect on bulk processes in uranium dioxide.

7.1.1 Transport in UO_2

What has not yet been understood fully is the effect of multiple Cr^{3+} cations on the migration of uranium vacancies as well as the influence of other larger trivalent cations. Furthermore, work should be carried out to identify trends for migration of V_U'''' defects from 2^{nd} nearest neighbour to an equivalent 2^{nd} nearest neighbour site but also other equivalent processes out to 3^{th} and 4^{th} neighbour sites. If there is a lowering of migration activation energies for these mechanisms, U^{4+} migration will be enhanced regardless of the

movement of the trivalent species, though highly dependent on the trivalent ion concentration. It would also be interesting to understand the role of clustering on the migration of species through UO_2; larger clusters may possibly initiate lower energy concerted migration processes. Oxygen migration in doped and un-doped hyperstoichiometric should also be considered.

7.1.2 Dopants and Fission Products at Grain Boundaries and Surfaces

Grain boundaries in the UO_2 system have been the subject of much recent work [214, 215]. Until recently, the research of UO_2 has generally focused on relatively clean and coherent grain boundaries. Future work should aim to consider the complex interactions between dopants and fission products with grain boundaries and surfaces, with emphasis on attempting to understand how dopants change to drive the segregation. Investigations into more complicated grain boundaries should be made such and in addition amorphous intergranular films should be considered. For example, the glassy phases that may form when SiO_2 is added to the UO_2 system as a dopant [216] should be investigated as they may show some advantageous effects on fission gas retention. Increased understanding of these grain boundaries will lead to a better description of the fission gas release processes and in turn allow improvements to be made to fuel performance codes.

The change in solution energy and migration energy of the fission gases, krypton and xenon, should be investigated as an increase in solubility or a decrease in diffusivity would have a advantageous effect on fission gas release, reducing the volume of gas released to the rod free volume.

UO_2 grain boundaries have been briefly explored, specifically looking at the interaction of one grain boundary with another, in the same supercell. The distance between the two grain boundaries in a supercell is increased and the system energy is calculated. The defect energy per unit area of grain boundary surface is then calculated for each separation (see Figure 7.1 for some preliminary simulations). The defect energy is observed to decrease with increasing grain boundary separation. The calculations suggest that having a large

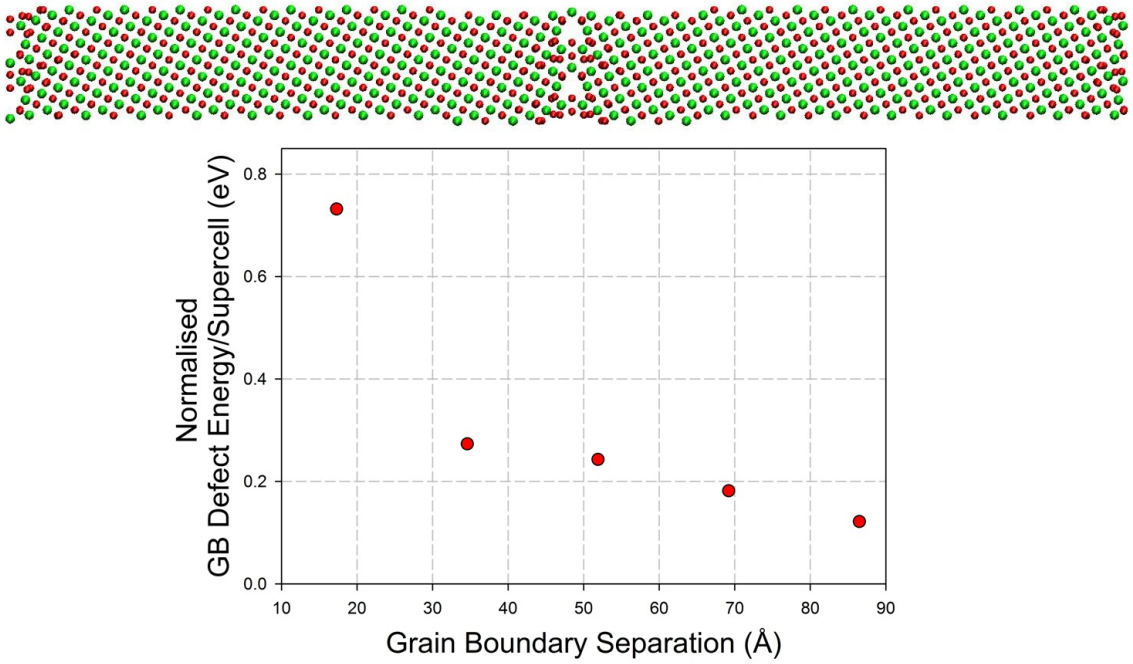


Figure 7.1: Image of a $\Sigma 5$ grain boundary in UO_2. The plot shows the interaction energy of the two grain boundaries in the system falling with increases in distance between them. This highlights the importance of using large enough system sizes when investigating grain boundaries.

enough system size is important for carrying out accurate static and dynamic calculations.

The relationship between surface energy due to dopants should also be explored. Intragranular bubble morphology is linked with the surface energy of UO_2. Killeen has already shown that bubble morphology changes with chromium doping [74], possibly due to the formation of chromium containing precipitates at the grain boundaries. The segregation of species to surfaces may also change with dopant and fission product concentration. A preliminary investigation into the interactions of trivacancies with surfaces has been made with a view to understanding the effects of dopant concentration (see Figure 7.2). It was found that the defect energy for a trivacancy reduced as the crystal surface was approached and therefore indicating a tendency towards segregation. It would be interesting to under-

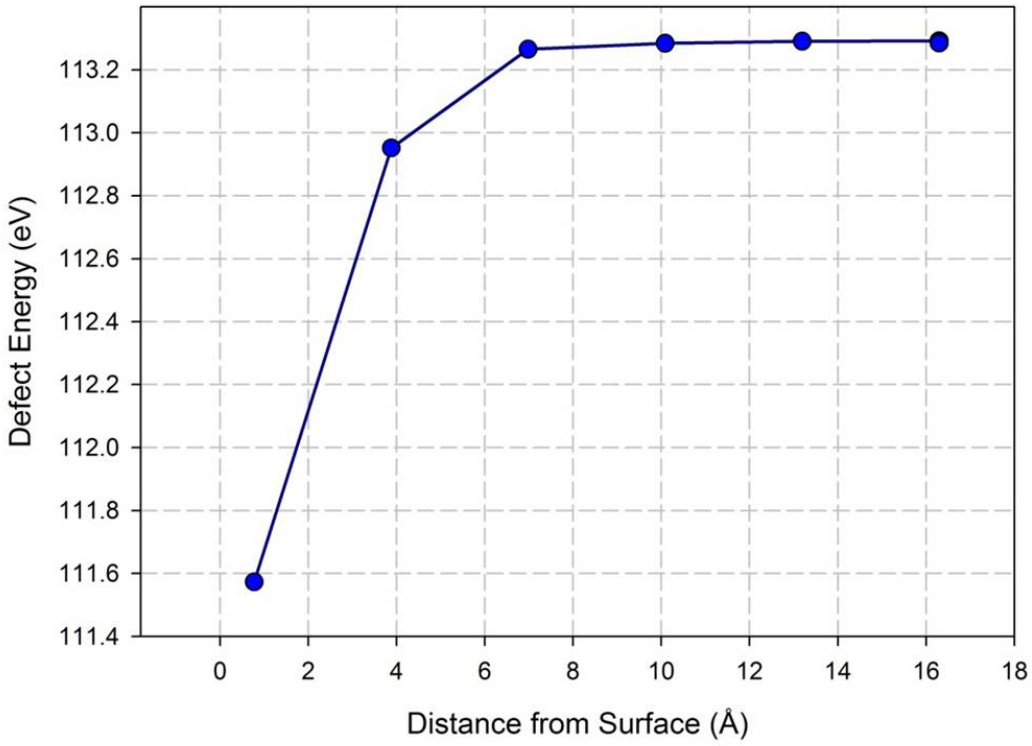


Figure 7.2: Change in defect energy of a Schottky trivacancy with distance from a UO_2 <110> grain surface. The plot shows the drive for trivacancies to move towards the surface.

stand how the solution energy of chromium and aluminium varies near a grain boundary.

7.1.3 Dopant and Fission Product Effect on the Formation of High Burnup Structure

High burnup structure (HBS) formation has been the subject of a great deal of research over the last decade [78, 66]. The difference in mechanical properties and morphology of the HBS compared to pristine UO_2 has driven research to understand the mechanism behind HBS structure formation and its behaviour under severe and accident conditions.

The possible reasons for HBS structure have been investigated and an understanding of dislocation interaction with dopants and fission products may yield some interesting results that could shed light on the subject. Dislocation movement will be hindered by precipitates and may be pinned. The build-up in concentration of dislocations may lead to grain subdivision. The interaction of dislocations with fission products should be researched and can be linked to experimental work such as microscopy coupled with electron backscatter diffraction (EBSD) analysis to understand the effect of dopants on grain subdivision.

In the same vein, it would be pertinent to understand the onset of high porosity in highly burnt up standard UO_2 fuel towards the centre of the pellet (see Figure 7.3). It is likely that the similarly structured phases (HBS and the high porosity structure in the centre of the pellet) are produced as a consequence of similar processes.

7.1.4 DFT Approach to Diffusion of Dopants in Uranium Dioxide

DFT calculations should be carried out to understand the migration processes discussed in Chapter 4. The advantages of using DFT include the ability to study the effects of other, non-metallic elements on the volume, diffusivity and solution properties of UO_2.

There are obviously some large challenges to using DFT including the limited system sizes and the need for not only a Mott-Hubbard correction [131], but also control of the occupation matrix when dealing when carrying out calculations [217]. As computing power increases more phenomena will be in reach of DFT calculations. Careful use of multi-scale modelling, where atomistic DFT results feed information into mesoscale and macroscopic

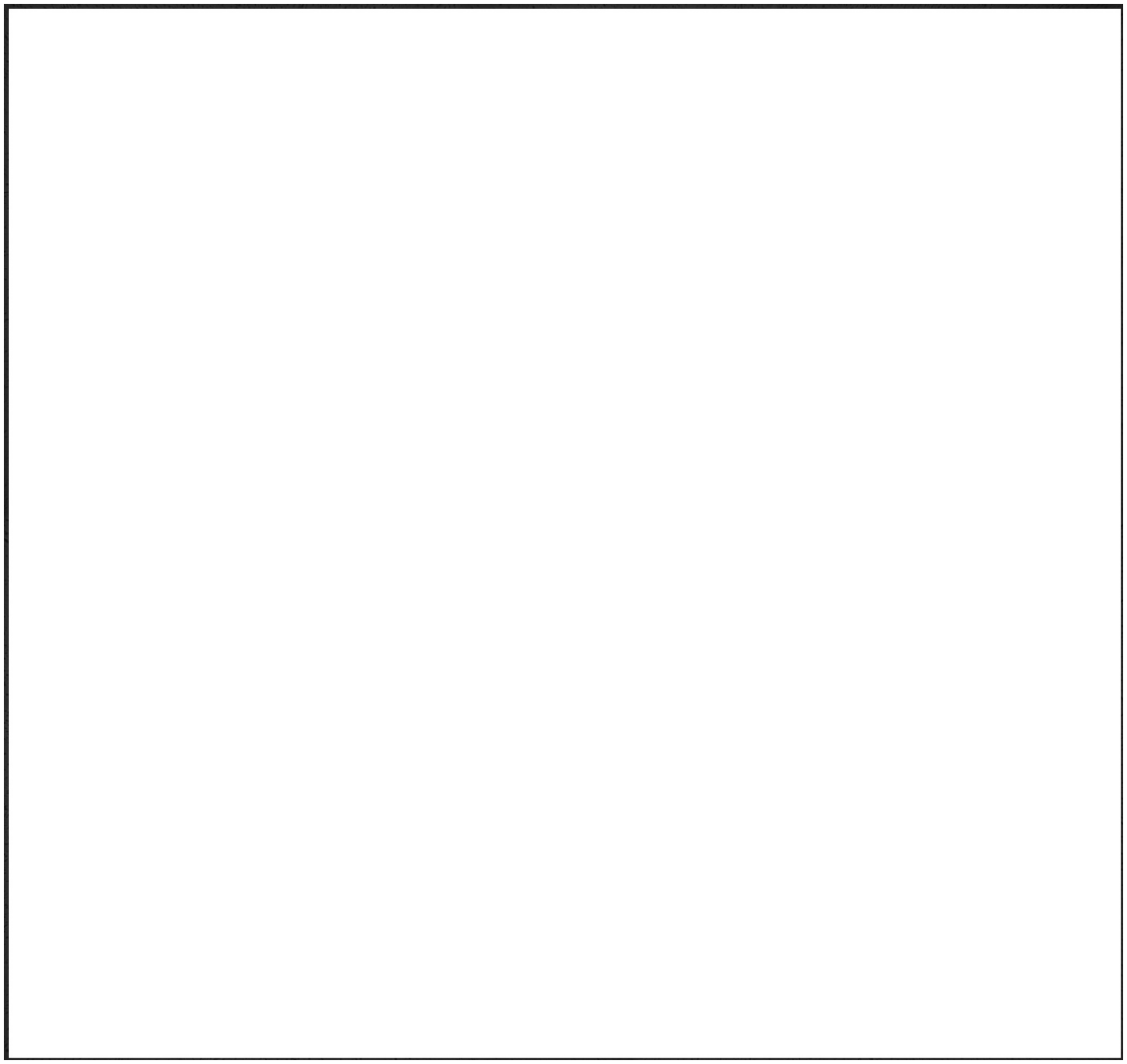


Figure 7.3: Image removed as instructed by funding body.

continuum models calculations at larger scales (such as finite element calculations) will prove beneficial in understanding phenomena currently outside of the computational reach of DFT and other *ab-initio* methods.

7.1.5 Doping of ThO_2 and (MA,U)O_2

Thoria and minor actinide dioxides are being considered for use in breeder and fast-breeder reactors and as such, a greater understanding of the behaviour of these potential fuels is required. All the work that has been carried out to understand the irradiation and in-pile behaviour of UO_2 and PuO_2 should be repeated with other potential fuels.

ThO_2 is different to UO_2 in that it does not oxidise readily from a "4+" charge state to a "5+" charge. Vacancies and other negatively charged defects are more likely to be charged by positive defects such as oxygen vacancies and interstitial cations rather than oxidised uranium ions.

Calculations could be carried out to investigate the oxidation of ThO_2 by the formation of peroxide ions as given in the equation below:

$$\frac{1}{2}O_2 + O_O^{\times} \rightarrow \{V_O^{\bullet\bullet} : 2O_i'\}^{\times} \tag{7.1}$$

If this is found to be the lowest energy mechanism to form ThO_{2+x}, other mechanisms that accommodate aliovalent cation fission products would also need to be investigated. One such reaction could be:

$$\frac{1}{2}Cr_2O_3 + Th_{Th}^{\times} + \{V_O^{\bullet\bullet} : 2O_i'\}^{\times} \rightarrow Cr_{Th}' + O_O^{\bullet} + ThO_2 \tag{7.2}$$

A possible and interesting fuel that could be produced for light water reactors that can use a very similar process to the standard UO_2 pellet production would be a ThO_2 coated UO_2 or doped UO_2 pellet (suggestions of a homogeneous (U,Th)O_2 mix have already been made [27]). The ThO_2 coated fuel is expected to have a number of interesting properties

and advantages over standard non-coated pellets:

- As ThO_2 exists at the periphery, the shielding effect that usually leads to an increase in plutonium concentration will instead breed U_{92}^{233}. This may be regarded as a slight improvement on proliferation resistance. Only a small layer of ThO_2 ($\sim$0.5 mm) would have to be added to prove effective at lowering the plutonium concentration in an irradiated pellet.

- ThO_2 is more difficult to reduce than UO_2 and may act as a barrier to the oxidation of the cladding material increasing the pellet clad mechanical interaction.

- The thermal conductivity of ThO_2 is higher than UO_2 and will therefore conduct heat away from the centre more efficiently allowing lower fuel centre point temperatures.

- The advantage of having ThO_2 as a coating is that the uranium does not need to be enriched significantly higher than for standard pellets (unlike a homogeneous (Th,U)O_2 pellet).

- Because ThO_2 is soluble in UO_2, there does not need be a sharp transition from ThO_2 to UO_2 in the pellet. Instead a boundary layer with increasing ThO_2 concentrations towards the pellet rim can be produced. It is possible that the material can be fabricated with a compositional gradient between the two oxides.

- The concentration of minor actinides in the waste will be lower as ThO_2 does not produce the trans-uranic elements. It is these minor actinides that mean spent fuel must be stored for extremely long times in a repository.

As with any new pellet design, it will have to be tested properly and the economic benefits of the fuel will have to be investigated.

7.2 Atomic Scale Simulations of Burnable Poisons

The defect processes of zirconium diboride have been investigated for the first time in this work. There is a great deal of scope for future work including:

- Investigating the swelling and He segregation characteristics and change in mechanical properties of ZrB_2 under irradiation. Swelling will be important to understand for the use of ZrB_2 as a burnable poison inside a fuel assembly.
- The effects of lithium in ZrB_2 solution on diffusion of other species in the crystal as lithium remains in the ZrB_2 lattice after transmutation.
- Understanding the addition of hafnium as HfB_2 is added to ZrB_2 to alter the mechanical properties of the ceramic in aerospace applications.
- Surface calculations of ZrB_2 will be interesting for aerospace and nuclear applications. Surface oxidation will be useful to understand for both industries and the adhesion of ZrB_2 to UO_2 would be an interesting study.

Each of these are now discussed in more detail.

7.2.1 Irradiation of ZrB_2

In this work, zirconium diboride was investigated using DFT. This limits the system size and therefore irradiation effects that involve large numbers of atoms may require the use of a more empirical (or at least more computationally tractable) description of the inter-atomic interactions. The residual defects left by a displacement cascade would be interesting to study as these may considerably outnumber the defects produced by intrinsic processes and therefore have an effect on the trapping of He and Li produced due to B_5^{10} transmutation.

A significant issue is that the transmutation of B_5^{10} will leave an overall Zr excess that can not be accommodated in the ZrB_2 lattice according to calculations that have been carried out in this work. Therefore, some research should be made into the doping of ZrB_2

that will enable the excess zirconium to be retained in the structure and not produce a secondary, low melting temperature phase. Otherwise, research should be carried out on the mechanical implications of producing a ZrB_{2+x} solid that allows a certain molar value of B_5^{10} to be transmutated without the formation of the secondary phase.

7.2.2 Li and Impurity Effects on Diffusion

As has already been encountered when investigating the effects of Cr^{3+} doping of UO_2, the increase in concentration of Li in the ZrB_2 lattice due to transmutation processes may affect the diffusion properties of the bulk material. Further work should be carried out to understand if the increase in Li concentration will pin vacancy defects, decreasing the overall substitutional defect migration, or alternatively enhance the diffusion, increasing the rate of diffusion of substitutional species (such as He trapped at a lattice site).

Impurities may have an effect on the mechanical properties of ZrB_2 and also initiate the formation of further defects in the lattice. Common impurities arising from the manufacturing of ZrB_2 include C, O, Ta, Fe, Mo, N and Hf. The solution properties and effects on intrinsic diffusion processes should be investigated. The effect of the impurities and defects on thermal conductivity will also be a useful investigation due to the application of ZrB_2 as a heat shield for re-entry vehicles.

7.2.3 HfB_2-ZrB_2-SiC System

HfB_2 and ZrB_2 are both considered as ultra high temperature ceramics and have been used in a number of aerospace applications. Some applications that have been conceived use the heterostructure: $(Hf,Zr)B_2$. SiC has been considered as a good addition to $(Hf,Zr)B_2$ ceramics as it increases the overall oxidation resistance of the solid, whilst also being able to tolerate extremely high temperatures and shock impulses. The relative solubility of Hf, Zr, C, B and Si in the lattices should be a useful investigation.

Surface calculations to investigate the grain boundaries between the three phases would

prove useful in understanding the crack propagation characteristics of the solids. DFT simulations would not provide a large enough system size so an empirical potential may be of more use for these calculations.

7.3 Atomic Scale Simulations of Beryllium

Defect processes in beryllium metal have been investigated in detail for the first time on the atomic scale. A number of interesting results have been outlined but there is plenty more science accessible to of current simulation techniques. Some of these will now be outlined:

- If a simple embedded atom potential (empirical, ideal for metals) were to be produced, calculations looking at radiation damage and the residual defects in beryllium under irradiation can be carried out. The effect of stacking faults and impurities could provide scope for further investigation along with high temperature, high pressure variations that may prove useful when considering the material's use as a plasma facing clad for future fusion reactors.

- The effect of irradiation will undoubtedly affect the migration characteristics of the common impurities and transmutation products He, O and H. Investigations into the changes would prove useful for fusion reactor applications.

- The formation of twins (special low angle grain boundaries) are a hot topic in HCP metals, Be included. The reorientation and movement of twins would be a very interesting topic of research. The influence of irradiation on twin behaviour should be considered and also the effect of the transmutation and dopants on the twin boundary.

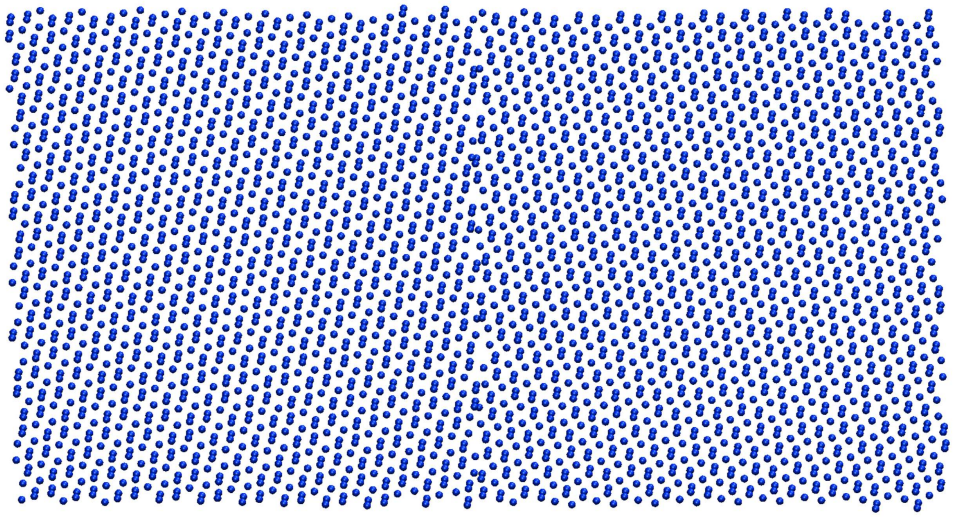


Figure 7.4: Twin in beryllium created using the program 'GBStudio'.

Appendix A

Kröger-Vink Nomenclature

The notation used by Kröger and Vink [65] is used throughout this thesis to describe defect reactions in a simple manner. A single defect can be described as given in Figure A.1.

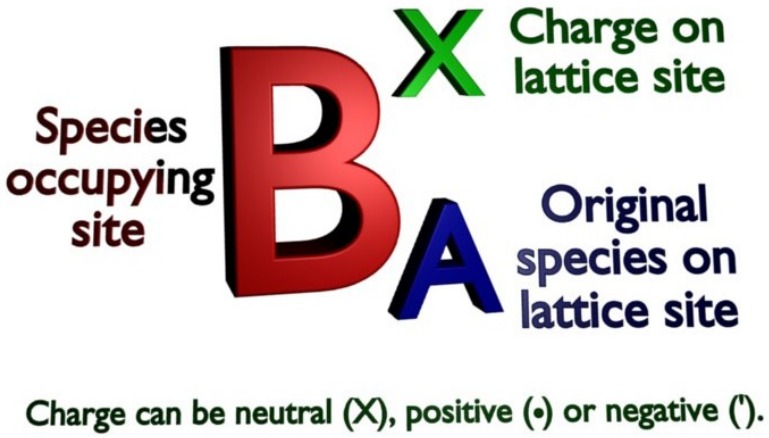


Figure A.1: Summary of the Kröger-Vink notation used throughout this thesis to describe defects.

Figure A.1 reports that 'A' is the original lattice site. In UO_2 this could be either a U, an O or and interstitial (denoted by an 'i'). This is then filled with a species 'B'. For example, a chromium ion residing on a uranium site in UO_2 would be written as Cr'_U. A vacancy on a site is denoted by a 'V' (for example an oxygen vacancy would be $V^{\bullet\bullet}_O$). The charge on the defect is then denoted by either a $\times$ for a neutral defect or varying numbers

of $'$ for negative defects or $^{\bullet}$ for positive defects (depending on the charge). For example, the oxygen vacancy has an overall +2 charge in UO_2 ($V_O^{\bullet\bullet}$) as there is a missing O^{2-} ion. A chromium on a uranium site has an overall -1 charge (Cr'_U) as the original U^{4+} ion is replaced by a chromium that has a +3 charge producing a negative charge.

Defect clusters are described by combining single defects using the Kröger-Vink notation inside brackets and then stating the overall charge after. For example, the neutral defect cluster containing two chromiums on two uranium sites and an oxygen vacancy in UO_2 would be given as $\{2Cr'_U{:}V_O^{\bullet\bullet}\}^{\times}$.

Bibliography

[1] AH Compton. The Birth of Atomic Power. *Bulletin of the Atomic Scientists*, 9(1):12, 1953.

[2] P D Wilson. *The Nuclear Fuel Cycle - from Ore to Wastes*. 1996.

[3] GF Hewitt and JG Coller. *Introduction to Nuclear Power*. 2000.

[4] Melvin A Miller. Sketching, 1946.

[5] RC Williams and PL Cantelon. *The American Atom - A documentary history of nuclear policies from the present 1939-1984*. 1984.

[6] Y Chikazawa, M Farmer and C Grandy. Technology Gap Analysis On Sodium-Cooled Reactor Fuel-Handelling System Supporting Avanced Burner Reactor Development. *Nuclear Technology*, 165, 2009.

[7] R Jeffrey. Lessons from UK nuclear experience. *Power Engineering Journal*, 16(4):186, 2002.

[8] K Jay. *Calder Hall - The Story of Britain's First Atomic Power Station*. 1956.

[9] H Aldersey-Williams. *Periodic Tales: The Curious Lives of the Elements*. 2011.

[10] PT Gillcrist. *Power Shift: The Transition to Nuclear Power in the U.S. Submarine Force As Told by Those Who Did It*. 2006.

[11] ARM Roulstone. Improving the breed : naval reactor technology development to PWR2. *Nuclear energy*, 34(2):73–83.

[12] D Bodansky. *Nuclear Energy - Principles, Practices and Prospects.* 4th edition, 1996.

[13] WNA. Nuclear Power Reactor Characteristics. Technical report, 2009.

[14] G Yadigariglu and J Dreier. Passive Advanced Light Water Reactor designs and the ALPHA program at the Paul Scherrer Institute. *Kerntechnik*, 63(1-2):39–46, 1998.

[15] K Hashimoto. Linear modal analysis of out-of-phase instability in boiling water reactor cores. *Annals of Nuclear Energy*, 20(12):789–797, 1993.

[16] TL Schulz. Westinghouse AP1000 advanced passive plant. *Nuclear Engineering and Design*, 236(14-16):1547–1557, 2006.

[17] Ian Sample. Japan's nuclear crisis: the causes and the risks,The Guardian, 2011.

[18] S Chetal, V Balasubramaniyan, P Chellapandi, P Mohanakrishnan, P Puthiyavinayagam, C Pillai, S Raghupathy and T Shanmugham. *Nuclear Engineering and Design*, 236(7-8):852–860, 2006.

[19] K Anantharaman, V Shivakumar and D Saha. Utilisation of thorium in reactors. *Journal of Nuclear Materials*, 383(1-2):119–121, 2008.

[20] K Fukuda, S Kashimura, T Tobita and T Kikuchi. Irradiation behavior of HTGR coated particle fuel at abnormally high temperature. *Nuclear Engineering and Design*, 157(1-2):221–230, 1995.

[21] RW Grimes. Simulating the Behaviour of Fission Products in UO2. *Materials Research Society Symposium Proceedings*, 257:361, 1992.

[22] RW Grimes, CRA Catlow and AM Stoneham. Calculations of Solution Energies of Fission Products in Uranium Dioxide. *Journal of the American Ceramic Society*, 72(10):1856–1860, 1989.

[23] L Leibowitz, RA Blomquist and AD Pelton. Thermodynamics of the Uranium-Zirconium System. *Journal of Nuclear Materials*, 167, 1989.

[24] C Guéneau. Thermodynamic assessment of the uranium-oxygen system. *Journal of Nuclear Materials*, 304(2-3):161–175, 2002.

[25] P Ch Sahu, M Yousuf and K Govinda Rajan. Electrical resistivity and phase-transition behaviour of uranium under pressure and temperature. *Physica B: Condensed Matterica*, 183(1-2):145–155, 2002.

[26] J Fink. Thermophysical properties of uranium dioxide. *Journal of Nuclear Materials*, 279(1):1–18, 2000.

[27] S Maris Oggianu, HEE Cheon No and MS Kazimi. Analysis Of Burnup and Economic Potential of Alternatice Fuel Materials in Thermal Reactors. *Nuclear Technology*, 143, 2003.

[28] Lisa Grande, Bryan Villamere, Leyland Allison, Sally Mikhael, Adrianexy Rodriguez-Prado and Igor Pioro. Thermal Aspects of Uranium Carbide and Uranium Dicarbide Fuels in Supercritical Water-Cooled Nuclear Reactors. *Journal of Engineering for Gas Turbines and Power*, 133(2):022901, 2011.

[29] FT Binford and RW Knight. Use of U_3O_8-Al Cermet Fuel in Research Reactors. *Transactions of the American Nuclear Society*, 27:834–835, 1977.

[30] M Finlay. Irradiation behaviour of uranium silicide compounds,. *Journal of Nuclear Materials*, 325(2-3):118–128, 2004.

[31] WNA. Uranium, from Mine to Mill. Technical report, 2010.

[32] A Berche, C Rado, O Rapaud, C Guéneau and J Rogez. Thermodynamic study of the U-Si system. *Journal of Nuclear Materials*, 389(1):101–107, 2009.

[33] A Deditius, S Utsunomiya and R Ewing. The chemical stability of coffinite, $USiO_4$-nH_2O; $0<n<2$, associated with organic matter: A case study from Grants uranium region, New Mexico, USA. *Chemical Geology*, 251(1-4):33–49, 2008.

[34] RE Zartman and JV Smith. Mineralogy and U-Th-Pb age of a uranium-bearing jasperoid vein, Sunshine Mine, Coeur d'Alene district, Idaho, USA. *Chemical Geology*, 261(1-2):185–195, 2009.

[35] S Villani and EW Becker. *Uranium enrichment*. 1979.

[36] CK Gupta and H Singh. *Uranium Resource Processing - Secondary Resources*. 2003.

[37] T K Ghosh and A P Mark. *Energy Resources and Systems - Volume 1: Fundamentals and Non-Renewable Resources*. 2009.

[38] J Arborelius, K Backman, L Hallstadius, M Limbäck, J Nilsson, B Rebensdorff, G Zhou, K Kitano, R Löfström and G Rönnberg. Advanced Doped UO_2 Pellets in LWR Applications. *Journal of Nuclear Science and Technology*, 43(9):967–976, 2006.

[39] P Balakrishna, BN Murty, KP Chakraborthy, RN Jayaraj and C Ganguly. Special Features in Powder Preparation, Pressing and Sintering of Uranium Dioxide. *Materials and Manufacturing Processes*, 15(5):679–693, 2000.

[40] T Kutty. Densification behaviour of UO_2 in six different atmospheres. *Journal of Nuclear Materials*, 305(2-3):159–168, 2002.

[41] J Opfermann. Simulation of the sintering behavior of a ceramic green body using advanced thermokinetic analysis. *Thermochimica Acta*, 318(1-2):213–220, 1998.

[42] MN Rahaman. *Ceramic Processing and Sintering*. 2005.

[43] Suk-Joong L Kang. *Sintering: Densification, Grain Growth and Microstructure*. 2005.

[44] AJ Stevenson, Xin Li, MA Martinez, JM Anderson, DL Suchy, ER Kupp, EC Dickey, KT Mueller and GL Messing. Effect of SiO_2 on Densification and Microstructure Development in Nd:YAG Transparent Ceramics. *Journal of the American Ceramic Society*, 94(5):1380–1387, 2011.

[45] K Lay and B Carter. Role of the O/U ratio on the sintering of UO_2. *Journal of Nuclear Materials*, 30(1-2):74–87, 1969.

[46] E Friedland, NG van der Berg, JB Malherbe, JJ Hancke, J Barry, E. Wendler and W. Wesch. Investigation of silver and iodine transport through silicon carbide layers prepared for nuclear fuel element cladding. *Journal of Nuclear Materials*, 410(1-3):24–31, 2011.

[47] A Einstein. Ist die Trägheit eines Körpers von seinem Energieinhalt abhängig? *Annalen der Physik*, 323(13):639–641, 1905.

[48] I Noddack. Über das Element 93. *Angewandte Chemie*, 47(37):653–655, 1934.

[49] N Bohr and J Wheeler. The Mechanism of Nuclear Fission. *Physical Review*, 56(5):426–450, 1939.

[50] H Anderson, E Booth, J Dunning, E Fermi, G Glasoe and F Slack. The Fission of Uranium. *Physical Review*, 55(5):511–512, 1939.

[51] RW Grimes and CRA Catlow. The Stability of Fission Products in Uranium Dioxide. *Philosophical Transactions of the Royal Society A: Mathematical, Physical and Engineering Sciences*, 335(1639):609–634, 1991.

[52] GH Kinchin and RS Pease. The Displacement of Atoms in Solids by Radiation. *Reports on Progress in Physics*, 18(1):1–51, 1955.

[53] CR Stanek, RW Grimes and MR Bradford. Segregation of Fission Products to Surfaces of UO_2. *Materials Research Society Symposium Proceedings*, 654:AA3.32, 2001.

[54] G Seaborg. Some Comments on the Mechanism of Fission. *Physical Review*, 85(1):157–158, 1952.

[55] R Feynman, F Dehoffmann and R Serber. Dispersion of the neutron emission in U-235 fission. *Journal of Nuclear Energy*, 3(1-2):64–69, 1956.

[56] R Brandt, F Carbonara, E Cieslak, I Jarstorff, J Piekarz, R Rinzivillo and J Zakrzewski. Ternary Fission of Uranium Nuclei Induced by High-Energy Protons. *Die Naturwissenschaften*, 1969.

[57] H Kleykamp. The chemical state of the fission products in oxide fuels. *Journal of Nuclear Materials*, 131(2-3):221–246, 1985.

[58] KJW Atkinson. Private communication - FISPIN 7A inventory predictions for PWR UO_2 fuel, 2007.

[59] K Une, K Nogita, S Kashibe and M Imamura. Microstructural change and its influence on fission gas release in high burnup UO_2 fuel. *Journal of Nuclear Materials*, 188:65–72, 1992.

[60] JH Davies and FT Ewart. The chemical effects of composition changes in irradiated oxide fuel materials. *Journal of Nuclear Materials*, 41(2):143–155, 1971.

[61] CRA Catlow. Recent problems and progress in the study of UO_2 and mixed UO_2-PuO_2. *Journal of the Chemical Society, Faraday Transactions 2*, 83(7):1065, 1987.

[62] CRA Catlow and RW Grimes. The charge state of Xe in UO_2. *Journal of Nuclear Materials*, 165(3):313–314, 1989.

[63] M Wenman, J Barton, K Trethewey, S Jarman and P Chard-Tuckey. *Finite Element Modelling of Transgranular Chloride Stress Corrosion Cracking in 304L Austenitic Stainless Steel.* 2008.

[64] CEA publication. *Nuclear Fuels.* 2009.

[65] FA Kröger and HJ Vink. Relations between the Concentrations of Imperfections in Crystalline Solids. *Solid State Physics*, 3:307–435, 1956.

[66] M Kinoshita. Temperature and fission rate effects on the rim structure formation in a UO_2 fuel with a burnup of 7.9% FIMA. *Journal of Nuclear Materials*, 252(1-2):71–78, 1998.

[67] R White. The fractal nature of the surface of uranium dioxide: a resolution of the short-lived/stable gas release dichotomy. *Journal of Nuclear Materials*, 295(2-3):133–148, 2001.

[68] J Turnbull and R Cornell. The re-solution of fission-gas atoms from bubbles during the irradiation of UO_2 at an elevated temperature. *Journal of Nuclear Materials*, 41(2):156–160, 1971.

[69] R White and M Tucker. A new fission-gas release model. *Journal of Nuclear Materials*, 118(1):1–38, 1983.

[70] Y Kim. Theoretical analysis of two-stage fission gas release processes: grain lattice and grain boundary diffusion. *Journal of Nuclear Materials*, 326(2-3):97–105, 2004.

[71] R White. The development of grain-face porosity in irradiated oxide fuel. *Journal of Nuclear Materials*, 325(1):61–77, 2004.

[72] S Kashibe, K Une and K Nogita. Formation and growth of intragranular fission gas bubbles in UO_2 fuels with burnup of 6-83 GWd/t. *Journal of Nuclear Materials*, 206(1):22–34, 1993.

[73] C Frinskney and J Turnbull. The characteristics of fission gas release from uranium dioxide during irradiation. *Journal of Nuclear Materials*, 79(1):184–198, 1979.

[74] J Killeen. Fission gas release and swelling in UO_2 doped with Cr_2O_3. *Journal of Nuclear Materials*, 88(2-3):177–184, 1980.

[75] J Killeen. The effect of additives on the irradiation behaviour of UO_2. *Journal of Nuclear Materials*, 58(1):39–46, 1975.

[76] C Ronchi and H Matzke. Calculations on the in-pile behavior of fission gas in oxide fuels. *Journal of Nuclear Materials*, 45(1):15–28, 1972.

[77] DC Parfitt and RW Grimes. Predicted mechanisms for radiation enhanced helium resolution in uranium dioxide. *Journal of Nuclear Materials*, 381(3):216–222, 2008.

[78] P Blair, A Romano, C Hellwig and R Chawla. Calculations on fission gas behaviour in the high burnup structure. *Journal of Nuclear Materials*, 350(3):232–239, 2006.

[79] J Kim, B Choi, J Baek and Y Jeong. Effects of oxide and hydrogen on the behavior of Zircaloy-4 cladding during the loss of the coolant accident (LOCA). *Nuclear Engineering and Design*, 236(22):2386–2393, 2006.

[80] H Okamoto. O-U (Oxygen-Uranium). *Journal of Phase Equilibria and Diffusion*, 28(5):497–497, 2007.

[81] J Spino and P Peerani. Oxygen stoichiometry shift of irradiated LWR-fuels at high burn-ups: Review of data and alternative interpretation of recently published results. *Journal of Nuclear Materials*, 375:8–25, 2007.

[82] A Leenaers, L de Tollenaere, Ch Delafoy, S Van den Berghe. On the solubility of chromium sesquioxide in uranium dioxide fuel. *Journal of Nuclear Materials*, 317(1):62–68, 2003.

[83] CRA Catlow. Oxidation reactions and dopants in non-stoichiometric UO_2. *Journal of Nuclear Materials*, 79(2):432–434, 1979.

[84] A Sengupta. Effect of titania addition on hot hardness of UO_2. *Journal of Nuclear Materials*, 325(2-3):141–147, 2004.

[85] K Song. A mechanism for the sintered density decrease of UO_2-Gd_2O_3 pellets under an oxidizing atmosphere. *Journal of Nuclear Materials*, 288(2-3):92–99, 2001.

[86] J Edwards, RD Grimoldby, SJ Marshall and RW Stratton. BNFL Supply of MOX Fuel Assemblies to the Beznau 1 PWR of NOK. *Proceedings of a Technical Committee meeting held in Newby Bridge, Windermere, United Kingdom, 3-7 July 1995*:57–67, 1995.

[87] WA Lambertson and MH Mueller. Uranium Oxide Phase Equilibrium Systems: I, UO_2-Al_2O_3. *Journal of the American Ceramic Society*, 36(10):329–331, 1953.

[88] S Kashibe and K Une. Effect of additives (Cr_2O_3, Al_2O_3, SiO_2, MgO) on diffusional release of Xe from UO_2 fuels. *Journal of Nuclear Materials*, 254(2-3):234–242, 1998.

[89] F Franceschini and B Petrović. Fuel with advanced burnable absorbers design for the IRIS reactor core: Combined Erbia and IFBA. *Annals of Nuclear Energy*, 36(8):1201–1207, 2009.

[90] Y Harada. Sintering behaviour of niobia-doped large grain UO_2 pellet. *Journal of Nuclear Materials*, 238(2-3):237–243, 1996.

[91] S Glasstone and A Sesonske. *Nuclear Reactor Engineering: Reactor systems engineering*. 1994.

[92] R Dubourg, H Austregesilo, C Bals, M Barrachin, J Birchley, T Haste, JS Lamy, T Lind, B Maliverney and C Marchetto. Understanding the behaviour of absorber elements in silverâĂŞindiumâĂŞcadmium control rods during PWR severe accident sequences. *Progress in Nuclear Energy*, 52(1):97–108, 2010.

[93] RJ Cox and J Walker. The control of nuclear reactors. *Proceedings of the IEE - Part B: Radio and Electronic Engineering*, 103(11):577–589, 1956.

[94] B Cox and C Wu. Transient effects of lithium hydroxide and boric acid on Zircaloy corrosion. *Journal of Nuclear Materials*, 224(2):169–178, 1995.

[95] K Iwasaki, T Matsui, K Yanai, R Yuda, Y Arita, T Nagasaki, N Yokoyama, I Tokura, K Une and K Harada. Effect of Gd_2O_3 Dispersion on the Thermal Conductivity of UO_2. *Journal of Nuclear Science and Technology*, 46(7):673–676, 2009.

[96] MIK Santala, AS Daavittila, HM Lauranto and RRE Salomaa. Odd-isotope enrichment studies of Gd by double resonance laser-ionization for the production of burnable nuclear reactor poison. *Applied Physics B: Lasers and Optics*, 64(3):339–347, 1997.

[97] S Taylor. Abundance of chemical elements in the continental crust: a new table. *Geochimica et Cosmochimica Acta*, 28(8):1273–1285, 1964.

[98] H Oberhummer. Stellar Production Rates of Carbon and Its Abundance in the Universe. *Science*, 289(5476):88–90, 2000.

[99] AW Fairhall. *No Title*. 1960.

[100] WA Sedlacek and VA Ryan. Prompt activation analysis for lithium-6. *Analytical Chemistry*, 40(4):678–682, 1968.

[101] H Bradt and B Peters. Abundance of Lithium, Beryllium, Boron and Other Light Nuclei in the Primary Cosmic Radiation and the Problem of Cosmic-Ray Origin. *Physical Review*, 80(6):943–953, 1950.

[102] WH Blake, DE Walling and Q He. Fallout beryllium-7 as a tracer in soil erosion investigations. *Applied radiation and isotopes : including data, instrumentation and methods for use in agriculture, industry and medicine*, 51(5):599–605, 1999.

[103] K Nishiizumi, M Imamura, M Caffee, J Southon, R Finkel and J Mcaninch. Absolute calibration of 10Be AMS standards. *Nuclear Instruments and Methods in Physics Research Section B: Beam Interactions with Materials and Atoms*, 258(2):403–413, 2007.

[104] E Thorson Brown, JM Edmond, GM Raisbeck, DL Bourlés, F Yiou, CI Measures. Beryllium isotope geochemistry in tropical river basins. *Geochimica et Cosmochimica Acta*, 56(4):1607–1624, 1992.

[105] E Vangioni-Flam, M Cassé and J Audouze. Lithium-beryllium-boron: origin and evolution. *Physics Reports*, 333-334:365–387, 2000.

[106] C Cole and H Bonin. The near boiling reactior: design of a small, inherently safe, nuclear reactor to extend the victoria-class submarine. *Nuclear Technology*, 2007.

[107] L Stewart. Neutron Spectrum and Absolute Yield of a Plutonium-Beryllium Source. *Physical Review*, 98(3):740–743, 1955.

[108] R Macklin, N Lazar and W Lyon. Neutron Activation Cross Sections with Sb-Be Neutrons. *Physical Review*, 107(2):504–508, 1957.

[109] H Kawamura. Application of beryllium intermetallic compounds to neutron multiplier of fusion blanket. *Fusion Engineering and Design*, 61-62:391–397, 2002.

[110] R Aymar, P Barabaschi and Y Shimomura. The ITER design. *Plasma Physics and Controlled Fusion*, 44(5):519–565, 2002.

[111] S Korff and W Danforth. Neutron Measurements with Boron-Trifluoride Counters. *Physical Review*, 55(10):980–980, 1939.

[112] SH Cohn, KK Shukla, CS Dombrowski and RG Fairchild. Design Be calibration source of a "broad-beam" for total-body neutron neutron activation. *Journal of Nuclear Medicine*, 13(7):487–492, 1972.

[113] J Tittman and WB Nelligan. Laboratory Studies of a Pulsed Neutron-Source Technique in Well Logging. *Journal of Petroleum Technology*, 12(7), 1960.

[114] IF Zhezherun. The study of neutron diffusion in beryllium by a pulse method. *Soviet Atomic Energy*, 16(3):264–268, 1964.

[115] WH Bragg. Bakerian Lecture: X-Rays and Crystal Structure. *Philosophical Transactions of the Royal Society A: Mathematical, Physical and Engineering Sciences*, 215(523-537):253–274, 1915.

[116] An Observation of Optick Glasses, Made of Rock-Crystal. *Philosophical Transactions of the Royal Society of London*, 1(1-22):362–362, 1665.

[117] AM Stoneham. *Theory of Defects in Solids*. 1975.

[118] F Agulló-López, CRA Catlow and PD Townsend. *Point Defects in Materials*. 1988.

[119] AC Damask, GJ Dienes and R Smoluchowski. Point Defects in Metals. *Physics Today*, 17(11):74, 1964.

[120] RE Howard and AB Lidiard. Thermoelectric power of ionic crystals. *Discussions of the Faraday Society*, 23:113, 1957.

[121] IM Boswarva and AB Lidiard. The energy of formation of Schottky defects in ionic crystals. *Philosophical Magazine*, 16(142):805–826, 1967.

[122] CRA Catlow. Defect clusters in doped fluorite crystals. *Journal of Physics C: Solid State Physics*, 6(4):L64–L70, 1973.

[123] CRA Catlow, J Corish and PWM Jacobs. A calculation of the Frenkel defect formation energy in silver chloride. *Journal of Physics C: Solid State Physics*, 12(17):3433–3445, 1979.

[124] CRA Catlow. Point Defect and Electronic Properties of Uranium Dioxide. *Proceedings of the Royal Society A: Mathematical, Physical and Engineering Sciences*, 353(1675):533–561, 1977.

[125] CL Bishop, RW Grimes and DC Parfitt. Establishing the isotropy of displacement cascades in UO_2 through molecular dynamics simulation. *Nuclear Instruments and Methods in Physics Research Section B: Beam Interactions with Materials and Atoms*, 268(19):2915–2917, 2010.

[126] MJ Norgett, MT Robinson and IM Torrens. A proposed method of calculating displacement dose rates. *Nuclear Engineering and Design*, 33(1):50–54, 1975.

[127] ST Murphy, BP Uberuaga, JB Ball, AR Cleave, KE Sickafus, R Smith, and RW Grimes. Cation diffusion in magnesium aluminate spinel. *Solid State Ionics*, 180(1):1–8, 2009.

[128] AR Allnatt and AB Lidiard. *Atomic Transport in Solids*. 1993.

[129] D Adams. *Life, the Universe and Everything*. 1982.

[130] RW Grimes. Solution of MgO, CaO and TiO_2, in alpha-Al_2O_3. *Journal of the American Ceramic Society*, 77:378–384, 1994.

[131] PV Nerikar, X-Y Liu, BP Uberuaga, CR Stanek, SR Phillpot and SB Sinnott. Thermodynamics of fission products in UO_{2x}. *Journal of physics. Condensed matter : an Institute of Physics journal*, 21(43):435602, 2009.

[132] M Abramowski, RW Grimes and S Owens. Morphology of UO_2. *Journal of Nuclear Materials*, 275(1):12–18, 1999.

[133] G Busker, RW Grimes and MR Bradford. The solution and diffusion of ruthenium in $UO_{2\pm x}$. *Journal of Nuclear Materials*, 312(2-3):156–162, 2003.

[134] S Nicoll, H Matzke, RW Grimes and CRA Catlow. The behaviour of single atoms of molybdenum in urania. *Journal of Nuclear Materials*, 240(3):185–195, 1997.

[135] M Pirzada, RW Grimes, L Minervini, JF Maguire and KE Sickafus. Oxygen migration in A_2B2O_7 pyrochlores. *Solid State Ionics*, 140(3-4):201–208, 2001.

[136] G Busker, A Chroneos, RW Grimes and I-W. Chen. Solution Mechanisms for Dopant Oxides in Yttria. *Journal of the American Ceramic Society*, 82(6):1553–1559, 2004.

[137] AHH Tan, RW Grimes and S Owens. Structures of UO_2 and PuO_2 surfaces with hydroxide coverage. *Journal of Nuclear Materials*, 344(1-3):13–16, 2005.

[138] K Atkinson, RW Grimes, MR Levy, ZL Coull and T English. Accommodation of impurities in α-Al_2O_3, α-Cr_2O_3 and α-Fe_2O_3. *Journal of the European Ceramic Society*, 23(16):3059–3070, 2003.

[139] M Sepliarsky, A Asthagiri, SR Phillpot, MG Stachiotti and RL Migoni. Atomic-level simulation of ferroelectricity in oxide materials. *Current Opinion in Solid State and Materials Science*, 9(3):107–113, 2005.

[140] B Dick and A Overhauser. Theory of the Dielectric Constants of Alkali Halide Crystals. *Physical Review*, 112(1):90–103, 1958.

[141] M Born and R Oppenheimer. Zur Quantentheorie der Molekeln. *Annalen der Physik*, 389(20):457–484, 1927.

[142] J Slater. The Normal State of Helium. *Physical Review*, 32(3):349–360, 1928.

[143] J Slater. Atomic Shielding Constants. *Physical Review*, 36(1):57–64, 1930.

[144] AD Becke. Real-space post-Hartree-Fock correlation models. *The Journal of chemical physics*, 122(6):064101, 2005.

[145] W Kohn and LJ Sham. Self-Consistent Equations Including Exchange and Correlation Effects. *Physical Review*, 140(4A):A1133–A1138, 1965.

[146] PAM Dirac. Note on Exchange Phenomena in the Thomas Atom. *Mathematical Proceedings of the Cambridge Philosophical Society*, 26(03):376, 2008.

[147] JP Perdew, K Burke and M Ernzerhof. Generalized Gradient Approximation Made Simple. *Physical Review Letters*, 77(18):3865–3868, 1996.

[148] JP erdew, K Burke and Y Wang. Generalized gradient approximation for the exchange-correlation hole of a many-electron system. *Physical Review B*, 54(23):16533–16539, 1996.

[149] F Bloch. Über die Quantenmechanik der Elektronen in Kristallgittern. *Zeitschrift fur Physik*, 52(7-8):555–600, 1929.

[150] E Fermi. Motion of neutrons in hydrogenous substances. *Ricerca Scientifica*, 7:13–52, 1936.

[151] MC Payne, TA Arias and JD Joannopoulos. Iterative minimization techniques for ab initio total-energy calculations: molecular dynamics and conjugate gradients. *Reviews of Modern Physics*, 64(4):1045–1097, 1992.

[152] MR Levy, CR Stanek, A Chroneos and RW Grimes. Defect chemistry of doped bixbyite oxides. *Solid State Sciences*, 9(7):588–593, 2007.

[153] G Henkelman, BP Uberuaga and H JoÌĄnsson. A climbing image nudged elastic band method for finding saddle points and minimum energy paths. *The Journal of Chemical Physics*, 113(22):9901, 2000.

[154] JD Gale. GULP: A computer program for the symmetry-adapted simulation of solids. *Journal of the Chemical Society, Faraday Transactions*, 93(4):629–637, 1997.

[155] NF Mott and MJ Littleton. Conduction in polar crystals. I. Electrolytic conduction in solid salts. *Transactions of the Faraday Society*, 34:485, 1938.

[156] L Minervini, MO Zacatea and RW Grimes. Defect cluster formation in M_2O_3-doped CeO_2. *Solid State Ionics*, 116(3-4):339–349, 1999.

[157] Eric Falkenstein. *Finding Alpha: The Search for Alpha When Risk and Return Break Down.* 2009.

[158] M Amaya, M Hirai, H Sakurai, K Ito, M Sasaki, T Nomata, K Kamimura and R Iwasaki. Thermal conductivities of irradiated UO_2 and (U,Gd)O_2 pellets. *Journal of Nuclear Materials*, 300(1):57–64, 2002.

[159] P Wilde and CRA Catlow. Defects and diffusion in pyrochlore structured oxides. *Solid State Ionics*, 112(3-4):173–183, 1998.

[160] M Zacate, L Minervini, DJ Bradfield, RW Grimes and KE Sickafus. Defect cluster formation in M_2O_3-doped cubic ZrO_2. *Solid State Ionics*, 128(1-4):243–254, 2000.

[161] Boris Dorado, Julien Durinck, Philippe Garcia, Michel Freyss and Marjorie Bertolus. An atomistic approach to self-diffusion in uranium dioxide. *Journal of Nuclear Materials*, 400(2):103–106, 2010.

[162] A Leyva, D Vegaa, V Trimarcob, D Marchi. Homogeneity characterisation of sintered (U,Gd)O_2 pellets by X-ray diffraction. *Journal of Nuclear Materials*, 303(1):29–33, 2002.

[163] B Dorado, P Garcia, G Carlot, C Davoisne, M Fraczkiewicz, B Pasquet, M Freyss, C Valot, G Baldinozzi, D Siméone and M Bertolus. First-principles calculation and experimental study of oxygen diffusion in uranium dioxide. *Physical Review B*, 83(3), 2011.

[164] DR Lide *CRC Handbook of Chemistry and Physics.* 85 edition, 2004.

[165] RJM Konings, R Conrad, G Dassel, BJ Pijlgroms, J Somers and E Toscano. The EFTTRA-T4 experiment on americium transmutation. *Journal of Nuclear Materials*, 282(2-3):159–170, 2000.

[166] Ch Hellwig, M Streit, P Blair, T Tverberg, FC Klaassen, RPC Schram, F Vettraino and T Yamashita. Inert matrix fuel behaviour in test irradiations. *Journal of Nuclear Materials*, 352(1-3):291–299, 2006.

[167] RD Shannon. Revised effective ionic radii and systematic studies of interatomic distances in halides and chalcogenides. *Acta Crystallographica Section A*, 32(5):751–767, 1976.

[168] WA Lambertson, MH Mueller and FH Gunzel. Uranium Oxide Phase Equilibrium Systems: IV, UO_2-ThO_2. *Journal of the American Ceramic Society*, 36(12):397–399, 1953.

[169] W Radorff and G Valet. Über das Ceruranblau und Mischkristalle im System CeO_2-UO_2-U_3O_8. *Zeitschrift fi£¡r anorganische und allgemeine Chemie*, 271(5-6):257–272, 1953.

[170] T Ohmichi, S Fukushima, A Maeda and H Watanabe. On the relation between lattice parameter and O/M ratio for uranium dioxide-trivalent rare earth oxide solid solution. *Journal of Nuclear Materials*, 102(1-2):40–46, 1981.

[171] GI Ploetz, AI Muccigrosso, LM Osika and WR Jacoby. Dysprosium Oxide Ceramics. *Journal of the American Ceramic Society*, 43(3):154–159, 1960.

[172] Jong-Goo Kim, Yeong-Keong Ha, Soon-Dal Park, Kwang-Yong Jee and Won-Ho Kim. Effect of a trivalent dopant, Gd^{3+}, on the oxidation of uranium dioxide. *Journal of Nuclear Materials*, 297(3):327–331, 2001.

[173] F Hund and U Peetz. Further Fluorite Phases in Mixed Oxides of Rare Earths With Uranium; Investigations of the Systems. *Zeitschrift für anorganische und allgemeine Chemie*, 271:6–16, 1952.

[174] T Yamashita, T Fujino and H Tagawa. Phase relations and crystal chemistry in the ternary $PrO_{1.5}$-UO_2-O_2 system. *Journal of Nuclear Materials*, 132(2):192–201, 1985.

[175] Y Hinatsu. Magnetic studies on (U, La)O_{2+x} solid solutions. *Journal of Solid State Chemistry*, 95(2):300–306, 1991.

[176] RJ Beals, JH Handwerk and BJ Wrona. Behavior of Urania-Rare-Earth Oxides at High Temperatures. *Journal of the American Ceramic Society*, 52(11):578–581, 1969.

[177] JS Anderson, DN Edgington, LEJ Roberts and E Wait. The oxides of uranium. Part IV. The system UO_2-ThO_2-O. *Journal of the Chemical Society (Resumed)*, page 3324, 1954.

[178] EJ McIver. Unit cell size of solid solutions of uranium dioxide and fission product oxides. Technical report, 1966.

[179] H Kleykamp. The chemical state of LWR high-power rods under irradiation. *Journal of Nuclear Materials*, 84(1-2):109–117, 1979.

[180] J Haberkorn and J Haberkorn. *Einstein's Trunk*. 2011.

[181] J Spino and J Papaioannou. Lattice parameter changes associated with the rim-structure formation in high burn-up UO_2 fuels by micro X-ray diffraction. *Journal of Nuclear Materials*, 281(2-3):146–162, 2000.

[182] C Bagger, M Mogensen and C Walker. Temperature measurements in high burnup UO_2 nuclear fuel: Implications for thermal conductivity, grain growth and gas release. *Journal of Nuclear Materials*, 211(1):11–29, 1994.

[183] R Jackson and CRA Catlow. Trapping and solution of fission Xe in UO_2.Part 1. Single gas atoms and solution from underpressurized bubbles. *Journal of Nuclear Materials*, 127(2-3):161–166, 1985.

[184] RGJ Ball and RW Grimes. Diffusion of Xe in UO_2. *Journal of the Chemical Society, Faraday Transactions*, 86(8):1257, 1990.

[185] R Shelton. *No direction home: the life and music of Bob Dylan*. 1997.

[186] S Zhu, WG Fahrenholtz, GE Hilmas and SC Zhang. Pressureless Sintering of Zirconium Diboride Using Boron Carbide and Carbon Additions. *Journal of the American Ceramic Society*, 90(11):3660–3663, 2007.

[187] WG Fahrenholtz, GE Hilmas, IG Talmy and JA Zaykoski. Refractory Diborides of Zirconium and Hafnium. *Journal of the American Ceramic Society*, 90(5):1347–1364, 2007.

[188] L Bsenko and T Lundstrom. The high-temperature hardness of ZrB_2 and HfB_2. *Journal of the Less Common Metals*, 34(2):273–278, 1974.

[189] V Milman, B Winkler and MIJ Probert. Stiffness and thermal expansion of ZrB_2 : an ab initio study. *Journal of Physics: Condensed Matter*, 17(13):2233–2241, 2005.

[190] MR Levy, KJW Atkinson, OH Odili and RW Grimes. Dielectric relaxation of lithium-doped zinc fluoride. *Physica B: Condensed Matter*, 365(1-4):147–154, 2005.

[191] SA Badikov, C Zhenpeng, AD Carlson, EV Gai, Gm Hale, Hambsch FJ, HM Hoffmann, T Kawano, NM Larson, VG Pronyaev, DL Smith, Soo-Youl Oh, S Tagesen and H Vonach. International Evaluation of Neutron Cross-Section Standards. Technical report, International Atomic Energy Agency, Vienna, 2007.

[192] RGJ Ball and PG Dickens. Computer-simulation study of alkali-metal insertion into α-U_3O_8. *Journal of Materials Chemistry*, 1(3):415, 1991.

[193] George Bernard Shaw. *Man and Superman.* 2008.

[194] H Krimmel. Hydrogen and vacancies in the tokamak plasma-facing material beryllium. *Journal of Nuclear Materials*, 255(1):72–74, 1998.

[195] H Krimmel and M. Fähnle. Properties of hydrogen isotopes in the tokamak plasma-facing material beryllium. *Journal of Nuclear Materials*, 231(1-2):159–161, 1996.

[196] A Allouche, M Oberkofler, M Reinelt and Ch Linsmeier. Quantum Modeling of Hydrogen Retention in Beryllium Bulk and Vacancies. *The Journal of Physical Chemistry C*, 114(8):3588–3598, 2010.

[197] B Souledebas. The electronic structure of Be and BeO: benchmark EMS measurements and LCAO calculations. *Journal of Physics and Chemistry of Solids*, 64(3):495–505, 2003.

[198] G Kresse. From ultrasoft pseudopotentials to the projector augmented-wave method. *Physical Review B*, 59(3):1758–1775, 1999.

[199] Georg Kresse, Martijn Marsman and Jürgen Furthmüller. Vienna Ab-initio Simulation Package. Technical report, 2011.

[200] S Jonsson, K Kaltenbach and G Petzow. Phase-relations in the berylliu-rich section of the system beryllium-copper-iron. *Zietshrift fun Metallkunde*, 73(8):534–539, 1982.

[201] JA Carrabine. Ternary AlMnBe4 phases in commercially pure beryllium. *Journal of Nuclear Materials*, 8(2):278–280, 1963.

[202] TW Baker. Interatomic distances in the intermetallic compounds $MgBe_{13}$ and $CaBe_{13}$. *Acta Crystallographica*, 15(3):175–179, 1962.

[203] P Rooksby. Intermetallic Phases in Commercial Beryllium. *Journal of Nuclear Materials*, 2(2):205–211, 1962.

[204] H Okamoto and LE Tanner. *Journal of Phase Equilibria and Diffusion*, 8:392, 1987.

[205] DH Carter and MAM Bourke. Neutron diffraction study of the deformation behavior of berylliumâĂŞaluminum composites. *Acta Materialia*, 48(11):2885–2900, 2000.

[206] P Cao, M Qian and D Stjohn. Grain coarsening of magnesium alloys by beryllium. *Scripta Materialia*, 51(7):647–651, 2004.

[207] SA Reed, ES Funston and WL Bridges. Analysis of beryllium carbide. *Analytica Chimica Acta*, 10:429–442, 1954.

[208] CT Tzeng, KD Tsuei and WS Lo. Experimental electronic structure of Be_2C. *Physical Review B*, 58(11):6837–6843, 1998.

[209] IN Fridlyander, KP Yatsenko, GA Nekrasova, VS Sandler, ZG Semenova and AN Gulin. Relationships between changes in the structure and properties of beryllium-aluminum alloys. *Metal Science and Heat Treatment*, 12(7):599–603, 1970.

[210] V Raghavan. Al-Be-Si (Aluminum-Beryllium-Silicon). *Journal of Phase Equilibria and Diffusion*, 28(6):538–539, 2007.

[211] H Okamoto. Al-Be (Aluminum-Beryllium). *Journal of Phase Equilibria & Diffusion*, 27(4):424–425, 2006.

[212] LE Tanner and H Okamoto. The Be-Fe (Beryllium-Iron) system. *Bulletin of Alloy Phase Diagrams*, 9(4):494–508, 1988.

[213] B Scovell. *Bill Nicholson: Football's Perfectionist*. 2011.

[214] P Nerikar, D Parfitt, L Casillas Trujillo, D Andersson, C Unal, S Sinnott, RW Grimes, BP Uberuaga and CR Stanek. Segregation of xenon to dislocations and grain boundaries in uranium dioxide. *Physical Review B*, 84(17), 2011.

[215] PV Nerikar, K Rudman, TG Desai, D Byler, C Unal, KJ McClellan, SR Phillpot, SB Sinnott, P Peralta, BP beruaga and CR Stanek. Grain Boundaries in Uranium Dioxide: Scanning Electron Microscopy Experiments and Atomistic Simulations. *Journal of the American Ceramic Society*, 94(6):1893–1900, 2011.

[216] NA Ivanova, Yu G Godin and VG Baranov. Nonstoichiometry Effect on the Thermodynamic Properties of Uranium Dioxide Containing Alumina, Silica and Niobia Additions. *INorganic Materials*, 39(7):710–714, 2003.

[217] B Dorado, B Amadon, M Freyss and M Bertolus. DFT+U calculations of the ground state and metastable states of uranium dioxide. *Physical Review B*, 79(23):1–8, 2009.



Moving On

Burg